Summer 8-21-2020

Wave Attenuation Capacity of Suspended Aquaculture Structures with Sugar Kelp and Mussels

Longhuan Zhu
University of Maine, longhuan.zhu@maine.edu

WAVE ATTENUATION CAPACITY OF SUSPENDED AQUACULTURE STRUCTURES WITH SUGAR KELP AND MUSSELS

By

Longhuan Zhu

B.S. Tianjin University, 2012

M.S. Tianjin University, 2015

A DISSERTATION

Submitted in Partial Fulfillment of the

Requirements for the Degree of

Doctor of Philosophy

(in Civil and Environmental Engineering)

The Graduate School

The University of Maine

August 2020

Advisory Committee:

Kimberly D. Huguenard, Assistant Professor of Civil and Environmental Engineering, Advisor

David W. Fredriksson, Professor of Naval Architecture and Ocean Engineering, Co-Advisor

William G Davids, Professor of Civil and Environmental Engineering

Lauren Ross, Assistant Professor of Civil and Environmental Engineering

Xudong Zheng, Associate Professor of Mechanical Engineering

WAVE ATTENUATION CAPACITY OF SUSPENDED AQUACULTURE STRUCTURES WITH SUGAR KELP AND MUSSELS

By Longhuan Zhu

Dissertation Advisors: Dr. Kimberly Huguenard and Dr. David W. Fredriksson

An Abstract of the Dissertation Presented
in Partial Fulfillment of the Requirements for the
Degree of Doctor of Philosophy
(in Civil and Environmental Engineering)

August 2020

Large aquaculture systems may have the potential to damp wave energy for coastal protection. The performance of these systems are influenced by the dynamics of components such as flexible kelp blades and mussel droppers. In this thesis, the dynamics of kelp blades and mussel droppers were investigated with a consistent-mass cable model with focus on understanding the asymmetric motion of kelp blades. The results showed the asymmetric blade motion in symmetric waves is caused by the spatial asymmetry of the encountered wave orbital velocities due to blade displacements and the asymmetric action on the blade by vertical wave orbital velocities. For the kelp grown from the bottom, the asymmetry of blade motion provides 'shelter' that could inhibit sediment suspension and coastal erosion. For suspended kelp attached to a longline, the asymmetric motion would induce the kelp to roll over the attachment in large wave conditions. With understanding the blade dynamics, physical model experiments using the morphological and mechanical properties of the cultivated *Saccharina latissima* at Saco Bay, Maine in the USA were conducted to investigate the wave attenuation characteristics of suspended kelp farms. The results indicated that 20 longlines with 100 plants/m could reduce up to 23% energy of 6.3 s waves. To predict wave attenuation under wider conditions, numerical and analytical wave attenuation models coupled with blade motion were developed for regular and irregular waves. With the analytical model, a case study at a site in Northeastern US showed the potential of suspended aquaculture farms to dissipate wave energy in a storm event. Compared to naturally occurring submerged aquatic vegetation (SAV), suspended aquaculture farms

were found to perform better at attenuating shorter waves and less impacted by water level changes due to tides, surge and sea level rise. Implementing offshore aquaculture structures in conjunction with SAV-based living shorelines that can enhance the coastal defense of SAV-based living shorelines. This research is useful for the design of suspended aquaculture structures for nature-based coastal protection. The analytical wave attenuation models are also convenient to implement in large-scale models to analyze the influences of wave attenuation on coastal morphology.

DEDICATION

To this era and to my parents, my elder brother and my wife.

ACKNOWLEDGEMENTS

"At thirty, I stood firm." ------*The Analects of Confucius*

Over the past five years of my Ph.D. study, I have had my ups and downs. However, I am very lucky to finish it in my thirtieth year. This cannot happen without the support and help from dedicated families, advisors and friends.

I would like to sincerely thank my former advisor Dr. Qingping Zou for leading me to this field and continuous suggestions for my research. I want to show my most sincere appreciation to my advisor Dr. Kimberly D. Huguenard and my co-advisor Dr. David W. Fredriksson for guiding and supporting me to finish the rest of my PhD journey. I appreciate for their patience, encouragement, and suggestions that would benefit my whole life. I also want to sincerely thank my committee, Dr. William G Davids, Dr. Lauren Ross, and Dr. Xudong Zheng for their insight and comments on my research.

I am grateful to Dr. Heidi Nepf and Dr. Jiarui Lei for supporting and assisting the laboratory experiments at MIT. I would like to thank Adam T. St. Gelais and Kathryn Johndrow for assistance in collecting and measuring *S. latissima* samples from the University of New England. I appreciate Dr. Shane Moeykens, Dr. Peter van Walsum, and Dr. Denise Skonberg for the support from SEANET project. I am thankful to Stephen Cousins and the Advanced Computing Group in The University of Maine System for computational support. I appreciate Dr. Neil Fisher for technical support and discussions about experimental instruments. I also want to express my thanks to Dr. Haifei Chen, Dr. Dongmei Xie, Zhilong Liu, Kristopher Bears, Dylan Schlichting, Sohaib Alahmed, Preston Spicer and other colleagues and friends (sorry for not listing here otherwise the acknowledgement page would be so long) for discussions, suggestions and help.

Finally, I would send my love to my family for their understanding and unconditionally support. $\theta\delta\theta\sigma\psi\pi\ \gamma\rho\sigma\beta\ \sigma\beta\ \gamma\rho\xi\ \lambda\xi\beta\gamma\ \pi\sigma o\gamma\ \gamma\omega\ \zeta\xi\phi\mu\omega\chi\xi\ \omega\delta\alpha\ \lambda\kappa\lambda\theta$.

This work was financially supported by National Science Foundation award #IIA-1355457 to Maine EPSCoR at the University of Maine.

TABLE OF CONTENTS

DEDICATION iii

ACKNOWLEDGEMENTS iv

LIST OF TABLES x

LIST OF FIGURES xi

Chapter

1. INTRODUCTION 1

    1.1 Asymmetric motion of flexible blades in waves 2

    1.2 Physical model experiments for wave attenuation by suspended kelp canopies 3

    1.3 Analytical wave attenuation model for flexible canopies 4

    1.4 Frequency dependent random wave attenuation by flexible canopies 6

    1.5 Outline 7

2. MECHANISMS FOR THE ASYMMETRIC MOTION OF SUBMERGED AQUATIC VEGETATION IN WAVES: A CONSISTENT-MASS CABLE MODEL 9

    2.1. Background 9

    2.2. Methodology 11

        2.2.1. 2D Cable model 12

        2.2.2. Hydrodynamic force coefficients 14

    2.3. Model-data comparison 15

        2.3.1. Blade motion in combined waves and currents 15

        2.3.2. Blade motion in waves 17

    2.4. Symmetric and asymmetric blade motions 25

        2.4.1. Definition 25

        2.4.2. Theory 26

        2.4.3. Case study 32

2.5. Discussion 35
2.5.1. Mechanisms for asymmetric blade motion 35
2.5.2. Conditions for symmetric blade motion 37
2.5.3. Properties and implications of asymmetric blade motion 38
2.6. Summary 39
2.7. Acknowledgments 40
3. WAVE ATTENUATION BY SUSPENDED CANOPIES WITH CULTIVATED KELP (*SACCHARINA LATISSIMA*) 41
3.1. Background 41
3.2. Materials and methods 44
3.2.1. Theory for blade dynamics and wave attenuation 44
3.2.2. Measurements for cultivated *S. latissima* 49
3.2.3. Experimental design 51
3.2.4. Wave decay measurements 53
3.3. Results 55
3.3.1. Morphological and mechanical properties of *S. latissima* compared with the model blade 55
3.3.2. Wave-induced motion of suspended blades 58
3.3.3. Horizontal force and wave attenuation 60
3.3.4. Bulk drag coefficient and effective blade length 63
3.4. Discussion 65
3.4.1. Roll-over of suspended flexible blades 65
3.4.2. Methods to predict wave attenuation 68
3.4.3. Suspended kelp aquaculture farms as nature-based coastal protection 68
3.4.4. Limitations 71
3.5. Summary 71

3.6. Acknowledgments 72
4. ANALYTICAL MODEL FOR WAVE ATTENUATION BY FLEXIBLE CANOPIES 73
4.1. Background 73
4.2. Methodology 76
4.2.1. Model set-up 76
4.2.2. Blade motion 77
4.2.3. Wave attenuation 80
4.2.4. Bulk drag coefficient and effective blade length 81
4.3. Results…. 83
4.3.1. Model-data comparison 83
4.3.2. Bulk drag coefficient and effective blade length 85
4.3.3. Case study for wave attenuation in different seasons 88
4.4. Discussion 91
4.4.1. Blade motion and the nonlinear effects 91
4.4.2. Evaluations of the methods to obtain bulk drag coefficient and effective blade length 93
4.4.3. Nature-based coastal protection strategies 93
4.5. Summary.. 94
4.6. Acknowledgments 95
5. AQUACULTURE FARMS AS NATURE-BASED COASTAL PROTECTION: RANDOM WAVE ATTENUATION BY SUSPENDED AND SUBMERGED CANOPIES 96
5.1. Background 96
5.2. Theory…. 100
5.2.1. Background on analytical wave attenuation models 100
5.2.2. Model set-up 103
5.2.3. Models for the motion of canopy components 105

5.2.3.1. Cantilever-beam model 106
5.2.3.2. Buoy-on-rope model 108
5.2.4. Solutions for random wave attenuation 109
5.3. Model-data comparison 110
5.3.1. Submerged canopy 110
5.3.2. Suspended canopy 114
5.4. Case study at the field site 116
5.4.1. Properties for the mussel farm and submerged aquatic vegetation 117
5.4.2. Mussel farm and SAV at the same water depth 119
5.4.3. Mussel farm and SAV at different water depths 123
5.5. Discussion 125
5.5.1. Wave attenuation characteristics of suspended aquaculture farms and SAV 125
5.5.2. Simplified analytical solutions 126
5.6. Summary.. 128
5.7. Acknowledgments 129
6. CONCLUSIONS 130
6.1. Chapter summary 130
6.2. Findings and academic contributions 130
6.2.1. Chapter 2: Asymmetric blade motion in waves 130
6.2.2. Chapter 3: Physical model experiments for wave attenuation by suspended kelp canopies 131
6.2.3. Chapter 4: Analytical wave attenuation model for flexible canopies 131
6.2.4. Chapter 5: Random wave attenuation by flexible canopies 132
6.3. Engineering implications for nature-based solutions 133
6.4. Suggestions for future research 134
BIBLIOGRAPHY 137

APPENDIX A: CONDITIONS FOR SYMMETRIC BLADE MOTION IN SYMMETRIC WAVES 154
APPENDIX B: WAVE HEIGHT FITTING ALONG A CANOPY WITH REFLECTIVE WAVES 156
APPENDIX C: PIECEWISE FUNCTION METHDOD REALTING KOBAYASHI AND DALRYMPLE WAVE ATTENUATION MODELS 157
Appendix C.1. Extension of the solution by Kobayashi et al. (1993) to suspended canopy 157
Appendix C.2. Extension of the solution by Dalrymple et al. (1984) to suspended canopy 158
Appendix C.3. Piecewise function method linking Kobayashi- and Dalrymple-based techniques 159
APPENDIX D: THE THREE-LAYER THEORETICAL SOLUTION FOR SUSPENDED AND SUBMERGED CANOPY BASED ON MOMENTUM AND CONTINUITY EQUATIONS 162
Appendix D.1. Governing equations 162
Appendix D.2. Linear solution 164
Appendix D.3. First-order approximation for the linear solution 167
APPENDIX E: NORMAL MODE SOLUTIONS FOR BLADE DISPLACEMENTS IN RANDOM WAVES 171
BIOGRAPHY OF THE AUTHOR 173

LIST OF TABLES

Table 2.1. Blade properties and wave conditions in the experiments by Zeller et al. (2014) and Luhar and Nepf (2016). 16

Table 2.2. Normalized time averaged error (ϵt) for the simulated excursions of the blade tip. 24

Table 2.3. Blade geometric and material properties for the selected species used in the present study following Lei and Nepf (2016). 32

Table 3.1. Morphological and mechanical properties of cultivated *S. latissima* and model kelp blades. 58

Table 3.2. Sheltering factor and wave attenuation measured in the experiments and projections to full scale. 61

Table 4.1. Canopy characteristics and wave conditions. 84

Table 5.1. Properties for the suspended canopies consisting of sphere components in the laboratory and field experiments (Seymour and Hanes, 1979). 115

Table 5.2. Properties of the mussel farm and submerged aquatic vegetation (SAV) meadow. 119

LIST OF FIGURES

Figure 2.1. Schematic diagram for the coordinate systems and the free-body diagram. 12

Figure 2.2. Model-data comparison for the normalized deflected blade-tip height (z_T/l) at the maximum horizontal displacement of the blade tip ($x_{T,max}$) vs the Cauchy number (Ca)..... 17

Figure 2.3. Measured horizontal component of the wave orbital velocity at $z = 0$ for the wave with period T_w = 2 s and amplitude a_w = 4 cm (Luhar & Nepf, 2016)..... 18

Figure 2.4. Comparisons for (a, b) the normalized horizontal displacement range of the blade-tip ($x_{T,max}$-$x_{T,min}$)/$2l$ and (c, d) the root-mean-square of the total horizontal force ($F_{x,\mathrm{rms}}$) normalized by the total horizontal force ($F_{x,\mathrm{rms,rigid}}$) for a rigid blade with the same geometry for (a, c) HPDE and (b, d) silicon foam blades, respectively.. 20

Figure 2.5. Blade postures and blade tip trajectory for the 20 cm-long (a) HDPE and (b) silicon foam blades over one wave period for the waves with period T_w = 2 s and amplitude a_w = 4 cm..... 21

Figure 2.6. Comparisons for (a-l) the 20 cm-long HDPE blade posture (x, z) normalized by blade length (l), (m) the differences between the simulated and observed blade-tip displacements (ϵ_T), and (n) the total horizontal force (F_x) normalized by the root-mean-square horizontal force by rigid plate with the same geometry $F_{x,\mathrm{rms,rigid}}$ along time (t). 22

Figure 2.7. Comparisons for (a-l) the 20 cm-long silicon foam blade posture (x, z) normalized by blade length (l), (m) the differences between the simulated and observed blade-tip displacements (ϵT), and (n) the total horizontal force (Fx) normalized by the root-mean-square horizontal force by rigid plate with the same geometry Fx, rms, rigid along time (t)..... 23

Figure 2.8. The blade posture asymmetry (β_{xT}) is defined as the ratio of time-averaged displacement of the blade tip (x_T) to the maximum absolute displacement ($x_{T\max}$)..... 26

Figure 2.9. Blade postures and blade tip trajectory for the 20 cm-long (a) HDPE and (b) silicon foam blades over one wave period for the symmetric waves with period T_w = 2 s and amplitude a_w = 4 cm. 27

Figure 2.10. The postures of the blade over one-half of a wave period ($\Delta t = T_w/2$) for symmetric motion. 29

Figure 2.11. Contour of the blade posture asymmetry (β_{xT}, in colors) vs the normal phase difference $\boldsymbol{\Psi_{nT}}$ and tangential phase difference $\boldsymbol{\Psi_{tT}}$ at the blade tip. 33

Figure 2.12. The blade posture asymmetry (β_{xT}) as a function of the ratio of blade length and wavelength ($\gamma = l/L$). 34

Figure 2.13. The postures of a 45 cm-long blade (in green) in the wave flow field with wave period T_w=3.2 s and amplitude a_w=5 cm in 1 m-deep water (intermediate water waves). 36

Figure 3.1. Sketch for the coordinate systems.. 44

Figure 3.2. (a) *S. latissima* sample with bending elastic modulus (E) at three positions along the blade length. (b) A specimen on a gridded cutting board. (c) Measuring the mass of a specimen with a digital analytical balance scale. (d) Bending test for a specimen. (e) Comparison between the measured and calculated blade postures. 50

Figure 3.3. Photos of (a) a model kelp longline and (b) the model kelp farms with waves propagating from left to right. Sketches of (c) the side view of the wave flume showing the setup of model kelp farms and wave gauges and (d) the front view of section A-A showing the setup of load cells. 52

Figure 3.4. Measured (black circles) and fitted (blue line, R^2=0.992) wave heights (H) normalized by the incident wave height (H_{I0}) along the model kelp farms for Case 1. 54

Figure 3.5. Morphological and mechanical properties of *S. latissima*. 56

Figure 3.6. Postures for (a, c, and e) a single blade and (b and d) a row of blades in waves with wave heights of (a and b) 1.5 cm, (c and d) 2.8 cm, and (e) 3.3 cm. 59

Figure 3.7. Comparisons for the measured and calculated (a) horizontal force ($F_{x,\,rms}$) for a row of blades and (b) wave decay coefficient (k_D).. 62

Figure 3.8. Measured and calculated wave decay coefficient (k_D) for the suspended model kelp canopy as a function of (a) kh, (b) H_{I0}/h, (c) l/h, and (d) d_1/h. 63

Figure 3.9. (a) Measured bulk drag coefficients (C_D) as a function of Keulegan-Carpenter number (KC) for the flexible part of the blade. 64

Figure 3.10. Suspended blade postures with flow field. 67

Figure 3.11. (a) Effects of the bending elastic modulus (E) and the length (l) of the blade as well as number of plants per meter on the wave energy dissipation ratio (EDR) of suspended kelp aquaculture farms. Wave attenuation as a function of the number of kelp longlines with (b) 100 plants/m and (c) 400 plants/m. 70

Figure 4.1. Sketch of the three-layer model for wave attenuation by suspended canopies (a) fixed at the bottom end and (b) fixed at the tip end. 77

Figure 4.2. Concept sketch for bulk drag coefficient (C_D) and effective blade length (l_e) methods. 82

Figure 4.3. (a) Comparisons between the numerical and analytical calculations for the wave decay coefficient k_{DB} for the flexible part of the blades. (b) Comparisons between the modified analytical solutions and the measurements for the wave decay coefficient k_D. 85

Figure 4.4. Comparisons for the bulk drag coefficients (C_D) of the flexible part of the blade between the measured, calculated using the analytical solution (4.16), and the fitted value for (a) suspended and (c) submerged canopies. Comparisons for the decay coefficient (k_D) calculated by fitted C_D and the analytically calculated C_D for (b) suspended and (d) submerged canopies. 86

Figure 4.5. Comparisons for the normalized effective blade length ($l_{f,e}/l_f$) of the flexible part of the blade (l_f) between the measured, calculated using the analytical solution (4.18), calculated using the empirical formula by Luhar and Nepf (2019b), and the fitted value for (a) suspended and (c) submerged canopies. Comparisons for the decay coefficient (k_D) calculated by the fitted $l_{f,e}$, the empirical formula in Lei and Nepf (2019b), and the analytically calculated $l_{f,e}$ for (b) suspended and (d) submerged canopies. 87

Figure 4.6. Design parameters for (a) kelp and (b) seagrass canopies over a year. 89
Figure 4.7. Wave energy dissipation rate (EDR) for the designed kelp (red lines) and seagrass (blue lines) canopies in a year around. 90
Figure 4.8. Comparisons between the analytical (linearized blade motion) and numerical (nonlinear blade motion) calculations for the (a1 and b1) blade postures (x, z), (a2, a3, b2, and b3) relative velocity (u_r), and (a4 and b4) time averaged drag flux $(f_d u_r)$ of the (a) suspended model kelp blade and (b) submerged model vegetation. 92
Figure 5.1. Canopy classification (from left to right): suspended aquaculture farms, floating wetlands, submerged plants, and emergent plants (figure credit: Yu-Ying Chen). 98
Figure 5.2. Definition sketch of variables and coordinate system for the three-layer theoretical model of waves propagating over a canopy. 104
Figure 5.3. Sketch for the cantilever-beam model and buoy-on-rope model for different species. 105
Figure 5.4. Comparisons of calculated frequency (*f*) dependent wave decay coefficient (β) by the present model and the data (black dotted lines) from Jacobsen et al. (2019a).. 113
Figure 5.5. Sketch of the suspended canopy consisting of sphere components according to the description of Seymour and Hanes (1979). 114
Figure 5.6. Comparisons between calculated and measured transmitted wave spectrum $(S_{\eta\eta})$ as well as spectral dissipation ratio (SDR) versus wave frequency (*f*) for suspended canopies with spheres in (a) laboratory and (b) field experiments by Seymour and Hanes (1979). 115
Figure 5.7. Comparisons between the calculated and measured wave energy dissipation ratio (EDR) for laboratory (blue +) and field experiments (red ×) by Seymour and Hanes (1979). 116
Figure 5.8. The study site at Saco Bay, Maine, USA (Sources: Esri, GEBCO, NOAA, National Geographic, DeLorme, HERE, Geonames.org, and other contributors). 118
Figure 5.9. Time evolution of (a) tide, storm tide and storm surge during the January 2015 North American blizzard, (b) significant wave height H_{s0} and the corresponding peak wave period T_p, (c) and (d)

calculated wave energy dissipation ratio (EDR) by the suspended mussel farm (blue lines) and submerged aquatic vegetation (SAV, red lines) using the wave spectrum data. 120

Figure 5.10. Comparisons of wave spectrum ($S_{\eta\eta}$) and wave spectral dissipation ratio (SDR) versus wave frequency (f) between the suspended mussel farm and submerged aquatic vegetation (SAV) with different canopy densities (shown in legend) at 10:00 UTC (a), 16:00 UTC (b), and 22:00 UTC (c) on Jan 27.. 122

Figure 5.11. (a) Comparisons of wave energy dissipation ratio (EDR) between the suspended mussel farm and submerged aquatic vegetation (SAV). 124

Figure 5.12. Relationship between the present solutions (5.22), (5.28), (5.29) and previous solutions by Chen and Zhao (2012), Jacobsen et al. (2019a), and Mendez and Losada (2004). 127

Figure A.1. The postures of a 20 cm-long blade in the wave flow field. 155

Figure C.1. A schematic illustration showing the piecewise function method. 159

Figure C.2. Relations between the wave height decay solutions by Kobayashi- and Dalrymple-based techniques from the perspective of the piecewise function method. 160

CHAPTER 1

INTRODUCTION

Approximately 40% of the world's population lives within 100 kilometers of the coast (MEA, 2005; Ferrario et al., 2014), and 71% of the coastal population lives within 50 kilometers of an estuary (UNEP, 2006). Coastal communities benefit from proximity to the marine environment, but also live at the risk of natural coastal hazards and extreme events. For example, from 1900 to 2017, 197 hurricanes with 206 landfalls in the US have caused about 2 trillion USD in normalized (2018) damage, or annually about 17 billion USD (Weinkle et al., 2018). Extreme waves and sea levels are likely to occur at an increasing frequency due to climate change (Izaguirre et al., 2011; Tebaldi et al., 2012; Ondiviela et al., 2014).

To prevent storm damage, conventional techniques typically include hard engineered structures such as seawalls, breakwaters, and bulkheads. Hardened structures, however, can reduce sediment sources, adversely impact water quality, and cause coastal habitat loss (Currin et al. 2010; Pace 2011; Sutton-Grier et al., 2015). If performance levels can be quantified, natural and nature-based infrastructure may be a viable alternative to hardened shorelines that may also have economic and ecological benefits (Borsje et al., 2011; Gedan et al., 2011).

A living shoreline represents a common example of nature-based infrastructure (Davis et al., 2015; Saleh & Weinstein, 2016). Living shorelines are natural, shallow water, protection structures that can also maintain or enhance a productive habitat (Currin et al., 2010; Scyphers et al., 2011; Bilkovic et al., 2016; Saleh & Weinstein, 2016; Gittman et al., 2016; Moosavi, 2017). These natural structures can include a variety of wetland plants, aquatic vegetation, kelp beds and oyster reefs. In a hybrid approach, these natural materials can be used in combination with hard-engineered structures. Usually, living shorelines at exposed, high-energy sites require some type of breakwater or sill to damp incident wave energy for more effective growth of the living organisms (McGehee, 2016).

Many aquaculture systems such as those comprised of kelp and mussels can also be considered as nature-based infrastructure with the ability to attenuate wave energy and provide coastal ecosystem service

as well. For example, Plew et al. (2005) observed that a 650 m × 2450 m mussel farm reduced wave energy by approximately 5%, 10%, and 17% at wave frequencies of 0.1, 0.2, and 0.25 Hz, respectively at low sea state. It was also found that naturally grown kelp may have advantageous wave attenuation characteristics (Mork, 1996). For instance, Mork (1996) measured a 70% to 85% wave energy reduction across a 258 m long kelp bed (dominated by *Laminaria hyperborea*) with the highest values observed during low tide. Unlike naturally grown kelp that attach to the seafloor, cultivated seaweeds are seeded on ropes in the water column (Peteiro and Freire, 2013; Peteiro et al., 2016; Walls et al., 2017). Since wave energy attenuates with depth, near surface cultivated seaweed are expected to have a larger impact on wave attenuation than beds growing on the bottom. Therefore, the overarching goal of this dissertation is to quantify the capacity and characteristics of suspended aquaculture structures with kelp and mussels on wave attenuation.

1.1 Asymmetric motion of flexible blades in waves

Chapter 2 describes the blade dynamics in waves. Wave attenuation capacity of nature-based infrastructure is mainly determined by the work of the drag induced by the biological components (Dalrymple et al., 1984; Kobayashi et al., 1993). For the shoreline structures with flexible components such as vegetation and kelp blades, the wave-induced motion of flexible blades reduces the drag and therefore diminish the wave dissipation by decrease the relative velocity between the flow and the blade (Mullarney and Henderson, 2010; Riffe et al., 2011; Houser et al., 2015; Rupprecht et al., 2017). The specific characteristics of blade motion in waves is also an important factor that influences the wave attenuation capacity of nature-based infrastructure.

The characteristics of blade motion in waves can be symmetric or asymmetric. Symmetric motion is a forward/backward oscillation over the wave period with near equal bending angles about the vertical axis. Asymmetric motion is oscillation with more bending in the direction of wave propagation. For instance, asymmetric behavior was described as a “whip-like” response by Rupprecht et al. (2017). Asymmetric motion could also induce drag asymmetry with less drag under the wave crest than the trough. According to Luhar et al. (2010 and 2013), the drag asymmetry effect could enhance mean flow in the direction of wave propagation. Enhanced mean flow could also reinforce asymmetry blade motion in a

meadow (Luhar et al., 2017). Blade inclination in the direction of wave propagation in a meadow may also provide "shelter" effects for sediment and further reduce bed-load transport and stabilize the seabed (Rupprecht et al., 2017). Although the asymmetric motion of single blades has been identified in laboratory experiments (e.g., Luhar and Nepf, 2016; Lei and Nepf, 2019b), the underlying mechanisms for asymmetric blade motion in waves could be further quantified.

To examine the effects of blade motion on wave attenuation, initial work focused on stiff vegetation with small amplitude motions (Asano et al., 1992; Dubi and Torum, 1995; Méndez and Losada, 1999; Mullarney and Henderson, 2010). Small-amplitude motion was modeled as forced linear vibration with one degree of freedom by Asano et al. (1992). This model was then used to analyze the small amplitude deflection of vegetation in Dubi and Torum (1994) and Méndez and Losada (1999). Euler-Bernoulli beam techniques were introduced by Mullarney and Henderson (2010) to analyze the mode shape of vegetation as well as its effects on wave dissipation. These models assume small deflections and therefore adopt linearized Euler-Bernoulli beam theory. To investigate large-amplitude motion, numerical techniques were developed considering the geometric nonlinearity, e.g., the vegetation models developed by Luhar and Nepf (2016) and the elastic-rod model coupled with Reynolds-averaged Navier-Stokes (RANS) and Volume of Fluid (VOF) solver proposed by Chen and Zou (2019). However, these vegetation dynamic models did not capture the asymmetric "whip-like" motion of flexible blades.

Therefore the objectives of Chapter 2 are to (1) develop a blade dynamic model that can capture the asymmetric "whip-like" motion of flexible blades, (2) simulate the mechanisms for the asymmetric motion of submerged aquatic vegetation in waves, (3) analyze the properties of blade asymmetric blade motion. Understanding the blade dynamics in waves is essential for the scaling of the physical model experiments and incorporating the blade motion effects into the wave attenuation model.

1.2 Physical model experiments for wave attenuation by suspended kelp canopies

Chapter 3 describes the physical model experiments for wave attenuation by suspended kelp farms based on the morphological and mechanical properties of cultivated *Saccharina latissima* (sugar kelp) at Saco Bay, Maine, USA. Experimental research into the hydrodynamic response of kelp started with the

investigation on the hydrodynamic characteristics of kelp blades in steady flow. Buck and Buchholz (2005) investigated the drag characteristics of both a single and an aggregate of *S. latissima* blades by towing the blades in still water. The results showed sheltering interactions among the blades so that the drag force of a bunch of kelp blades cannot be estimated by simply superimposing the drag of individual blades. To be more realistic, Vettori and Nikora (2019) investigated the turbulent flow interaction with single blades of *S. latissima* in an open-channel flume. At low current speed, the flapping motion of kelp blades of *S. latissima*, *M. pyrifera*, and *N. luetkeana* can significantly enhance the nutrient flux to the blade surface (Huang et al., 2011). Using polyethylene to model *S. latissima*, Vettori and Nikora (2018) found that the model kelp blades increase the turbulence intensity and reduce the mean longitudinal velocity. By comparing the hydrodynamic performance of *S. latissima* with the performance of the model blades considering dynamic similarity, Vettori and Nikora (2020) showed that the model blades replicated many aspects of *S. latissima* blade dynamics, although the drag force and reconfiguration were underestimated. To avoid the issues induced by downscaling, Fredriksson et al. (2020) conducted full-scale model experiments to understand the hydrodynamics of a bunch of model *S. latissima* blades in steady flow. Fredriksson et al. (2020) determined the threshold for the hydrodynamic force to transit from drag dominated to friction dominated. To date, no experimental studies demonstrate wave attenuation by suspended kelp aquaculture structures, and appropriate parameters from these experiments are essential for modeling wave attenuation with canopy models.

The objectives of Chapter 3 are to (1) measure the morphological and mechanical properties of cultivated *S. latissima* at Saco Bay, Maine, USA, (2) investigate the wave attenuation capacity of suspended kelp canopies with model laboratory experiments, and (3) develop bulk drag coefficient and effective blade length for suspended kelp canopy.

1.3 Analytical wave attenuation model for flexible canopies

Chapter 4 describes the analytical wave attenuation model for flexible canopies by incorporating the blade motion. Many wave attenuation models are based on the wave attenuation theories developed by

Dalrymple et al. (1984) and Kobayashi et al. (1993) assuming rigid vegetation without motion. Wave attenuation is dependent on the work of the canopy drag, which is proportional to the square of the relative velocity between the flow and the blade. Neglecting the blade motion can overestimate drag and therefore wave attenuation. In an effort to represent these uncertainties, a bulk drag coefficient (C_D) approach has been applied (e.g., Kobayashi et al., 1993; Mendez and Losada, 2004). Luhar et al. (2017) proposed a technique that considers the effects of blade motion by using a reduced effective blade length (l_e) rather than reduce the original drag coefficient (C_d). The effective blade length (l_e) is defined as the length of a rigid blade that dissipates the same wave energy as the flexible blade with the original length (l). The bulk drag coefficient and effective blade length methods reduce the complexity to model the wave-vegetation interaction so that these models are computationally efficient and convenient to be implemented on large scales. However, experiments are required to calibrate C_D and l_e. Conventionally, C_D is expressed as a function of Reynolds number (Re) or Keulegan–Carpenter number (KC) independent from vegetation flexural rigidity. Therefore, the Re- and KC-based empirical formulas for C_D are different for vegetation with different flexibilities, e.g., the different formulas in Mendez and Losada (2004), Sanchez-Gonzalez et al. (2011), Jadhav et al. (2013), Anderson and Smith (2014), and Ozeren et al. (2014) as summarized in Chen et al. (2018) and van Veelen et al. (2020). The empirical formula for l_e is expressed as a function of the Cauchy number (Ca) incorporating vegetation flexural rigidity and therefore applicable for a wider range of canopy types. Accurate parameterization of C_D and l_e is important to predict the wave attenuation (Fringer, 2019), which requires a full understanding of wave-vegetation interaction.

To quantify the blade motion, the blade is modeled as a cantilever beam assuming that the Euler-Bernoulli beam approach is applicable. By simplifying the blade motion as a balance between drag force and blade bending resistance, Mullarney & Henderson (2010) obtained linear normal mode solutions for the blade displacement along the length. The model was recently extended to include the effects of buoyancy by Henderson (2019). With the normal mode technique, Zhu et al. (2020a) obtained frequency dependent analytical solutions for blade displacements in random waves considering the effects of inertial

forces. As the analytical solutions are limited to small-amplitude blade motion, a more precise solution for the large-amplitude blade motion can be obtained with numerical techniques (e.g., Zeller et al., 2014; Zhu and Chen, 2015; Luhar and Nepf, 2016; Leclercq and de Langre, 2018; Zhu et al., 2018; Chen and Zou, 2019). The consistent-mass cable model described in Zhu et al. (2020b) was able to capture asymmetric ‘‘whip-like’’ blade motion. These analytical solutions have shown to be useful to describe the mechanisms that influence of blade motion related to wave attenuation. Analytical solutions are also easier to be implemented into large-scale models. As the analytical wave attenuation model is developed based on the small-amplitude blade motion. The nonlinearity effects induced by the large-amplitude blade motion on the wave attenuation model as well as its application has not been understood yet.

The objectives of Chapter 4 are to (1) develop an analytical wave attenuation model with resolving the blade motion, and (2) derive the analytical solutions for bulk drag coefficient and effective blade length.

1.4 Frequency dependent random wave attenuation by flexible canopies

Chapter 5 describes the extension of the analytical wave attenuation model to random waves and the application to analyze the wave attenuation capacity of suspended aquaculture structures in the field. At many sites, sea surface profiles are better represented by random waves. Random waves can be formulated as a superposition of monochromatic waves with a set of random phases. To represent the frequency dependent energy of random waves, the wave spectrum is often used. Assuming a narrow-banded wave spectrum, Mendez & Losada (2004) extended Dalrymple et al. (1984) model to consider random non-breaking and breaking waves propagating over a mildly sloped vegetation seabed. The modification developed by Mendez & Losada (2004) has been implemented in the SWAN (Simulating WAves Nearshore) model by Suzuki et al. (2012), and the MDO (Mellor-Donelan-Oey) wave model for wind-generated waves and swells in deep and shallow waters by Marsooli et al. (2017). Also based on the Dalrymple et al. (1984) technique, Chen & Zhao (2012) developed two submerged vegetation models for random waves by implementing the energy dissipation of random waves as described in Hasselmann & Collins (1968) and the joint distribution of wave heights and wave periods proposed by Longuet-Higgins

(1983). The Kobayashi et al. (1993) model was extended by Mendez et al. (1999) for irregular waves, wave reflection, and evanescent modes. Recently, Jacobsen et al. (2019a) developed a frequency dependent model for wave attenuation by submerged vegetation and identified that the wave attenuation for different frequency components of random waves are different. Like submerged vegetation, the wave attenuation capacity of suspended canopies in the field is also expected to be frequency dependent, which still need to be fully understood. As the blade motion influences the wave attenuation, there is still a need to extend the blade dynamic model for random waves and implement it into the random wave attenuation model.

The objectives of Chapter 5 are therefore to (1) extend the analytical wave attenuation model for random waves, (2) characterize the effects of suspended aquaculture structures on wave attenuation in the field, and (3) provide an approach to use suspended aquaculture structures as a potential nature-based solution for wave attenuation.

1.5 Outline

This thesis includes six chapters. The remainder of this thesis is organized to support each set of chapter objectives as following:

Chapter 2 describes the cable model developed to examine the blade motion as a function of blade geometry and wave properties. The cable model is compared with experimental data and previous vegetation models for the large-amplitude motions of blades in waves with and without currents. With the cable model, the theory for the symmetric and asymmetric motion of a flexible blade is developed. The model is then used to investigate the effects of blade length and flexural rigidity as well as wave height and wave period on the symmetric and asymmetric blade motions. Finally, the mechanisms for asymmetric blade motion and the conditions in which the asymmetry becomes negligible as well as the properties and implications of asymmetric blade motion are discussed. The material in this chapter has been published as Zhu et al. (2020b).

Chapter 3 describes the physical laboratory experiments for wave attenuation by a suspended model kelp canopy. The morphological and mechanical properties of cultivated *S. latissima* at Saco Bay, Maine, USA are measured. The scaled physical model is designed based on the morphological and mechanical

properties of *S. latissima* considering dynamical similarity. The wave attenuation and forces are measured. The bulk drag coefficient and effective blade length for suspended canopies for wave attenuation are developed based on the data.

Chapter 4 describes the analytical wave attenuation model with resolving blade motion. The analytical model is compared with the experiments for both suspended and submerged canopies. The analytical model is also compared with the numerical model in Chapter 3 to analyze the effects of the nonlinearity of large-amplitude blade motion. With the analytical model, the analytical solutions for bulk drag coefficient and effective blade length are derived and compared with the fitted formulas. After validation with experiments, the model is then used to analyze the seasonal impacts on the wave attenuation capacity of submerged vegetation and suspended canopies.

Chapter 5 describes the frequency dependent theoretical model for random wave attenuation, which is extended from the analytical wave attenuation model in Chapter 4. The analytical wave attenuation model is coupled with cantilever-beam and buoy-on-rope vegetation models to consider the motion of canopies with different type components. The coupled flow and vegetation model is validated with laboratory experimental datasets for submerged canopies (Jacobsen et al., 2019a) and laboratory and field datasets for suspended canopies (Seymour and Hanes, 1979). The validated coupled model is then applied in the field near Saco, Maine in the Northeastern USA to investigate the potential of a mussel farm to damp storm during the January 2015 North American blizzard. The effectiveness of using a suspended aquaculture farm alone and in combination with submerged aquatic vegetation (SAV) close to shore for wave attenuation is also investigated. The material in this chapter has been published as Zhu et al. (2020a).

Chapter 6 conclude the thesis with a summary of the major findings and contributions to the field, engineering implications for nature-based solutions, and suggestions for future research.

CHAPTER 2

MECHANISMS FOR THE ASYMMETRIC MOTION OF SUBMERGED AQUATIC VEGETATION IN WAVES: A CONSISTENT-MASS CABLE MODEL[1]

2.1. Background

Submerged aquatic vegetation (SAV) including salt-marshes, seagrass beds, and kelp forests, provides a wide range of ecosystem services. SAV can attenuate wave energy, mitigate coastal erosion, reduce storm damage, and create habitats for fish and shellfish (Arkema et al., 2015; Dalrymple et al., 1984; Guannel et al., 2015; K. Hu et al., 2018; J. Hu et al., 2019; Z. Hu et al., 2014; Kobayashi et al., 1993; Lowe et al., 2007; Maza et al., 2015; Mendez & Losada, 2004; Nepf, 2012; Ondiviela et al., 2014; Suzuki et al., 2019). The storm attenuation capacity of SAV needs to be quantified to develop effective and resilient coastal protection, management and adaptation strategies. While the effectiveness of SAV in coastal protection is dependent on its coastal coverage, population, size and density, the dynamics of a single blade in waves is critical to the understanding of the hydrodynamics and morphodynamics within a vegetation meadow. The dynamic motion of vegetation changes the flow and produces eddies which, in turn, alter the flow forcing on the blade and blade motion. The blade motion due to flexibility reduces the relative velocity between flow and vegetation as well as the frontal area, resulting in a reduced drag that decreases velocity attenuation and wave attenuation in the vegetation meadow (Abdolahpour et al., 2018; Bouma et al., 2005; Houser et al., 2015; Mullarney & Henderson, 2010; Paul et al., 2012; Riffe et al., 2011; Rupprecht et al., 2017; Zeller et al., 2014). Numerical models have been developed to solve a force balance equation for the vegetation motion, considering gravity, buoyancy, structural damping, bending stiffness as restoring forces, as well as drag and inertia as driving forces (Ikeda et al., 2001; Leclercq & de Langre, 2018; Luhar & Nepf, 2016; Zeller et al., 2014; Zhu & Chen, 2015).

[1] This chapter has been published as Zhu, L., Zou, Q., Huguenard, K., & Fredriksson, D. W. (2020). Mechanisms for the Asymmetric Motion of Submerged Aquatic Vegetation in Waves: A Consistent-Mass Cable Model. Journal of Geophysical Research: Oceans, 125(2), 1–31. https://doi.org/10.1029/2019JC015517

Blade motion in waves can be symmetric or asymmetric. Symmetric motion is a horizontal oscillation over the wave period with near-equal bending angles about the vertical axis. Asymmetric motion is an oscillation with more bending in the direction of wave propagation. This asymmetric behavior was described as a "whip-like" response by Rupprecht et al. (2017). Asymmetric blade motion could also induce drag asymmetry with less drag under the wave crest than the trough. According to (Luhar et al., 2010; 2013), this effect could enhance the mean flow in the direction of wave propagation. Enhanced mean flow could also rein- force the asymmetry of the blade motion in a meadow (Luhar et al., 2017). Blade inclination in the direction of wave propagation in a meadow may also provide "shelter" effects for sediment and further reduce bedload transport and stabilize the seabed (Rupprecht et al., 2017).

Asymmetric motion of a single blade has been identified in laboratory experiments (e.g., Jacobsen et al., 2019b; Lei &Nepf, 2019b). Döbken (2015) attribute the asymmetric behavior of blade motion to that of orbital velocities assuming the blade motion exactly follows the wave excursion. This interpretation only holds when the blade deflection is comparable to wave excursion. Using a numerical model of a single blade, Gijón Mancheño (2016) concluded that the vertical component of wave orbital velocity is the major contributing factor for the asymmetric blade motion based on the results that the blade motion is symmetric once the vertical component of wave orbital velocity is removed. Wave orbital asymmetry caused by wave nonlinearity, bottom slope, bottom friction and the presence of a structure (Elgar et al., 1990; Peng et al., 2009; Zou & Peng, 2011; Zou et al., 2003) also leads to asymmetric response. For instance, this asymmetric motion was observed in a set of laboratory experiments by Luhar and Nepf (2016) conducted with horizontal wave velocities having greater values under the wave crest rather than the trough. Also, with experimental techniques, Rupprecht et al. (2017) observed a transition from symmetric to asymmetric blade motion with increasing wave orbital velocities, which indicates that the asymmetric motions of *Puccinellia* and *Elymus* only occur when the wave orbital velocities reached critical values. Since previous work focused on the influence of wave forcing characteristics that produces asymmetric motion, a need now exists to investigate the role of blade characteristics, including geometry and flexural rigidity that produces similar behavior.

The objective of this work is to identify the mechanisms for the asymmetric motion of SAV with focus on blade geometric and material properties. A cable model with consistent-mass properties is developed to examine the blade motion as a function of blade geometry and wave properties. The cable model is compared with experimental data and previous vegetation models for the large-amplitude motions of blades in waves with and without currents. With the cable model, the theory for the symmetric and asymmetric motion of a flexible blade is developed. The model is then used to investigate the effects of blade length and flexural rigidity as well as wave height and wave period on the symmetric and asymmetric blade motions. Finally, the mechanisms for asymmetric blade motion and the conditions in which the asymmetry becomes negligible as well as the properties and implications of asymmetric blade motion are discussed.

2.2. Methodology

The wave-induced motion of a flexible blade is often characterized by large deflections which are difficult to resolve with analytical approaches. Therefore, recent studies of blade dynamics have focused on numerical techniques such as the finite-difference and finite-element methods to consider large-deflection-induced geometric nonlinearity. Using a spring-mass model to consider blade rigidity, Zeller et al. (2014) reduced the governing equations of blade dynamics to a system of ordinary differential equations (ODEs). In order to improve the model accuracy, consistent-mass models with partial differential equations (PDEs) were introduced to model the vegetation motion. The vegetation models developed by Luhar and Nepf (2016) and the elastic-rod model coupled with RANS-VOF Navier-Stokes solver proposed by Chen and Zou (2019) perform better for simulating the “first-normal-mode-like” blade motion rather than the “second-normal-mode-like” blade motion. To capture the “second-normal-mode-like” blade motion properly in this study, the consistent-mass cable model developed to represent the dynamics of flexible slender structures including steel cables (Howell, 1992; Tjavaras et al., 1998; Triantafyllou & Howell, 1994), risers (Chatjigeorgiou, 2008), and mooring lines (Li et al., 2018), is extended to simulate the motions of SAV.

2.2.1. 2D Cable model

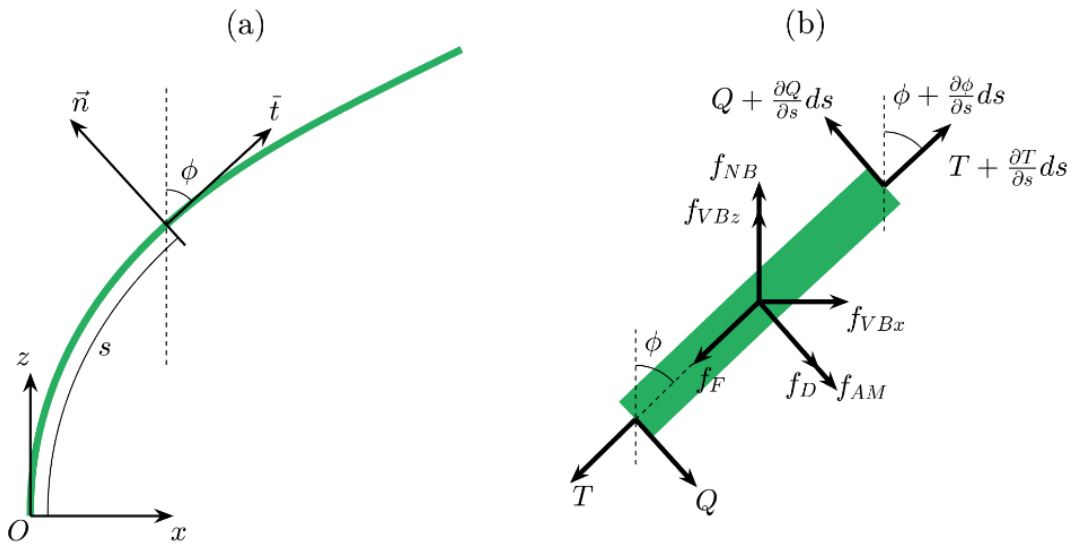

Figure 2.1. Schematic diagram for the coordinate systems and the free-body diagram. (a) Fixed global Cartesian reference frame (x, z) with origin at the blade base. A local Lagrangian coordinate system ($\vec{t}$, $\vec{n}$) along the blade length (s) associated with the angle of ϕ between the tangential direction ($\vec{t}$) and the vertical direction (z). (b) The free-body diagram for one segment of flexible blade ds with effective tension (T), shear (Q), net buoyancy (f_{NB}), drag (f_D), friction (f_F), virtual buoyancy (f_{VBx}, f_{VBz}), and added mass force (f_{AM}).

To apply the 2D cable model, an individual blade of SAV was treated as a slender structure fixed at the base and free at the tip as shown on Figure 2.1(a). A fixed global Cartesian reference frame (x, z) with the origin at the blade base is defined on Figure 2.1(a), where x and z indicate the horizontal and vertical directions, respectively. The flow field is described by the horizontal and vertical components, $U(x, z, t)$ and $W(x, z, t)$, where t denotes time. To derive the governing equations for the blade motion, a local Lagrangian coordinate system ($\vec{t}$, $\vec{n}$) along the blade length is used with $\vec{t}$ representing the blade-tangential direction and $\vec{n}$ as the blade-normal direction. The velocity components of the blade segment (ds) in the blade-tangential direction and the blade-normal direction are u and w, respectively. The distance along the length of the blade (l) from the base is defined as s such that $s = l$ at the tip of the blade. The local bending angle of the blade relative to the vertical direction (z) is ϕ, where $\phi = 0$ denotes a vertical

upright posture for defining symmetric or asymmetric motion. The points in the Lagrangian coordinate system $(\vec{t}, \vec{n})$ can be obtained by rotating the global Cartesian coordinates (x, z) counterclockwise by $(\pi/2 - \phi)$.

Blade dynamics are governed by the force and momentum balances given by

$$\rho_v bd \left(\frac{\partial u}{\partial t} + w\frac{\partial \phi}{\partial t}\right) = Q\frac{\partial \phi}{\partial s} + \frac{\partial T}{\partial s} + f_{NB}\cos\phi + f_{VBx}\sin\phi + f_{VBz}\cos\phi - f_F, \tag{2.1}$$

$$\rho_v bd \left(\frac{\partial w}{\partial t} - u\frac{\partial \phi}{\partial t}\right) = \frac{\partial Q}{\partial s} - T\frac{\partial \phi}{\partial s} + f_{NB}\sin\phi - f_{VBx}\cos\phi + f_{VBz}\sin\phi - f_D - f_{AM}, \tag{2.2}$$

and

$$Q = EI\frac{\partial^2 \phi}{\partial s^2}, \tag{2.3}$$

as well as the compatibility relations for geometrical continuity given by

$$\frac{\partial u}{\partial s} + w\frac{\partial \phi}{\partial s} - \frac{1}{Ebd}\frac{\partial T}{\partial t} = 0, \tag{2.4}$$

and

$$\frac{\partial w}{\partial s} - u\frac{\partial \phi}{\partial s} + \frac{\partial \phi}{\partial t} = 0. \tag{2.5}$$

In equations (2.1) to (2.5), ρ_v is the vegetation density, b is the blade width, d is the blade thickness, E is the elastic modulus, $I = bd^3/12$ is the second moment of the cross-section area of the blade, T is the effective tension in the blade-tangential direction, Q is the shear force in the blade-normal direction, f_{NB} is the net buoyancy force per unit blade length (the following forces are per unit length) acting upward, f_{VBx} and f_{VBz} are the horizontal and vertical components of virtual buoyancy (Denny et al., 1997; Gaylord et al., 2003; Rosman et al., 2013), f_F is the skin friction in the blade-tangential direction, f_D is the drag force, and f_{AM} is the added mass force in the blade-normal direction. The effective tension is the sum of the real tension and the product of the hydrostatic pressure and the cross-section area. The usage of effective tension makes *Archimedes principle* applicable to calculate the buoyancy of the segment that is not completely enclosed in fluid due to the neighboring segment (Howell, 1992; Sparks, 2009; Tjavaras et al., 1998). It should be noted that the hydrostatic pressure should be removed from the effective tension when calculating the real tension.

The static net buoyancy force f_{NB} is defined as the difference of the buoyancy and weight, given by

$$f_{NB} = (\rho - \rho_v) g b d, \tag{2.6}$$

where ρ is the fluid density, and g is the gravitational acceleration. The hydrodynamic forces on the right-hand side of equations (2.1) and (2.2) including virtual buoyancy (f_{VBx}, f_{VBz}), drag force (f_D), skin friction (f_F), and added mass force (f_{AM}), which are given by modified Morison equations \cite{Morison1950},

$$f_{VBx} = \rho b d \frac{\partial U}{\partial t}, \tag{2.7}$$

$$f_{VBz} = \rho b d \frac{\partial W}{\partial t}, \tag{2.8}$$

$$f_D = \frac{1}{2} C_d \rho b \, |w + U\cos\phi - W\sin\phi| \, (w + U\cos\phi - W\sin\phi), \tag{2.9}$$

$$f_F = \frac{1}{2} C_f \rho 2(\, b + d) \, | \, u - U\sin\phi - W\cos\phi | (\, u - U\sin\phi - W\cos\phi), \tag{2.10}$$

and

$$f_{AM} = m_a \frac{\partial}{\partial t} (\, w + U\cos\phi - W\sin\phi), \tag{2.11}$$

where C_d is the drag coefficient, C_f is the skin friction coefficient, m_a is the added mass. The added mass is given by $m_a = C_m \rho \pi b^2/4$ using the cylinder-equivalent blade cross-section following Luhar and Nepf (2016) and C_m is the added mass coefficient.

The boundary conditions for the bottom-rooted blade are set as $u = 0$, $w = 0$ and $\phi = 0$ at the blade base ($s = 0$), as well as $T = 0$, $\partial\phi/\partial s = 0$ and $\partial^2\phi/\partial s^2 = 0$ at the blade tip ($s = l$). The governing equations (1) to (5) are a system of nonlinear partial differential equations solved by discretization using a finite difference scheme, the Keller Box method (Anderson et al., 2016; Keller, 1971), which is implicit, second order accurate, single step, unconditionally stable and convergent. The Newton-Raphson iteration method was used to solve the discretized equations.

2.2.2. Hydrodynamic force coefficients

The drag coefficient and added mass coefficient for blades are considered a function of Keulegan-Carpenter number (KC). The KC number is defined as $KC = U_m T_w/b$, where U_m is the maximum

oscillatory flow velocity and T_w is the wave period. Based on datasets for rigid plates in oscillatory flows with $KC = 1.7{\sim}118.2$ (Keulegan & Carpenter, 1958; Sarpkaya & O'Keefe, 1996), Luhar and Nepf (2016) developed formulas for drag coefficient and added mass coefficient, given by

$$C_d = \max\left(10KC^{-1/3}, 1.95\right) \tag{2.12}$$

and

$$C_m = \min(C_{m1}, C_{m2}), \tag{2.13}$$

respectively, where $C_{m1} = \begin{cases} 1 + 0.35KC^{2/3}, & KC < 20 \\ 1 + 0.15KC^{2/3}, & KC \geq 20 \end{cases}$ and $C_{m2} = 1 + (KC - 18)^2/49$ as described in Luhar (2012).

The friction coefficient is taken as a function of Reynolds number (Re). The Reynolds number is defined as $Re = U_m b/\nu$, where ν is the kinematic viscosity of the water. According to Zeller et al. (2014) and Abdelrhman (2007), the friction coefficient is given by

$$C_f = 0.074\, Re^{-1/5}. \tag{2.14}$$

Luhar and Nepf (2016) noted that the exact value of C_f had little effect on their model results because the ratio of the calculated root-mean-square forces for $C_f = 0.1$ and $C_f = 0.01$ was distributed with mean and standard deviation 1.00 ± 0.01. For simplicity, Zeller et al. (2014) selected an approximated value of 0.02. In contrast, Luhar and Nepf (2016) used a larger value of $C_f = 0.1$ because their model was found unstable for the cases with high Cauchy number if $C_f = 0.01$. The Cauchy number (Ca) is the ratio of the hydrodynamic force to the restoring force due to plant stiffness and given by $Ca = \rho b U_m^2 l^3/EI$. In this study, equation (2.14) is used to calculate the friction coefficient.

2.3. Model-data comparison

2.3.1. Blade motion in combined waves and currents

The cable model results were first compared with the laboratory experiments by Zeller et al. (2014) for the blades in combined waves and currents. During the experiments, six wave-current conditions were produced, where the wave period $T_w = 2.80 \sim 5.19$ s, the amplitude of the horizontal wave velocity $U_w =$

9.45 ~ 25.8 cm/s, and the currents $U_c = 3.66 \sim 13.7$ cm/s (Table 2.1). The still water depth was 40 cm. The model blades were made of low-density polyethylene (LDPE) with $\rho_v = 920$ kg/m^3 and $E = 0.3$ GPa (Ghisalberti & Nepf, 2002). Four 1 cm-wide model blades with different lengths and thicknesses were used. Three of the blades were 15 cm long with thicknesses of 0.20, 0.25, and 0.30 mm. The fourth blade was 20 cm long with a thickness of 0.25 mm. Therefore, $Ca = 101 \sim 2883$, $KC = 40 \sim 197$ and $Re = 1441 \sim 3790$. Details of the experiments can be found in Zeller et al. (2014).

Table 2.1. Blade properties and wave conditions in the experiments by Zeller et al. (2014) and Luhar and Nepf (2016).

Experiment	Blade property	Wave			Current
		T_w (s)	a_w (cm)	U_w (cm/s)	U_c (cm/s)
Blade in waves and currents	LDPE:	5.19	-	25.8	12.1
(Zeller et al., 2014)	$\rho_v = 920$ kg/m^3	4.29	-	17.3	13.2
	$E = 0.3$ GPa	2.8	-	9.45	12.9
	$b = 1$ cm	5.19	-	24.4	6
	$d = 0.2, 0.25, 0.3$ mm	4.29	-	15.9	5.63
	$l = 15, 20$ cm	2.8	-	9.64	4.77
Blade in waves	0.4 mm-thick HDPE:	2	1(0.9)	5.0	-
(Luhar & Nepf, 2016)	$\rho_v = 950$ kg/m^3	2	2(1.9)	10.1	-
	$E = 0.93$ GPa	2	3(2.9)	15.4	-
	1.9 mm-thick silicon foam:	2	4(3.9)	20.6	-
	$\rho_v = 670$ kg/m^3	1.4	2(1.7)	8.9	-
	$E = 0.5$ MPa	1.4	4(3.5)	16.7	-
	$b = 2$ cm	1.1	2(1.7)	6.6	-
	$l = 5, 10, 15, 20$ cm	1.1	4(3.6)	12.8	-

To drive the model, the wave-current flow is considered as a superposition of currents and linear waves. The hydrodynamic force coefficients for waves as described in section 2.2.2 are assumed to be also applicable for combined waves and currents conditions following Lei and Nepf (2019a). The calculated deflected blade-tip heights (z_T) at the maximum horizontal displacements ($x_{T,\max}$) are shown on Figure

2.2 along with the data and the model results from Zeller et al. (2014). The root-mean-square-error (RMSE) for the cable model results is RMSE = 0.043 and smaller than that of the model results from Zeller et al. (2014) with RMSE = 0.103. The improvement of RMSE is possible because the present cable model is a consistent-mass model while the Zeller et al. (2014) model is a spring-mass model. Additionally, the compatibility relations described in equation (4) and (5) are not included in Zeller et al. (2014). Therefore, the Zeller et al. (2014) model has difficulty to converge for some test cases with large $Ca \gg 10^3$ (e.g., missed points on Figure 2.2), where the blade is so flexible that can curl over. In comparison, the cable model is stable and convergent for all the test cases.

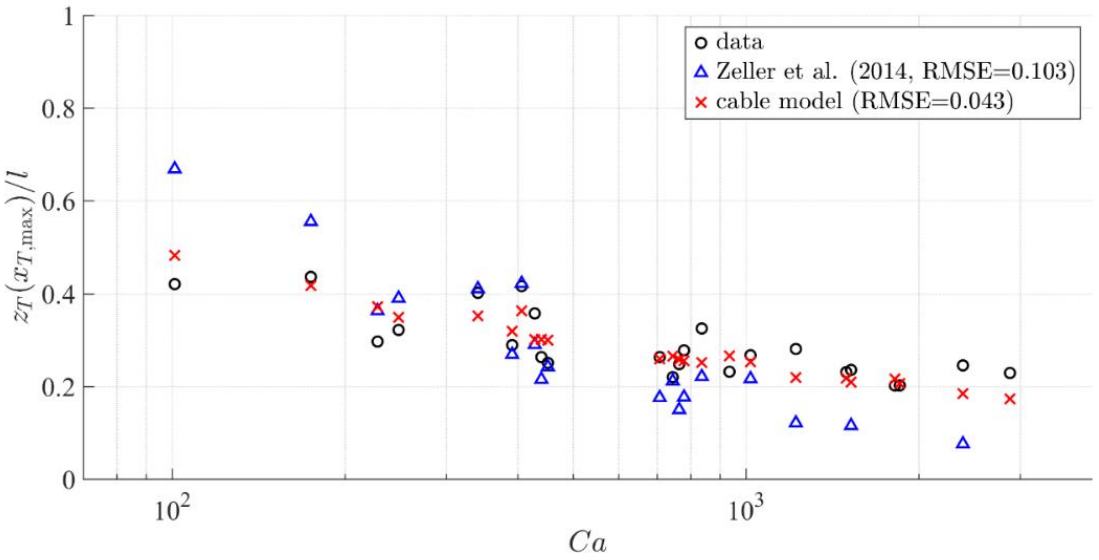

Figure 2.2. Model-data comparison for the normalized deflected blade-tip height (z_T/l) at the maximum horizontal displacement of the blade tip ($x_{T,\max}$) vs the Cauchy number (Ca). The data is denoted by black circles, the model results from Zeller et al. (2014) are denoted by blue triangles and those from the cable model are denoted by red crosses. The associated root-mean-square-error (RMSE) is shown in the legend.

2.3.2. Blade motion in waves

The cable model results were also compared with the data from the laboratory experiments by Luhar and Nepf (2016) for waves only. Eight wave conditions were produced with wave period $T_w = 1.1 \sim 2.0$ s and wave amplitude $a_w = 1 \sim 4$ cm (Table 2.1). The still water depth (h) was 30 cm. The model

blades were made of high-density polyethylene (HDPE, $\rho_v = 950$ kg/m^3 and $E = 0.93$ GPa) and silicon foam ($\rho_v = 670$ kg/m^3 and $E = 0.5$ MPa). The blades were 2 cm wide with lengths of 5, 10, 15, and 20 cm. The thicknesses were 0.4 mm and 1.9 mm for the HDPE and silicon foam blades, respectively. Therefore, $Ca = 0.02 \sim 1200$, $KC = 3.7 \sim 20.6$, and $Re = 1000 \sim 4120$. Details of the experiments can be found in Luhar and Nepf (2016).

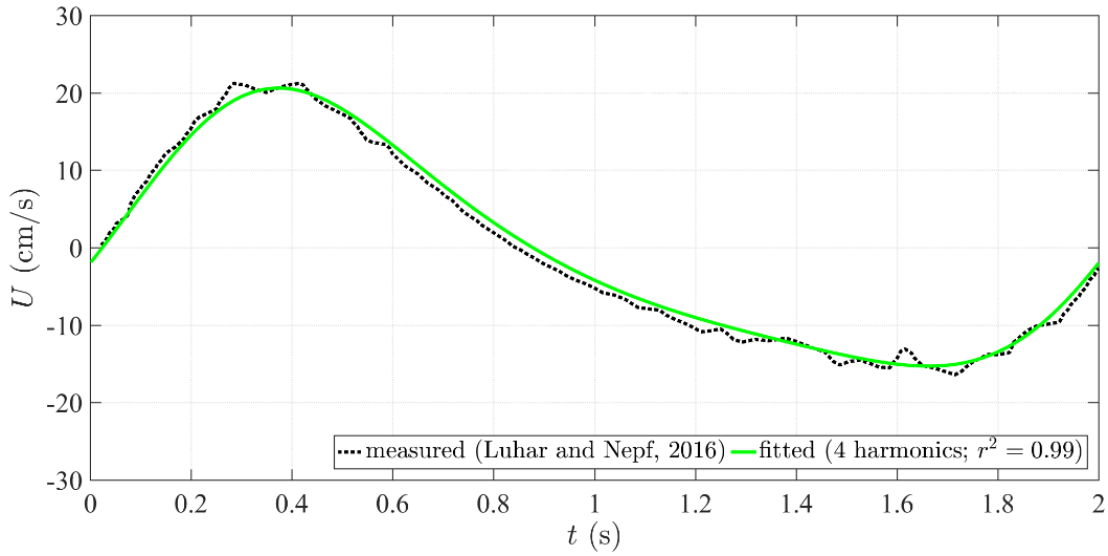

Figure 2.3. Measured horizontal component of the wave orbital velocity at $z = 0$ for the wave with period $T_w = 2$ s and amplitude $a_w = 4$ cm (Luhar & Nepf, 2016). The measured horizontal component of the wave orbital velocity is denoted by the dotted black line and the first four harmonics fit is denoted by solid green line.

The velocity profile was measured using particle image velocimetry (PIV, details referred to Luhar & Nepf, 2016) that captures the instantaneous flow velocity resulting from the superposition of the incident and reflected waves, where the wave reflection ratio of the wave flume is 7% (Lei & Nepf, 2019b). The first four harmonics fit of the measured flow velocity ($r^2 = 0.99$, Figure 2.3) at one horizontal position was used as an approximation for the input flow field in Luhar and Nepf (2016). This approximation only represents the temporal variation of the velocity profile at that horizontal position. Due to the effects of wave reflection on the velocity amplitude, this approximation for the flow profile at other horizontal

position may has a small $r^2 = 0.91$ for the wave reflection of 7%. To represent the spatial variation of the wave flow field, the wave number (k) is used and obtained by solving the dispersion relation, $\omega^2 = gk \tanh kh$ (Dean & Dalrymple, 1991), where the wave radian frequency $\omega = 2\pi/T_w$. By incorporating the effects of the spatial variance into the wave phase, the modified approximation for the input flow field reduces the effects of wave reflection on the flow field and enhances r^2 to be greater than 0.98 at all the horizontal positions in the range of the blade motion. In addition, the wave reflection-induced change of the velocity amplitude at all the horizontal positions has limited effects (< 2.5%) on the drag coefficient. Therefore, the modified approximation for the input flow field by incorporating spatial variance is adequately precise to drive the cable model.

The comparisons between the cable model results and the data, as well as the model results from Luhar and Nepf (2016) are shown on Figure 2.4 for the horizontal displacement range of the blade-tip ($x_{T,\max} - x_{T,\min}$) and the root-mean-square of the total horizontal force ($F_{x,\mathrm{rms}}$) at the blade base. To normalize $F_{x,\mathrm{rms}}$, the root-mean-square of the total horizontal force on a rigid blade with the same geometry is used and given by

$$F_{x,\mathrm{rms,rigid}} = \sqrt{\frac{1}{T_w}\int_0^{T_w}\left[\int_0^{l}\left(\frac{1}{2}C_d\rho b|U|U + m_a\frac{\partial U}{\partial t} + \rho b d\frac{\partial U}{\partial t}\right)dz\right]^2 dt}. \tag{2.15}$$

For the HDPE blades, the RMSE of the cable model results is 0.050 for the blade-tip range and 0.184 for the total horizontal force, which are a little larger than those of the model results from Luhar and Nepf (2016) with RMSE = 0.048 for the blade-tip range and RMSE = 0.174 for the total horizontal force. However, the cable model shows improvements in simulating the motion of the silicon foam blade with RMSE = 0.126 for the blade-tip range and RMSE = 0.043 for the total horizontal force, which are smaller than those by the model of Luhar and Nepf (2016) with RMSE = 0.151 for the blade-tip range and RMSE = 0.049 for the total horizontal force.

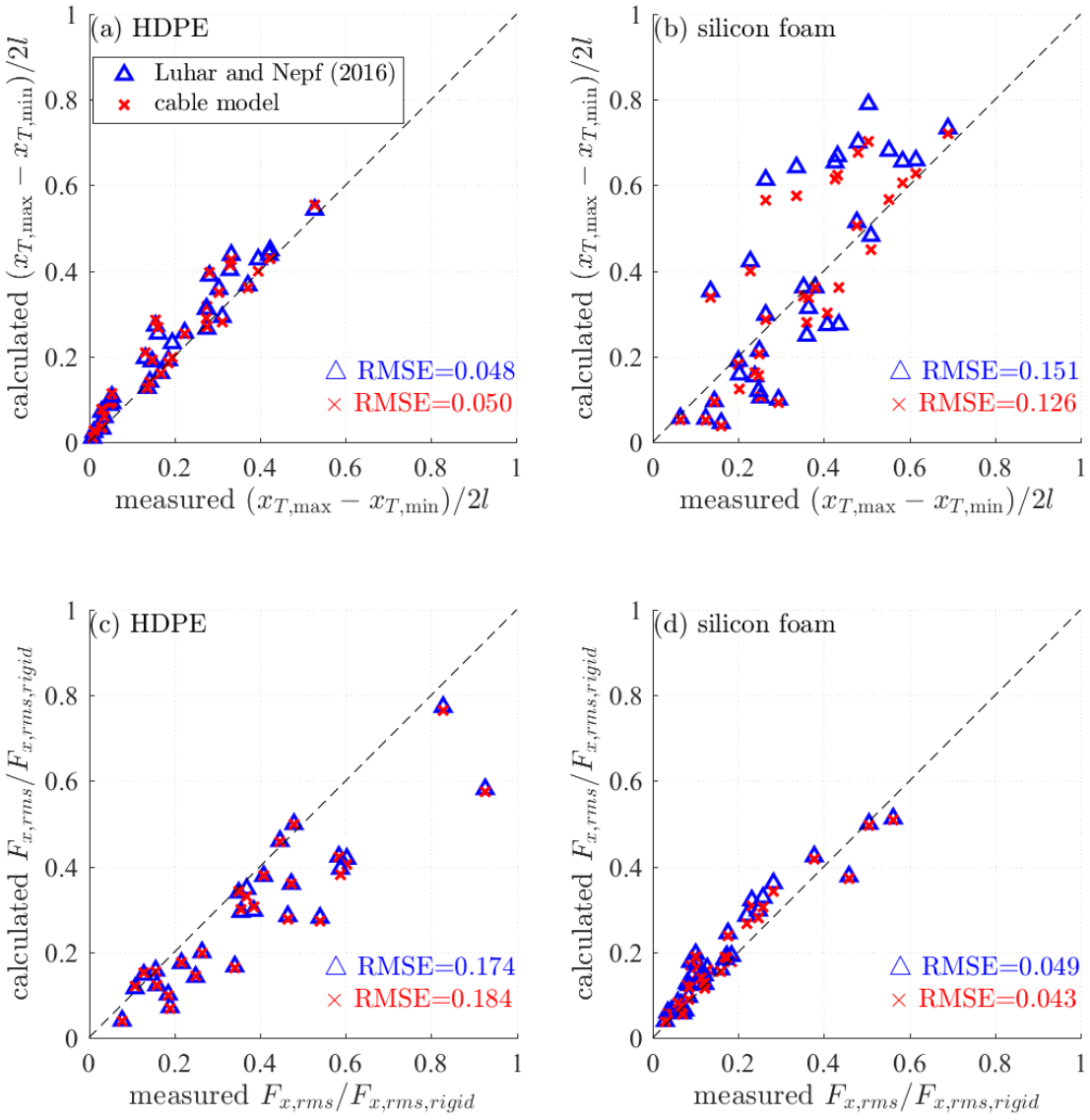

Figure 2.4. Comparisons for (a, b) the normalized horizontal displacement range of the blade-tip $(x_{T,max} - x_{T,min})/2l$ and (c, d) the root-mean-square of the total horizontal force ($F_{x,\mathrm{rms}}$) normalized by the total horizontal force ($F_{x,\mathrm{rms,rigid}}$) for a rigid blade with the same geometry for (a, c) HPDE and (b, d) silicon foam blades, respectively. The model results from Luhar and Nepf (2016) are denoted by blue triangles with root-mean-square-error (RMSE) in blue text while the cable model results are denoted by red crosses with RMSE in red text.

To further evaluate the performance of the numerical models, the model results for the blade tip trajectory are shown on Figure 2.5 and the blade postures associated with the total horizontal force (F_x) are

shown on Figure 2.6 and Figure 2.7. We note that the blade motion shown on Figure 2.5 is asymmetric with respect to the vertical line x=0, which will be further examined in section 2.4.

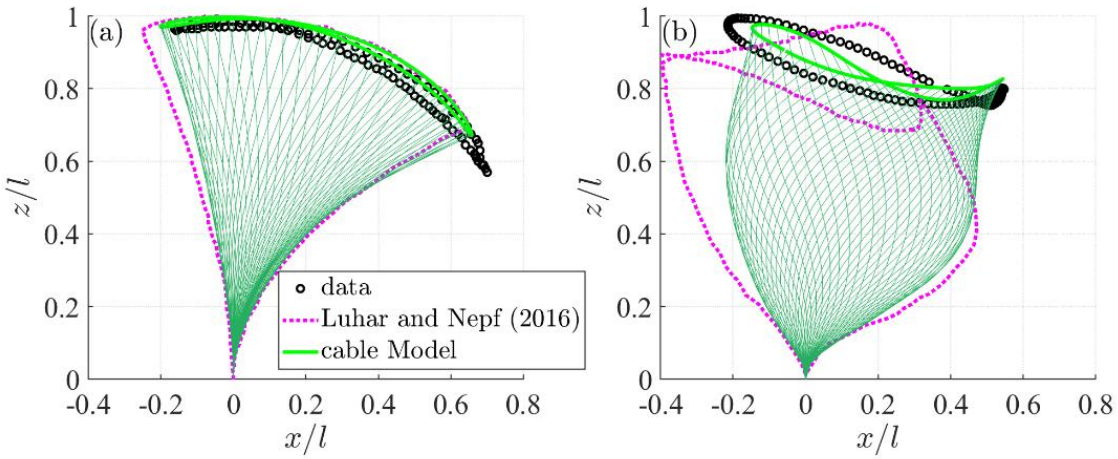

Figure 2.5. Blade postures and blade tip trajectory for the 20 cm-long (a) HDPE and (b) silicon foam blades over one wave period for the waves with period $T_w = 2$ s and amplitude $a_w = 4$ cm. The data is denoted by black open circles, the model results from Luhar and Nepf (2016) are denoted by magenta dotted lines, and those from the cable model are denoted by green lines (thick green lines indicate the trajectory of the blade tip while the thin green lines indicate the postures of the blade at selected time steps).

Both model blades exhibit periodic motion, but with different dynamic characteristics. For instance, the HDPE model blade behaves like the "first normal mode" of a cantilever beam (Figure 2.5a and Figure 2.6a-l) since the wave frequency $f_w = 1/T_w = 0.5$ Hz is smaller than the first natural frequency $f_1 = 1.875^2 f_0 = 1.54$ Hz of the HDPE blade, where $f_0 = \sqrt{EI/[(\rho_v bd + m_a)l^4]}$ (Rao, 2010). The silicon foam model blade, however, behaves like a "second normal mode" (Figure 2.5b and Figure 2.7a-l) since the wave frequency f_w is between the first natural frequency $f_1 = 0.36$ Hz and the second natural frequency $f_2 = 4.694 f_0 = 2.26$ Hz of the silicon foam blade. The normal mode theory for linear vibration is not suitable to analyze the nonlinear vibration of the blades, but it is the basis to analyze the nonlinear normal mode for large-amplitude vibration of a cantilever beam (Hsieh et al., 1994).

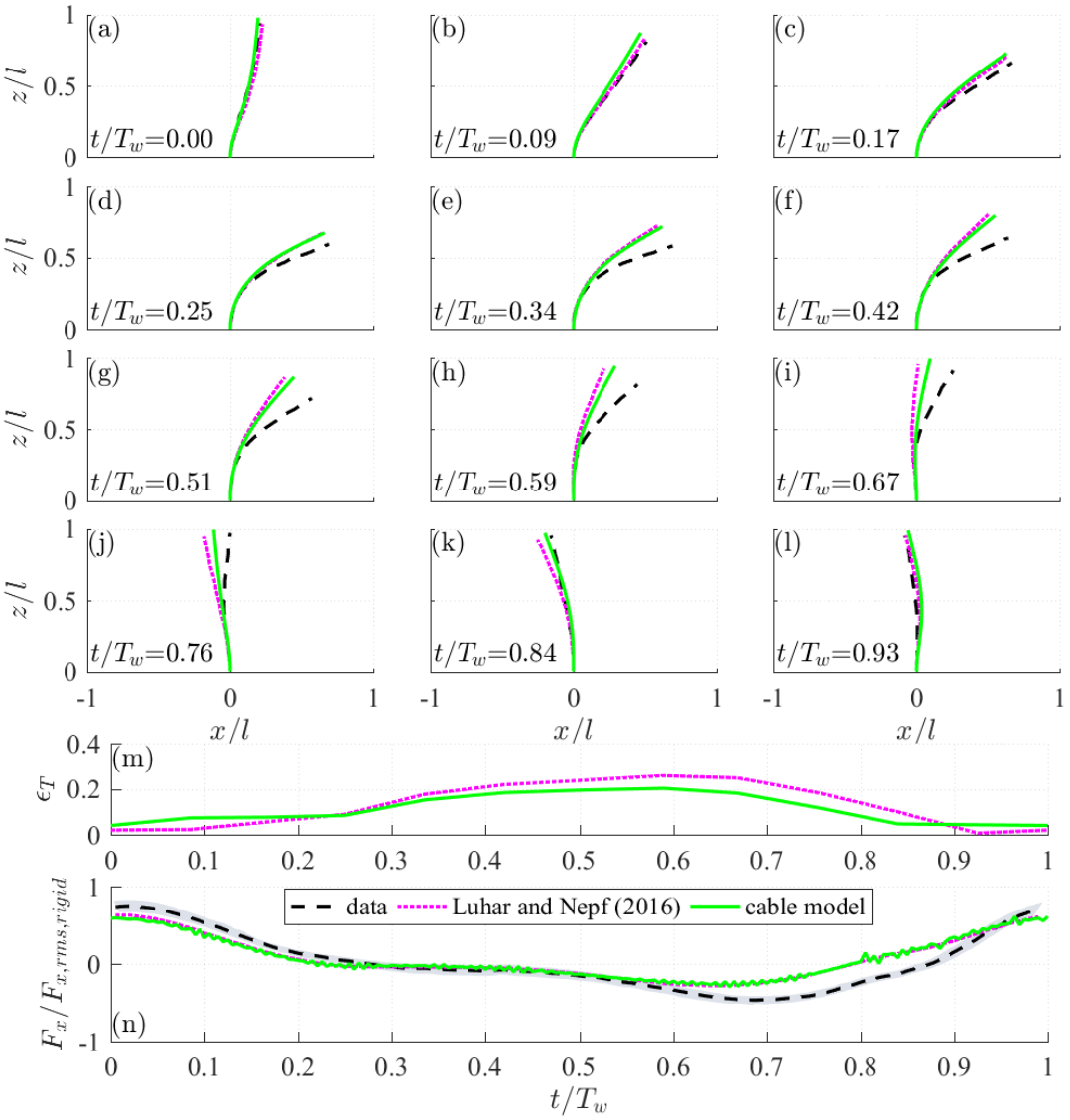

Figure 2.6. Comparisons for (a-l) the 20 cm-long HDPE blade posture (x, z) normalized by blade length (l), (m) the differences between the simulated and observed blade-tip displacements (ϵ_T), and (n) the total horizontal force (F_x) normalized by the root-mean-square horizontal force by rigid plate with the same geometry $(F_{x,\mathrm{rms,rigid}})$ along time (t). The waves with period $T_w = 2$ s and amplitude $a_w = 4$ cm propagate from left to right. Black dashed lines: the data from Luhar and Nepf (2016); magenta dotted lines: the model results from Luhar and Nepf (2016); green solid lines: the cable model results; grey shaded region: the estimated uncertainty in the experiments (Luhar & Nepf, 2016).

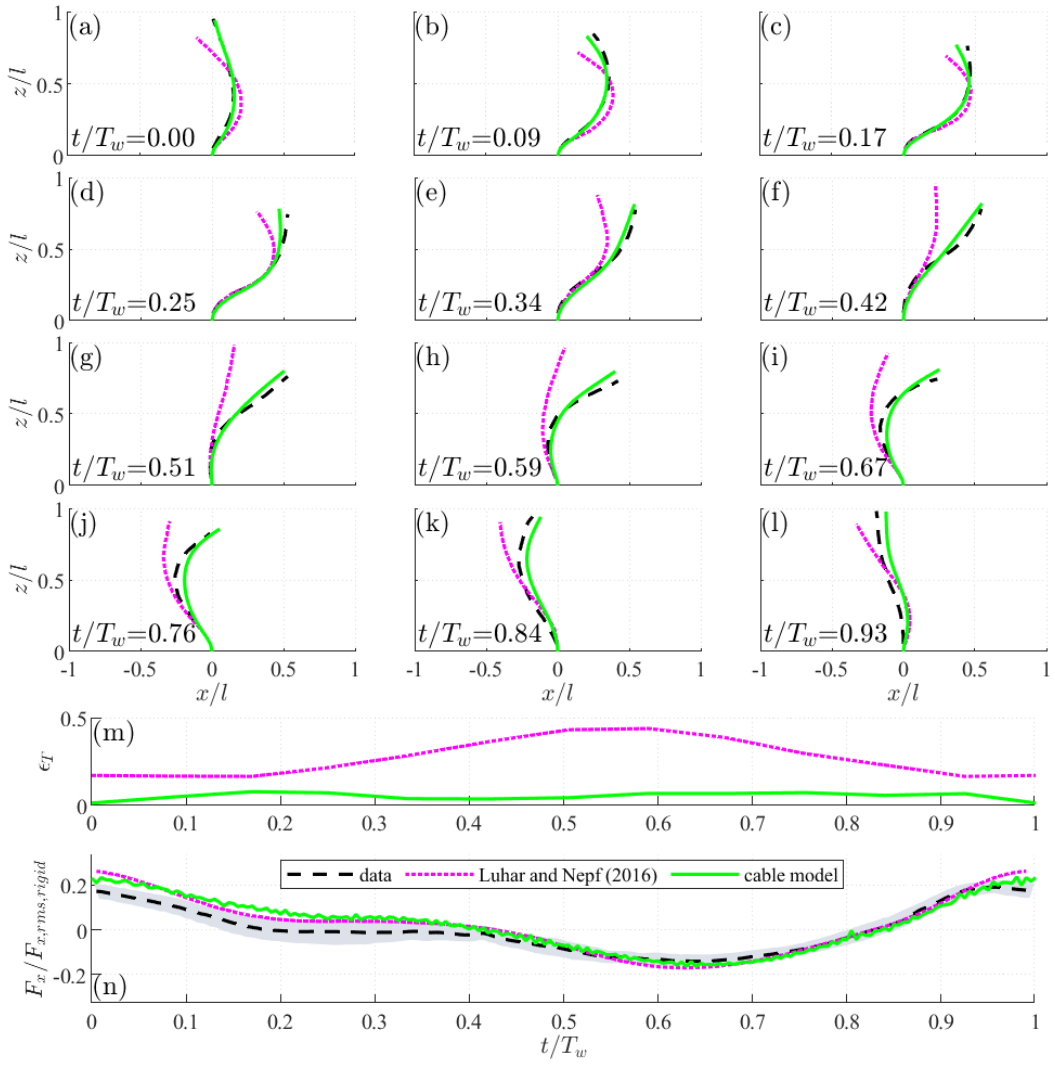

Figure 2.7. Comparisons for (a-l) the 20 cm-long silicon foam blade posture (x, z) normalized by blade length (l), (m) the differences between the simulated and observed blade-tip displacements (ϵ_T), and (n) the total horizontal force (F_x) normalized by the root-mean-square horizontal force by rigid plate with the same geometry $(F_{x,\mathrm{rms,rigid}})$ along time (t). The waves with period $T_w = 2$ s and amplitude $a_w = 4$ cm propagate from left to right. Black dashed lines: the data from Luhar and Nepf (2016); magenta dotted lines: the model results from Luhar and Nepf (2016); green solid lines: the cable model results; grey shaded region: the estimated uncertainty in the experiments (Luhar & Nepf, 2016).

To quantify the performance of the numerical simulations for blade postures, the normalized error (ϵ_T) between the simulated and observed displacements of the blade tip is used and given by

$$\epsilon_T(t) = \sqrt{(x_T - x_T^*)^2 + (z_T - z_T^*)^2}/l, \tag{2.16}$$

where (x_T, z_T) and (x_T^*, z_T^*) are the simulated and observed Cartesian coordinates of the blade tip, respectively. A smaller value of ϵ_T indicates a closer simulation. For the HDPE blade shown on Figure 2.6(m), ϵ_T of the cable model results is smaller than that of the model results from Luhar and Nepf (2016) under wave trough. The time averaged ϵ_T over one wave period for the cable model is $\overline{\epsilon}_T = 0.116$ and 14.1% less than that of the model from Luhar and Nepf (2016) with $\overline{\epsilon}_T = 0.135$ for HDPE blade (Table 2.2). For the silicon foam blade shown on Figure 6(m), ϵ_T of the cable model is smaller than that of the model from Luhar and Nepf (2016) during the entire wave period. The $\overline{\epsilon}_T$ of the cable model is 0.056 and 79.7% less than that of the model from Luhar and Nepf (2016) with $\overline{\epsilon}_T = 0.276$ for silicon foam blade (Table 2.2).

Table 2.2. Normalized time averaged error ($\overline{\epsilon_t}$) for the simulated excursions of the blade tip.

Blades	Luhar and Nepf (2016) (a)	Cable model (b)	$(a-b)/a \times 100\%$
Silicon foam	0.276	0.056	79.7%
HDPE	0.135	0.116	14.1%

The calculated total horizontal force by the cable model is consistent with the data with a normalized root-mean-square error (NRMSE) of 0.151 for the HDPE blade and 0.045 for the silicon foam blade. The NRMSE of F_x by the cable model is comparable to the model results from Luhar and Nepf (2016) with NRMSE = 0.139 for the HDPE blade and NRMSE = 0.041 for the silicon foam blade. Although the results of the two models are quite different for the blade postures, the results for the total horizontal force are similar because the total horizontal force is the integration of the horizontal force distributed along the blade. The variance of the distributed force and the momentum along the blade cannot be represented by the total horizontal force, but it imposes significant influences on the blade postures. Therefore, the difference in the total horizontal force comparison with the results from Luhar and Nepf (2016) is small, but the difference in posture comparison is large. As the postures of the blade represent the combined action

of the distributed force and momentum along the blade, the posture is used to demonstrate the blade dynamics rather than the integration of the horizontal forces along the blade length.

Compared with the model of Luhar and Nepf (2016), the cable model showed an advantage to simulate the blade dynamics, in particular for the simulations of blade postures in waves. The improvements for the posture simulations are mainly due to the incorporation of (i) the influences of the blade-motion-induced rotations of local Lagrangian coordinates along the blade on the added mass force as shown in equation (2.11), (ii) the dynamic equilibrium for the geometric continuity of the segments as shown in the compatibility relations from equations (4) and (5), and (iii) the spatial variation of the wave orbital velocity encountered by the blade due to blade displacements. Since the blade acts as a solid moving boundary in the fluid domain, its motion influences the flow structure. Therefore, accurate blade posture predictions are required to fully resolve the flow-vegetation interaction, wave-driven currents in a vegetation meadow, and the wave attenuation by vegetation. This model can also be used to estimate the internal stress of the blade and the total force at the bottom of the blade in order to analyze the breakage and the sediment holding properties of the blade.

2.4. Symmetric and asymmetric blade motions

2.4.1. Definition

To quantify the asymmetric motion, the blade posture asymmetry (β_{xT}) is defined as the ratio of the time-averaged horizontal displacement of the blade tip ($\overline{x}_T$) to the maximum absolute horizontal displacement ($|x_T|_{\max}$) over one wave period (Figure 2.8) and given by

$$\beta_{xT} = \frac{\overline{x}_T}{|x_T|_{\max}}, \tag{2.17}$$

where ($\overline{x}_T$) is always smaller than ($|x_T|_{\max}$) such that $\beta_{xT} \in (-1, 1)$. The posture asymmetry is positive when the blade inclines to the direction of wave propagation. For example, the motions of the blades shown on Figure 2.5 are asymmetric with $\beta_{xT} = 0.30$ and $\beta_{xT} = 0.27$ for HDPE and silicon foam blades, respectively.

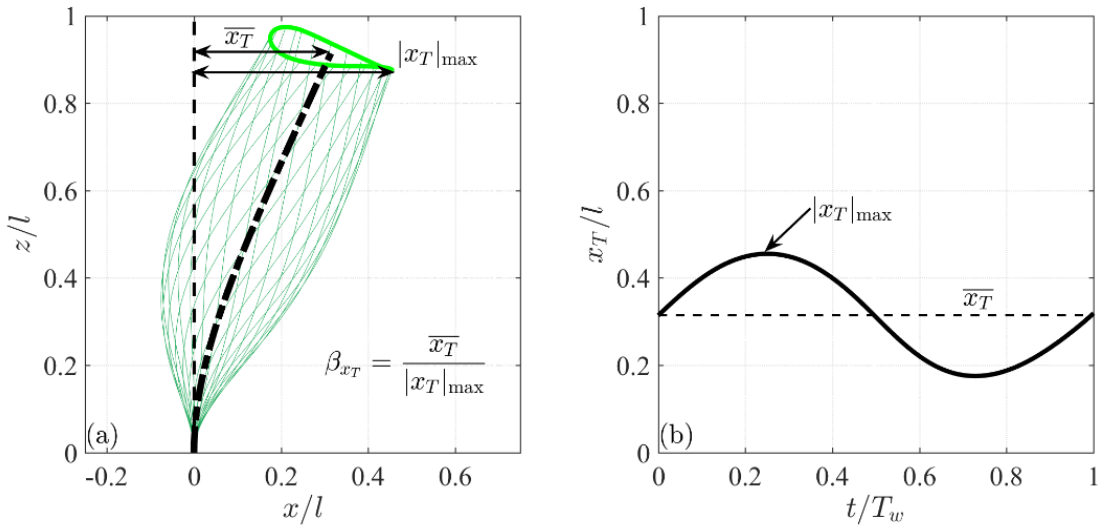

Figure 2.8. The blade posture asymmetry (β_{xT}) is defined as the ratio of time-averaged displacement of the blade tip ($\overline{x}_T$) to the maximum absolute displacement ($|x_T|_{\max}$). (a) Blade postures and tip trajectory. The horizontal and vertical coordinates (x, z) are normalized by the blade length (l). The thin green lines indicate the blade postures and the thick green line indicate the excursion of the blade tip. The black dash-dotted line indicates the time-averaged posture of the blade postures over one wave period and the thin dashed line indicate the vertical center. (b) The time series of the horizontal displacement of the blade tip. The time (t) is normalized by wave period (T_w).

2.4.2. Theory

Asymmetric blade motions shown on Figure 2.5 are partially induced by the weak asymmetry of wave motion as shown on Figure 2.3. However, using linear waves to drive the model without the influences of wave asymmetry still results in asymmetric blade motion (Figure 2.9) with $\beta_{xT} = 0.31$ and $\beta_{xT} = 0.32$ for HDPE and silicon foam blades, respectively. The magnitude of the blade posture asymmetry in linear waves is similar to that in weak asymmetric waves, suggesting that other mechanisms may have contributed to the observed asymmetric blade motion.

The mechanisms that contribute to the blade asymmetric motion in linear waves are identified according to the governing equations of blade motion. Substituting equations (2.3) and (2.6) to (2.11) into (2.1) and (2.2) yields

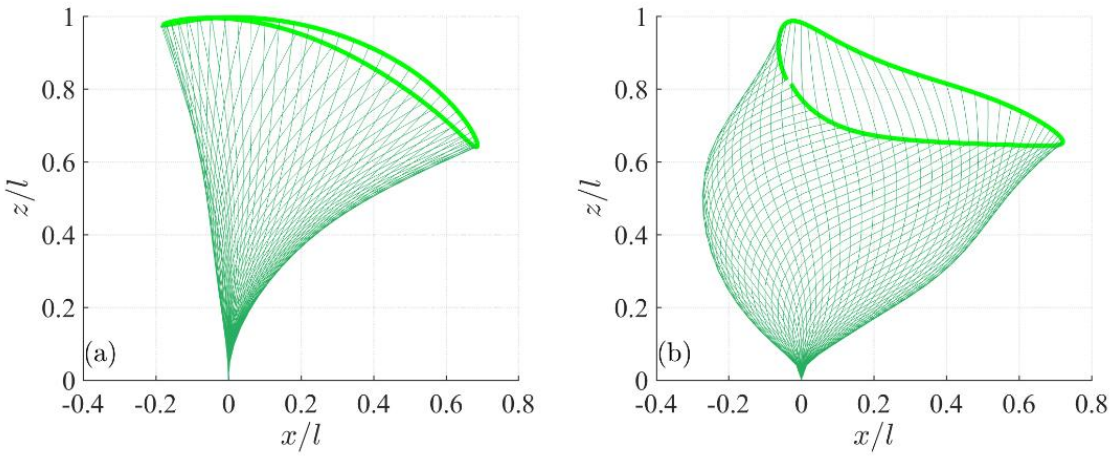

Figure 2.9. Blade postures and blade tip trajectory for the 20 cm-long (a) HDPE and (b) silicon foam blades over one wave period for the symmetric waves with period $T_w = 2$ s and amplitude $a_w = 4$ cm. Thick green lines indicate the trajectory of the blade tip while the thin green lines indicate the postures of the blade at selected time steps.

$$EI\frac{\partial\phi}{\partial s}\frac{\partial^2\phi}{\partial s^2} + \frac{\partial T}{\partial s} + (\rho - \rho_v)gbd\cos\phi + \frac{1}{2}C_f\rho 2(b+d)|-u + u_w(x,z,t)|[-u + u_w(x,z,t)] + \rho bd\left[-\frac{\rho_v}{\rho}\left(\frac{\partial u}{\partial t} + w\frac{\partial\phi}{\partial t}\right) + \frac{\partial u_w(x,z,t)}{\partial t} + w_w(x,z,t)\frac{\partial\phi}{\partial t}\right] = 0 \quad (2.18)$$

and

$$EI\frac{\partial^3\phi}{\partial s^3} - T\frac{\partial\phi}{\partial s} + (\rho - \rho_v)gbd\sin\phi + \frac{1}{2}C_d\rho b|-w + w_w(x,z,t)|[-w + w_w(x,z,t)] + C_m\rho\frac{\pi}{4}b^2\left[-\frac{\partial w}{\partial t} + \frac{\partial w_w(x,z,t)}{\partial t}\right] + \rho bd\left[-\frac{\rho_v}{\rho}\left(\frac{\partial w}{\partial t} - u\frac{\partial\phi}{\partial t}\right) + \frac{\partial w_w(x,z,t)}{\partial t} - u_w(x,z,t)\frac{\partial\phi}{\partial t}\right] = 0, \quad (2.19)$$

where

$$u_w(x,z,t) = U\sin\phi + W\cos\phi \quad (2.20)$$

and

$$w_w(x,z,t) = -U\cos\phi + W\sin\phi \quad (2.21)$$

are the encountered flow velocities (wave motion related to the blade) in the blade tangential and normal direction, respectively. According to linear wave theory (Dean & Dalrymple, 1991), the horizontal and vertical components of the wave orbital velocity are given by

$$U(x,z,t) = a_w\omega\frac{\cosh kz}{\sinh kh}\cos(kx - \omega t) \quad (2.22)$$

and

$$W(x,z,t) = a_w\omega\frac{\sinh kz}{\sinh kh}\sin(kx-\omega t). \tag{2.23}$$

Substituting equations (2.22) and (2.23) into equations (2.20) and (2.21) yields

$$u_w(x,z,t) = a_w\omega\frac{\cosh kz}{\sinh kh}\cos\phi\cosh kx\frac{\tan\phi\tan kx-\tanh kz}{\cos\left[kx+\arctan\left(\frac{\tan\phi}{\tanh kz}\right)\right]}\sin\psi_t \tag{2.24}$$

and

$$w_w(x,z,t) = \frac{a_w\omega\cosh kz}{\sinh kh}\cos\phi\cosh kx\frac{-1+\tan\phi\tan kx\tanh kz}{\cos[kx+\arctan(\tan\phi\tanh kz)]}\cos\psi_n, \tag{2.25}$$

where the velocity phase $\psi_t = \omega t - [kx + \arctan(\tan\phi / \tan kz)]$ and $\psi_n = \omega t - [kx + \arctan(\tan\phi\tanh kz)]$.

It is assumed that the blade moves at the same period as the wave period (T_w). It is also assumed that there is a unique solution to the governing equations (2.18), (2.19), (2.4), and (2.5). The existence of symmetric motion is explored by examining a pair of symmetric solutions, i.e., $\{T(s,t), u(s,t), w(s,t), \phi(s,t)\}$ at the position (x,z) at time t and $\{T(s,t+\Delta t), u(s,t+\Delta t), w(s,t+\Delta t), \phi(s,t+\Delta t)\} = \{T(s,t), u(s,t), -w(s,t), -\phi(s,t)\}$ at the symmetric position $(-x,z)$ at time $t+\Delta t$, as demonstrated on Figure 2.10. It takes Δt to move from position (x,z) to $(-x,z)$ and it also takes the same time Δt to move back to (x,z) due to symmetric motion, yielding $\Delta t = T_w/2$.

Taking $\{T(s,t), u(s,t), w(s,t), \phi(s,t)\}$ as the solution at time t, $\{T(s,t), u(s,t), -w(s,t), -\phi(s,t)\}$ is shown to satisfy the compatibility relations by substituting it into the compatibility relation equations (2.4) and (2.5). The next step is to check if $\{T(s,t), u(s,t), -w(s,t), -\phi(s,t)\}$ also satisfies equations (2.18) and (2.19) at $t+\Delta t$. Substituting $\{T(s,t), u(s,t), -w(s,t), -\phi(s,t)\}$ into equations (2.18) and (2.19) for time $t+\Delta t$ yields

$$EI\frac{\partial\phi}{\partial s}\frac{\partial^2\phi}{\partial s^2} + \frac{\partial T}{\partial s} + (\rho-\rho_v)gbd\cos\phi + \frac{1}{2}C_f\rho 2(b+d)\left|-u+u_w\left(-x,z,t+\frac{T_w}{2}\right)\right|\left[-u+u_w\left(-x,z,t+\frac{T_w}{2}\right)\right] + \rho bd\left[-\frac{\rho_v}{\rho}\left(\frac{\partial u}{\partial t}+w\frac{\partial\phi}{\partial t}\right)+\frac{\partial u_w\left(-x,z,t+\frac{T_w}{2}\right)}{\partial t}-w_w\left(-x,z,t+\frac{T_w}{2}\right)\frac{\partial\phi}{\partial t}\right] = 0 \tag{2.26}$$

and

$$EI\frac{\partial^3\phi}{\partial s^3} - T\frac{\partial\phi}{\partial s} + (\rho-\rho_v)gbd\sin\phi + \frac{1}{2}C_d\rho b\left|-w - w_w\left(-x,z,t+\frac{T_w}{2}\right)\right|\left[-w - w_w\left(-x,z,t+\frac{T_w}{2}\right)\right] +$$

$$C_m\rho\frac{\pi}{4}b^2\left[-\frac{\partial w}{\partial t} - \frac{\partial w_w\left(-x,z,t+\frac{T_w}{2}\right)}{\partial t}\right] + \rho bd\left[-\frac{\rho_v}{\rho}\left(\frac{\partial w}{\partial t} - u\frac{\partial\phi}{\partial t}\right) - \frac{\partial w_w\left(-x,z,t+\frac{T_w}{2}\right)}{\partial t} - u_w\left(-x,z,t+\frac{T_w}{2}\right)\frac{\partial\phi}{\partial t}\right] =$$

$$0. \qquad (2.27)$$

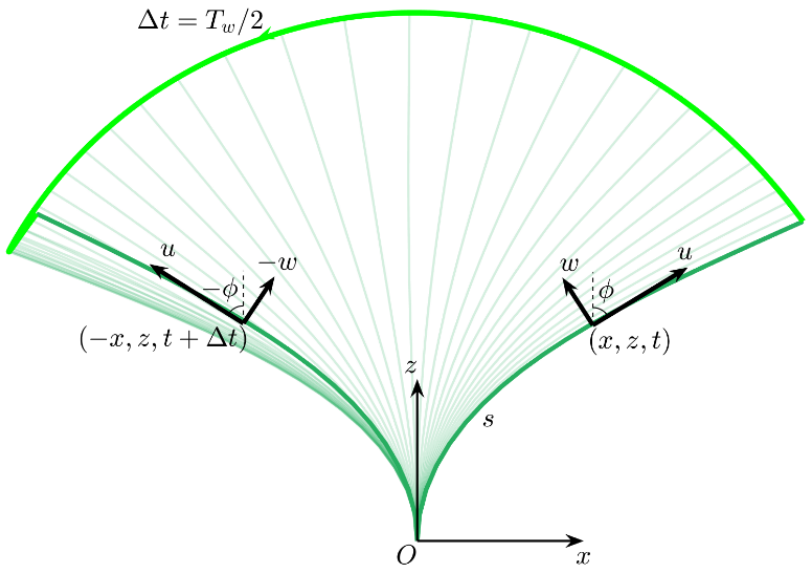

Figure 2.10. The postures of the blade over one-half of a wave period ($\Delta t = T_w/2$) for symmetric motion. The thin arrows show the global coordinate system (x,z) with origin O while the thick arrows show the velocity of the blade segments at the distance of s. The thin green lines indicate the selected blade postures. The thick dark green lines indicate the blade posture with velocity (u,w) and bending angle ϕ at the position (x,z) at time t and the symmetric blade posture with symmetric velocity $(u,-w)$ and symmetric bending angle $-\phi$ at the symmetric position $(-x,z)$ after half wave period. The thick light green line indicates the excursion of the blade tip.

The differences between equations (2.26) and (2.18), and between equations (2.27) and (2.19) are the terms involving flow velocities, u_w and w_w. In order for (2.26) to equal (2.18) and (2.27) to equal (2.19), it requires

$$u_w\left(-x,z,t+\frac{T_w}{2}\right) = u_w(x,z,t) \qquad (2.28)$$

and

$$w_w\left(-x,z,t+\frac{T_w}{2}\right) = -w_w(x,z,t). \qquad (2.29)$$

Replacing (x, z, t) by $(-x, z, t + T_w/2)$ in equations (2.24) and (2.25) yields the velocity at $(-x, z, t + T_w/2)$, i.e.,

$$u_w\left(-x, z, t + \frac{T_w}{2}\right) = a_w\omega\frac{\cosh kz}{\sinh kh}\cos\phi\cosh kx\frac{\tan\phi\tan kx - \tanh kz}{\cos\left[kx + \arctan\left(\frac{\tan\phi}{\tan kz}\right)\right]}\sin(\psi_t + \Delta\psi_t) \quad (2.30)$$

and

$$w_w\left(-x, z, t + \frac{T_w}{2}\right) = -a_w\omega\frac{\cosh kz}{\sinh kh}\cos\phi\cosh kx\frac{-1 + \tan\phi\tan kx\tanh kz}{\cos[kx + \arctan(\tan\phi\tan kz)]}\cos(\psi_n + \Delta\psi_n), \quad (2.31)$$

where

$$\Delta\psi_t = 2\left[kx + \arctan\left(\frac{\tan\phi}{\tan kz}\right)\right] + \pi \quad (2.32)$$

and

$$\Delta\psi_n = 2[kx + \arctan(\tan\phi\tan kz)]. \quad (2.33)$$

By comparing (2.30) and (2.24) as well as (2.31) and (2.25), equations (2.28) and (2.29) are not always guaranteed due to the phase differences $\Delta\psi_t$ and $\Delta\psi_n$. Thus, $\{T(s,t), u(s,t), -w(s,t), -\phi(s,t)\}$ is not a solution to the governing equations (2.18) and (2.19) and therefore the blade motion is asymmetric. The phase differences lying within the interval $[-\pi, \pi)$ are given by

$$\Psi_t = 2\left[kx + \arctan\left(\frac{\tan\phi}{\tan kz}\right)\right] \text{ fmod } 2\pi - \pi \quad (2.34)$$

in the tangential direction and

$$\Psi_n = \{2[kx + \arctan(\tan\phi\tan kz)] + \pi\} \text{ fmod } 2\pi - \pi \quad (2.35)$$

in the normal direction, where the "fmod" operator is defined as $a \text{ fmod } b = a - nb$ and $n \in N$ such that $nb \le a < (n+1)b$. The phase differences shown in equations (2.34) and (2.35) are explicitly expressed as functions of blade displacements, bending angle and wave number (representing wavelength), but implicitly functions of wave conditions and blade characteristics.

The phase differences consist of two terms corresponding to two major mechanisms that induce asymmetric motion, i.e., (i) the blade horizontal displacement (kx) and (ii) the action of vertical wave orbital velocity ($\tanh kz$, the ratio of vertical component to the horizontal component of wave orbital velocity) associated with blade vertical displacement (kz). The effects of bending angle (ϕ) are not

considered as a major mechanism because the term including $\tan\phi$ is dependent on the vertical wave orbital velocity. If the vertical wave orbital velocity does not exist, the effects of $\tan\phi$ will disappear. On the other hand, when $\phi > 45°$, $\tan\phi > 1$ acts as an amplification factor such that the action of vertical wave orbital velocity is more pronounced than the horizontal displacement of the blade.

Due to the phase differences in the encountered flow velocities, the drag and inertial forces are asymmetric, as well as the blade motion. The tangential phase difference Ψ_t describes the phase difference of the combined tangential force acting on the blade and driving the asymmetric blade motion. The tangential forces include friction and the tangential component of the virtual buoyancy. The normal phase difference Ψ_n describes the phase difference of the combined normal force acting on the blade and driving the asymmetric blade motion. The normal forces include drag, added mass force, and the normal component of the virtual buoyancy. In the case of perfect symmetric blade motion, both Ψ_t and Ψ_n should equal zero at each time step. The onset of asymmetric motion will occur, however, relatively symmetric motion (defined as $\beta_{xT} \ll 1$) can occur when

$$|\Psi_t| \ll 1 \tag{2.36}$$

and

$$|\Psi_n| \ll 1. \tag{2.37}$$

The drag dominates compared to the frictional and inertial forces, so the normal forces are much larger than the tangential forces. Therefore, the contribution of normal phase difference Ψ_n to the asymmetric motion is expected to be much larger than that of tangential phase difference Ψ_t. Thus, the motion is symmetric as long as equation (2.37) is satisfied.

Asymmetric blade motion is caused by the phase differences Ψ_t and Ψ_n of the encountered flow velocity due to the blade displacements. However, the magnitude of the asymmetry is also impacted by other factors including the blade characteristics and wave properties, which determine the blade displacements. The impacts of these factors on the magnitude of blade asymmetry will be further investigated using the cable model in the following sections.

2.4.3. Case study

The dynamic response of blades to symmetric wave forcing is investigated using the cable model. Blade geometric and material properties are adopted from those summarized in Lei and Nepf (2016), which are also provided in Table 2.3. In this case study, the blade length $l = 0.05 \sim 0.60$ m and the flexural rigidity $EI = 0.13 \times 10^{-5} \sim 3.9 \times 10^{-5}$ Nm^2 are used to represent a variety of blade characteristics. Water depth is set as $h = 1$ m such that $l/h = 0.05 \sim 0.60$. Wave period $T_w = 0.9 \sim 12.2$ s is selected such that the ratio of water depth to wavelength is $h/L = 0.026 \sim 0.791$. This would correspond to a wide range of wave conditions from shallow to deep water. The wave height is set as $H/h = 0.02 \sim 0.30$ to consider the influence of wave heights on asymmetric motion. To make equations (2.12) to (2.14) applicable to calculate the hydrodynamic force coefficients, the selected results for analysis are from the cases with $KC = 0.1 \sim 113.6$. The corresponding $Re = 9.7 \sim 3822.5$ and $Ca = 3.1 \sim 14742.8$.

Table 2.3. Blade geometric and material properties for the selected species used in the present study following Lei and Nepf (2016).

	Elastic modulus E (GPa)	Density ρ_v (kg/m^3)	Thickness d (mm)	Width b (mm)	Length l (m)	Flexural rigidity EI ($\times 10^{-5}$ Nm^2)
Thalassia testudinum[a]	0.4 ~ 2.4	940	0.30 ~ 0.37	10	0.1 ~ 0.25	-
Zostera marina[b]	0.3	700	0.15 ~ 0.23	3 ~ 5	0.15 ~ 0.6	-
Posidonia oceanica[c]	0.5	910	0.2	10	0.15 ~ 0.5	-
Blades for case study	0.1 ~ 0.3	900	0.25	10	0.05 ~ 0.6	0.13 ~ 3.9

[a]Bradley and Houser (2009), Weitzman et al. (2013). [b]Abdelrhman (2007), Fonseca et al. (2007), McKone (2009), Moore (2004). [c]Folkard (2005), Infantes et al. (2012).

To investigate the onset of asymmetric blade motion, Ψ_t and Ψ_n at the blade tip are calculated using the displacements and bending angles of the blade tip defined as Ψ_{tT} and Ψ_{nT}, respectively. The results of the blade posture asymmetry (β_{xT}) are shown on Figure 2.11, where waves propagate to the right such that $\beta_{xT} > 0$. The results for the cases where waves propagate to the left are omitted here because β_{xT}

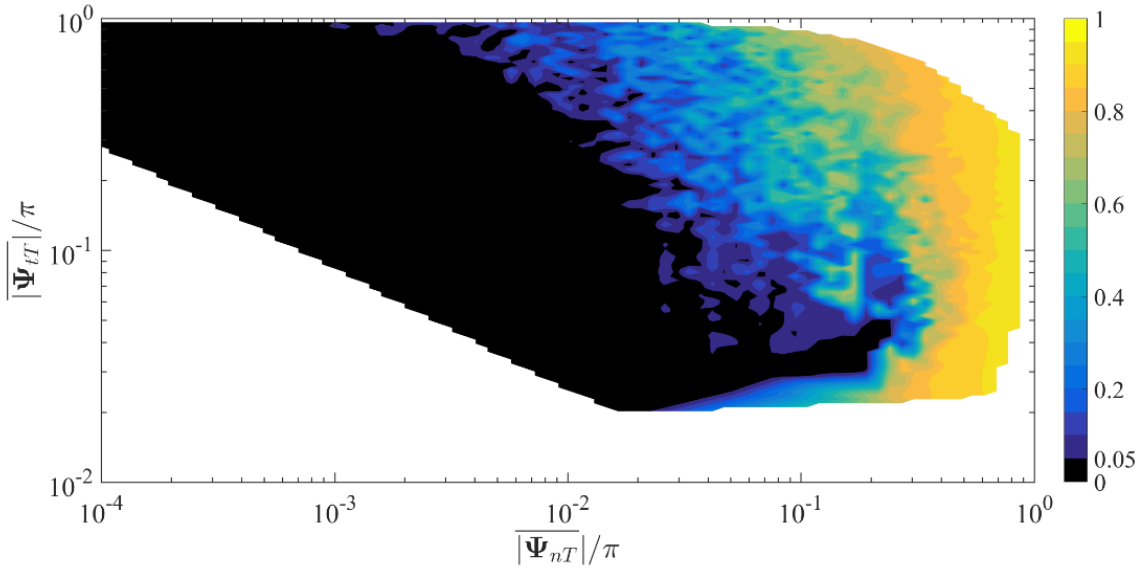

Figure 2.11. Contour of the blade posture asymmetry (β_{xT}, in colors) vs the normal phase difference Ψ_{nT} and tangential phase difference Ψ_{tT} at the blade tip. Waves propagate to the right such that $\beta_{xT} > 0$.

keeps the same magnitude but with an opposite sign. The blade motion is near symmetric ($\beta_{xT} < 0.05$) when $|\Psi_{nT}|/\pi < 0.003$, regardless of the value of Ψ_{tT}. If $|\Psi_{tT}|/\pi < 0.3$, $\beta_{xT} < 0.05$ when $|\Psi_{nT}|/\pi < 0.01$. Posture asymmetry increases with increasing Ψ_{tT} and Ψ_{nT}. "Ripples" appear in the contours on Figure 2.11 because Ψ_{tT} and Ψ_{nT} are the factors that only induce asymmetry. However, when the asymmetry occurs, the magnitude is influenced by the blade material and geometric characteristics, as well as the wave conditions.

The blade posture asymmetry is also examined as a function of the ratio of blade length to wave length ($\gamma = l/L$) for the wave conditions and blade characteristics shown on Figure 2.12. The results show that the motion is almost symmetric ($\beta_{xT} < 0.05$) when $\gamma < 0.01$. As γ increases, β_{xT} increases to a peak value defined as peak asymmetry (β_p) and the corresponding γ is defined as peak length ratio (γ_p), which characterizes the resonant condition. As shown on Figure 2.12, β_p increases with wave height and blade length. It is also evident that $\beta_p$decreases with increasing blade flexural rigidity (Figure 2.12a-d). However, for longer blades such that $l/h \geq 0.45$ as shown on Figure 2.12(e) and (f), the decrease in β_p is less than 5\% for $H/h \geq 0.1$. This might be because long blades ($l/h \geq 0.45$) are so flexible that their postures are

close to a bending limit. Near the limit, the posture changes slowly with flexural rigidity and so does the peak asymmetry. In general, the motion of a longer blade with smaller flexural rigidity in larger-amplitude waves behaves more asymmetric.

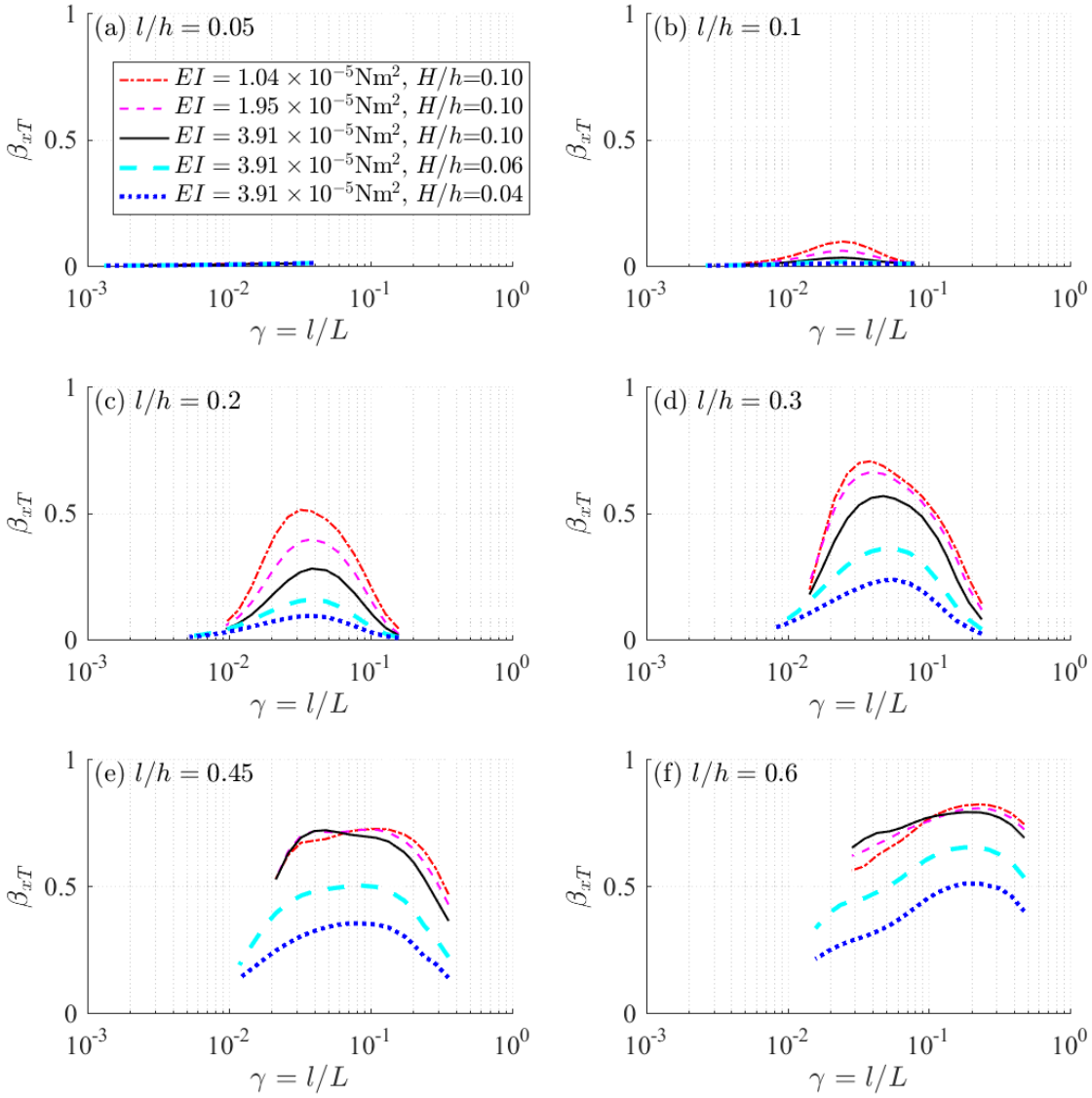

Figure 2.12. The blade posture asymmetry (β_{xT}) as a function of the ratio of blade length and wavelength ($\gamma = l/L$). The blade lengths normalized by water depth (l/h) are (a) 0.05, (b) 0.1, (c) 0.2, (d) 0.3, (e) 0.45 and (f) 0.6. The wave heights normalized by water depth (H/h) are 0.04, 0.06 and 0.1. The blade flexural rigidities (EI) are 1.04×10^{-5}, 1.95×10^{-5} and 3.9×10^{-5} Nm^2.

2.5. Discussion

2.5.1. Mechanisms for asymmetric blade motion

In symmetric waves, asymmetric blade motion is due to the phase differences of the encountered flow velocity and induced by two mechanisms: (i) the blade displacements and (ii) the vertical component of the wave orbital velocity. The effect of the vertical component of the orbital velocity is more pronounced than that of blade displacements, especially for a larger deflected blade with the posture being more horizontal. Previous research attributed the asymmetric motion to the wave orbital trajectory based on the assumption that the blade motion is at the same scale as the wave excursion (Döbken, 2015). However, the generalized mechanisms for the asymmetric blade motion may be derived from the wave flow field relative to the blade motion without that assumption.

The blade postures as a function of wave orbital velocities at 8 wave phases over one wave period are shown on Figure 2.13, where the waves propagate to the right. The blade is initially vertical at $t/T_w = 0$ and reaches steady state after up to 30 wave cycles. The steady state position of the blade is independent of its initial conditions. The blade motion is governed by the driving force and the bending stiffness of the blade. To simply demonstrate the underlying mechanisms, it is assumed that the driving force is dominated by drag and the blade velocity (u, w) is smaller than the wave orbital velocity (U, W) such that the force direction acts in the direction of the flow velocity (U, W). For the steady scenario at position 0 under wave crest, the driving force is directed to the right following wave orbital velocity, which causes the blade to bend to the right (Figure 2.13c). From position 0 to position 2, the horizontal component of wave orbital velocity U is directed to the right in the direction of wave propagation, while the vertical component of wave orbital velocity W points downward. From position 2 to 4, U changes direction toward the left, but W is still directed downward. Ultimately, there is a net force imposed on the blade due to W acting downward on the blade for the first half of the wave cycle, which promotes the downward motion of the blade and prevents it from moving back to position 0. In the second half of the wave period (positions 4 to 7), the blade begins slightly inclined to the right compared to position 0. Over the second half of the wave

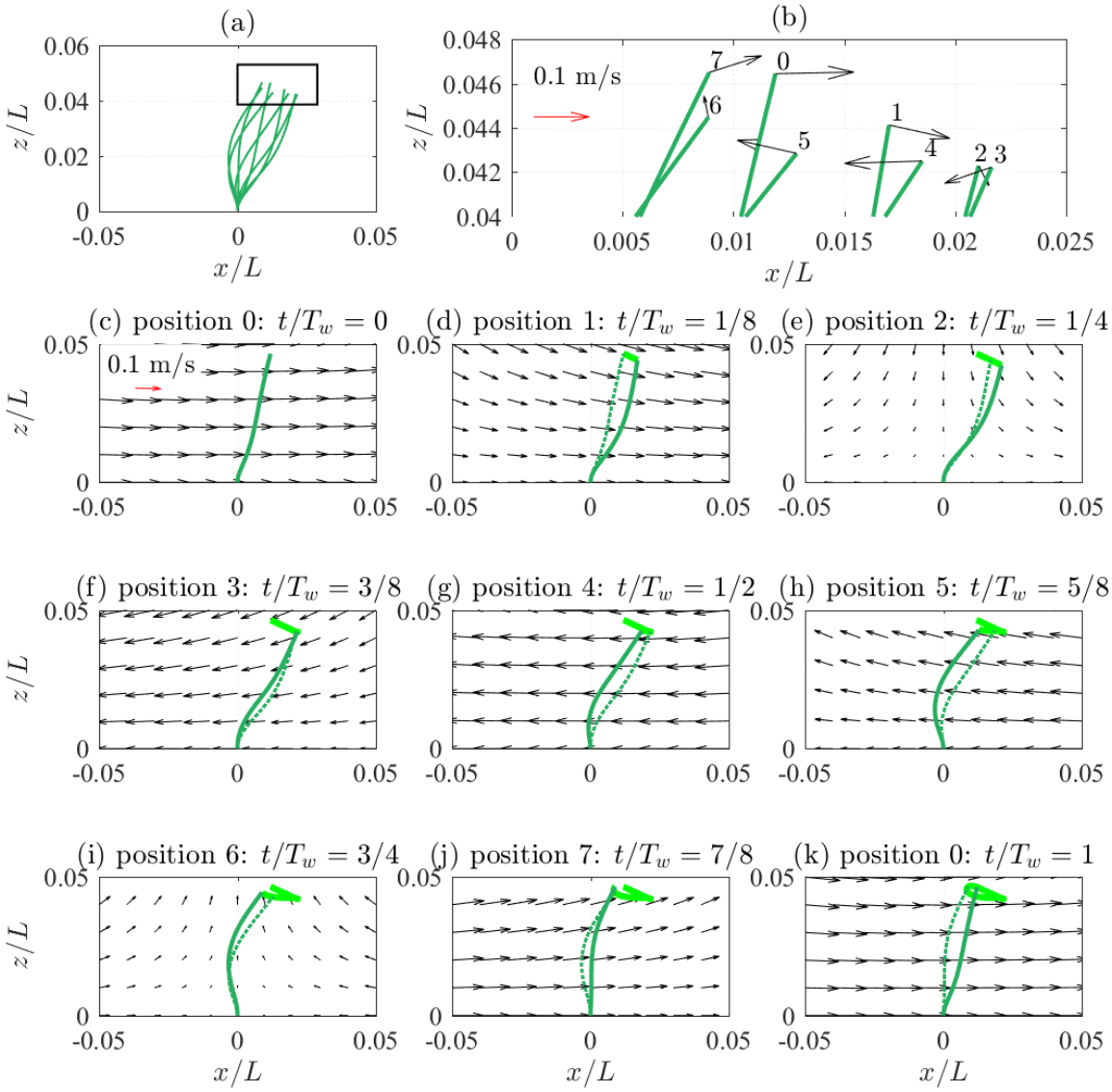

Figure 2.13. The postures of a 45 cm-long blade (in green) in the wave flow field with wave period T_w = 3.2 s and amplitude $a_w = 5$ cm in 1 m-deep water (intermediate water waves). The blade posture asymmetry is $\beta_{xT} = 0.7$. The waves propagate from left to right. The dark thin green lines indicate the blade postures. The blade displacements (x, z) are normalized by wavelength (L). (a) The blade postures from positions 0 to 7. (b) The upper parts (zoom in) of the blade postures labeled number 0 to 7, which indicate the blade positions at 8 wave phases with $t/T_w = 0$, 1/8, 1/4, 3/8, 1/2, 5/8, 3/4, 7/8, and 1. The black arrows indicate wave orbital velocity at the blade tip. (c) to (k) show the blade postures and wave flow field. The green solid line indicates the current blade posture and the dashed green lines indicate the blade posture at previous one position. The light thick green line indicate the trajectory of the blade tip. The black arrows indicate the wave flow field.

period, U points to the left from positions 4 to 6 and changes direction toward the right from positions 6 to 0. However, W is directed upward from positions 4 to 0, which prevents the downward motion of the blade on the left side of the vertical axis. The net effect of W is a blade that is inclined in the direction of wave propagation.

Blade displacement influences the asymmetric flow velocity encountered by the blade. For example, by comparing U during the second half of the wave period (position 4-7, Figure 2.13g-j) with the first half (position 0-3, Figure 2.13c-f), the positive horizontal velocity U towards the right is larger than the negative U towards the left. Therefore, the net horizontal component is directed to the right, causing the blade to incline to the right.

Even though wave orbital velocities are symmetric over the wave period, blade inclination occurs due to the blade displacement and the asymmetric action of the vertical component of the wave orbital velocity. This inclination is more pronounced in shorter waves, as the vertical velocity increases to the same magnitude as the horizontal velocity, and the blade displacement becomes more comparable with the shortened wavelength.

2.5.2. Conditions for symmetric blade motion

Blade displacements and vertical wave orbital velocities induce blade asymmetry. Symmetric blade motion therefore occurs if these variables are very small, which are satisfied when (i) blade length is much smaller than the wavelength ($l/L \ll 1$), (ii) in shallow water waves ($h/L \ll 1$) and (iii) the blade length is much smaller than water depth ($l/h \ll 1$) in finite-depth-water waves. These conditions are derived from equations (2.36) and (2.37) and the detail derivations are provided in Appendix A.

For short blades in long waves ($l/L \ll 1$), the blade displacement and W are negligible to the scale of wavelength so that phase differences between the encountered wave orbital velocities at asymmetric positions are also negligible, resulting in symmetric blade motion.

Similarly, in shallow water waves ($h/L \ll 1$), the blade motion is symmetric because the effects of blade displacement and W are negligible due to the small blade displacement compared to the

wavelength and negligible W in shallow water waves. One example of the symmetric blade motion in shallow water waves is shown on Figure A.1.

For short blades ($l/h \ll 1$) in finite-depth-water waves ($h/L \sim O(1)$), the blade motion behaves symmetric because the horizontal displacement of the blade is small, and W is close to 0 when approaching the blade near the bottom. In the field, at the initial growth phase of SAV, the blade is so short that the motion is symmetric. When the blade grows longer, the blade motion may become asymmetric.

2.5.3. Properties and implications of asymmetric blade motion

Strict conditions for symmetric motion indicate that the occurrence of symmetric motion is limited. Therefore, the blade motion is typically asymmetric for most situations. The peak asymmetry occurs when the ratio of blade length to wavelength reaches the peak length ratio. The results showed that the peak asymmetry is a function of wave conditions and blade characteristics. Generally, the peak asymmetry of blade motion becomes larger in waves with a larger amplitude. When the blade grows longer, the peak asymmetry also increases because longer blade has larger deflection and encounters larger wave orbital velocities. However, the blade flexural rigidity reduces the peak asymmetry.

The behavior of asymmetric blade motion can be used to guide planting strategies of SAV for sediment settlement. The asymmetric motion is expected to benefit sediment settlement because the "shelter" created by the blade inclination could hinder sediment suspension at the seabed. To take advantage of the peak asymmetry, it is recommended to choose the SAV species such that the ratio of the blade length and the dominant wavelength is close to the peak length ratio. Longer blades are preferred because they increase the peak asymmetry and provide a larger "shelter".

The asymmetric blade motion may also influence the morphological characteristics and the fatigue life of SAV. The cross-section of the vegetation and even the elastic modulus may become asymmetric in response to the asymmetric blade motion. For example, asymmetric motion induces the stress imbalance on the cross section. Thus, the tension side of the cross section becomes thinner while the compression side becomes thicker. Asymmetric blade motion and sheltering may lead to morphological change which in turn

may affect flow pattern near the vegetation. The influences of asymmetric motion on the vegetation morphology and fatigue life will be investigated in the future work.

In the field, waves are usually superimposed with background currents (Weitzman et al., 2013, 2015). Following currents are expected to enhance the asymmetry of the blade motion while opposing currents are expected to decrease the asymmetry. With following currents, the asymmetry of blade motion increases with increasing currents (e.g., Figure 6 of Lei & Nepf, 2019a).

A single vegetation blade likely has little influence on waves, however, numerous blades as a SAV meadow can significantly impact waves by generating turbulence (Abdolahpour et al., 2018; Tan et al., 2019; Tang et al., 2019; Zhang et al., 2018), reducing wave energy (Garzon et al., 2019; Henderson et al., 2017; Infantes et al., 2012; Nowacki et al., 2017; Paul et al., 2012), and inducing mean currents (Abdolahpour et al., 2017; Chen et al., 2019; Luhar & Nepf, 2011). The wave-driven currents in a vegetation meadow are expected to enhance the asymmetry of blade motion (e.g., Figure 8 of Lei & Nepf, 2019b). In return, the asymmetric motion of blades as a meadow are likely to impact the wave-driven current and consequently the mass transport, which warrants further investigation. The asymmetric blade motion in a meadow is observed to modify the wave orbital velocity and further influence wave attenuation with a magnitude larger than the influences of blade stiffness (Paul et al., 2012). The wave shape may also be changed with the asymmetric blade motion due to the asymmetric wave attenuation.

2.6. Summary

The asymmetric behavior of SAV in waves was investigated using a mass-consistent cable model. Implementing the cable model improves blade motion modeling. This was especially true for "second-normal-mode-like" blade motion by incorporating the effects of the blade-motion-induced rotations of local Lagrangian coordinates along the blade on inertial force, the compatibility relations for geometrical continuity of the blade segments and the spatial variation of wave orbital velocity encountered by the blade due to blade displacements. With this cable model, two major factors were found to influence asymmetric blade motion other than wave orbital motion asymmetry. These factors are (i) the spatial asymmetry of the encountered wave orbital velocities induced by the blade displacements and (ii) the asymmetric action on

the blade by the vertical wave orbital velocities. When near symmetric motion exists ($\beta_{xT} \ll 1$), conditions are (i) the blade length is much smaller than the wavelength with $l/L \ll 1$, (ii) in shallow water waves with $h/L \ll 1$ or (iii) the blade length is much smaller than the water depth with $l/h \ll 1$ in finite-depth-water waves. Peak asymmetry occurs when the ratio of blade length to wavelength (l/L) reaches the critical value. Peak asymmetry is found to increase with wave height and blade length but decrease with increasing blade flexural rigidity.

Asymmetric blade motion in a vegetation meadow is expected to influence the wave-driven currents, wave attenuation and wave shape. Meanwhile, the wave-driven currents and wave asymmetry also influence the asymmetry of blade motion. It is therefore worthwhile not only to investigate the dynamics of vegetation, but to also incorporate the two-way feedback between the asymmetric blade motion and the wave flow field in wave-vegetation models, such as the coupled CFD and immersed boundary method model by Chen and Zou (2019) and N-box model (Zeller et al., 2015). Improved blade posture simulations by the present consistent-mass cable model will yield more accurate predictions for wave-vegetation interaction. In the future work, the cable model will be coupled with a 3D wave hydrodynamics model to investigate the capacity of SAV for wave attenuation, as well as its influence on wave-driven currents in a vegetation meadow.

2.7. Acknowledgments

This work was completed as part of the PhD research of Longhuan Zhu who is supported by National Science Foundation Award IIA-1355457 to Maine EPSCoR at the University of Maine. The authors gratefully acknowledge the assistance of the Advanced Computing Group of the University of Maine System in producing and storing the numerical data, which are accessible through this site (http://dataverse.acg.maine.edu/dvn/dv/SAV_Motion_In_Waves_JGR_ Oceans). The authors would like to sincerely thank Jeffrey Koseff for the guidance to get the data used on Figure 2.2, Mitul Luhar and Heidi Nepf for providing the data used on Figure 2.3-2.7, and Dylan Schlichting for reviewing the paper for style and grammar. The authors would also sincerely thank two anonymous reviewers for exceptionally constructive and helpful comments that greatly improved this manuscript.

CHAPTER 3

WAVE ATTENUATION BY SUSPENDED CANOPIES WITH CULTIVATED KELP (*SACCHARINA LATISSIMA*)

3.1. Background

Kelp is considered one of many types of brown macroalgae seaweeds that contribute to coastal ecosystems by providing food, shelter, and enhanced oxygen habitats for fish and marine animals. Kelp also provides services such as recycling inorganic nutrients, preventing eutrophication, reducing carbon dioxide concentration, and potentially mitigating ocean acidification (Duarte et al., 2017; Stévant et al., 2017; Xiao et al., 2017; Campbell et al., 2019). Furthermore, the existence of kelp can physically influence the environmental hydrodynamics. For example, *Macrocystis pyrifera* (giant kelp) forests can significantly reduce currents (Jackson 1997; Gaylord et al., 2007; Rosman et al., 2007) and internal wave amplitudes (Jackson 1984; Rosman et al., 2007) off west coast of California, USA. However, no significant (surface) wave attenuation was observed over *M. pyrifera* forests by Elwany et al. (1995), which is likely due to the compliant nature of the kelp, the sparse canopy density (~0.1 plants/m^2) and the limited canopy height related to the water depths (typical averages of 10 m). Similar results are also observed for highly flexible *Nereocystis luetkeana* (bull kelp, Gaylord et al., 2003) and deeply submerged *Ecklonia radiata* (<10% of the water column, Morris et al., 2019). However, *Laminaria hyperborea* (tangle) with 25 plants/m^2 in shallow water (5 m) have been observed to reduce wave energy by 70-85% over a distance of 258 m (Mork, 1996).

Unlike wild kelp that grows on the seafloor, kelp aquaculture farms that float may also have the potential to dissipate wave energy, especially since surface wave energy is concentrated near the surface. Furthermore, many kelp aquaculture farms are densely seeded to maximize economic output. With large cultivated kelp plant density, the wave attenuation performance could provide better performance than naturally occurring kelp beds.

Wave attenuation theories for submerged canopies including wild kelp beds have been developed by Dalrymple et al. (1984) and Kobayashi et al. (1993). These approaches were extended to floating and suspended canopies by Plew et al. (2005) and Zhu and Zou (2017), respectively. Zhu and Zou (2017) showed that the suspended and floating canopies can reduce more wave energy than submerged canopies in the same conditions because wave energy decreases toward the bottom, especially for shorter waves. However, these approaches assumed a rigid canopy component without motion, which may overestimate the wave attenuation. Recently, Zhu et al. (2020a) extended the wave attenuation methods to be frequency dependent for random waves and incorporated the motion of the flexible canopy component. Compared to nearshore submerged aquatic vegetation (SAV), suspended aquaculture structures are less affected by water level changes since suspended aquaculture structures float near the water surface (Zhu et al., 2020a). In one case study, Zhu et al. (2020a) demonstrated that the implementation of aquaculture structures offshore can extend the wave attenuation capacity of SAV-based living shorelines over wider ranges of wave frequency and water level. With numerical techniques, such as the SWASH (Simulating WAves till SHore, Zijlema et al., 2011) model, Chen et al. (2019) investigated the wave-driven circulation cell induced by suspended canopies and found that the vertical position of the canopy also has significant effects on the wave-driven current in the canopy. Although these studies have provided important insight into the wave attenuation potential of suspended aquaculture farms, experimental research to quantify the performance of suspended kelp aquaculture is still needed.

Research to examine the hydrodynamic characteristics of kelp blades in steady flow was conducted by Buck and Buchholz (2005). In their study, the drag characteristics of both a single and an aggregate of *Saccharina latissima* (sugar kelp) blades were investigated with tow tests in still water. The results showed sheltering interactions among the blades so that the drag force of an aggregate of kelp blades cannot be estimated by simply superimposing the drag of individual blades. Vettori and Nikora (2019) investigated the turbulent flow interaction with single blades of *S. latissima* in an open-channel flume and showed enhanced turbulence in blade wakes. At low current speeds, the flapping motion of kelp blades of *S. latissima*, *M. pyrifera*, and *N. luetkeana* can significantly enhance the nutrient flux to the blade surface

(Huang et al., 2011). Using polyethylene to model *S. latissima*, Vettori and Nikora (2018) found that the model kelp blades increase the turbulence intensity and reduce the mean longitudinal velocity. By comparing the hydrodynamic performance of *S. latissima* with the performance of the model blades, Vettori and Nikora (2020) showed that the model blades replicated many aspects of *S. latissima* blade dynamics, although the drag force and reconfiguration were underestimated. To avoid the dynamic similarity issues, Fredriksson et al. (2020) conducted full-scale model experiments to understand the hydrodynamics of an aggregate of model *S. latissima* blades in steady flow. Fredriksson et al. (2020) showed a threshold for reconfiguration as the tow speed at which the horizontal component of tangential drag was equal or exceeded the horizontal component of the normal drag. To build upon this work, it is important to examine the dynamics of suspended kelp blades in waves and the value of suspended kelp aquaculture structures for wave attenuation in a laboratory environment. Appropriate parameters from these experiments are essential for modeling wave attenuation with canopy models.

The objective of this study is to quantify the wave attenuation capacity of suspended kelp canopies with a scaled physical model in a set of laboratory experiments. To predict wave attenuation under a wider range of conditions, a simple numerical model was developed based on the blade dynamic model in Zhu et al. (2020b). This model was also used to perform dynamic similarity analysis in preparation for the model tests. The physical model kelp material was chosen from the measured morphological and mechanical properties of cultivated *S. latissima* at Saco Bay, Maine in the USA considering dynamic similarity. The motions of both a single and an aggregate of blades were recorded to analyze the blade dynamics with focus on the mechanisms for observed roll-up of suspended blades. The horizontal forces on unsheltered single blades and sheltered blades were measured to examine the differences. The wave height evolution along the suspended canopy was also measured to investigate wave attenuation performance. With the experimental results, bulk drag coefficient and effective blade length estimates for the suspended canopy were developed. The numerical model was compared with the datasets and then used to investigate the potential of using suspended kelp aquaculture structures as nature-based coastal protection.

3.2. Materials and methods

3.2.1. Theory for blade dynamics and wave attenuation

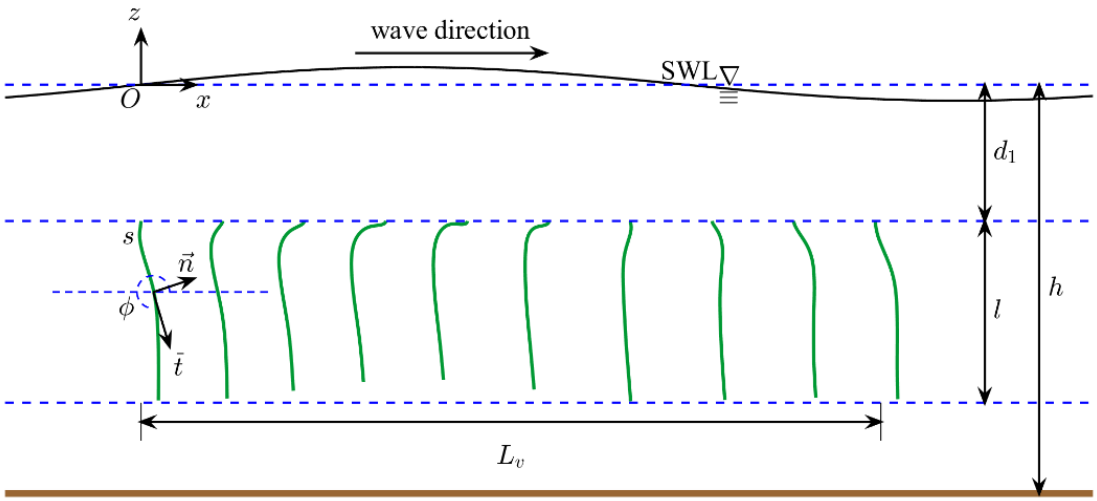

Figure 3.1. Sketch for the coordinate systems. The global Cartesian reference frame (x, z) with $x = 0$ at the leading edge of the canopy and $z = 0$ at the still water level (SWL). The local Lagrangian coordinate system $(\vec{t}, \vec{n})$ along the blade length (s) associated with the angle of ϕ between the horizontal line and the blade tangential direction $(\vec{t})$. The blade length is l. The suspended blade is fixed at the upper end with distance of d_1 below the SWL. The canopy length is L_v. The water depth is h.

The dynamics of kelp blades in waves can be described using the cable model in Zhu et al. (2020b) by representing the structure as a cantilever beam discretized as blade segments (ds). The velocity components of the blade segment are defined using a local Lagrangian coordinate system $(\vec{t}, \vec{n})$ along the blade length with $\vec{t}$ representing the blade-tangential direction and $\vec{n}$ as the blade-normal direction (Figure 3.1). The velocity components in the blade-tangential direction (u) and normal direction (w) are a function of the distance (s) along the blade length (l) from the fixed end with time (t). The wave velocity field (U, W) is defined using global Cartesian coordinates (x, z), where the horizontal coordinate x is positive in the direction of wave propagation with $x = 0$ at the leading edge of the kelp canopy and the vertical coordinate z is positive upward with $z = 0$ at the still water level (SWL). The angle of the tangential direction $(\vec{t})$ relative to the horizontal direction (x) is ϕ. Thus, the points in the Lagrangian coordinate

system $(\vec{t},\vec{n})$ can be obtained by rotating the global Cartesian coordinates (x,z) counterclockwise by ϕ. In the procedure, a set of normalized variables were applied to the governing equations in Zhu et al. (2020b) and described as,

$$\hat{s}=\frac{s}{l},\ \hat{t}=t\omega,\ \hat{u}=\frac{u}{l\omega},\ \hat{w}=\frac{w}{l\omega},\ \hat{T}=T\frac{l^2}{EI},\ \hat{U}=\frac{U}{U_m},\text{ and }\hat{W}=\frac{W}{U_m}, \tag{3.1}$$

where T is the effective tension of the blade, E is the bending elastic modulus, $I=bd^3/12$ is the second moment of the cross-section area of the blade with b being the blade width and d being the blade thickness, $\omega=2\pi/T_w$ is the wave angular frequency with T_w being the wave period, and U_m is the magnitude of the horizontal wave orbital velocity. Therefore, the dimensionless governing equations are given by

$$\frac{\partial\phi}{\partial\hat{s}}\frac{\partial^2\phi}{\partial\hat{s}^2}+\frac{\partial\hat{T}}{\partial\hat{s}}+B\sin\phi+\frac{1}{2}C_f2(1+\delta)Ca\left|-L\hat{u}+\hat{U}\cos\phi+\hat{W}\sin\phi\right|\left(-L\hat{u}+\hat{U}\cos\phi+\hat{W}\sin\phi\right)+2\pi\frac{Ca\delta}{KC}\left[-\rho'L\left(\frac{\partial\hat{u}}{\partial\hat{t}}-\hat{w}\frac{\partial\phi}{\partial\hat{t}}\right)+\frac{\partial\hat{U}}{\partial\hat{t}}\cos\phi+\frac{\partial\hat{W}}{\partial\hat{t}}\sin\phi\right]=0, \tag{3.2}$$

$$-\frac{\partial^3\phi}{\partial\hat{s}^3}+\hat{T}\frac{\partial\phi}{\partial\hat{s}}+B\cos\phi+\frac{1}{2}C_dCa\left|-L\hat{w}-\hat{U}\sin\phi+\hat{W}\cos\phi\right|\left(-L\hat{w}-\hat{U}\sin\phi+\hat{W}\cos\phi\right)+C_m\frac{2\pi^2}{4}\frac{Ca}{KC}\left[-L\frac{\partial\hat{w}}{\partial\hat{t}}+\frac{\partial}{\partial\hat{t}}\left(-\hat{U}\sin\phi+\hat{W}\cos\phi\right)\right]+2\pi\frac{Ca\delta}{KC}\left[-\rho'L\left(\frac{\partial\hat{w}}{\partial\hat{t}}+\hat{u}\frac{\partial\phi}{\partial\hat{t}}\right)-\frac{\partial\hat{U}}{\partial\hat{t}}\sin\phi+\frac{\partial\hat{W}}{\partial\hat{t}}\cos\phi\right]=0, \tag{3.3}$$

$$\frac{\partial\hat{u}}{\partial\hat{s}}+\hat{w}\frac{\partial\phi}{\partial\hat{s}}-\frac{1}{12}\delta^2S^2\frac{\partial\hat{T}}{\partial\hat{t}}=0, \tag{3.4}$$

and

$$\frac{\partial\hat{w}}{\partial\hat{s}}-\hat{u}\frac{\partial\phi}{\partial\hat{s}}+\frac{\partial\phi}{\partial\hat{t}}=0. \tag{3.5}$$

The dimensionless parameters governing the blade dynamics include the aspect ratio,

$$\delta=d/b, \tag{3.6}$$

the slenderness,

$$S=b/l, \tag{3.7}$$

the length ratio,

$$L=l/A_w, \tag{3.8}$$

the Keulegan-Carpenter number,

$$KC = U_m T_w / b, \tag{3.9}$$

the density ratio,

$$\rho' = \rho_v / \rho, \tag{3.10}$$

the buoyant parameter,

$$B = (\rho - \rho_v) g b d l^3 / EI = (1 - \rho') C_a / F_r^2, \tag{3.11}$$

and the Cauchy number,

$$Ca = \rho b U_m^2 l^3 / EI, \tag{3.12}$$

where ρ_v is the blade mass density, ρ is the water density, g is the gravitational acceleration, $A_w = U_m/\omega$ is the wave orbital excursion, and $F_r = U_m/\sqrt{gb}$ is the Froude number. In (3.4), the friction coefficient is $C_f = 0.074 Re^{-1/5}$ (Abdelrhman, 2007; Zeller et al., 2014) with the Reynolds number $Re = U_m b/\nu$ and ν being the fluid kinematic viscosity. In (3.5), the drag coefficient is $C_d = \max(10KC^{-1/3}, 1.95)$ and the added mass coefficient is $C_m = \min(C_{m1}, C_{m2})$ with $C_{m1} = \begin{cases} 1 + 0.35KC^{2/3}, & KC < 20 \\ 1 + 0.15KC^{2/3}, & KC \geq 20 \end{cases}$ and $C_{m2} = 1 + (KC - 18)^2/49$ (Luhar, 2012; Luhar and Nepf, 2016). The formulas for C_d and C_m are obtained from the experiments by Keulegan & Carpenter (1958) and Sarpkaya & O'Keefe (1996) with $KC = 1.7 \sim 118.2$.

The dynamic similarity for the blade motion requires the same dimensionless parameters in (3.6) to (3.12) for the model and the full-scale prototype. The aspect ratio (δ), slenderness (S), and length ratio (L) represent the geometrical property and the KC number represent the inertia property of fluid. The similarity for δ, S, L, and KC can be satisfied by Froude similarity criteria (including geometrical similarity). The density ratio ρ', buoyant parameter B, and Cauchy number Ca represent the blade material properties. However, they are not independent as $B = (1 - \rho')C_a/F_r^2$ (3.11). Therefore, two of the following parameters: ρ', B, and Ca are the required criteria to select the material to fabricate the model blades. In a similar approach, Fryer et al. (2015) used ρ' and Ca as the similarity criteria to fabricate the model kelp blade for *Macrocystis* with a silicone-based polymer.

In this study, the blade is fixed and suspended at the upper end ($s = 0$) with tangential direction downward such that $\phi = 3\pi/2$ for the initial static state (Figure 3.1). Thus, the boundary conditions are set as $\hat{u} = 0$, $\hat{w} = 0$ and $\phi = 3\pi/2$ at the fixed end with $\hat{s} = 0$, as well as $\hat{T} = 0$, $\partial\phi/\partial\hat{s} = 0$ and $\partial^2\phi/\partial\hat{s}^2 = 0$ at the free end with $\hat{s} = 1$. The relationships between s and (x, z) are

$$x = \int_0^s \cos\phi \, ds, \tag{3.13}$$

and

$$z = -d_1 - \int_0^s \sin\phi \, ds, \tag{3.14}$$

where d_1 is the distance from the upper fixed end of the blade to SWL (Figure 3.1). Equations (3.13) and (3.14) are required to calculate the blade posture and transit the flow velocity from global Cartesian coordinates to local Lagrangian coordinates. Solving the blade dynamical equations (3.2) to (3.5) with boundary conditions yields the blade velocity (u, w) and direction angle (ϕ).

For linear waves, the wave orbital velocities are expressed as (Dean & Dalrymple, 1991)

$$U = \frac{H}{2}\omega \frac{\cosh k(h+z)}{\sinh kh} \cos(kx - \omega t), \tag{3.15}$$

and

$$W = \frac{H}{2}\omega \frac{\sinh k(h+z)}{\sinh kh} \sin(kx - \omega t), \tag{3.16}$$

where H is the wave height, h is the water depth, and $k = 2\pi/\lambda$ is the wave number with λ being the wavelength and determined by dispersion equation $\omega^2 = gk \tanh kh$.

Wave energy dissipation is assumed to be the work of canopy drag following Zhu et al. (2020a) for which the conservation equation becomes

$$\frac{\partial E c_g}{\partial x} = -\int_0^l N\alpha_S \overline{\frac{1}{2} C_d \rho b \, |U_R| \, U_R^2} \, ds, \tag{3.17}$$

where $E = \rho g H^2/8$ is the local wave energy per unit horizontal area, $c_g = \omega(1 + 2kh/\sinh 2kh)/2k$ is the wave group velocity, N is the canopy density defined as the number of blades per unit horizontal area, $\alpha_S \leq 1$ is a factor to consider the sheltering effects between blades with $\alpha_S = 1$ for no sheltering, and U_R is the relative velocity normal to the blade with

$$U_R = -w - U\sin\phi + W\cos\phi. \tag{3.18}$$

Solving (3.17) yields the transmitted wave height at distance x in relation to the incident wave height H_0 at $x = 0$,

$$\frac{H(x)}{H_0} = \frac{1}{1+k_D H_0 x}, \tag{3.19}$$

where the wave decay coefficient (k_D) is expressed as

$$k_D = \frac{8\alpha_S bNk^2 \sinh^2 kh}{H_0^3 \omega^3 (2kh+\sinh 2kh)} \int_0^l \overline{C_d |U_R| U_R^2}\, ds. \tag{3.20}$$

For a rigid blade with $(u, w) = 0$ and $\phi = 3\pi/2$, (3.20) becomes

$$k_{D,R} = \frac{\alpha_S C_d bNk}{9\pi} \frac{9\sinh k(h-d_1) - 9\sinh k(h-d_1-l) + \sinh 3k(h-d_1) - \sinh 3k(h-d_1-l)}{\sinh kh(2kh+\sinh 2kh)}. \tag{3.21}$$

For a sparse canopy with $\alpha_S = 1$, (3.21) reduces to the solution by Zhu and Zou (2017), which can be further reduced to the solutions of Dalrymple et al. (1984) and Kobayashi et al. (1993) for bottom-rooted vegetation with $d_1 = h - l$. As (3.20) is computationally expensive by resolving the wave-blade interaction, (3.21) is often used with a bulk drag coefficient ($C_D \le C_d$) or an effective blade length ($l_e \le l$) such that

$$k_D = \frac{\alpha_S C_D bNk}{9\pi} \frac{9\sinh k(h-d_1) - 9\sinh k(h-d_1-l) + \sinh 3k(h-d_1) - \sinh 3k(h-d_1-l)}{\sinh kh(2kh+\sinh 2kh)} \tag{3.22}$$

and

$$k_D = \frac{\alpha_S C_d bNk}{9\pi} \frac{9\sinh k(h-d_1) - 9\sinh k(h-d_1-l_e) + \sinh 3k(h-d_1) - \sinh 3k(h-d_1-l_e)}{\sinh kh(2kh+\sinh 2kh)}. \tag{3.23}$$

The objective of using C_D instead of C_d or l_e instead of l is to reduce the overestimation of wave attenuation by neglecting the blade motion. The bulk drag coefficient and effective blade length methods also reduce the computation requirements to represent wave-blade interaction, which makes the wave attenuation model more straightforward to implement into large-scale models. However, the empirical values of C_D and l_e need to be determined from detailed laboratory experiments. Some empirical formulas for C_D (e.g., Kobayashi et al., 1993; Mendez and Losada, 2004; Sanchez-Gonzalez et al., 2011; Jadhav et al., 2013; Anderson and Smith, 2014; Ozeren et al., 2014; Chen et al., 2018; van Veelen et al., 2020) and

l_e (e.g., Luhar et al., 2017; Lei and Nepf, 2019a, b) have been developed for submerged canopies. However, a need exists to develop C_D and l_e formulas of suspended canopies for wave attenuation applications.

3.2.2. Measurements for cultivated *S. latissima*

The model kelp material is selected based on the properties of the *S. latissima* cultivated on a 60 m kelp aquaculture longline in Saco Bay, Maine, USA. *S. latissima* is one of the most extensively farmed kelp species in Maine and in the USA (Grebe et al., 2019). Two sets of kelp samples were collected from two nonadjacent 10 cm regions of the longline on May 17, 2018, with 43 and 38 samples, respectively. Therefore, the averaged plant density was about 405 m^{-1}. The kelp samples were stored in seawater. The morphological and mechanical properties of the kelp samples were measured within 24 hours after collection to minimize the effects of kelp deterioration.

S. latissima consists of holdfast, stipe and blade (Figure 3.2a). Compared to the dimensions of kelp blade, the holdfast and stipe are small and difficult to match in the physical model. To illustrate this characteristic, consider the 1.9 m-long kelp on Figure 3.2a as an example, the stipe length is 15 cm and 8.6% of the blade length at 175 cm. The diameter of the stipe is 5.8 mm and 4.5% of the blade width at 130.4 mm. In a 1:10 physical model, the model stipe diameter is less than 0.58 mm. Thus, the holdfast and stipe are not geometrically modeled in this study. The contribution to wave attenuation was compensated by the rigid part of the model blade for fixing the suspended blade.

The kelp blade morphological characteristics were measured from 77 samples using a ruler for the blade length, a caliper for the blade width and a micrometer for the blade thickness. The blade width was determined by taking the average from three positions: near the stipe, in the middle and near the tip. Thickness values were obtained along the blade width at intervals of 1.27 cm (0.5 in) with at least five positions.

The mass density and bending elastic modulus were measured from 41 rectangular specimens (Figure 3.2b) cutout from 6 to 9 different positions along the blade length of 6 blades. Since the kelp tissue started to degrade and die after cuts were made, measurements for each specimen were completed within 2 min and one whole kelp blade sample was completed within 1 hour. The specimens were cut out from

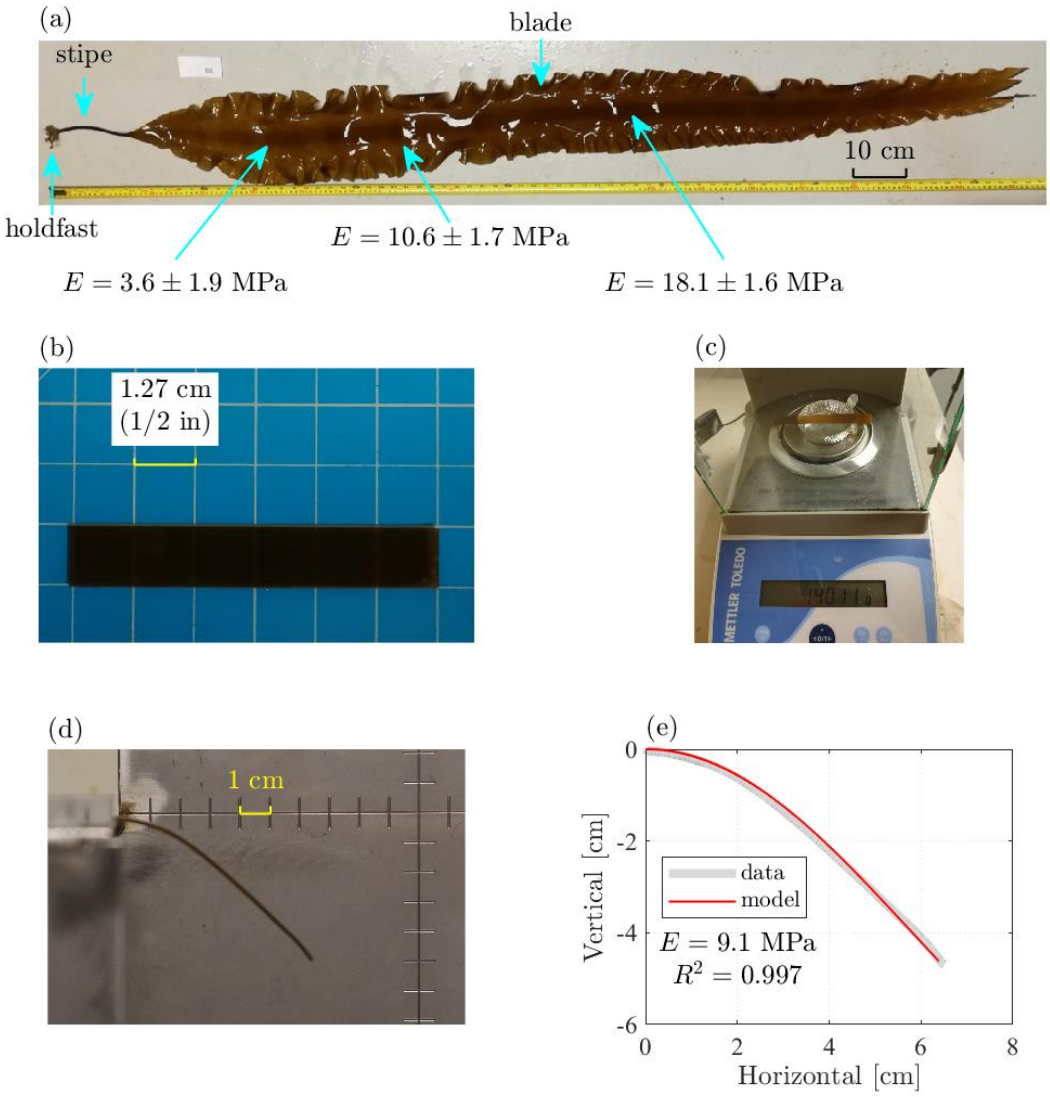

Figure 3.2. (a) *S. latissima* sample with bending elastic modulus (E) at three positions along the blade length. (b) A specimen on a gridded cutting board. (c) Measuring the mass of a specimen with a digital analytical balance scale. (d) Bending test for a specimen. (e) Comparison between the measured and calculated blade postures. The measured E is the value with which the calculated blade posture has the largest R^2 compared with the data. Photo credit: Yu-Ying Chen.

the center part of the blade where the blade thickness varies slightly with an averaged standard deviation of less than 0.05% of the averaged thickness. Thus, the cross section can be considered as a rectangular section and the volume of the specimen can be calculated using the averaged thickness, width and length. The mass

of the specimen was measured using a digital balance scale with the precision of 0.1 mg (Figure 3.2c). To control the effects of the wetness of the specimen, the specimen was placed between two layers of a paper towel to reduce the seawater attached on the specimen surface. The specimen was still wet, but not dripping during the measurements. Due to the loss of surface water and kelp degradation, the measured mass values decreased by 4% during the course of the experiment. The averaged mass value was used in this study.

The bending elastic modulus of the kelp blade was measured using the cantilever beam bending test (Figure 3.2d). Four bending tests were conducted for each specimen with measurements taken on both ends and both sides, for 164 tests. For each bending test, a photo of the bending blade was taken to record the blade posture. The blade posture was extracted using ImageJ (a Java-based image processing program, Schneider et al., 2012; Liang et al., 2017). Given a value of E, solving (3.2) and (3.3) by setting $u = 0$, $w = 0$, and $\rho = 0$ with boundary conditions yields ϕ, which can be used to calculate the blade posture with (3.13) and (3.14). The measured E is set as the value with which the calculated blade posture fits best with the measured blade posture (Figure 3.2e). The calculated blade postures compared well with the measured blade postures, with $R^2 > 95\%$ for 160 tests and $R^2 = 88\%$, 89%, 92%, and 93% for the other 4 tests.

3.2.3. Experimental design

The laboratory experiments were conducted in the 24 m-long, 38 cm-wide, and 60 cm-high wave flume in the Environmental Fluid Mechanics Laboratory at Massachusetts Institute of Technology. The model experiments were designed at a scale of 1:10 to match the dimensions of the wave flume. The wave conditions were designed based on Froude similarity. The model kelp blade was made to satisfy the similarity for (3.6) to (3.12).

In the physical model experiments, the holdfast, stipe, the ruffle of the kelp blade, and the variance of thickness were too small to scale so that the kelp was modeled as a rectangular flat plate with a constant thickness. The material selected for modeling kelp blades was silicon film with $\rho_v = 1.2$ g/cm^3, $E = 2.04$ MPa and $d = 0.1$ mm. The model kelp was designed as a 10.16 cm (4 in) long and 0.95 cm (3/8 in) wide rectangular plate. The corresponding full-scale kelp blade was 101.6 cm long, 9.5 cm wide and 1 mm thick.

To satisfy dynamical similarity, the mass density and bending elastic modulus of the full scale kelp blade were designed as $\rho_v = 1.23$ g/cm^3 and $E = 21$ MPa, such that

$$\frac{(\rho\prime)_M}{(\rho\prime)_F} = 1,\ \frac{(B)_M}{(B)_F} = 1,\ \frac{(Ca)_M}{(Ca)_F} = 1,\ \frac{(L)_M}{(L)_F} = 1,\ \frac{(\delta)_M}{(\delta)_F} = 1,\ \frac{(KC)_M}{(KC)_F} = 1,\ \frac{(S)_M}{(S)_F} = 1, \qquad (3.24)$$

where $(\ \ )_M$ denotes the dimensionless parameter for the model and $(\ \ )_F$ denotes the dimensionless parameter for the full scale prototype. The properties of the full-scale model blade will be compared with the measurements for *S. latissima* blade in the section 3.3.1.

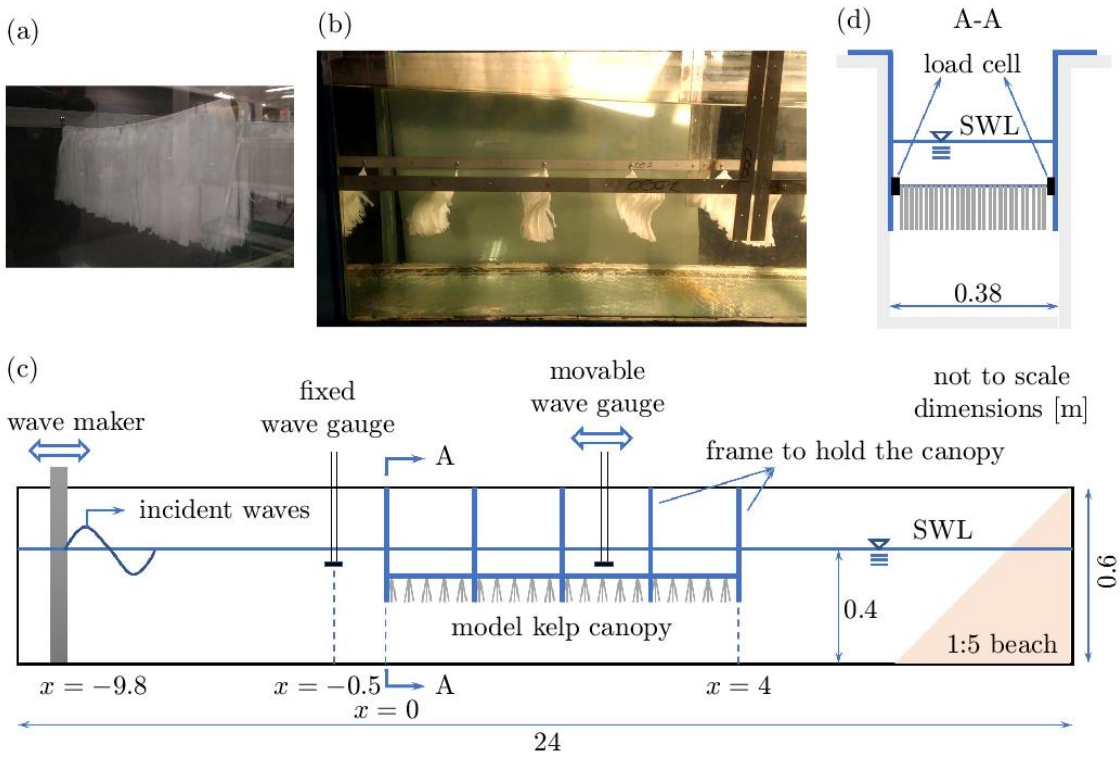

Figure 3.3. Photos of (a) a model kelp longline and (b) the model kelp farms with waves propagating from left to right. Sketches of (c) the side view of the wave flume showing the setup of model kelp farms and wave gauges and (d) the front view of section A-A showing the setup of load cells.

A kelp farm includes numerous kelp plants attached to a horizontal rope. In this laboratory experiment, the horizontal rope was modeled using a rigid stainless steel welding rod with a diameter of 0.89 mm (0.035 in). For each model longline, 31 aggregates of model kelp blades with 10 blades for each aggregate were fixed to the model longline (Figure 3.3a). The fixed part of the blade was $l_r = 0.5$ cm so

that the flexible part of the blade was $l_f = 9.66$ cm. The plant density for the model longline was 10 plants/cm associated with 100 plants/m for the full scale, which was less than the measured values at 405 plants/m in this study. The rod was mounted to a stainless steel frame attached to the flume walls (Figure 3.3b). The model kelp farm consisted of 20 model sections with a distance of 20 cm apart in the flume. Thus, the total canopy length was $L_v = 3.8$ m corresponding to 38 m in the full scale. The canopy density N was 5263 plants/m^2. Three vertical positions of the model kelp farm beneath the SWL with $d_1 = 6, 11, 16$ cm were compared in the experiments.

A set of experiments were then conducted to investigate the dynamics of a single blade and a blade in the canopy in a water depth of 40 cm. The suspended blade was fixed at 11 cm below the still water level. The wave height ranged from 1.4 cm to 6 cm with 4 wave periods of 0.8 s, 1 s, 1.4 s and 2 s. The blade motion was recorded by a camera.

After the blade dynamics were investigated, another set of experiments were then conducted to assess the wave attenuation. As the suspended blades were observed to roll over the attachment rod in large wave heights, the largest wave heights were set at 3.8 cm to prevent the blade roll up in the wave attenuation experiments. For the wave attenuation experiments, the incident wave height was $H_{I0} = 1.8\sim3.8$ cm, wave period was $T = 0.8\sim2$ s, and water depth was $h = 30\sim40$ cm with $kh = 0.58\sim2.41$ and $H_{I0}/h = 0.05\sim0.11$. The wave length was $\lambda = 102\sim370$ cm so that the canopy would cover 1 to 3.7 wavelengths. Thus, for the corresponding full-scale model, the waves are 18 cm to 38 cm in amplitude with period of 2.6 to 6.3 s in 3 to 4 m-deep water with $C_a = 35\sim13930$, $L = 6\sim284$, $KC = 0.2\sim10.8$ and $Re = 24\sim488$.

3.2.4. Wave decay measurements

The wave decay experiment setup is shown on Figure 3.3. During the tests, the wave height was measured using two resistance-type wave gauges with one permanently mounted at 50 cm before the canopy and the other moving along the canopy to measure the wave height evolution for each case. The fixed wave gauge provided a reference measurement to show that the wave conditions were steady throughout one case. The movable wave gauge collected data along the canopy at an interval of 5 cm or up to 15 cm

depending on the wave length (with at least 20 horizontal positions for one wavelength). At each horizontal position, the wave gauge measured the water elevation at 1000 Hz for 1 min (including 30 to 74 wave periods).

The wave reflection ratio of the flume is estimated at 7% (Lei and Nepf, 2019a), yielding an oscillating wave height along the canopy (Figure 3.4). Assuming that the incident wave height and reflected wave height decay follow (3.19) at the same decay coefficient k_D along the canopy, a local wave height in the canopy can be obtained (with derivation in Appendix B),

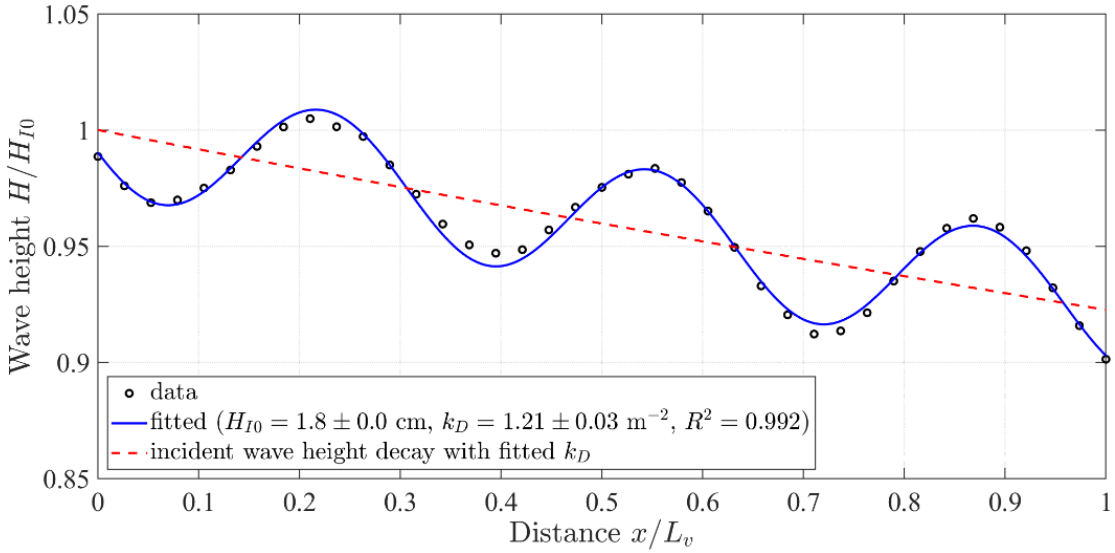

Figure 3.4. Measured (black circles) and fitted (blue line, $R^2 = 0.992$) wave heights (H) normalized by the incident wave height (H_{I0}) along the model kelp farms for Case 1. The calculated incident wave height decay with fitted H_{I0} and k_D is denoted by red dashed line. The horizontal distance is normalized by canopy length as x/L_v.

$$H(x) = \sqrt{\left(\frac{H_{I0}}{1+k_D H_{I0} x}\right)^2 + \left(\frac{H_{RL_v}}{1+k_D H_{RL_v}(L_v - x)}\right)^2 + 2\frac{H_{I0}}{1+k_D H_{I0} x}\frac{H_{RL_v}}{1+k_D H_{RL_v}(L_v - x)}\cos(2kx + \epsilon)}, \quad (3.25)$$

where H_{I0} is the incident wave height at $x = 0$, H_{RL_v} is the reflected wave height at $x = L_v$, ϵ is the phase lag. The spatial oscillation period of the wave height is 1/2 wavelength as shown in the term $\cos(2kx + \epsilon)$. Equation (3.25) provided a good fit ($R^2 > 0.99$) for the incident wave height and decay coefficient as shown on Figure 3.4.

The model kelp farms consisted of 20 rows (rods) of blades. The rods were 20 cm apart, which was more than four times of the amplitude of the blade deflection. For each rod, 31 aggregates of blades were attached separately with 1 aggregate/cm (Figure 3.3a). For each aggregate, 10 blades were mounted together so that the front blades sheltered the blades behind them. The sheltering effects between rods were not considered in this study. However, the significant sheltering effects between the blades in the same aggregate were significant were considered using a sheltering factor α_S, which is defined as the force ratio of the sheltered and unsheltered blades and given by

$$\alpha_S = \frac{F_{x,rms}}{n_S f_{x,rms}}. \tag{3.26}$$

In (3.26), $F_{x,rms}$ is the root-mean-square (RMS) of the measured horizontal force on aggregates of sheltered blades, $f_{x,rms}$ is the RMS of the measured horizontal force on unsheltered single blades, and n_S is the ratio of the number of sheltered blades to the number of unsheltered blades with $n_S = 10$ in this study. A smaller α_S indicates more sheltering. The horizontal forces on one row of blades were measured at 2000 Hz for 1 min with two submerged load cells fixed to both ends of the rod (Figure 3.3d).

3.3. Results

3.3.1. Morphological and mechanical properties of *S. latissima* compared with the model blade

To evaluate the design of model kelp blade, the results section begins with understanding the morphological and mechanical properties of real cultivated *S. latissima* in Saco Bay, Maine of the USA. The kelp blade length (l) showed a quasi-linear relationship with the averaged blade width (b) as

$$b = (0.090 \pm 0.003)l + 1.406 \pm 0.197, \tag{3.27}$$

with $R^2 = 0.898$ (Figure 3.5a), where l and b are in cm. The blade width has the following relation with the maximum thickness ($d_{\max}$) at the center of the blade width,

$$d_{max} = (0.040 \pm 0.007)b + 0.386 \pm 0.078, \tag{3.28}$$

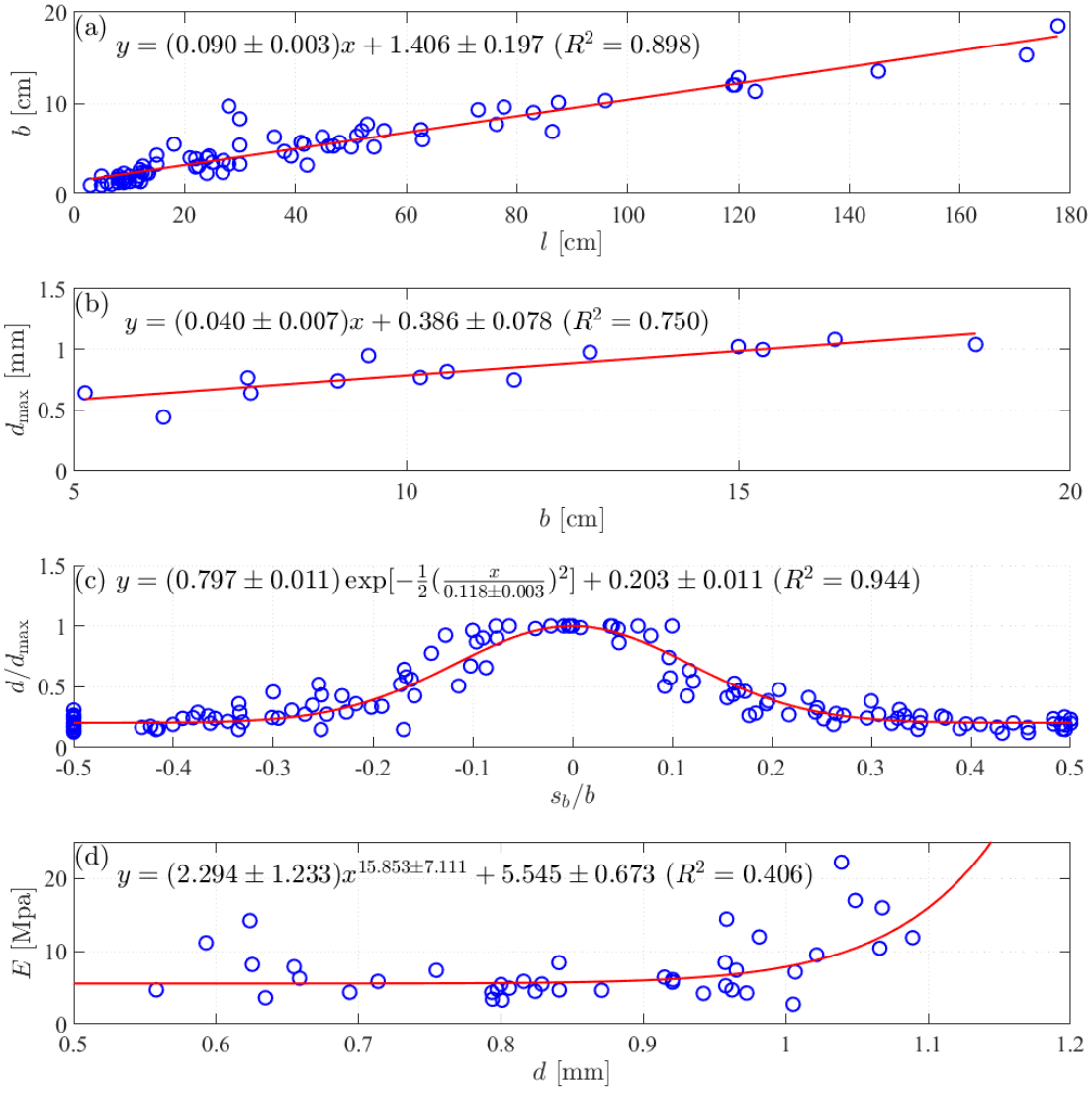

Figure 3.5. Morphological and mechanical properties of *S. latissima*. (a) Relation between the averaged blade width (b) and the blade length (l). (b) Relation between the maximum thickness ($d_{\max}$) and the averaged blade width. (c) The distribution of the normalized blade thickness ($d/d_{\max}$) along the normalized distance (s_b/b) from the blade center. (d) Bending elastic modulus (E).

with $R^2 = 0.750$ (Figure 3.5b), where d_{max} is in mm while b is in cm. The blade thickness (d) showed a normal-like distribution along the blade width following

$$\frac{d}{d_{max}} = (0.797 \pm 0.011)e^{-\frac{1}{2}\left(\frac{s_b/b}{0.118 \pm 0.003}\right)^2} + 0.203 \pm 0.011, \quad (3.29)$$

with $R^2 = 0.944$ (Figure 3.5c), where s_b is the distance from the center of the blade width toward the blade edge.

The bending elastic modulus increases along the blade length from near the stipe to near the tip (Figure 3.2a). As more mature elements of the blade are near the tip, E is expected to relate to the maturity of the kelp tissue. The relation between E and d is

$$E = (2.294 \pm 1.233)d^{15.853 \pm 7.111} + 5.545 \pm 0.673, \quad (3.30)$$

with $R^2 = 0.406$ (Figure 3.5d), where d is in mm and E is in MPa. The measured E from all specimens ranges from 2.71±1.37 to 22.20±5.88 MPa (Figure 3.5d). The measurements in Vettori and Nikora (2017) and Fredriksson et al. (2020) with 3.73 ± 2.71 MPa and 1.28±0.43 MPa, respectively, are also in this range.

The measured mass density of *S. latissima* is 1.053±0.031 g/cm^3, which is smaller than the measurement in Fredriksson et al. (2020) with 1.26±0.27 g/cm^3, but comparable to the value of 1.092±0.091 g/cm^3 in Vettori and Nikora (2017). The difference may be caused by the "wetness" of the kelp sample since the measured mass of wetter kelp is larger, resulting in a larger mass density. The measurements are summarized in Table 3.1 along with measurements from published literature.

The designed properties of the full-scale model kelp blade are also shown in Table 3.1 to compare with the measurements in this study and from published literature. Based on the measurements, for a given blade length $l = 101.6$ cm, the expected blade width is $b = 10.5 \pm 0.5$ cm using (3.27), the maximum blade thickness is $d_{\max} = 0.81 \pm 0.17$ mm using (3.28), and the bending elastic modulus is $E = 5.63 \pm 1.11$ MPa using (3.30). The designed width ($b = 9.5$ cm) of the full-scale model blade is slightly smaller than the calculated averaged width ($b = 10.5 \pm 0.5$ cm) of *S. latissima* with the same blade length, while the maximum thickness ($d_{\max} = 1$ mm) is slightly larger than that ($d_{\max} = 0.81 \pm 0.17$ mm) of the real *S. latissima*. However, the designed dimensions of the full scale kelp blade are within the range of the measurements as shown in Table 3.1. The designed mass density ($\rho_v = 1.23$ g/cm^3) of the full-scale model blade is larger than the measured value of 1.053 ± 0.031 g/cm^3, but comparable to the measurement in Fredriksson et al. (2020) with 1.26 ± 0.27 g/cm^3 for cultivated *S. latissima* in Maine. The designed bending

elastic modulus $E = 21$ MPa of the full-scale model kelp blade is large but still within the range of the measurements (2.71±1.37 to 22.20±5.88 MPa). The designed plant density 100 plants/m is smaller than the measured value of 405 plants/m.

Table 3.1. Morphological and mechanical properties of cultivated S. latissima and model kelp blades.

	Study sites	Mass density ρ_v (g/cm^3)	Elastic modulus E (MPa)	Blade length l (cm)	Blade width b (cm)	Maximum blade thickness d_{max} (mm)	Blades per meter (m^{-1})
Model kelp blade (scale:1:10)		1.2	2.04	10.16	0.95	0.1	1000
Full scale kelp blade		1.23	21	101.6	9.5	1	100
Measured in this study	Saco, Maine, US	1.053 ± 0.031	$5.63 \pm 1.11^{***}$ (2.71 ± 1.37 ~22.20 ± 5.88)	101.6 (3~177.7)	$10.5 \pm 0.5^{*}$ (1~18.5)	$0.81 \pm 0.17^{**}$ (0.44~1.08)	405
Fredriksson et al. (2020)	Maine, US	1.26 ± 0.27	1.28 ± 0.43	Up to 300		0.4 ± 0.1	
Vettori and Nikora (2017)	Loch Fyne, Scotland, UK	1.092 ± 0.091	3.73 ± 2.71	15~65	3.6~13.1	0.42~1.8	
Augyte et al. (2017)	Bristol, Maine, US			220.4	4.67		330
				56.9	8.72		
	Sorrento, Maine, US			147.4	2.76		400
				71.4	7.38		
Peteiro and Freire (2013)	Ares, Spain			152.9	12.1		745
	Sada, Spain			123.2	11.4		728

* Calculated b using (3.27) for the given $l = 101.6$ cm. ** Calculated $d_{\max}$ using (3.28) for given $b = 10.5 \pm 0.5$ cm. *** Calculated E using (3.28) for given $d = 0.81 \pm 0.17$ mm.

3.3.2. Wave-induced motion of suspended blades

To understand the wave-induced dynamics of suspended blades as well as the blade to blade sheltering effects, the motion of a single suspended blade is compared with that of an aggregate of suspended blades on Figure 3.6, where the waves propagate from left to right with a period of 1.4 s at 40 cm water depth. Due to high flexibility, the blade shows a higher-mode (>3) motion (Figure 3.6a and c) with large asymmetry (Figure 3.6a5 and c5). Unlike submerged vegetation inclining to the wave

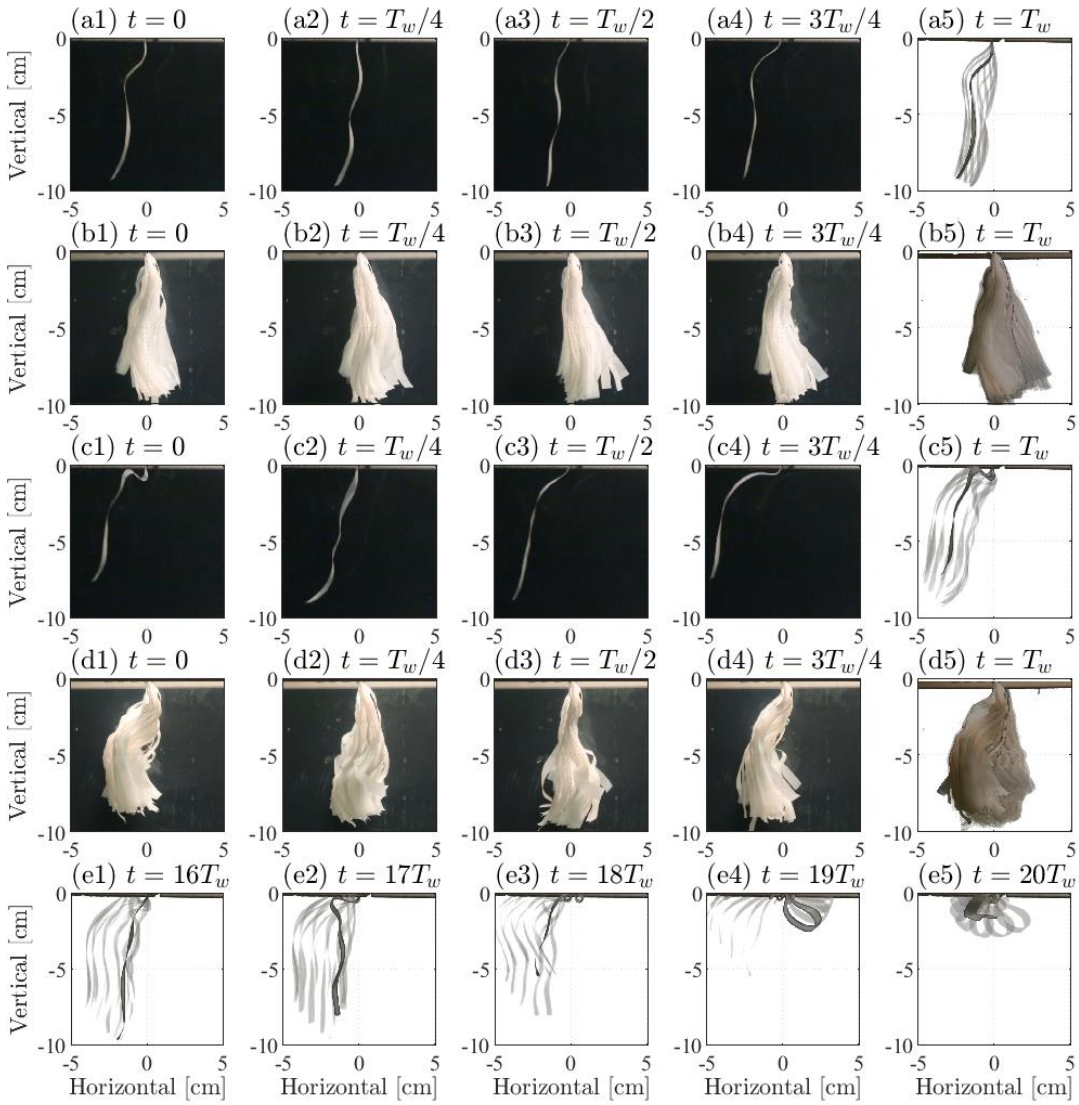

Figure 3.6. Postures for (a, c, and e) a single blade and (b and d) a row of blades in waves with wave heights of (a and b) 1.5 cm, (c and d) 2.8 cm, and (e) 3.3 cm. The wave period is 1.4 s and water depth is 40 cm. The blade is fixed at 11 cm below the still water level. The waves propagate from left to right. In (a5, b5, c5, d5 and e), the black line indicates the posture at the given time (t) while the gray lines indicate the previous postures in that wave period (T_w). For wave amplitude of 3.3 cm in (e), the single blade starts to wrap up and roll over the rod after 17 wave periods.

propagation direction (Zhu et al., 2020b), the suspended blade fixed at the upper end inclines to the opposite direction of wave propagation. For waves propagating to the right, the action of the vertical wave orbital velocity on the blade provides clockwise momentum that drives the submerged blade also to the right (Zhu

et al., 2020b) but drives the suspended blade to the left. The asymmetry of blade motion increases with blade deflection and wave height (Figure 3.6a and c). More information about the mechanisms and properties of asymmetric blade motion in waves can be found in Zhu et al. (2020b).

The motion of the blade in an aggregate of blades shows a smaller-amplitude motion than a single blade in the same wave conditions (e.g., Figure 3.6a and b). This is caused by the sheltering from neighboring blades in the same aggregate, which reduces the flow velocity to the sheltered blades. Therefore, the deflection of a sheltered blade is smaller than that of an unsheltered single blade. Accordingly, the motion asymmetry of the sheltered blade is also smaller than that of the unsheltered single blade (e.g., Figure 3.6a and b).

The blade was observed to wrap up and roll over the longline when the wave height exceeded a critical value (Figure 3.6e). The unsheltered single blade rolled over when the wave height reached 2.8 cm for $T_w = 2$ s, 3.3 cm for $T_w = 1.4$ s (Figure 3.6e), 3.7 cm for $T_w = 1$ s, and 3.5 cm for $T_w = 0.8$ s. Due to sheltering effects, the threshold values increased for the sheltered blades in an aggregate, especially for the blade in the center of the aggregate that was sheltered by more blades. The mechanisms for the rolling over will be discussed in section 3.4.1.

3.3.3. Horizontal force and wave attenuation

The measured sheltering factor α_S, wave decay coefficient k_D, wave transmission ratio ($HTR = H_{I0}/H_{L_v}$, where H_{Lv} is the wave height at the ending edge of the canopy), and wave energy dissipation ratio ($EDR = 1 - H_{Lv}^2/H_{I0}^2$) are listed in Table 3.2. For this study, α_S ranges from 0.526 to 0.991 with mean value of 0.728. The numerically calculated horizontal force ($F_{x,rms}$) for a row of blades and k_D for the canopy are compared with the measurements (Figure 3.7). With the averaged sheltering factor, the calculated $F_{x,rms}$ and k_D show good agreement with the experiments with normalized root-mean square-errors (NRMSE) of 0.197 (Figure 3.7a) and 0.184 (Figure 3.7b), respectively. The overestimation of k_D is 11% (calculated using the slope of the linear fitting line), indicating that the constant averaged sheltering factor is appropriate to predict the wave attenuation in this study.

Table 3.2. Sheltering factor and wave attenuation measured in the experiments and projections to full scale.

Case #	Experiments (1:10)						Sheltering factor	Projections to full scale						HTR	EDR
	d_1 (cm)	h (cm)	T (s)	H_{I0} (cm)	λ (cm)	k_D (m^{-2})	α_S	d_1 (m)	h (m)	T (s)	H_{I0} (m)	λ (m)	k_D (m^{-2})		
1	11	40	1.4	1.8	247	1.21	0.552	1.1	4	4.5	0.18	24.7	0.0121	0.92	15%
2	6	30	2.0	2.9	325	1.28	0.760	0.6	3	6.3	0.29	32.5	0.0128	0.88	23%
3	11	40	1.4	2.4	244	0.84	0.537	1.1	4	4.5	0.24	24.4	0.0084	0.93	14%
4	6	30	1.4	2.9	219	1.19	0.739	0.6	3	4.5	0.29	21.9	0.0119	0.88	22%
5	11	40	1.0	3.1	149	1.18	0.616	1.1	4	3.2	0.31	14.9	0.0118	0.88	23%
6	11	40	2.0	3.5	370	0.39	0.679	1.1	4	6.3	0.35	37.0	0.0039	0.95	10%
7	16	40	2.0	3.8	369	0.25	0.986	1.6	4	6.3	0.38	36.9	0.0025	0.97	7%
8	11	40	2.0	3.7	368	0.24	0.526	1.1	4	6.3	0.37	36.8	0.0024	0.97	6%
9	16	40	1.4	3.2	248	0.62	0.848	1.6	4	4.5	0.32	24.8	0.0062	0.93	14%
10	11	40	1.4	3.2	247	0.70	0.672	1.1	4	4.5	0.32	24.7	0.0070	0.92	15%
11	11	40	1.0	3.6	150	1.04	0.887	1.1	4	3.2	0.36	15.0	0.0104	0.87	23%
12	6	30	0.8	3.2	102	2.34	0.991	0.6	3	2.6	0.32	10.2	0.0234	0.78	39%
13	16	40	0.8	3.2	104	0.94	0.722	1.6	4	2.6	0.32	10.4	0.0094	0.90	20%
14	11	40	0.8	3.2	105	1.43	0.677	1.1	4	2.6	0.32	10.5	0.0143	0.85	28%

Note, d_1 is the vertical distance from the still water line to the longline, h is the water depth, T is the wave period, H_{I0} is the incident wave height, λ is the wavelength, k_D is the wave decay coefficient, α_S is sheltering factor, HTR is the wave height transmission ratio, and EDR is the wave energy dissipation ratio.

The designed model kelp canopy can reduce up to 39% of the wave energy when the canopy occupied a larger portion of the water column ($l/h = 0.34$), was located at higher position ($d_1/h = 0.2$), covered more wavelengths ($L_v/\lambda = 3.72$) and featured larger amplitude waves ($H_{I0}/h = 0.107$) as shown in Table 3.2.

The measured wave decay coefficients k_D for the suspended model kelp canopy in different wave conditions and with different canopy vertical positions are shown on Figure 3.8 as a function of the dimensionless parameters, kh, H_{I0}/h, l/h, and d_1/h. The numerically calculated k_D using (3.20) is also shown on Figure 3.8 to help analyze the trend of k_D. It is noted that k_D increases with kh (Figure 3.8a) showing a different behavior from submerged canopies, where k_D decreases with kh (e.g., Figure 3.6c in

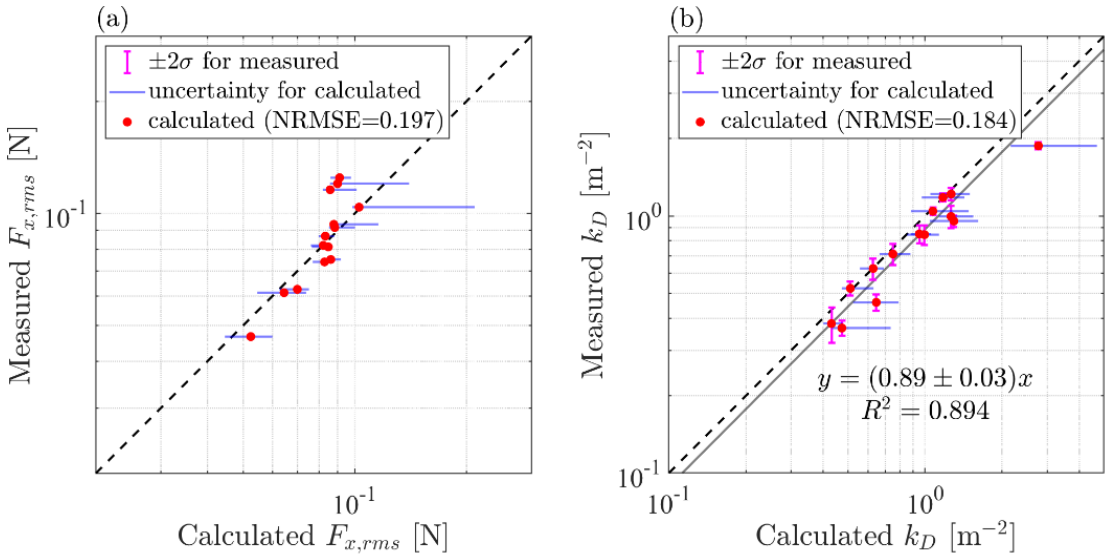

Figure 3.7. Comparisons for the measured and calculated (a) horizontal force ($F_{x,rms}$) for a row of blades and (b) wave decay coefficient (k_D). The vertical error bars indicate two standard deviations (2σ) for the measurements while the horizontal bars indicate the computation uncertainty induced by using the minimum and maximum sheltering factors. The normalized root mean square error (NRMSE) for the calculated values is shown in the legend. The solid gray line in (b) is the linear fit for the calculated k_D with expressions and R^2 nearby.

Luhar et al., 2017). k_D decreases with H_{I0}/h (Figure 3.8b), but increases with l/h (Figure 3.8c). Increasing incident wave height may increase the amplitude of the blade motion and therefore decrease the relative velocity, resulting in smaller drag and k_D. The canopy occupies less of the water column in deeper water so that k_D decreases. It should be noted that k_D decreases with increasing incident wave height, but the wave attenuation of the canopy does not because the total wave attenuation depends on $k_D H_{I0} L_v$ based on (3.19). For example, k_D decreases by 42% when H_{I0}/h increases by 77% from 0.046 to 0.081 (Figure 3.8b), but $k_D H_{I0} L_v$ increases by 3.4%. The results also demonstrate that moving the canopy upward (reducing d_1/h) can improve the wave attenuation (Figure 3.8d) as expected. The numerical calculations have shown a small overestimation for k_D for most cases (Figure 3.8). This may be because the numerical solution (3.20) uses the incident wave orbital velocity to calculate the wave attenuation without considering the flow

reduction in the canopy (Lowe et al., 2005). Ignoring the flow reduction in the canopy would result in an overestimation of the wave attenuation.

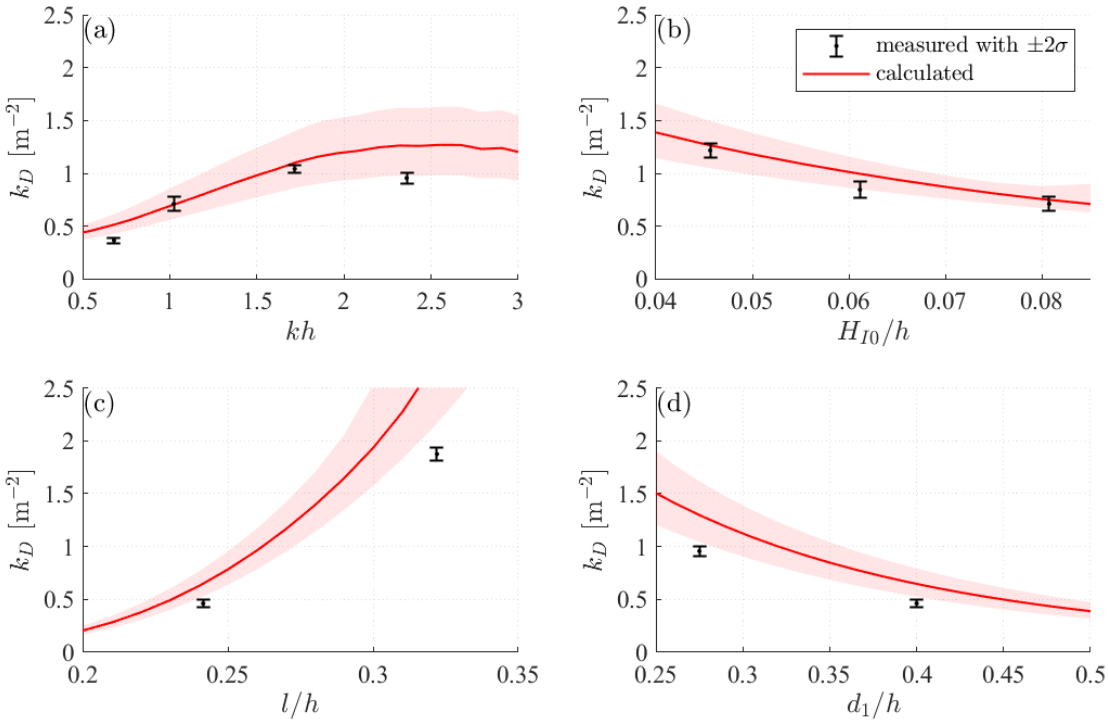

Figure 3.8. Measured and calculated wave decay coefficient (k_D) for the suspended model kelp canopy as a function of (a) kh, (b) H_{I0}/h, (c) l/h, and (d) d_1/h. The water depth is h, the wave number is k, the incident wave height is H_{I0}, the blade length is l and the vertical distance from the longline to the still water line is d_1. The measured k_D is shown in black dots with error bars indicating two standard deviation (2σ). The calculated k_D with averaged sheltering factor is denoted by read lines, where the shaded areas indicate the computation uncertainty induced by using the minimum and maximum sheltering factors.

3.3.4. Bulk drag coefficient and effective blade length

For convenience in implementing kelp farms into in large scale models and to improve computational efficiency, the bulk drag coefficient and the effective blade length of the suspended canopy for wave attenuation were fitted based on the datasets. The blade length (l) includes a rigid (l_r) and flexible part (l_f) with wave decay coefficients k_{Dr} and k_{Df}, respectively. The k_{Dr} of the rigid part is calculated using (3.21). The measured k_{Df} is obtained by subtracting k_{Dr} from the measured k_D. With measured k_{Df},

the bulk drag coefficient (C_D) and the effective blade length ($l_{f,e}$) for the flexible part of the blades are solved from (3.22) and (3.23), respectively. For unsteady flow, C_D is better fitted as a function of KC (Van Veelen et al., 2020). The fitted relation between C_D and KC for the suspended model kelp canopy is

$$C_D = (0.34 \pm 0.02)KC^{-0.25\pm0.05}, \tag{3.31}$$

with $R^2 = 0.80$ (Figure 3.9a). Based on the scaling analysis with linear blade motion, Luhar and Nepf (2016) argued that l_e is proportional to $(CaL)^{-0.25}$. However, the blade motion is nonlinear since the large-amplitude blade motion induces geometrical nonlinearity. Thus, l_e is fitted with a varying power of CaL. The best fit for l_e is

$$\frac{l_{f,e}}{l_f} = (20.37 \pm 13.32)(CaL)^{-0.54\pm0.07}, \tag{3.32}$$

with $R^2 = 0.90$ (Figure 3.9b).

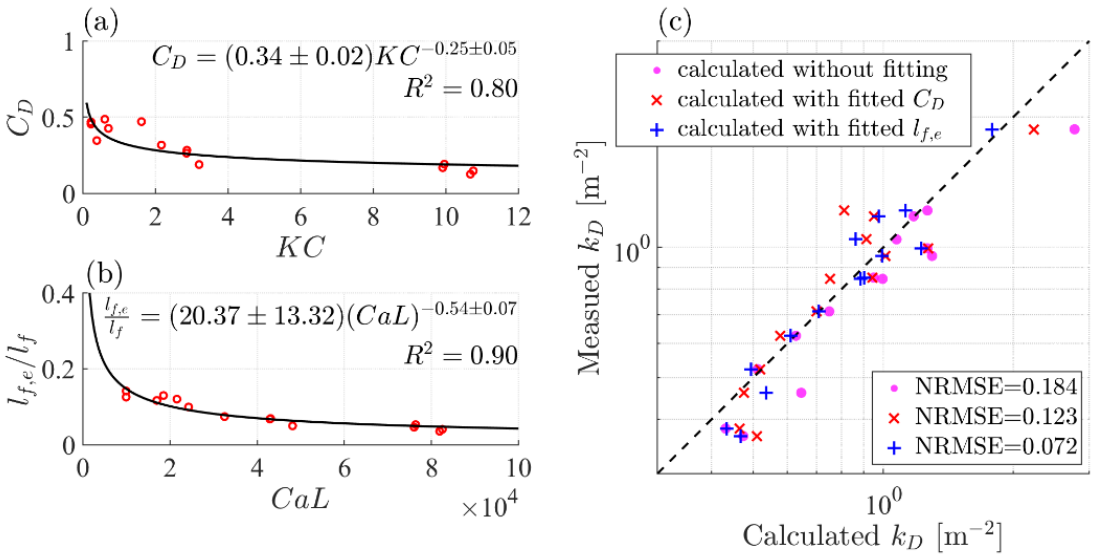

Figure 3.9. (a) Measured bulk drag coefficients (C_D) as a function of Keulegan-Carpenter number (KC) for the flexible part of the blade. (b) Measured effective blade length ($l_{f,e}$) for the flexible part (l_f) of the blade length as a function of the product of Cauchy number (Ca) and length ratio (L). (c) Comparisons between the measured wave decay coefficient k_D and the calculations using (3.20) without fitting (denoted by magenta filled circles), using (3.22) with fitted C_D (denoted by red ×), and using (3.23) with fitted $l_{f,e}$ (denoted by blue +). The normalized root mean square error (NRMSE) is shown in the legend.

To evaluate the performance of the fitted formulas for C_D and $l_{f,e}$, the calculated k_D using (3.22) with fitted C_D in (3.31) and using (3.23) with fitted $l_{f,e}$ in (3.32) are compared with the measured k_D as well as the numerically calculated k_D using (3.20) as shown on Figure 3.9c. The NRMSE for the calculated k_D with fitted C_D is 0.123, which is larger than the calculations with fitted $l_{f,e}$ (NRMSE = 0.072). The improved performance of the effective blade length method is due to the better fit for $l_{f,e}$ with a larger $R^2 = 0.90$ than the bulk drag coefficient method ($R^2 = 0.80$). This may be because $l_{f,e}$ is expressed as a function of $C_a L$, which incorporates the blade flexural rigidity. Both the bulk drag coefficient and the effective blade length methods have shown a smaller NRMSE than that of the numerical calculations without fitting (NRMSE=0.184). This indicates that the simplified methods using the bulk drag coefficient ($R^2 = 0.80$) and effective blade length ($R^2 = 0.90$) that are fitted with experiments are successful for considering the influences of blade motion on wave attenuation. In fact, they performed even better than the numerical methods (3.20) that resolves the blade motion. This is because the fitted values incorporated all the uncertainties, such as the velocity reduction in the canopy (Lowe, 2005), that the numerical methods did not consider.

3.4. Discussion

The blade roll-over phenomenon is expected to influence wave attenuation, therefore, understanding the wave induced dynamics is important to assess if this is anticipated in the field. Additionally, it is critical to analyze if simplified methods (i.e. the bulk drag coefficient and effective blade length) can be used to enhance computational efficiency in wave attenuation simulations. Before kelp farms can be implemented as nature-based coastal protection measures, it is essential to identify the key parameters affecting wave attention.

3.4.1. Roll-over of suspended flexible blades

The suspended blade fixed at the upper end exhibited different dynamics compared to the submerged blade fixed at the sea floor. The differences are represented by the opposite asymmetric motion and roll-over property of the suspended blade. The opposite asymmetric motion of suspended blades is

mainly induced by the asymmetric action of the vertical wave orbital velocity. In waves propagating to the right as an example, the wave orbital motion provides a clockwise momentum that drives submerged blade to incline to the right while drives suspended blades to incline to the left. Similarly, the rolling over motion of the suspended blades also results from the interaction of the blade with wave orbital motion.

The blade motion is driven by the wave orbital motion. For a long flexible blade in transitional and deep water waves, the blade motion is asymmetric (Zhu et al., 2020b). When the wave height increases to a critical value, the asymmetry becomes so large that the blade is almost horizontal, providing conditions for the onset of rolling over. For example on Figure 3.10, the blade is almost horizontal at the 17th period. At time $t = 17.25T_w$ (Figure 3.10d), the wave orbital velocity points upward and drives the blade to bend upward and exceeds where the fixed end is located. After $t = 17.5T_w$, the wave orbital velocity points to the right and drives the blade to the right (Figure 3.10e) to pass over the attachment (Figure 3.10f). Then at $t = 17.75T_w$ (Figure 3.10g), the wave orbital velocity points downward and drives the blade downward. Therefore, the portion of the blade that passed over the attachment moves down below the attachment. Although the wave orbital velocity changes direction back toward after $t = 17.75T_w$, the blade does not unravel due to the presence of the longline (Figure 3.10h). After $t = 18.375T_w$, the restoring force induced by the second curvature of the blade acts clockwise in the same direction of the wave orbital motion. Thus, the blade passes the longline in a shape like a "fly casting loop" (Figure 3.10k to p). The whole blade rolls over the longline by the 18th period. In the following time, the blade rolls over the blade again.

For aquaculture farms, the blades are closely seeded as an aggregate. The sheltering effects and blade-blade interaction may inhibit the rolling over cycle by cycle. In the experiments, only waves were considered. In the field, the strong background currents can streamline the blade and therefore inhibit rolling over. However, the rolling over can still happen for sparsely seeded kelp in large wave conditions. The blade roll-over induces a large curvature resulting in a large inner stress that increases the risk of blade breakage. Long-term roll-over is expected to also impact kelp growth and morphology. The blade roll-over reduce canopy height and increase blade-blade sheltering and interaction that may decrease wave attenuation. However, the roll-over effects may reduce the blade motion amplitude and move the lower part

of the blade upward that may enhance wave attenuation. The roll-over effects are still unclear that warrant further investigation in the future.

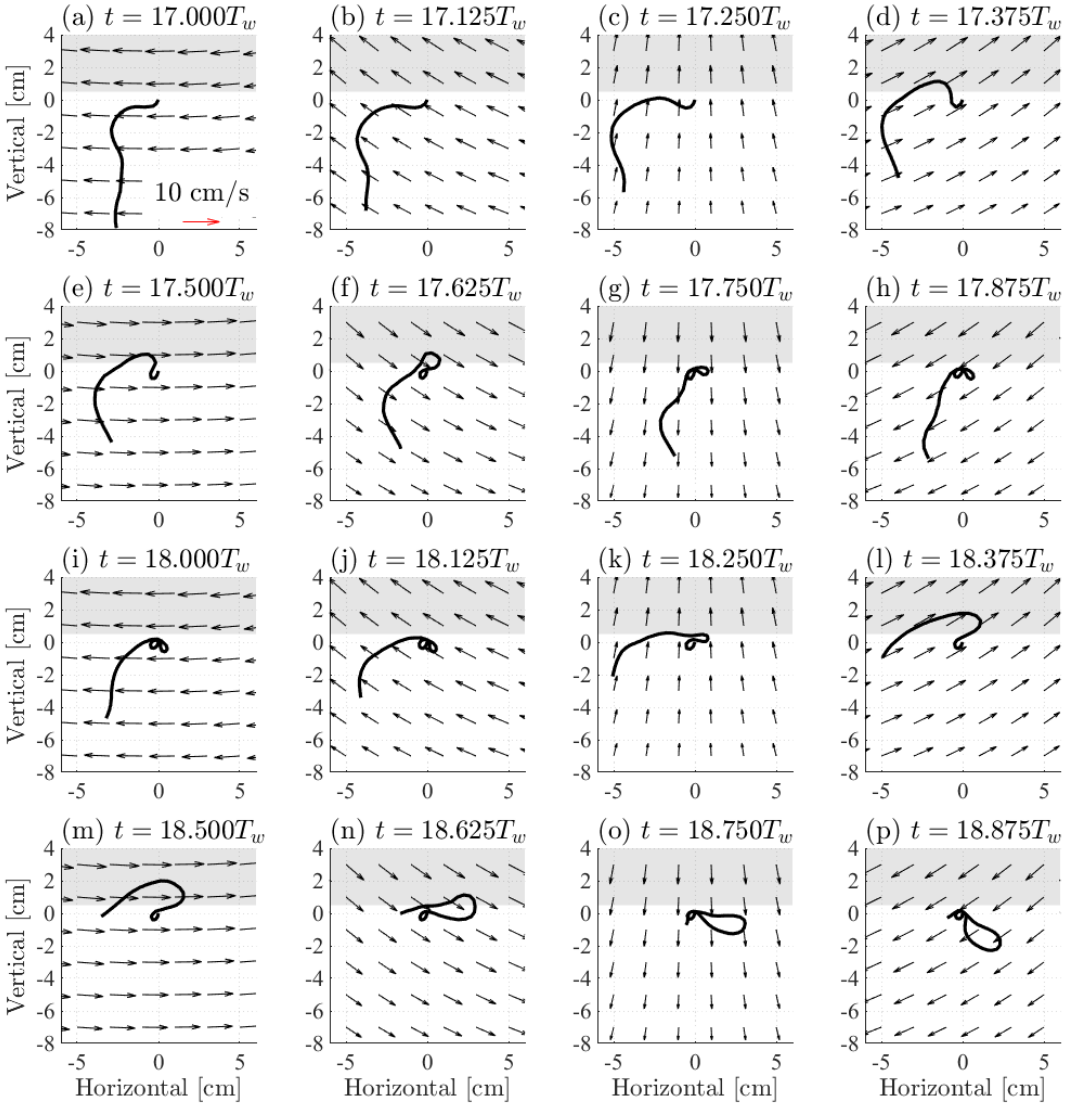

Figure 3.10. Suspended blade postures with flow field. The waves propagate from left to right with wave height of 3.3 cm and wave period $T_w = 1.4$ s at water depth of 40 cm. The flow field is calculated using linear wave theory (Dean & Dalrymple, 1991). The blade is fixed at 11 cm below the still water level. The blade starts to roll over the longline at time $t = 17.5T_w$ for this case (e). The shaded regions indicate the position of the supporting frame above 0.75 cm. The part of the blade in the shaded region was plotted using a smoothing curve that connect the visible blade segments. This does not impact the analysis on the mechanisms for the rolling over of suspended blades.

3.4.2. Methods to predict wave attenuation

The aquaculture kelp blades are seeded closely together on the longline for economic benefits. High plant density (e.g., 745/m in Peteiro and Freire, 2013) is also beneficial for wave attenuation. However, the sheltering effects from neighboring blades and the blade-blade interaction present uncertainties for wave attenuation prediction. A simple sheltering factor defined as the force ratio in (3.26) is acceptable since the numerical calculations with the sheltering factor present a small NRMSE of 0.184 (Figure 3.7b). As the plant density and blade configurations influence the sheltering effects, a more sophisticated sheltering factor as a function of plant density and blade properties as well as wave conditions is warranted.

Compared to the numerical wave decay coefficient calculated with (3.20), the bulk drag coefficient and effective blade length methods have improved the calculations by reducing the NRMSE by 33% and 61%, respectively. The improvements are attributed to the fits for C_D ($R^2 = 0.80$) and l_e ($R^2 = 0.90$) because the fitted values have incorporated all the uncertainties influencing wave attenuation that are not fully considered in the numerical solution (3.20). The bulk drag coefficient and effective blade length methods are simple and convenient to implement into large-scale models. The effective blade length method is better than the bulk drag coefficient method due to an improved fitted value that considers the blade flexural rigidity. Incorporating the blade flexural rigidity in the fitting formula for the bulk drag coefficient is expected to improve the bulk drag coefficient method. Although the bulk drag coefficient and effective blade length methods could provide favorable results with fitted C_D and l_e, physical experiments are required to calibrate C_D and l_e. Thus, the numerical solution (3.20) could be an alternative when reliable C_D and l_e are not available.

3.4.3. Suspended kelp aquaculture farms as nature-based coastal protection

The model kelp canopy has shown the capacity for wave attenuation in the laboratory experiments. In the full scale, a suspended kelp aquaculture farm consisting of 20 longlines with 100 plants per meter in 3 to 4 m-deep water is expected to reduce 6% to 23% energy of coastal waves with a period of 6.3 s and wave height between 0.29 to 0.38 m (Table 3.2). Though, this anticipated wave attenuation is overestimated because the model blade thickness is $d = d_{\max}$ as constant while the thickness of real kelp reduces towards

the blade edge (Figure 3.5c). Based on the thickness distribution in (3.29), the second momentum of the cross section of *S. latissima* is

$$I = \int_{-\frac{1}{2}d_{\max}}^{\frac{1}{2}d_{\max}} 2|s_b|\left(\frac{d}{2}\right)^2 \mathrm{d}d \approx 0.2\frac{bd_{\max}^3}{12}, \tag{3.33}$$

indicating that the flexural rigidity of the real *S. latissima* blade is only 20% of the same wide plate but with the maximum thickness. To reduce the overestimation and obtain more reliable results for the wave attenuation in the field, an effective blade width $b_e = 0.2b$ is used in the following discussion. By removing the overestimation due to using maximum thickness, the wave energy dissipation ratio (EDR) drops from 10% to 2.3% (Figure 3.11a) for Case 6 in Table 3.2. In addition, the bending elastic modulus (E) of the full scale model blade is designed as 21 MPa, which is near the largest measured E. The measured E ranges from 2.71 ± 1.37 to 22.20 ± 5.88 MPa (Table 3.1) and varies along the blade length (Figure 3.2a). For the given blade thickness of 0.81 mm, the expected bending elastic modulus is $E = 5.63$ MPa based on (3.30). However, the numerical results show that E has a small influence on wave attenuation (Figure 3.11). For example in Case 6, the EDR reduces from 2.3% to 1.9% by 17% when E decreases from 21 MPa to 5 MPa (Figure 3.11a).

The plant density is 100 plants/m for the model kelp longline, which is smaller than the measured value of 405 plants/m. In fact, the plant density can be as large as 745 plants/m (Peteiro and Freire, 2013), which can significantly enhance the wave attenuation. Assuming the measured sheltering factor is applicable for larger plant density, the simulated EDR for Case 6 increases to 7.1% with 400 plants/m and to 11.9% with 700 plants/m with effective blade width $b_e = 0.2b$ and $E = 5$ MPa (Figure 3.11a). As the growth of kelp, the blade length increases yielding larger wave attenuation. For instance with 400 plants/m and $E = 5$ MPa, the EDR increases from 7.1% to 24.6% when the blade length grows from 1 m to 2 m. The increase of EDR is even more significant (37.6%) for a greater plant density of 700 plants/m.

The wave attenuation of suspended aquaculture kelp is dependent on the growth of kelp including the blade size and plant density, where a denser longline with longer kelp yields more wave attenuation. Another important parameter determining the wave attenuation of a suspended kelp farm is the number of

longlines. For the suspended kelp farm with 200 longlines with 100 plants/m in the same conditions with Case 6, the EDR are 16.4% for 1 m-long blades with $E = 5$ MPa and 47.5% for 2 m-long blades with $E = 5$ MPa (Figure 3.11b). If the plant density increases to 400 plants/m as measured in this study, the EDR increase to 47.1% and 84.3% (Figure 3.11c), respectively. The plant density and number of longlines are key design parameters that can maximize the wave attenuation performance of suspended kelp aquaculture farms in practice.

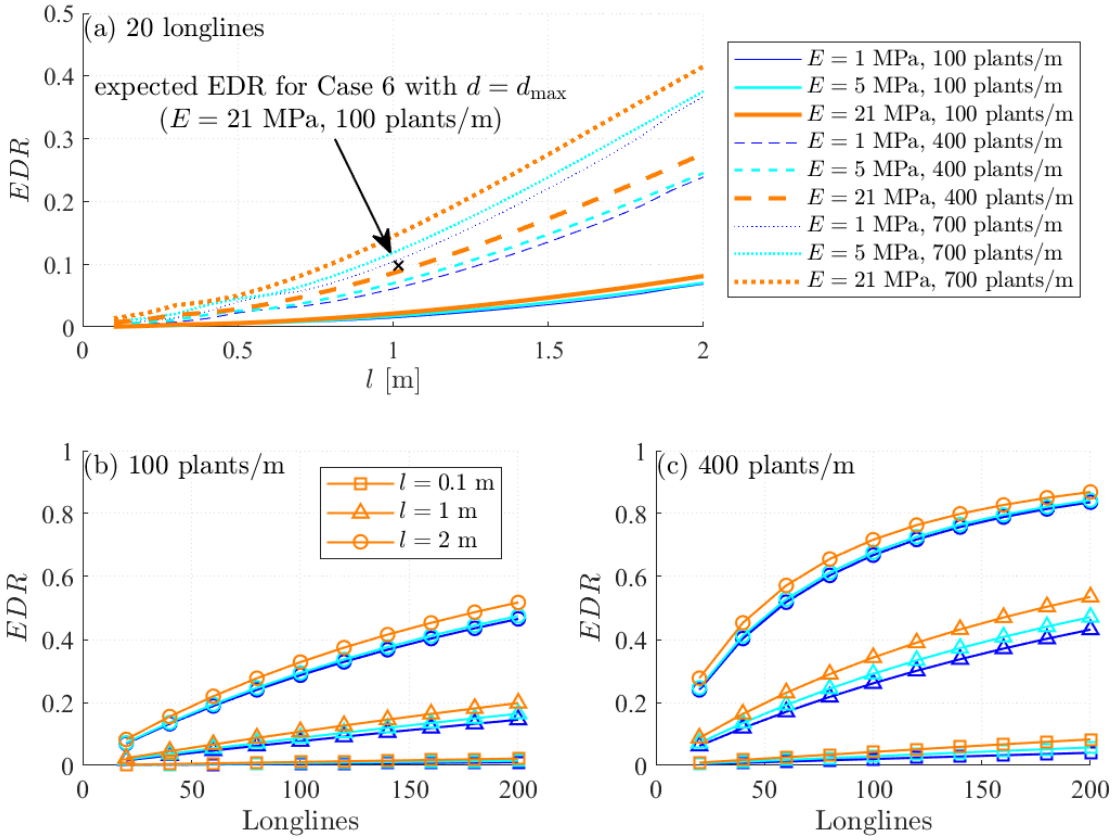

Figure 3.11. (a) Effects of the bending elastic modulus (E) and the length (l) of the blade as well as number of plants per meter on the wave energy dissipation ratio (EDR) of suspended kelp aquaculture farms. Wave attenuation as a function of the number of kelp longlines with (b) 100 plants/m and (c) 400 plants/m. The water depth is 4 m, wave height is 0.35 m, and wave period is 6.3 s. The kelp longline is 1.1 m beneath the still water line. The blade thickness is d and the maximum thickness is $d_{\max}$.

3.4.4. Limitations

This preliminary study has proposed simple methods to quantify the wave attenuation of suspended kelp aquaculture structures. However, there are still some limitations of these methods due to the complexity of the kelp morphology and flow environment in the field. The kelp blade morphology is more flat in exposed sites and more ruffled in sheltered sites (Koehl et al., 2008). The ruffle and thickness variance of the blade may impact the hydrodynamic coefficients. Like kelp stipe and holdfast, these small morphological features cannot be fully considered in the downscaled model and the effects of these small morphological features on wave attenuation are unclear. In the field, there would be a background current in addition to waves that may have significant influences on the wave attenuation, which is not considered in the current study. When the current exceeds a critical value, the kelp becomes streamlined so that the drag force decreases and the friction dominates (Fredriksson et al., 2020), after which a smaller wave attenuation is anticipated. At this point, the energy conservation equation (3.17) should be modified by using friction rather than drag. Gaylor et al. (2003) observed that the alongshore currents decrease the wave attenuation of *Nereocystis luetkeana*. However, the reconfiguration of kelp in waves and currents can enhance the survival rate and reduce the effects of wave attenuation service on the biomass productivity (Gerard, 1987). Lastly, the kelp longline mooring system and the motion of the longline were not considered due to the small width of the flume, which may lead to overestimation of the wave attenuation.

3.5. Summary

The wave attenuation by suspended kelp canopies was investigated with a set of physical model experiments with dynamic similarity to the cultivated *S. latissima* at Saco, Maine in the USA. A full-scale model kelp canopy reduced up to 23% of the energy of 6.3 s waves. The motion of the blades was asymmetric, similar to submerged blades, but yielded a blade inclination that opposed the direction of wave propagation. In waves propagating to the right, the clockwise motion of water particles induces a clockwise momentum that drive submerged blades to incline to the right while driving suspended blades to the left. This strong asymmetric motion promoted a roll over motion of the suspended blades in large wave heights, which has not been previously reported. A simple wave attenuation model based on the blade dynamic

model in Zhu et al. (2020b) was developed and showed good agreement with the experiments, with a slight overestimation of 11%. The numerical model results indicated that plant density and the number of longlines are the key design parameters that can significantly improve wave attenuation performance. Furthermore, the empirical formulas for the bulk drag coefficient and effective blade length of suspended kelp canopy for wave attenuation were also developed, which are convenient to implement in large-scale models to examine the role of kelp farms as nature-based coastal protection measures on coastal morphology, inner shelf circulation and material transport. Though this study focused on waves without currents, a natural extension of this work would be to include background currents, which likely streamline the kelp blades and influence the wave attenuation performance.

3.6. Acknowledgments

This work was completed as part of the PhD research of Longhuan Zhu who was supported by National Science Foundation award #IIA-1355457 to Maine EPSCoR at the University of Maine. Longhuan Zhu would like to sincerely thank Neil Fisher and Allen Treadwell for assisting designing and manufacturing the kelp supporting frames, Adam St. Gelais and Kathryn Johndrow for assisting collecting *S. latissima* samples from the kelp longline of the University of New England, Kathryn Johndrow for measuring the blade length and width of kelp samples. Longhuan Zhu also want to thank Yu-Ying Chen for assisting to measure the morphological and mechanical properties of *S. latissima* and his colleagues in the coastal research group of the University of Maine and friends for help in preparing model kelp longlines.

CHAPTER 4

ANALYTICAL MODEL FOR WAVE ATTENUATION BY FLEXIBLE CANOPIES

4.1. Background

Coastal communities are exposed to the increasing risks from coastal erosion and flooding from storm tides and sea level rise (Izaguirre et al., 2011; Tebaldi et al., 2012; Ondiviela et al., 2014; Weinkle et al., 2018). As conventional hard structures are recognized to have adverse impacts on the environment and become less sustainable in a changing climate (Syvitski et al., 2009; Currin et al., 2010; Pace, 2011; Temmerman et al., 2013; Sutton-Grier et al., 2015), a more ecological approach that uses nature-based infrastructure for coastal defense is in growing need (Morris et al., 2017; Möller, 2019). Nature-based infrastructure include wetland plants, mangroves, aquatic vegetation, kelp beds, coral reefs, and shellfish reefs. Based on the vertical position of the biomaterial in the water column, nature-based infrastructure is classified as either submerged (e.g., submerged aquatic vegetation located at the seafloor), emerged (e.g., saltmarsh and mangroves located at the seafloor and emerged out of the water surface), suspended (e.g., kelp and mussel aquacultures suspended in the water column with gaps below and above the canopy), or floating (e.g., floating wetland) canopies. These canopies have the potential to protect coastal regions by damping wave energy while reducing the adverse effects of hardened shorelines.

The wave attenuation by canopies has been investigated with laboratory and field experimental techniques as well as analytical and numerical models. Many of these methods are based on the wave attenuation theories developed by Dalrymple et al. (1984) and Kobayashi et al. (1993) assuming a rigid canopy component (referred to as 'blade' herein and after) without motion. Wave dissipation is dependent on the work of the canopy drag, which is proportional to the square of the relative velocity between the flow and the blade. Neglecting the blade motion can overestimate drag and therefore wave attenuation. In an effort to represent these uncertainties, a bulk drag coefficient (C_D) approach has been applied (e.g., Kobayashi et al., 1993; Mendez and Losada, 2004). Alternatively, Luhar et al. (2017) proposed a technique that considers the effects of blade motion by using a reduced effective blade length (l_e) rather than reducing

the original drag coefficient (C_d). The effective blade length (l_e) is defined as the length of a rigid blade that dissipates the same wave energy as the flexible blade with the original length (l). The bulk drag coefficient and effective blade length methods reduce the complexity to model the wave-vegetation interaction so that these models are computationally efficient and convenient to implement in large-scale models. However, numerous experiments are required to calibrate C_D and l_e. Conventionally, C_D is expressed as a function of Reynolds number (Re) or Keulegan–Carpenter number (KC) independent from vegetation flexural rigidity. Thus, the Re- and KC-based empirical formulas for C_D are different for vegetation with different flexibilities, e.g., the different formulas in Mendez and Losada (2004), Sanchez-Gonzalez et al. (2011), Jadhav et al. (2013), Anderson and Smith (2014), and Ozeren et al. (2014) as summarized in Chen et al. (2018) and van Veelen et al. (2020). The empirical formula for l_e is expressed as a function of the Cauchy number (Ca) incorporating vegetation flexural rigidity. Accurate parameterizations of C_D and l_e are important to predict wave attenuation (Fringer, 2019), which requires a full understanding of wave-vegetation interaction.

To quantify the blade motion, the blade is modeled as a cantilever beam using Euler-Bernoulli beam approach. By simplifying the blade motion as a balance between drag force and blade bending resistance, Mullarney & Henderson (2010) obtained linear normal mode solutions for the blade displacement along the length. The model was recently extended to include the effects of buoyancy by Henderson (2019). With the normal mode technique, Zhu et al. (2020a) obtained frequency dependent analytical solutions for blade displacements in random waves considering the effects of inertial forces. As the analytical solutions are limited to small-amplitude blade motion, a more precise solution for the large-amplitude blade motion can be obtained with numerical techniques (e.g., Zeller et al., 2014; Zhu and Chen, 2015; Luhar and Nepf, 2016; Leclercq and de Langre, 2018; Zhu et al., 2018; Chen and Zou, 2019; Zhu et al., 2020b). The consistent-mass cable model described in Zhu et al. (2020b) was able to capture asymmetric ‘‘whip-like’’ blade motion. These analytical solutions are useful to describe the mechanisms that influence blade motion related to wave attenuation. The benefit of analytical solutions are that they are easier to

implement into large-scale models to analyze the influences of wave attenuation on coastal morphology, inner shelf circulation and material transport. The analytical wave attenuation model is developed based on the small-amplitude blade motion and the nonlinearity effects induced by the large-amplitude blade motion on the wave attenuation model, as well as its application has not yet been understood.

Wave attenuation by vegetation is determined by wave conditions and vegetation characteristics including morphological (e.g., plant density and blade length, width and thickness) and mechanical properties (e.g., blade flexural rigidity). The vegetation characteristics depend on the growth of vegetation and therefore show a seasonal variation (Moller and Spencer, 2002; Moller, 2006; Koch et al., 2009). Most salt-marsh grasses, such as *Spartina alterniflora* (Marsooli et al., 2017), *Spartina anglica* (Schulze et al., 2019), *Spartina foliosa* (Foster-Martinez et al., 2018), *Salicornia pacific* (Foster-Martinez et al., 2018), and *Elymus athericus* (Schulze et al., 2019), contribute more wave energy during summer than winter and spring due to larger plant stem stiffness, canopy height, and aboveground biomass in summer than other seasons. Most seagrasses, such as *Ruppia maritima* (Chen et al., 2007), *Zostera marina* (Hansen and Reidenbach, 2013), and *Zostera noltii* (Paul and Amos, 2011), also show a similar pattern to dissipate more wave energy in summer with larger blade length, blade width, canopy height, and canopy density in summer than other seasons. In winter, more vegetation break or die off that may also reduce the wave attenuation capacity (Marsooli et al., 2017; Vuik et al., 2018). Therefore, Ondiviela et al. (2014) proposed that the large, long living and slow growing seagrass species, such as *Posidonia oceanica*, with biomass being largely independent of seasonal fluctuations may provide a favorable coastal protection. Like vegetation, kelp, especially for cultivated kelp, also grow seasonally with seasonal impacts on wave attenuation, which are not fully understood. The seasonal variation of natural materials used to attenuate waves is essential to understand, so that the appropriate species and design strategies can be selected for nature-based coastal protection.

The objectives of this study are to develop an analytical wave attenuation model with resolving the blade motion and investigate the seasonal wave attenuation capacity of cultivated kelp canopies as well as its implications for nature-based coastal protection. The analytical model was compared with the

experiments by Luhar et al. (2017) and Lei and Nepf (2019a) for submerged aquatic vegetation and the experiments in Chapter 3 for suspended kelp canopies. The analytical model was also compared with the numerical model in Chapter 3 to analyze the effects of the nonlinearity of large-amplitude blade motion. With the analytical model, the analytical solutions for the bulk drag coefficient and effective blade length were derived and compared with the fitted values from the datasets. After the data-model comparison, the model was then used to analyze the seasonal impacts on the wave attenuation capacity of submerged vegetation and suspended canopies.

4.2. Methodology

4.2.1. Model set-up

To derive the wave attenuation model for suspended canopies, the three-layer model is used (Figure 4.1). The horizontal coordinate (x) is positive in the direction of wave propagation with $x = 0$ at the leading edge of the canopy and $x = L_v$ at the ending edge. The vertical coordinate (z) is positive upward with $z = 0$ at the still water level (SWL). The canopy height (d_2) is defined as the average submerged length of the canopy blades. The thicknesses of the water layers above and below the canopy are d_1 and d_3, respectively. The water depth from the SWL is $h = d_1 + d_2 + d_3$, where the seafloor is located at $z = -h$ and assumed horizontal. This generalized three-layer model can be used to analyze the wave attenuation characteristics of (i) submerged ($d_1 \neq 0$ and $d_3 = 0$), (ii) emerged ($d_1 = 0$ and $d_3 = 0$), (iii) suspended ($d_1 \neq 0$ and $d_3 \neq 0$), and (iv) floating ($d_1 = 0$ and $d_3 \neq 0$) canopies.

Based on linear wave theory (Dean and Dalrymple, 1991), the horizontal wave orbital velocity (u) is given by

$$u = \frac{H}{2}\omega\Gamma(z)\cos(kx - \omega t), \tag{4.1}$$

where H is the wave height, ω is the wave angular frequency, t is the time, $\Gamma = \cosh k(h+z) / \sinh kh$ is the vertical decay factor, and k is the wave number obtained from the dispersion relation, $\omega^2 = gk \tanh kh$, with g being the gravitational acceleration.

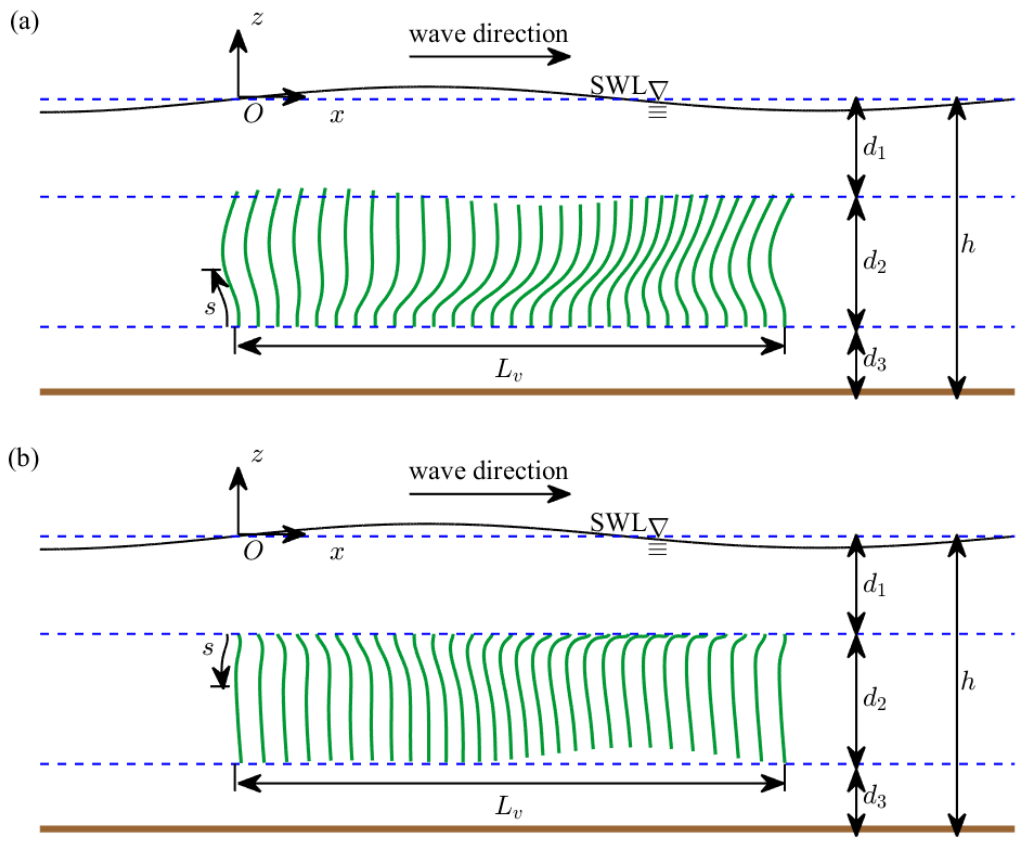

Figure 4.1. Sketch of the three-layer model for wave attenuation by suspended canopies (a) fixed at the bottom end and (b) fixed at the tip end. The coordinate (x, z) is originated at the leading edge of the canopy ($x = 0$) and the still water level (SWL, $z = 0$). The distance from the fixed end of the blade is s. The canopy length is L_v and the canopy height is d_2. The thicknesses of the layers above and below the canopy are d_2 and d_3, respectively. The water depth from the SWL is $h = d_1 + d_2 + d_3$.

4.2.2. Blade motion

The blade is modeled as a cantilever beam with the simplified governing equation for the horizontal blade displacement (ξ),

$$\rho_v A_c \ddot{\xi} + EI\xi'''' = f_x, \tag{4.2}$$

where ξ is a function of time (t) and the distance s along the blade length (l) from the fixed end ($s = 0$), the dot ($\dot{}$) indicates derivative with respect to t, the prime ($'$) indicates derivative with respect to s, ρ_v is the blade mass density, A_c is the blade cross section area, and EI is the blade flexural rigidity with E being

the elastic modulus and I being the second moment of the cross section. The relation between s and z (Figure 4.1) is

$$z = \begin{cases} -d_1 - d_2 + s, & \text{blade fixed at the bottom end,} \\ -d_1 - s, & \text{blade fixed at the tip end.} \end{cases} \tag{4.3}$$

The right-hand side of equation (4.2) is the hydrodynamic force per unit length (f_x) consisting of virtual buoyancy (f_{VB}), drag (f_d), and added mass force (f_{AM}) given by the modified Morison equation (Morison et al., 1950),

$$f_x = \alpha_F(f_{VB} + f_d + f_{AM}), \tag{4.4}$$

where α_F is the sheltering factor to consider the sheltering effects between blades, $f_{VB} = \rho_w A_c \dot{u}$, $f_d = \frac{1}{2} C_d \rho_w b \left|u - \dot{\xi}\right| \left(u - \dot{\xi}\right)$, $f_{AM} = C_m \rho_w A_c (\dot{u} - \ddot{\xi})$, ρ_w is the water density, b is the projected width of the blade, C_d is the drag coefficient, and C_m is the added mass coefficient. The drag coefficient (C_d) and added mass coefficient (C_m) are $C_d = \max(10KC^{-1/3}, 1.95)$ and $C_m = \min(C_{m1}, C_{m2})$, respectively, with $C_{m1} = \begin{cases} 1 + 0.35\mathrm{KC}^{2/3}, \mathrm{KC} < 20 \\ 1 + 0.15\ \mathrm{KC}^{2/3}, \mathrm{KC} \geq 20 \end{cases}$ and $C_{m2} = 1 + (\mathrm{KC} - 18)^2/49$ (Luhar, 2012; Luhar and Nepf, 2016). The formulas for C_d and C_m are obtained from the experiments for rigid flat plates in oscillatory flows (Keulegan and Carpenter, 1958; Sarpkaya and O'Keefe, 1996) with $1.7 \leq KC = uT/b \leq 118.2$. To obtain an analytical solution, the nonlinear drag is linearized as

$$f_d = \frac{1}{2} C_d \rho_w b \left|u - \dot{\xi}\right| \left(u - \dot{\xi}\right) \approx c\left(u - \dot{\xi}\right), \tag{4.5}$$

where the linearization coefficient (c) is obtained from the Lorentz's condition of equivalent work (Sollitt & Cross, 1972). This requires that the nonlinear and linear drag accounts for the same amount of energy dissipation averaged over one wave period such that $\int_{-d_1-d_2}^{-d_1} \overline{\frac{1}{2} \alpha_F C_d \rho_w b \left|u - \dot{\xi}\right| \left(u - \dot{\xi}\right)^2} dz = \int_{-d_1-d_2}^{-d_1} \overline{c\left(u - \dot{\xi}\right)^2} dz$, yielding

$$c = \frac{\int_{-d_1-d_2}^{-d_1} \overline{\alpha_F \frac{1}{2} C_d \rho_w b \left|u - \dot{\xi}\right| \left(u - \dot{\xi}\right)^2} dz}{\int_{-d_1-d_2}^{-d_1} \overline{\left(u - \dot{\xi}\right)^2} dz}, \tag{4.6}$$

where the overbar indicates the time average over one wave period. The linearization of the drag force in random waves is typically done using the Borgman (1967) method based on the distribution of the wave orbital velocity resulting in a different expression of the linearization coefficient (detailed in Zhu et al., 2020b).

Substituting (4.1), (4.4) with linearized drag (4.5) into (4.2) yields

$$m\ddot{\xi} + c\,\dot{\xi} + EI\xi'''' = \frac{H}{2}\omega\Gamma[c\cos(kx-\omega t) + \omega m_I \sin(kx-\omega t)], \tag{4.7}$$

where $m = (\rho_v + \alpha_F C_m \rho_w)A_c$ and $m_I = (1+C_m)\alpha_F \rho_w A_c$. The boundary conditions for a cantilever beam are set as $\xi(0,t)=0$, $\xi'(0,t)=0$, $\xi''(l,t)=0$, and $\xi'''(l,t)=0$. Solving (4.7) with the normal mode approach (Rao, 2007) yields

$$\xi = \frac{H}{2}\Gamma[\gamma_s \sin(kx-\omega t) + \gamma_c \cos(kx-\omega t)]. \tag{4.8}$$

In (4.8), γ_s and γ_c are the transfer functions and expressed as

$$\gamma_s = \frac{\omega}{\Gamma}\sum_{n=1}^{\infty}\phi_n \frac{\omega I_n(\lambda_n^2-\omega^2) - D_n 2\zeta_n\lambda_n\omega}{(\lambda_n^2-\omega^2)^2 + (2\zeta_n\lambda_n\omega)^2} \tag{4.9}$$

and

$$\gamma_c = \frac{\omega}{\Gamma}\sum_{n=1}^{\infty}\phi_n \frac{D_n(\lambda_n^2-\omega^2) + \omega I_n 2\zeta_n\lambda_n\omega}{(\lambda_n^2-\omega^2)^2 + (2\zeta_n\lambda_n\omega)^2}, \tag{4.10}$$

where $\phi_n = (\cos\mu_n l + \cosh\mu_n l)(\sin\mu_n s - \sinh\mu_n s) + (\sin\mu_n l + \sinh\mu_n l)(\cosh\mu_n s - \cos\mu_n s)$ is the nth normal mode of the cantilever beam with μ_n being the nth solution of $1+\cos\mu l\cosh\mu l = 0$, $\lambda_n = \mu_n^2\sqrt{EI/m}$ is the nth natural frequency of the blade, $2\zeta_n\lambda_n = c/m$, $D_n = c/m\int_0^l \Gamma\phi_n ds \,/\int_0^l \phi_n^2 ds$ and $I_n = m_I/m\int_0^l \Gamma\phi_n ds \,/\int_0^l \phi_n^2 ds$. Since Γ is expressed in z and ϕ_n is expressed in s, the relation between s and z in (3) is required to calculate the integral $\int_0^l \Gamma\phi_n ds$. Substituting (4.8) into (4.6) yields the expression of the linearization coefficient in terms of the transfer functions,

$$c = \frac{1}{2}\alpha_F C_d \rho_w b \frac{H}{2}\omega\frac{8}{3\pi}\frac{\int_{-d_1-d_2}^{-d_1}\Gamma^3[(1+\gamma_s)^2+\gamma_c^2]^{3/2}dz}{\int_{-d_1-d_2}^{-d_1}\Gamma^2[(1+\gamma_s)^2+\gamma_c^2]dz}. \tag{4.11}$$

The linearization coefficient can be obtained iteratively. Starting from a static blade, an initial c is calculated from equation (4.11) by assuming $\gamma_s = 0$ and $\gamma_c = 0$. Once the transfer functions are obtained from (4.9) and (4.10), c can be updated from (4.11). The procedure is repeated until a convergent solution is obtained.

4.2.3. Wave attenuation

The wave energy dissipation is assumed to be attributed to the work of canopy drag following Zhu et al. (2020a). The drag force described in Section 4.2.2 is derived assuming a small-amplitude blade motion with linear beam theory. In fact, the blade motion is large-amplitude with geometrical nonlinearity. To consider the effects of geometrical nonlinearity on wave attenuation, a factor α_N is induced in the energy conservation equation such that

$$\frac{\partial Ec_g}{\partial x} = -\int_{-d_1-d_2}^{-d_1} N\alpha_N \overline{\alpha_S f_d\left(u - \dot{\xi}\right)}\, dz, \tag{4.12}$$

where $E = \rho_w g H^2/8$ is the local wave energy per unit horizontal area, $c_g = \omega(1 + 2kh/\sinh 2kh)/2k$ is the wave group velocity, N is the canopy density defined as the number of blades per unit horizontal area, and α_S is the sheltering factor to consider the sheltering effects between blades. The factor α_N can be calibrated through numerical methods or experiments. In this study, α_N is fitted through numerical methods. Substituting the quadratic drag force (4.5) into (4.12) yields the transmitted wave height at distance x in relation to the incident wave height H_0 at $x = 0$,

$$\frac{H(x)}{H_0} = \frac{1}{1 + k_D H_0 x}, \tag{4.13}$$

where the wave decay coefficient (k_D) is expressed as

$$k_D = \frac{4\alpha_N \alpha_S C_d b N k^2}{3\pi \sinh kh(2kh + \sinh 2kh)} \int_{-d_1-d_2}^{-d_1} \left[\sqrt{(1+\gamma_s)^2 + \gamma_c^2}\right]^3 \cosh^3 k(h+z)\, dz. \tag{4.14}$$

It should be noted that equation (4.13) is obtained using a quadratic drag. Using the linearized drag (4.5) yields an exponential decayed wave height as $H = H_0 e^{-k_D H_0 x}$, which is also often used in practice (e.g., Kobayashi et al., 1993; Mendez et al., 1999; Zhu & Zou, 2017). The two wave decay forms are linked through a piecewise method (Appendix C). The piecewise method indicates that the exponential decay form

with linearized drag would overestimate the wave attenuation. Therefore, the fractional decay form in (4.13) is recommended. However, for weak wave attenuation such that $k_D H_0 x < 0.5$, the difference between $1/(1 + k_D H_0 x)$ and $e^{-k_D H_0 x}$ is less than 10%.

For a rigid canopy with unsheltered blades such that $\alpha_N = 1$, $\alpha_S = 1$, $\gamma_s = 0$, and $\gamma_c = 0$, the solution (4.14) reduces to the solution of Zhu and Zou (2017), i.e.,

$$k_{D,R} = \frac{C_d bNk}{9\pi} \frac{9\sinh k(d_2+d_3) - 9\sinh kd_3 + \sinh 3k(d_2+d_3) - \sinh 3kd_3}{\sinh kh(2kh+\sinh 2kh)}. \tag{4.15}$$

For bottom rooted vegetation such that $d_3 = 0$, solution (4.15) can be further reduced to the solutions by Dalrymple et al. (1984) and Kobayashi et al. (1993).

4.2.4. Bulk drag coefficient and effective blade length

The wave dissipation ratio is proportional to $\int_{-d_1-d_2}^{-d_1} \overline{f_d\left(u - \dot{\xi}\right)}\, dz \propto \overline{\int_0^l C_d |u_r|^3 ds}$ with $u_r = u - \dot{\xi}$ being the relative velocity. This requires computing the relative velocity to consider the wave-blade interaction. To reduce the computation for the relative velocity with resolving the blade motion, the bulk drag coefficient and effective blade length methods with a rigid blade assumption are often used, especially for implementation into large-scale models. The bulk drag coefficient (C_D) is a reduced drag coefficient such that $\int_0^l C_D |u|^3 ds = \int_0^l C_d |u_r|^3 ds$ while the effective blade length (l_e) is a reduced blade length such that $\int_0^{l_e} C_d |u|^3 ds = \int_0^l C_d |u_r|^3 ds$ as shown on Figure 4.2. Traditionally, C_D and l_e are calibrated with experiments. However, with the analytical model developed in this study, the analytical solutions for C_D and l_e can be obtained.

Replacing C_d in (4.15) by C_D and substituting the result into (4.14) yields the bulk drag coefficient,

$$C_D = \frac{12k\alpha_N\alpha_S \int_{-d_1-d_2}^{-d_1} \cosh^3 k(h+z) \left[\sqrt{(1+\gamma_s)^2+\gamma_c^2}\right]^3 dz}{9\sinh k(d_2+d_3) - 9\sinh kd_3 + \sinh 3k(d_2+d_3) - \sinh 3kd_3} C_d. \tag{4.16}$$

For shallow water waves with $kh < 0.1\pi$, (4.16) reduces to

$$C_D = \frac{\alpha_N\alpha_S}{\mathrm{d}_2} \int_{-d_1-d_2}^{-d_1} \left[\sqrt{(1+\gamma_s)^2+\gamma_c^2}\right]^3 dz\, C_d. \tag{4.17}$$

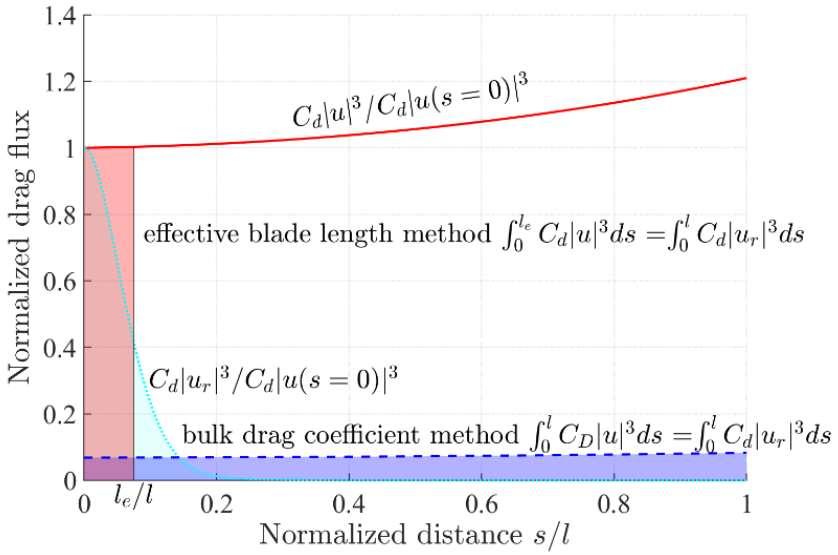

Figure 4.2. Concept sketch for bulk drag coefficient (C_D) and effective blade length (l_e) methods. The bulk drag coefficient method is denoted by blue patch such that $\int_0^l C_D|u|^3 ds = \int_0^l C_d|u_r|^3 ds$ while the effective blade length method is denoted by red patch such that $\int_0^{l_e} C_d|u|^3 ds = \int_0^l C_d|u_r|^3 ds$, where u is flow velocity, u_r is the relative velocity between the blade and flow, C_d is the original drag coefficient, s is the distance along the blade length, and l is the blade length.

Replacing d_2 in (4.15) by l_e and substituting the result into (4.14) yields the solution for the effective blade length,

$$9\sinh k(l_e + d_3) + \sinh 3k(l_e + d_3) = 9\sinh kd_3 + \sinh 3kd_3 + 12k\alpha_N\alpha_S \int_0^l \cosh^3 k(h + z)\left[\sqrt{(1+\gamma_s)^2 + \gamma_c^2}\right]^3 ds. \quad (4.18)$$

For submerged vegetation with $d_3 = 0$, (4.18) reduces to

$$9\sinh kl_e + \sinh 3kl_e = 12k\alpha_N\alpha_S \int_0^l \cosh^3 k(h + z)\left[\sqrt{(1+\gamma_s)^2 + \gamma_c^2}\right]^3 ds, \quad (4.19)$$

If l_e is far less than wave length with $kl_e < 0.1\pi$ ($l_e < 0.05\lambda$), (4.19) reduces to

$$l_e = \alpha_N\alpha_S \int_0^l \cosh^3 k(h + z)\left[\sqrt{(1+\gamma_s)^2 + \gamma_c^2}\right]^3 ds. \quad (4.20)$$

For shallow water waves with ($kh < 0.1\pi$ or $h < 0.05\lambda$), (4.18) reduces to

$$l_e = \alpha_N\alpha_S \int_0^l \left[\sqrt{(1+\gamma_s)^2 + \gamma_c^2}\right]^3 ds. \quad (4.21)$$

4.3. Results

4.3.1. Model-Data comparison

The analytical model is compared with the experiments for suspended kelp canopy in Chapter 3 as well as the experiments for submerged vegetation in Luhar et al. (2017) and Lei and Nepf (2019b). The numerical model in Chapter 3 is used to calibrate the factor α_N for the analytical model to consider the effects of the geometrical nonlinearity induced by large-amplitude blade motion.

In the experiments for suspended kelp canopies, the kelp blade was made of silicon film with $\rho_v = 1.2$ g/m^3 and $E = 2.04$ MPa. The model blade was 10.16 cm long, 0.95 cm wide and 0.1 mm thick. The suspended kelp canopy consisted of 20 rows of blades and the rows were 20 cm apart. For each row, there were 31 aggregates of blades with 1 aggregate/cm. For each aggregate, 10 blades were fixed together at the top end with the fixed part of the blade being 0.5 cm and the flexible part being 9.66 cm. The sheltering effects between the blades in an aggregate were considered using a sheltering factor $\alpha_S = 0.728$, proposed in Chapter 3. The canopy length was 3.8 m and the canopy density was $N = 5263$ blades/m^2. Three vertical positions of the suspended canopy beneath the SWL with $d_1 = 6, 11, 16$ cm were compared in the experiments. The incident wave height was 1.8~3.8 cm, wave period was 0.8~2 s, and water depth was 30~40 cm with $kh = 0.58$~2.41, $H_{I0}/h = 0.05$~0.11, $C_a = 35$~13930, $L = 6$~284, $KC = 0.2$~10.8 and $Re = 24$~488. The details of the experiments can be found in Chapter 3.

In the experiments for submerged vegetation (Luhar et al., 2017; Lei and Nepf, 2019b), the vegetation was modeled using a 14 cm-long, 3 mm-wide, and 0.1 mm-thick low-density polyethylene (LDPE) film with $\rho_v = 0.92$ g/cm^3 and $E = 0.3$ GPa. The rigid part of the blade was 1 cm while the flexible part was 13 cm. The blades were located separately such that the sheltering factor $\alpha_S = 1$. The canopy density was 280~1800 stems/m^2 with 1680~10800 blades/m^2. The wave height was 1 to 11.2 cm, wave period was 0.8 to 2 s, and the water depth was 16 to 45 cm with $kh = 0.44$~2.7, $l/h = 0.29$~0.8, $KC = 10.3$~138, $Ca = 87$~3764, and $L = 2$~26. Details of the experiments for the submerged

vegetation can be found in Luhar et al. (2017) and Lei and Nepf (2019b). The canopy characteristics and wave conditions are summarized in Table 4.1.

Table 4.1. Canopy characteristics and wave conditions.

	Canopy characteristics	Wave conditions
Suspended kelp canopy in Chapter 3	Silicon film blade Mass density: 1.2 g/cm3 Elastic modulus: 2.04 MPa Dimensions: 10.16 cm long, 0.95 cm wide, and 0.1 mm thick with rigid part of 0.5 cm and flexible part of 13 cm Canopy density: 526.3 bunches/m2 and 5263 blades/m2 Fixed at the top end of blade with 6, 11, 16 cm below the still water line Sheltering factor: $\alpha_S = 0.728$	Water depth: 30~40 cm Wave height: 1.8~3.8 cm Wave period: 0.8~2 s Wave length: 1.03 ~ 3.70 m
Submerged vegetation in Luhar et al. (2017) and Lei and Nepf (2019)	Low-density polyethylene (LDPE) blade Mass density: 0.92 g/cm3 Elastic modulus: 0.3 GPa Dimensions: 14 cm long, 0.3 cm wide, and 0.1 mm thick with rigid part of 1 cm and flexible part of 13 cm Canopy density: 280~1800 bunches/m2 and 1680~10800 blades/m2 Fixed at the bottom end of blade Sheltering factor: $\alpha_S = 1$	Water depth: 16~45 cm Wave height: 1~11.2 cm Wave period: 0.8~2 s Wave length: 0.90~3.88 m

The analytical model with linearization of the blade motion underestimates the wave decay coefficient k_{DB} for the flexible part of the blades as shown on Figure 4.3a. To compensate for the linearization-induced underestimation in wave attenuation, the nonlinear effects coefficient α_N to consider the nonlinearity is developed by comparing the nonlinear numerical results and linear analytical results. The nonlinear results are found to be averagely 1.63 times of the linear results (Figure 4.3a). Thus, the nonlinear effects coefficient is set as $\alpha_N = 1.63$ for this study. The modified analytical solutions for k_D with $\alpha_N = 1.63$ showed good agreement with the experiments with underestimation of 10% (Figure 4.3b).

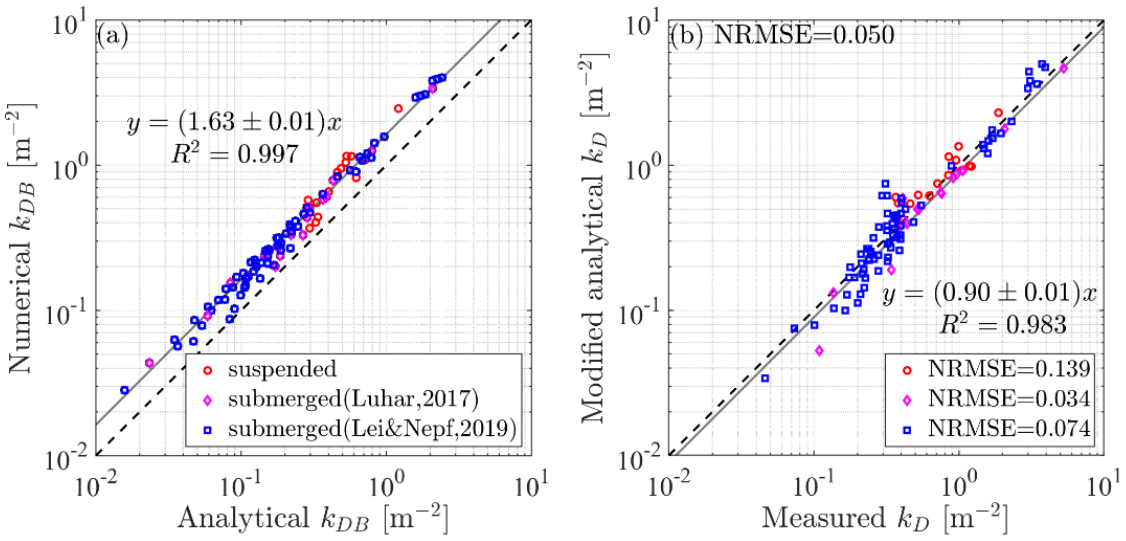

Figure 4.3. (a) Comparisons between the numerical and analytical calculations for the wave decay coefficient k_{DB} for the flexible part of the blades. (b) Comparisons between the modified analytical solutions and the measurements for the wave decay coefficient k_D. The solid gray lines are the linear fits for the comparisons with expressions and R^2 nearby. The normalized root mean square error (NRMSE) is shown in the legend and text.

4.3.2. Bulk drag coefficient and effective blade length

Bulk drag coefficient and effective blade length methods are simple ways to consider the effects of blade motion on wave attenuation. The values of C_D and l_e are for the flexible part of the blade with length of l_f. The analytically calculated C_D is compared with the fitted and measured C_D on Figure 4.4, where C_D is expressed as a function of KC. As KC does not include all the parameters governing the blade motion, there might be several values of C_D for different blade motions with the same KC. Thus, C_D is scattered, especially for the submerged vegetation dataset that has more cases with more wave conditions and more types of blade motions (Figure 4.4c). For KC-based C_D, the analytically calculated C_D has a similar NRMSE of 0.202 to the fitted C_D with NRMSE=0.187 for suspended kelp canopy (Figure 4.4a). For submerged vegetation (Figure 4.4c), the NRMSE of analytically calculated C_D is 0.202 and also similar to the fitted C_D with NRMSE=0.190. For the comparisons between the decay coefficient (Figure 4.4b and d), the results calculated with the analytically calculated C_D (NRMSE=0.123 for the suspended kelp and 0.051

for the submerged vegetation) also showed a similar precision to those with the fitted C_D (NRMSE = 0.139 for the suspended kelp and 0.052 for the submerged vegetation).

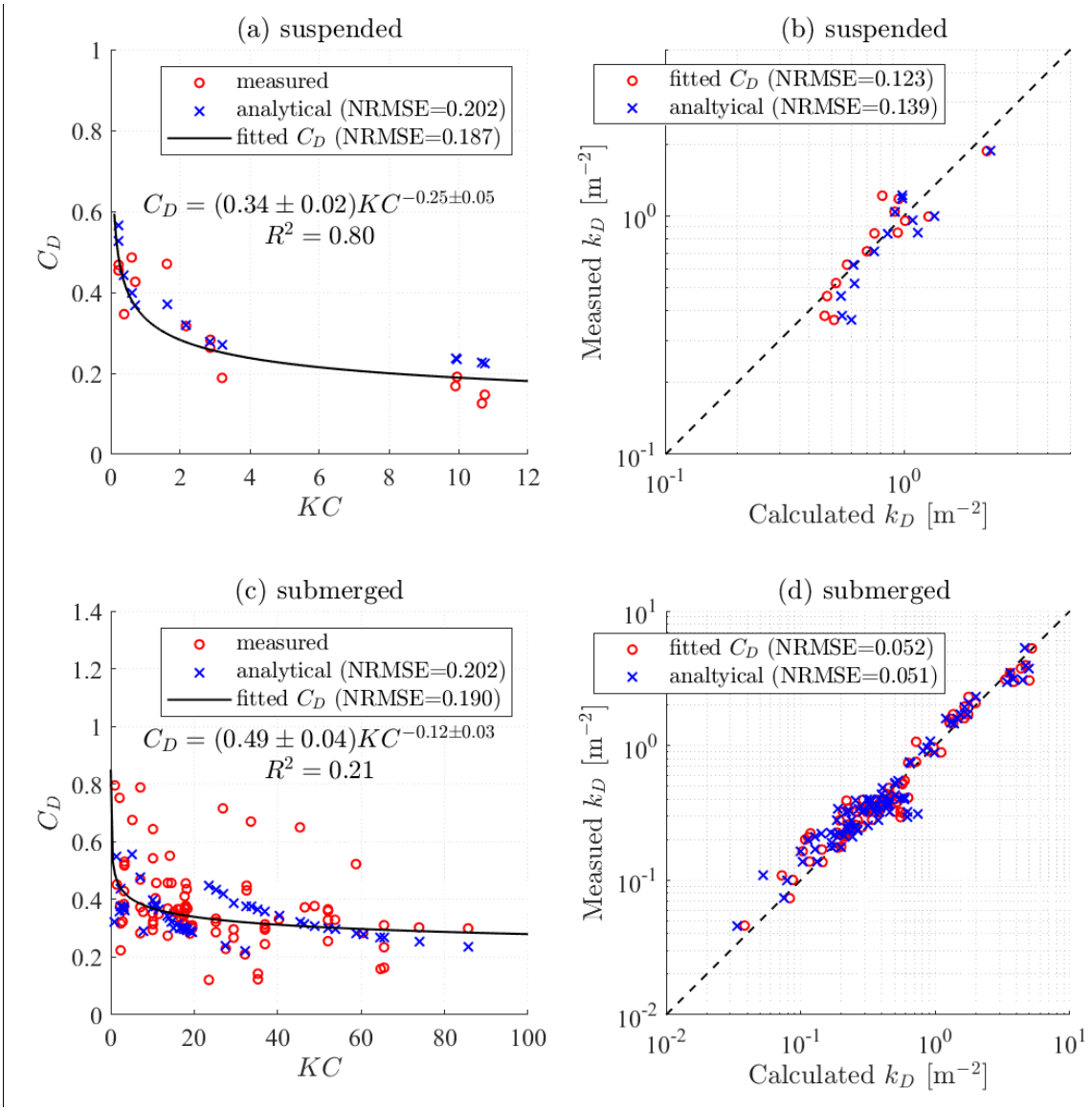

Figure 4.4. Comparisons for the bulk drag coefficients (C_D) of the flexible part of the blade between the measured, calculated using the analytical solution (4.16), and the fitted value for (a) suspended and (c) submerged canopies. Comparisons for the decay coefficient (k_D) calculated by fitted C_D and the analytically calculated C_D for (b) suspended and (d) submerged canopies.

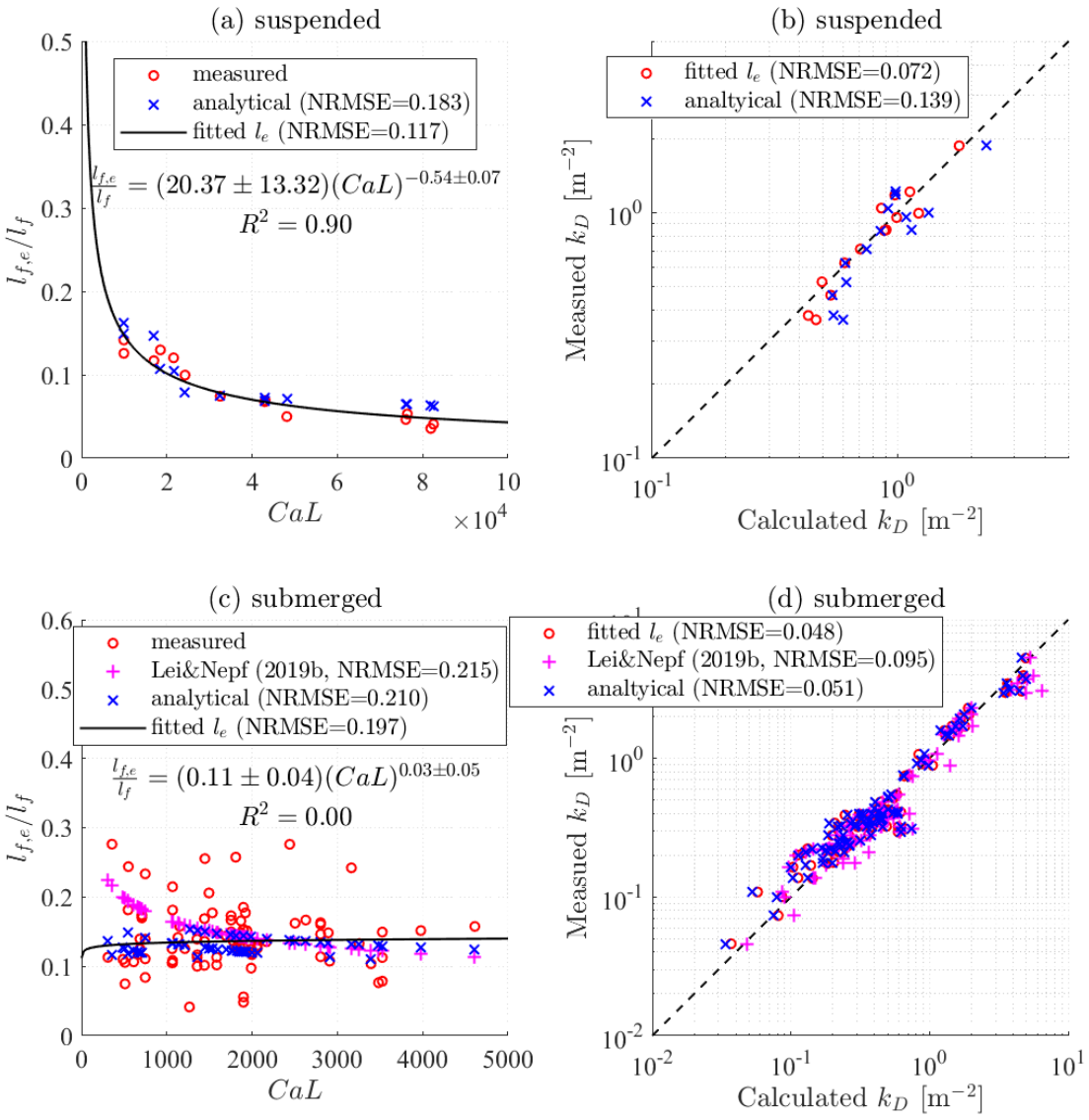

Figure 4.5. Comparisons for the normalized effective blade length ($l_{f,e}/l_f$) of the flexible part of the blade (l_f) between the measured, calculated using the analytical solution (4.18), calculated using the empirical formula by Luhar and Nepf (2019b), and the fitted value for (a) suspended and (c) submerged canopies. Comparisons for the decay coefficient (k_D) calculated by the fitted $l_{f,e}$, the empirical formula in Lei and Nepf (2019b), and the analytically calculated $l_{f,e}$ for (b) suspended and (d) submerged canopies.

The analytically calculated effective blade length of the flexible part of blade ($l_{f,e}$) is compared with the fitted and measured $l_{f,e}$ as well as the empirical formula by Lei and Nepf (2019b) on Figure 4.5, where $l_{f,e}$ is expressed as a function of CaL. As CaL does not include all the parameters governing the

blade motion, there might be several values of $l_{f,e}$ for different blade motions with the same CaL. Thus, $l_{f,e}$ is also scattered, especially for the submerged vegetation datasets that has more cases with more wave conditions and more types of blade motions (Figure 4.5c). For CaL-based $l_{f,e}$, the analytically calculated $l_{f,e}$ has a slightly larger NRMSE of 0.183 than the fitted $l_{f,e}$ with NRMSE=0.117 for suspended kelp canopies. For submerged vegetation, NRMSE is nearly 0.2 for all the methods. For the comparisons between the decay coefficients (Figure 4.5b and d), the results calculated with the analytically calculated $l_{f,e}$ (NRMSE=0.139 for suspended kelp and 0.051 for submerged vegetation) show less precision than those with the fitted $l_{f,e}$ (NRMSE = 0.072 for the suspended canopy and 0.048 for the submerged vegetation). Compared to the $l_{f,e}$ (NRMSE = 0.095) from the formula developed by Lei and Nepf (2019b), the analytically calculated $l_{f,e}$ has improved the NRMSE by 46%.

4.3.3. Case study for wave attenuation in different seasons

The validated analytical model is used to investigate the seasonal wave attenuation capacity of kelp farms compared with seagrass. The designed length of the kelp blade is following the measured data by Augyte et al. (2017) for *Saccharina latissima* (sugar kelp) at coastal Maine, USA. The corresponding blade width, thickness and elastic modulus are calculated using (3.27) to (3.30) in Chapter 3 (Figure 4.6a). The effective blade width with $b_e = 0.2b$ based on (3.33) is used to consider the effects of thickness variance along the blade width. The designed mass density of kelp is 1053 kg/m^3 (Table 3.2 in Chapter 3) and plant density is 330 plants/m (Augyte et al., 2017). The sheltering factor of 0.728 from the laboratory experiments in Chapter 3 is assumed applicable for this case study. The kelp longline is designed at 1.2 m below the still water level and 4 m apart in 8 m-deep water.

Regarding the parameters of seagrass, the designed length of the seagrass blade is following the measured data by Gaeckle and Short (2002) for the *Zostera marina* (eelgrass) at coastal Maine, USA. The corresponding blade width and thickness as well as the length and width of the sheaths are calculated based on the formulas in Abdelrhman (2007) and shown on Figure 4.6b. The designed mass density and elastic modulus are 700 kg/m^3 (Abdelrhman, 2007) and 0.26 GPa (Fonseca et al., 2007), respectively. The designed

shoot density is 335 shoots/m and the leaf number is 3 for each shoot (Mattila et al., 1999). Two water depths of 8 m (at the same water depth with kelp) and 5 m are designed for the seagrass for comparison.

The wave energy dissipation rate (EDR) is used to evaluate the wave attenuation performance of the canopies and is defined as

$$EDR = 1 - \frac{H(L_v)^2}{H(0)^2} = 1 - \left(\frac{1}{1+k_D H_0 L_v}\right)^2, \tag{4.22}$$

where L_v is the canopy length in the direction of wave propagation. The calculated EDR of the designed kelp and seagrass canopies are shown on Figure 4.7. The designed wave height is 1 m.

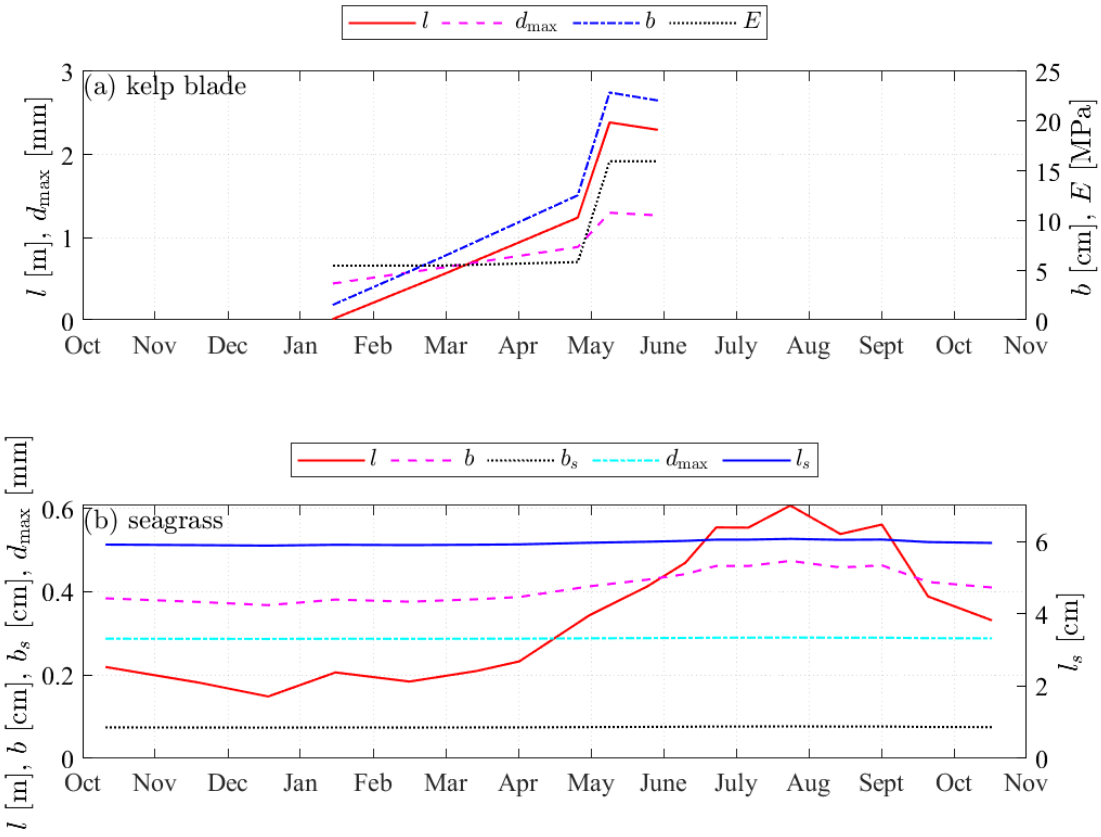

Figure 4.6. Design parameters for (a) kelp and (b) seagrass canopies over a year. The parameters include blade length (l), blade width (b), blade maximum thickness ($d_{\max}$), and elastic modulus (E). The length and width for the seagrass sheets are l_s and b_s.

The growth period of kelp has a significant impact on the wave attenuation. The kelp is usually seeded in December and grows slowly over the first few months, resulting in a small EDR (<10%) during

this time. When the kelp length exceeds 1 m after April, the wave attenuation is considerably larger with EDR>10%, reaching up to 21% with 25 longlines ($L_v = 100$ m) and 36% with 50 longlines ($L_v = 200$ m) for coastal waves with 6 s periods. For longer waves with a period of 10 s, the EDR decreases to 15% and 27% for 25 longlines and 50 longlines, respectively. This is consistent with the wave attenuation characteristics of suspended canopies that are better attenuating shorter waves (Zhu et al., 2020b). The wave attenuation improves with more longlines and as kelp growth continues until it is harvested in June.

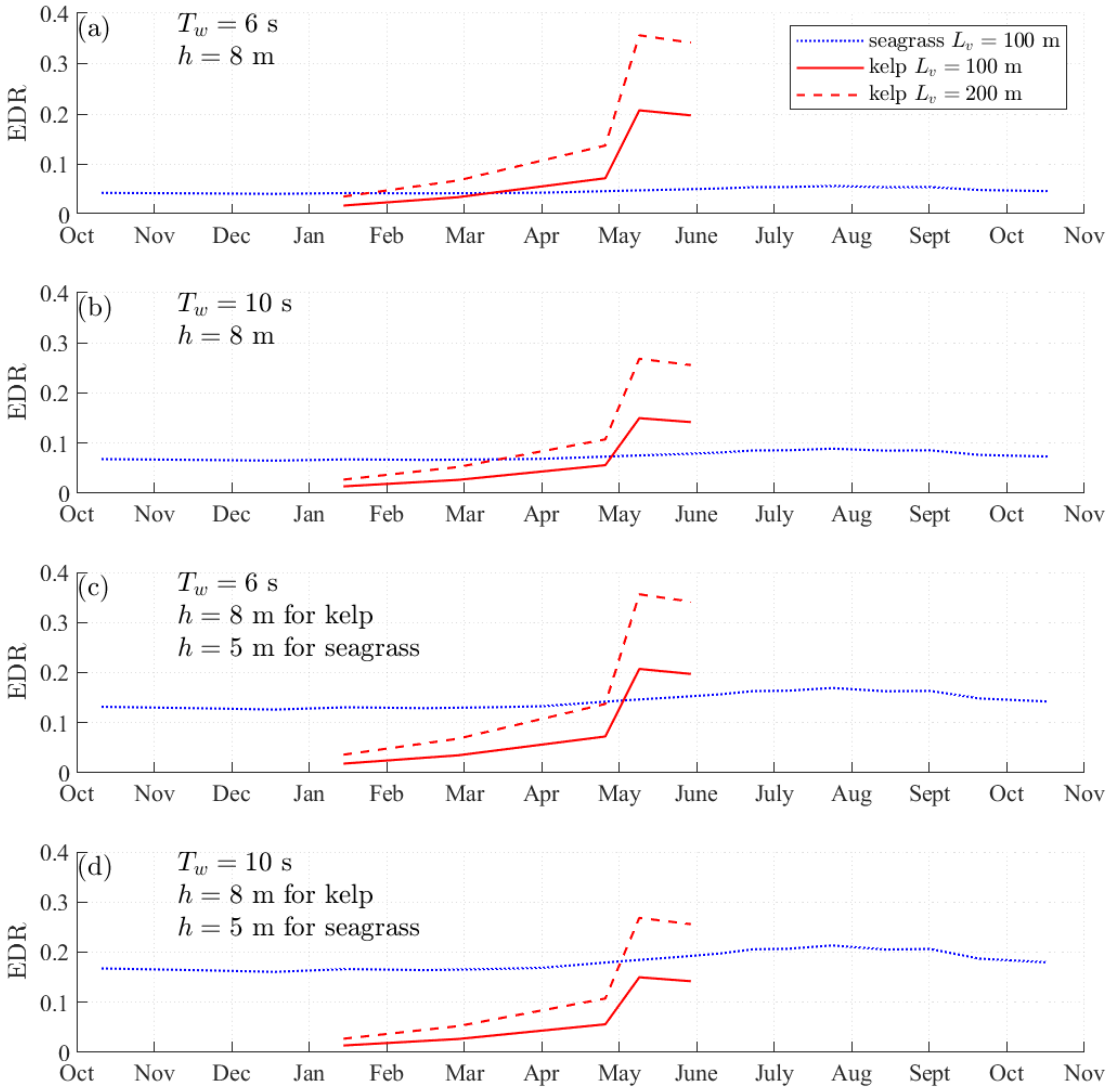

Figure 4.7. Wave energy dissipation rate (EDR) for the designed kelp (red lines) and seagrass (blue lines) canopies in a year around. Two wave periods (T_w) and water depths (h) are compared. The canopy lengths (L_v) for the canopies are shown in the legend.

Unlike the newly seeded kelp with blade growing from millimeters to meters in the growing season, the averaged blade length for a perennial seagrass meadow changes from 15 to 61 cm (Figure 4.6). Therefore, seagrass is less impacted by seasonal growth patterns that are typical of kelp farms. Due to the short blade length, the EDR of the seagrass in the same water depth of kelp is small (<6% for 6 s waves in Figure 4.7a and <9% for 10 s waves in Figure 4.7b). However, when the seagrass is located in shallower water at a 5 m depth, the EDR can increases to up to 17% for 6 s waves (Figure 4.7c) and 21% for 10 s waves (Figure 4.7d).

4.4. Discussion

4.4.1. Blade motion and the nonlinear effects

The discussion begins with blade dynamics, which has a significant influence on the wave attenuation performance. The results show that the linearized analytical solution is smaller than the nonlinear numerical solutions (Figure 4.3). The underestimation is attributed to neglecting the nonlinearity of the blade motion. To investigate the nonlinearity effects on wave attenuation, the linear analytical solutions and nonlinear numerical solutions for the blade postures, the relative velocities (u_r), and the drag force flux ($f_d u_r$) are compared on Figure 4.8.

The wave dissipation is determined by the drag flux ($f_d u_r \propto |u_r|^3$) as shown in (4.12), which is proportional to the cubic of relative velocity. Not considering the nonlinear effects induces a larger amplitude blade motion, particularly near the fixed end (Figure 4.8a1 and b1), resulting in a smaller amplitude relative velocity (Figure 4.8a2, a3, b2 and b3). Consequently, neglecting the nonlinear effects underestimates wave attenuation. The asymmetry of the blade motion (Figure 4.8b1) induced by the interaction between the blade and wave orbital motion (Zhu et al., 2020a) is not considered in the linear model.

The blade is so flexible that the free tip moves passively with the flow, resulting a small relative velocity. Thus, that section of the blade has little contribution to wave dissipation. For example on Figure 4.8b, the blade locations $s > 0.26l$ have a small $|u_r| < 0.4 \max(|u_r|)$ (Figure 4.8b2) yielding $F_d u_r < 5\% \max(F_d u_r)$ (Fig 4.8b4), indicating little contribution to wave dissipation. In other words, only the

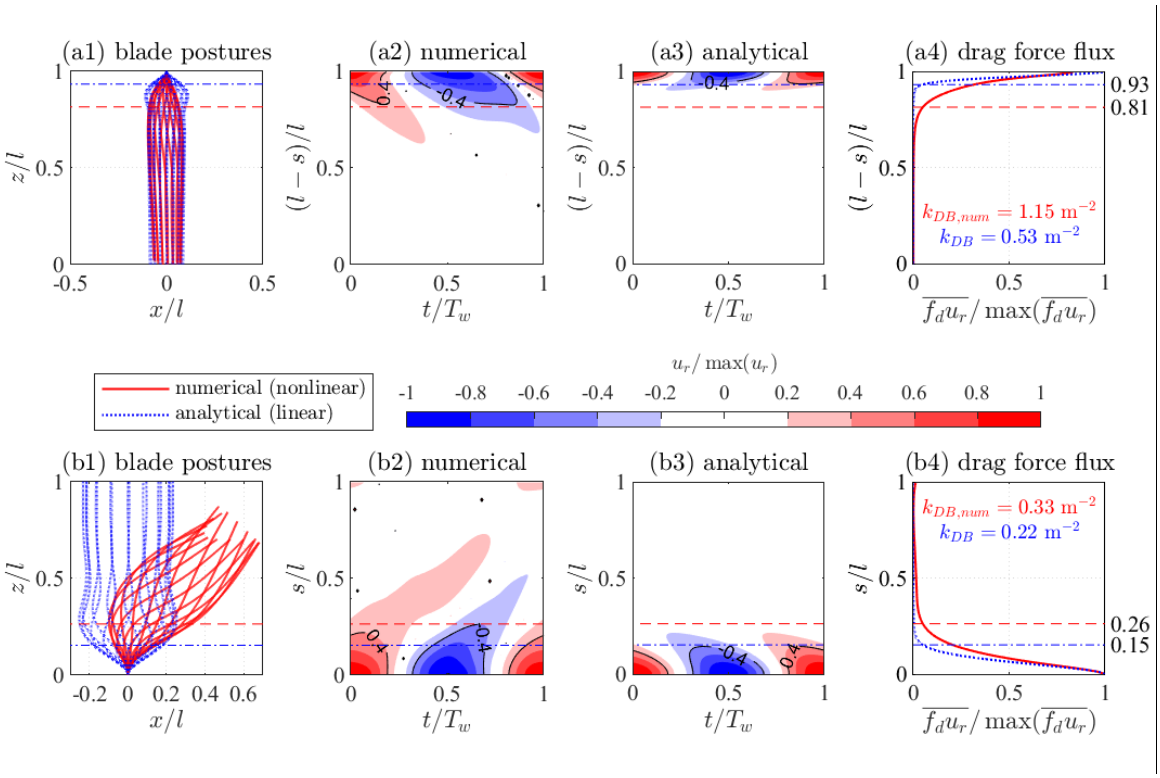

Figure 4.8. Comparisons between the analytical (linearized blade motion) and numerical (nonlinear blade motion) calculations for the (a1 and b1) blade postures (x, z), (a2, a3, b2, and b3) relative velocity (u_r), and (a4 and b4) time averaged drag flux $(\overline{f_d u_r})$ of the (a) suspended model kelp blade and (b) submerged model vegetation. The global coordinates (x, z) and local coordinate (s) are normalized by blade length (l). The time (t) is normalized by wave period (T_w). The horizontal lines indicate the vertical position where $\overline{f_d u_r} = 5\% \max(\overline{f_d u_r})$ with numerical calculations in red dashed lines and analytical calculations in blue dash dotted lines.

blade location near the fixed end ($s < 0.19l$ on Figure 4.8a and $s < 0.26l$ on Figure 4.8b) contributes to the wave dissipation. That is why the linear analytical model provides a good estimate for wave attenuation although the asymmetric large-amplitude blade motion is not well captured. To incorporate the nonlinear effects, a factor $\alpha_N = 1.63$ fitted from the comparison between the linear and nonlinear solutions is used. This constant factor works well for a wide range of $kh = 0.44$~2.7, $l/h = 0.25$~0.8, $KC = 0.22$~138, $Ca = 35$~13930, and $L = 2$~284 for the experiments used in this study. One benefit of using a constant factor is that it can be directly used for random waves without modification to match wave components with different frequencies.

4.4.2. Evaluations of the methods to obtain bulk drag coefficient and effective blade length

Bulk drag coefficient (C_D) and effective blade length (l_e) methods are simple approaches to consider the effects of blade motion on wave attenuation. Without resolving the blade motion as well as the wave-blade interaction, these methods are computationally efficient and more convenient to implement in large-scale models. Conventionally, C_D and l_e are fitted from experimental datasets. Since the complicated wave-blade interaction is not fully understood, sophisticated parameters to obtain good fits (e.g., $R^2 > 0.8$) of C_D and l_e for a wide range of wave conditions and blade properties are difficult to achieve. Therefore, C_D and l_e are traditionally fitted based on KC and CaL without incorporating all the information for wave-blade interaction, resulting in a small R^2. The results showed that the analytical solutions for C_D and l_e developed in this paper showed similar precision to the fitted C_D and l_e based on KC and CaL, respectively. Therefore, the analytical solutions for C_D and l_e can be an alternative when reliable C_D and l_e are not available. The analytical solutions for C_D and l_e are also convenient to implement in large-scale models. As the analytical solutions for C_D and l_e have given the parameters that govern C_D and l_e, which may provide insight in the appropriate parameters and relations to obtain a good fit for C_D and l_e.

4.4.3. Nature-based coastal protection strategies

The case study showed the wave attenuation capacity of *S. latissima* is significantly influenced by the growing age. After about 5 months from seeding, the kelp blade grows longer than 1 m and can provide considerable wave attenuation. The large wave conditions (with significant wave height greater than Hs>1.5 m) with storm events usually occurs in the Gulf of Maine in winter and spring from October to May (data from Maine EPSCoR SEANET Buoy C0502 in Saco Bay). To develop large kelp blades to provide considerable wave attenuation in winter, the kelp can be seeded earlier in May. As kelp grows faster in cold water, the kelp can be submerged near to the seafloor during summer and then move upward to the surface in winter. To keep considerable wave attenuation of kelp farms for coastal protection around the year, the harvesting can be changed from once per year to once per two years. As a result, the kelp older than one year can be several meters long, which could provide more favorable wave attenuation. One recommend

strategy is to harvest every other longline every other year. However, the kelp may get biofouled and ragged through the summer months that may impact the quality of the harvest. Thus, efforts can be paid to explore the methods to remove the biofouling or explore other seaweed species that can grow throughout the year without detrimental effects to the quality of the product.

Compared to cultivated kelp, the wave attenuation capacity of seagrass is less impacted by seasonality. Due to large canopy density, seagrass in shallow water showed considerable wave attenuation for long waves. Zhu et al. (2020a) demonstrated the advantages of suspended aquaculture structures to damp shorter waves over seagrass and proposed that implementing suspended aquaculture structures offshore could improve the wave attenuation capacity of seagrass for a wider ranges of wave periods and water levels. Therefore, planting seagrass nearshore and cultivating seaweed offshore is an attractive alternative for coastal protection.

4.5. Summary

In this study, an analytical wave attenuation model that resolves blade motion was developed by linearizing the blade motion. To compensate for the linearization-induced underestimation in wave attenuation, a factor $\alpha_N = 1.63$ fitted from the comparisons between the analytical linear solutions and numerical nonlinear solutions was used to improve the analytical model. Compared with a wide range of experiments for both suspended and submerged flexible canopies with $kh = 0.44\sim2.7$, $l/h = 0.25\sim0.8$, $KC = 0.22\sim138$, $Ca = 35\sim13930$, and $L = 2\sim284$, the analytical model showed good agreement with the experimental data with NRMSE=0.05 and underestimation of 10%. With the analytical model, the analytical solutions for bulk drag coefficient (C_D) and effective blade length (l_e) are derived. The analytical solutions for C_D and l_e showed similar precision with the experimentally fitted C_D and l_e. Therefore, the analytical solutions are an effective way to obtain these values. A case study showed the wave attenuation of *S. latissima* is impacted by growth age. Only large kelp blade provide considerable wave attenuation. To keep the considerable wave attenuation around the year, the kelp harvesting should be postponed or changed to once per two years rather than annually. In this study, the effects of background currents are not considered, which likely significant impacts on blade posture and wave attenuation. Therefore, a natural

extension of this work should focus on incorporating the effects of currents on blade motion in the analytical model.

4.6. Acknowledgments

This work was completed as part of the PhD research of Longhuan Zhu who is supported by National Science Foundation award #IIA-1355457 to Maine EPSCoR at the University of Maine.

CHAPTER 5

AQUACULTURE FARMS AS NATURE-BASED COASTAL PROTECTION: RANDOM WAVE ATTENUATION BY SUSPENDED AND SUBMERGED CANOPIES[2]

5.1. Background

Approximately 40% of the world's population lives within 100 kilometers of the coast (MEA, 2005; Ferrario et al., 2014), and 71% of the coastal population lives within 50 kilometers of an estuary (UNEP, 2006). While coastal communities benefit from proximity to seascapes, they are more vulnerable to natural coastal hazards and extreme events from the sea. For example, from 1900 to 2017, 197 hurricanes with 206 landfalls in the USA caused about 2 trillion USD damage (normalized to 2018 value by considering the effects of inflation, wealth, and population), or annually about 17 billion USD (Weinkle et al., 2018). Due to climate change, more frequent and severe storms and rising sea level are likely to occur (Izaguirre et al., 2011; Tebaldi et al., 2012; Ondiviela et al., 2014).

To mitigate storm damage, hard structures such as seawalls, breakwaters, and bulkheads have been used as coastal defenses. These structures, however, may aggravate land subsidence due to soil drainage, inhibit natural accumulation of sediments by tides and waves, adversely impact water quality, and cause coastal habitat loss (Syvitski et al., 2009; Currin et al., 2010; Pace, 2011; Temmerman et al., 2013; SuttonGrier et al., 2015). Additionally, these conventional hard engineering defenses are also seriously challenged due to their continual and costly maintenance, as well as their reconstruction and reinforcement to keep up with increasing flood risk are becoming unsustainable (Temmerman et al., 2013). Natural and nature-based infrastructure may be a viable alternative to hardened shoreline protection system with added economic and ecological benefits and ability to adapt to sea level rise and climate change (Borsje et al., 2011; Gedan et al., 2011; Temmerman et al., 2013).

[2] Zhu, L., Huguenard, K., Zou, Q., Fredriksson, D. W., & Xie, D. (2020). Aquaculture farms as nature-based coastal protection: Random wave attenuation by suspended and submerged canopies. Coastal Engineering, 103737. https://doi.org/10.1016/j.coastaleng.2020.103737

As an example of nature-based infrastructure, living shorelines including a variety of wetland plants, aquatic vegetation, kelp beds and oyster reefs have become a complement to hardened shoreline stabilization. Unlike many hardened coastal protection techniques, living shorelines can mitigate storm damage and erosion while enhancing productive habitat, improving water quality, producing food and adapting to rising sea level (Currin et al., 2010; Scyphers et al., 2011; Davis et al., 2015; Bilkovic et al., 2016; Gittman et al., 2016; Saleh and Weinstein, 2016; Vuik et al., 2016; Moosavi, 2017; Leonardi et al., 2018; Möller, 2019). The protection of coastal ecosystems by wave attenuation is more effective in areas with relatively small tidal ranges (Bouma et al., 2014). Living shorelines at exposed, high-energy sites require structure such as breakwater or sill offshore to damp incident wave energy to sustain health growth of the living organisms (McGehee, 2016).

Aquaculture systems may also act as nature-based infrastructure to attenuate wave energy and produce food at the same time. For example, Plew et al. (2005) observed that a 650 m × 2450 m mussel farm reduced wave energy by approximately 5%, 10%, and 17% at wave frequencies of 0.1, 0.2, and 0.25 Hz, respectively at low sea state. It was found that densely grown kelp may have advantageous wave attenuation characteristics (Mork, 1996). For instance, Mork (1996) observed a 70% to 85% wave energy reduction across a 258 m long kelp bed (dominated by *Laminaria hyperborea*) with the highest wave attenuation observed during low tide. Unlike the natural kelp beds rooted at the seabed, cultivated kelp is suspended near the surface from a longline (Peteiro and Freire, 2013; Peteiro et al., 2016; Walls et al., 2017; Campbell et al., 2019; Grebe et al., 2019; Zhu et al., 2019), as shown on Figure 5.1. Near surface cultivated kelp may damp more wave energy than bottom-rooted kelp since the wave motion decreases towards the bottom. Kelp can also absorb carbon to mitigate climate change impacts and reduce nutrients to improve water quality, therefore, increase the growth rate of marine species (Duarte et al., 2017; Campbell et al., 2019). Other environmental benefits of kelp and seaweed farming include recycling inorganic nutrients and preventing eutrophication conditions (Yang et al., 2015; Stévant et al., 2017; Xiao et al., 2017; Campbell et al., 2019).

Both mussels and kelp are often farmed near the surface on a horizontal type mooring system (Figure 5.1). The wave attenuation characteristics of these aquaculture farms can be modeled in a similar way as natural, bottom-rooted submerged and emergent canopies such as kelp forests, seagrasses and salt marshes. In this study, the aquaculture structures are treated as suspended canopies according to the classification shown on Figure 5.1. The classification is based on the vertical position in the water column and the ‘‘plant’’ height relative to the water depth (e.g., Plew, 2011; Huai et al., 2012; Chen et al., 2016; Zhu and Zou, 2017). The horizontal mussel and kelp farms shown on Figure 5.1 are placed at an elevation with optimum light, temperature and nutrient conditions within the water column to achieve maximum growth. Figure 5.1 also shows a row of nature-based floating wetlands and natural submerged and emergent plants.

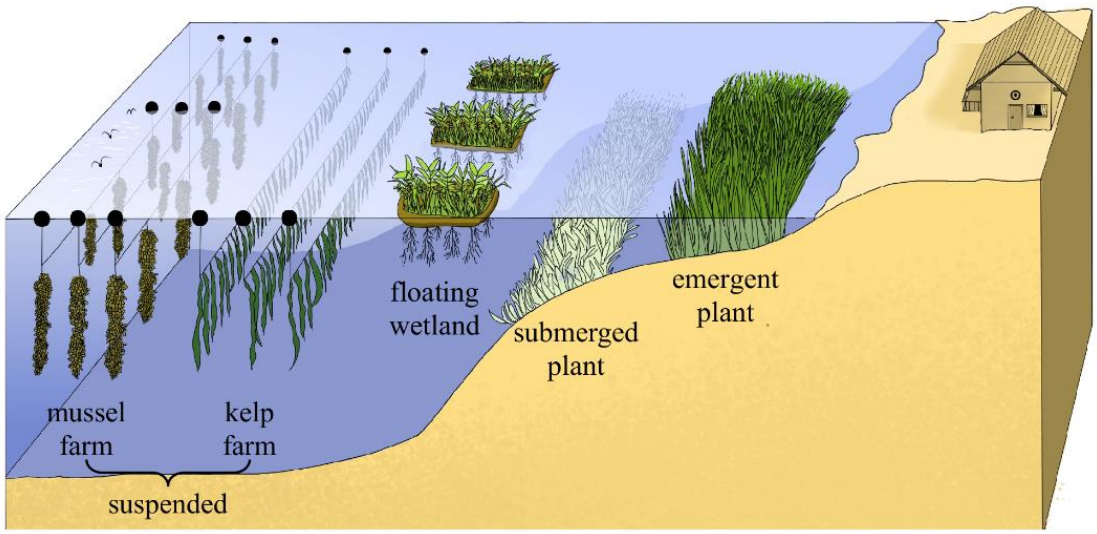

Figure 5.1. Canopy classification (from left to right): suspended aquaculture farms, floating wetlands, submerged plants, and emergent plants (figure credit: Yu-Ying Chen).

Extensive studies have been dedicated to better understanding and predicting wave attenuation by submerged and emergent vegetation as reviewed later in Section 5.2.1. To model the wave attenuation by suspended canopies, Plew et al. (2005) developed a two-layer analytical solution for a floating longline mussel farm based on energy conservation equation with linear wave theory (Dalrymple et al., 1984). They

represented random wave conditions using root-mean square wave height and peak wave period. Zhu and Zou (2017) extended the two-layer solution by Kobayashi et al. (1993) for submerged vegetation to a generalized three-layer theoretical solution for suspended and submerged vegetation. Zhu and Zou (2017) found that the wave attenuation by a submerged canopy decreases while the wave attenuation by a floating canopy increases with increasing wave frequency. The wave attenuation by a suspended canopy first increases and then decreases with increasing wave frequency. Combining an OpenFOAM (Higuera et al., 2013) hydrodynamics model with an immersed element vegetation model, Chen and Zou (2019) observed a strong jet formed at the top of a submerged flexible canopy in the opposite direction as the wave. Using a SWASH (Simulating WAves till SHore, Zijlema et al., 2011) model, Chen et al. (2019) investigated the wave-driven circulation cell induced by suspended canopies and found that the vertical position of the canopy also has significant effects on the wave-driven current in the canopy. Recently, SWASH was improved by Suzuki et al. (2019) to consider the drag of horizontal vegetation stems, vegetation canopy porosity and vegetation inertia, which can influence the wave dissipation. The effects of vegetation porosity on wave dissipation is of importance for dense vegetation. As time domain numerical models, OpenFOAM and SWASH are able to simulate waves with arbitrary frequency shape. However, the existing analytical models developed for suspended canopies in single characteristic frequency waves still need to be extended to frequency dependent models for random waves, which are a better representation of field conditions.

The objective of this study is to develop a generalized three-layer frequency dependent theoretical model for random wave attenuation by submerged and suspended canopies. The analytical wave attenuation model is coupled with cantilever-beam and buoy-on-rope vegetation models to consider the motion of canopies with different type components. The coupled flow and vegetation model is validated with laboratory experimental datasets for submerged canopies (Jacobsen et al., 2019a) and laboratory and field datasets for suspended canopies (Seymour and Hanes, 1979). The validated coupled model is then applied in the field near Saco, Maine in the Northeastern USA to investigate the potential of a mussel farm to damp storm during the January 2015 North American blizzard. The effectiveness of using a suspended

aquaculture farm alone and in combination with submerged aquatic vegetation (SAV) close to shore for wave attenuation is also investigated.

5.2. Theory

5.2.1. Background on analytical wave attenuation models

Theoretical models have been developed to study the wave attenuation characteristics of submerged and emergent canopies by Dalrymple et al. (1984) and Kobayashi et al. (1993). Both studies represented the canopy as arrays of rigid, homogeneous cylinders subject to monochromatic wave action. Assuming the wave energy loss as the work performed by the drag of vegetation, Dalrymple et al. (1984) obtained the wave decay coefficient by solving the energy conservation equation using linear wave theory. By solving the linearized incompressible Euler equations with assumptions of exponentially decayed wave height along the canopy and linearized drag, Kobayashi et al. (1993) obtained the same wave decay coefficient as Dalrymple et al. (1984). The wave decay coefficient is an explicit function of hydrodynamic conditions and canopy characteristics including blade length, width, and canopy density (defined as blade number per unit area).

Both these analytical solutions have been widely used for calculating wave attenuation by submerged vegetation. The solution by Dalrymple et al. (1984) was modified by Mendez and Losada (2004) to consider random non-breaking and breaking waves propagating over a mildly sloped vegetation seabed by using the unmodified Raleigh distribution method and assuming a narrow-banded wave spectrum. The modification developed by Mendez and Losada (2004) has been implemented in the SWAN (Simulating WAves Nearshore) model by Suzuki et al. (2012), and the MDO (Mellor-Donelan-Oey) wave model for wind-generated waves and swells in deep and shallow waters by Marsooli et al. (2017). Recently, Losada et al. (2016) extended Mendez and Losada (2004) solution for combined wave and currents. The solution by Mendez and Losada (2004) was also used by Garzon et al. (2019) to analyze the wave attenuation by Spartina Saltmarshes in the Chesapeake Bay under storm surge conditions. These models based on the Mendez and Losada (2004) approach are limited to ideal narrowbanded waves. If applied to wide-banded waves, the Mendez and Losada (2004) based models would overestimate the dissipation for the wave

components with higher frequency than the characteristic peak frequency and underestimate the dissipation for the wave components with lower frequency than the characteristic peak frequency (Jacobsen et al., 2019a).

To investigate the spectral distribution of energy dissipation, Chen and Zhao (2012) developed two analytical frequency dependent wave attenuation models for random waves and rigid vegetation by implementing the energy dissipation of random waves in Hasselmann and Collins (1968) and the joint distribution of wave heights and wave periods proposed by Longuet-Higgins (1983). To derive the wave attenuation solution based on the random waves in Hasselmann and Collins (1968), Chen and Zhao (2012) used the root mean square velocity to linearize the drag force following Madsen et al. (1988) such that $|u| \approx \sqrt{2}\sigma_u$, where σ_u is the horizontal wave velocity and σ_u is the standard deviation of u. Recently, Jacobsen et al. (2019a) obtained a frequency distributed wave dissipation model by linearizing the drag force such that $|u| \approx \sqrt{8/\pi}\sigma_u$ estimated from 270,000 numerical cases under JONSWAP spectrum so the linearization-induced mean error $\left||u|/\left(\sqrt{8/\pi}\sigma_u\right) - 1\right|$ is less than 0.01%. Borgman (1967) obtained the same result $|u| \approx \sqrt{8/\pi}\sigma_u$ by minimizing the mean square of the difference between the nonlinear drag and linearized drag for u in normal distribution. The Borgman (1967) method for the drag linearization can also be used for other probability distributions of u.

Since most vegetation are flexible, the wave-induced motion of vegetation would reduce the relative velocity between wave-induced flow and vegetation and therefore the drag force, yielding less wave attenuation than rigid vegetation (Mullarney and Henderson, 2010; van Veelen et al., 2020). To consider the effects of vegetation motion, one common practice is using a reduced bulk drag coefficient (e.g., Paul and Amos, 2011; Jadhav et al., 2013; Pinsky et al., 2013; Anderson and Smith, 2014; Hu et al., 2014; Zeller et al., 2014; Möller et al., 2014; Losada et al., 2016; Wu et al., 2016; Marsooli et al., 2017; Nowacki et al., 2017; Garzon et al., 2019; van Veelen et al., 2020). The bulk drag coefficient should be dependent on the Cauchy number (C_a) incorporating the blade flexural rigidity related to vegetation motion. However, most of the empirical formulas in literature for the bulk drag coefficient of flexible vegetation are expressed as a

function of Reynolds number (R_e) or Keulegan–Carpenter number (KC) without incorporating the blade flexural rigidity. Consequently, the empirical formulas of bulk drag coefficient have different expressions for vegetation with different flexural rigidities for the same set of R_e and KC numbers. This introduces uncertainty in modeling wave attenuation by flexible vegetation. To apply the original (unreduced) drag coefficient as previous studies and incorporate the effects of blade motion at the same time, Luhar et al. (2017) proposed a reduced, effective blade length instead of a reduced drag coefficient to incorporate the effects of blade motion. The empirical formula for the effective blade length is dependent on blade flexural rigidity, therefore, can be readily applied to vegetation of various flexural rigidities. The formula for the effective blade length was recently modified by considering the effects of rigid sheath of seagrass (Lei and Nepf, 2019b) and applied to combined waves and currents conditions (Lei and Nepf, 2019a). These empirical approaches do not need to resolve blade motion and therefore improve the computational efficiency by reducing the iterative computation for coupling wave and vegetation motion. These approaches, however, require numerous datasets to derive the formulas for bulk drag coefficient and effective blade length. If the blade motion is directly resolved by the model, then the original unreduced drag coefficient and blade length can be used directly without modification. Therefore, the number of experiments and model runs to calibrate the bulk drag coefficient and the uncertainty associate with the bulk drag coefficient are reduced.

To resolve the blade motion, Asano et al. (1992) simplified the blade motion as an oscillator with one degree of freedom by assuming blade deflection is linearly distributed along the length and also averaging deflection along the length. This method was then extended to consider irregular waves, wave reflection, and evanescent modes by Méndez et al. (1999) for submerged vegetation. To analyze the depth dependence of the blade deflection as well as its effects on wave dissipation, Mullarney and Henderson (2010) modeled the blade as a continuous beam with Euler–Bernoulli techniques, where the governing equation for the blade motion is simplified as a balance between the flexural rigidity-induced restoring force and the drag force, assuming the inertia force and buoyancy are negligible. Recently, Henderson (2019) extended this model by including buoyancy but still neglected the inertia force, therefore the model is valid

only for blades with small cross sectional area. In addition, the mass of vegetation influences the natural frequency of the vegetation and further impacts the blade motion as well as the resonant conditions. To fully consider the gravity, buoyancy, structural damping, bending stiffness, virtual buoyancy, friction, drag and inertia forces, numerical models are often used to simulate the blade dynamics (e.g., Zeller et al., 2014; Zhu and Chen, 2015; Luhar and Nepf, 2016; Leclercq and de Langre, 2018; Zhu et al., 2018; Chen and Zou, 2019; Zhu et al., 2020). Recently, Zhu et al. (2020) used a cable model to capture the asymmetric ‘‘whip-like’’ blade motion and proposed mechanisms for the asymmetric blade motion in symmetric waves.

To derive a generalized wave attenuation model for suspended and submerged canopies, the water column is divided into 3 layers with model set-up in Section 5.2.2. The effects of canopy motion are incorporated by resolving the motion of individual canopy component using a cantilever-beam model or a buoy-on-rope model based on the type of the canopy component in Section 5.2.3. These two structural dynamics models consider inertia force and are therefore applicable for large diameter structure such as mussel droppers. The frequency dependent theoretical wave attenuation model incorporating canopy motion is developed in Section 5.2.4.

5.2.2. Model set-up

The mathematical approach is based on the three-layer model set-up shown on Figure 5.2. As shown on Figure 5.2, the horizontal coordinate, x, is positive in the direction of wave propagation (assumed to be perpendicular to the coast), with $x = 0$ at the leading edge of the canopy. The horizontal length of the canopy is defined as L_v such that $x = L_v$ at the end of the canopy. The vertical coordinate, z, is positive upward with $z = 0$ at the still water level (SWL).

The water column is divided into three layers with Layer 1 above the canopy, Layer 2 within the canopy, and Layer 3 below the canopy. The initial static thicknesses for each layer are denoted by d_1, d_2, d_3, respectively. The thickness of Layer 2 (d_2) also named the canopy height, is defined as the average submerged length of the canopy components. The water depth from the SWL is defined as $h = d_1 + d_2 + d_3$, where the seafloor is located at $z = -h$ and assumed to be horizontal. This generalized three-layer

model can be used to analyze the wave attenuation characteristics of the following four types of canopy configurations: (3.1) submerged ($d_1 \neq 0$ and $d_3 = 0$), (2) emergent ($d_1 = 0$ and $d_3 = 0$), (3) suspended in the water column ($d_1 \neq 0$ and $d_3 \neq 0$), and (4) floating on the surface ($d_1 = 0$ and $d_3 \neq 0$).

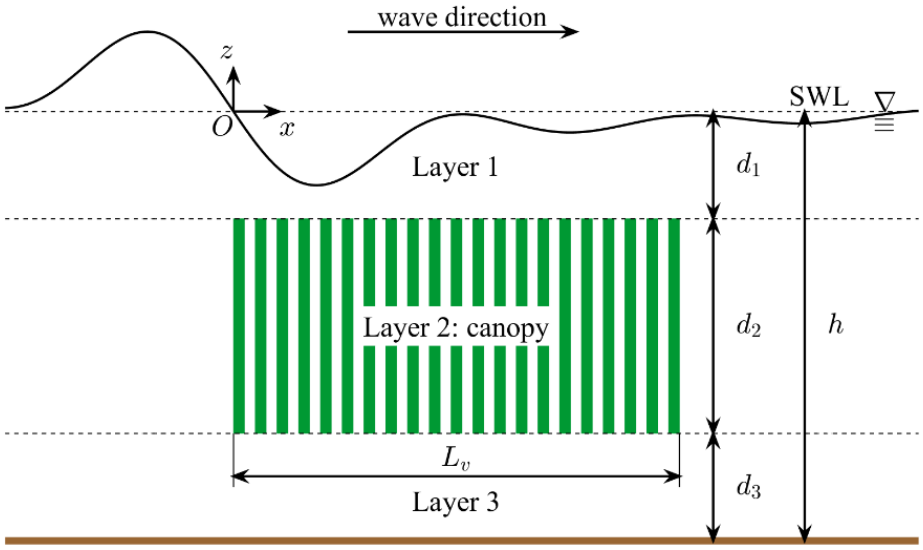

Figure 5.2. Definition sketch of variables and coordinate system for the three-layer theoretical model of waves propagating over a canopy. The coordinate system (x, z) with the origin at the leading edge of the canopy ($x = 0$) and the still water level (SWL, $z = 0$), where x is positive in the wave propagation direction from left to right and z is positive upward. The water column is divided into three layers by the canopy. The thicknesses of layer 1, 2, and 3 are denoted as d_1, d_2, and d_3, respectively. The canopy length is L_v. The water depth from the SWL is defined as $h = d_1 + d_2 + d_3$.

At many sites, sea surface profiles are better represented by random waves, which can be formulated as a superposition of monochromatic waves with a set of random phases. Thus, the water elevation can be expressed as

$$\eta = \sum_{i=1}^{\infty} a_i \cos(k_i x - \omega_i t + \psi_i), \tag{5.1}$$

where t is time, a_i is the wave amplitude, k_i is the wave number, ω_i is the angular frequency and ψ_i is the random phase of the ith monochromatic wave component. As a sum of infinite independent random variables, the water elevation tends toward a normal distribution according to the central limit theorem. Assuming that the random phase is distributed uniformly on $(0, 2\pi)$, the water elevation is normally

distributed with a zero mean ($\langle\eta\rangle = 0$, where $\langle\ \ \rangle$ indicates expected value) and a variance of $\sigma_\eta^2 = \langle\eta^2\rangle = \sum_{i=1}^{\infty} a_i^2/2 = \int_0^\infty S_{\eta\eta}(\omega, x)d\omega$, where $S_{\eta\eta}(\omega, x)$ is the wave spectrum. For the convenience of expression, the index of summation i is omitted and ω is used to indicate the summation such that

$$\eta = \sum_\omega a(kx - \omega t + \psi). \tag{5.2}$$

According to linear wave theory (Dean and Dalrymple, 1991), the wave number and angular frequency satisfy the dispersion relation, $\omega^2 = gk\tanh kh$, where g is the gravitational acceleration. The wave orbital velocity (u) at a given level z is then written as

$$u = \sum_\omega a\ \omega\Gamma\cos(kx - \omega t + \psi)\ , \tag{5.3}$$

where $\Gamma = \cosh k(h + z)\ /\ \sinh kh$ when $z \le \eta$ and $\Gamma = 0$ when $z > \eta$.

5.2.3. Models for the motion of canopy components

The wave-induced motion of a canopy component is simulated by different models depending on the morphology and physical properties of the species. In this paper, we introduce cantilever-beam and buoy-on-rope models. The cantilever-beam model is applicable for slender species such as vegetation blades, kelp blades, and mussel droppers (Figure 5.3). The buoy-on-rope model is applicable for species with concentrated mass and buoyancy supported by a tethered stipe whose mass and stiffness can be ignored, e.g., the bull kelp, *Nereocystis luetkeana* (Figure 5.3).

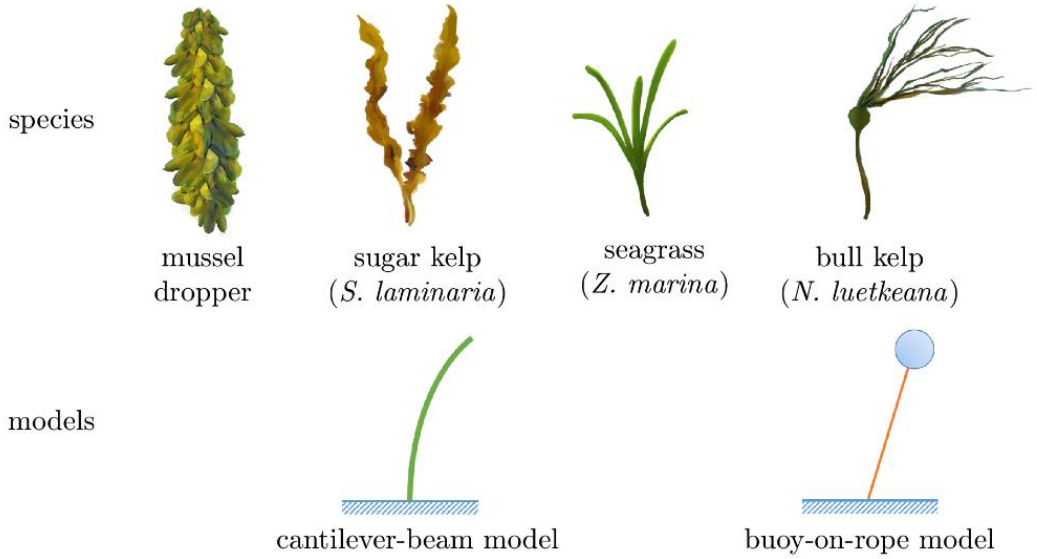

Figure 5.3. Sketch for the cantilever-beam model and buoy-on-rope model for different species.

5.2.3.1. Cantilever-beam model

The individual component of the canopies such as seagrass meadow, kelp forest and mussel farms is modeled as a slender cantilever beam (Figure 5.3), referred as a blade hereinafter. A typical blade having the averaged geometrical and physical properties of the canopy components is used to represent the canopy components. To simulate the large-amplitude deflection of a flexible blade, Zhu et al. (2020) introduced a cable model that can capture the asymmetric "whip like" motion of a flexible blade (Luhar & Nepf, 2016). To obtain the analytical solution for the horizontal displacement (ξ) of the blade, the governing equations in Zhu et al. (2020) are linearized by assuming a small-amplitude motion such that the vertical displacement of the blade is negligible. The horizontal displacement, $\xi(s,t)$ is a function of time t and the distance s along the blade length from the fixed end. The relation between the local coordinate s and the global coordinate z is given by

$$z = \begin{cases} -d_1 - d_2 + s, & \text{blade fixed at the bottom end,} \\ -d_1 - s, & \text{blade fixed at the tip end.} \end{cases} \tag{5.4}$$

Neglecting tension and buoyancy, the linearized governing equation is given by

$$\rho_v A_c \ddot{\xi} + EI\xi'''' = \rho_w A_c \dot{u} + \frac{1}{2} C_d \rho_w b \left|u - \dot{\xi}\right| \left(u - \dot{\xi}\right) + C_m \rho_w A_c \left(\dot{u} - \ddot{\xi}\right), \tag{5.5}$$

where the dot ($\dot{}$) indicates derivative with respect to t, the prime ($'$) indicates derivative with respect to s, ρ_w is the water density, ρ_v is the blade mass density, b is the projected blade width, A_c is the blade cross sectional area, E is the Young's modulus of the blade, I is second moment of the blade cross sectional area, C_d is the drag coefficient and C_m is the added mass coefficient. The terms on the right-hand side of (5.5) are virtual buoyancy, drag and added mass force per unit length modified from the Morison formula (Morison et al., 1950). To obtain an analytical solution to (5.5), the nonlinear drag $1/2 C_d \rho_w b \left|u - \dot{\xi}\right| \left(u - \dot{\xi}\right)$ is linearized as $c\left(u - \dot{\xi}\right)$, where the linearization coefficient (c) is calculated using the Borgman (1967) method. Substituting (5.3) into (5.5) yields

$$m\ddot{\xi} + c\dot{\xi} + EI\xi'''' = \sum_{\omega} a\omega\Gamma[c\cos(kx - \omega t + \psi) + \omega m_I \sin(kx - \omega t + \psi)]\,, \tag{5.6}$$

where $m = (\rho_v + C_m\rho_w)A_c$ and $m_I = (1 + C_m)\rho_w A_c$. The boundary conditions for a cantilever beam are given by $\xi(0,t) = 0$, $\xi'(0,t) = 0$, $\xi''(l,t) = 0$ and $\xi'''(l,t) = 0$. Using a normal mode approach (Rao, 2007), the solution for the blade displacement is obtained in Appendix E as

$$\xi = \sum_\omega a\Gamma[\gamma_s \sin(kx - \omega t + \psi) + \gamma_c \cos(kx - \omega t + \psi)], \tag{5.7}$$

where γ_s and γ_c are the transfer functions given by

$$\gamma_s = \frac{\omega}{\Gamma}\sum_{n=1}^{\infty} \phi_n \frac{\omega I_n(\lambda_n^2 - \omega^2) - D_n 2\zeta_n\lambda_n\omega}{(\lambda_n^2 - \omega^2)^2 + (2\zeta_n\lambda_n\omega)^2} \tag{5.8}$$

and

$$\gamma_c = \frac{\omega}{\Gamma}\sum_{n=1}^{\infty} \phi_n \frac{D_n(\lambda_n^2 - \omega^2) + \omega I_n 2\zeta_n\lambda_n\omega}{(\lambda_n^2 - \omega^2)^2 + (2\zeta_n\lambda_n\omega)^2}. \tag{5.9}$$

where $\phi_n = (\cos\mu_n l + \cosh\mu_n l)(\sin\mu_n s - \sinh\mu_n s) + (\sin\mu_n l + \sinh\mu_n l)(\cosh\mu_n s - \cos\mu_n s)$ is the nth normal mode of the cantilever beam with μ_n being the nth solution of $1 + \cos\mu l \cosh\mu l = 0$, $\lambda_n = \mu_n^2\sqrt{\int_0^l EI\phi_n^2 ds \,/\, \int_0^l m\phi_n^2 ds}$ is the n th natural frequency of the blade, $2\zeta_n\lambda_n = \int_0^l c\phi_n^2 ds \,/\, \int_0^l m\phi_n^2 ds$, $D_n = \int_0^l c\Gamma\phi_n ds \,/\, \int_0^l m\phi_n^2 ds$, and $I_n = \int_0^l m_I\Gamma\phi_n ds \,/\, \int_0^l m\phi_n^2 ds$. Since Γ is expressed in terms of z and ϕ_n is expressed in terms of s, the relation between s and z in (5.4) is required to calculate the integral $\int_0^l \Gamma\phi_n ds$.

The relative velocity of flow to blade $u_r = u - \xi$ is given by

$$u_r = \sum_\omega a\omega\Gamma[(1 + \gamma_s)\cos(kx - \omega t + \psi) + \gamma_c \sin(kx - \omega t + \psi)]. \tag{5.10}$$

According to the central limit theorem, the relative velocity also asymptotically approaches a normal distribution with zero mean ($\langle u_r\rangle = 0$) and the variance

$$\sigma_{u_r}^2 = \langle u_r^2\rangle = \int_0^\infty \omega^2\Gamma^2[(1 + \gamma_s)^2 + \gamma_c^2]S_{\eta\eta}(\omega, x)d\omega. \tag{5.11}$$

Hence, the probability density function of u_r is given by

$$p(u_r) = \frac{1}{\sigma_{u_r}\sqrt{2\pi}} e^{-\frac{u_r^2}{2\sigma_{u_r}^2}}. \tag{5.12}$$

Using the Borgman (1967) method, the linearization coefficient (c) is obtained by minimizing the mean square difference between the nonlinear and linearized drag so that $\partial \int_{-\infty}^{\infty}(1/2\, C_d\rho_w b|u_r|u_r - cu_r)^2 p(u_r)du_r\,/\partial c = 0$, yielding

$$c = \frac{1}{2}C_d\rho_w b\frac{\int_{-\infty}^{\infty}|u_r|u_r^2 p(u_r)du_r}{\int_{-\infty}^{\infty}u_r^2 p(u_r)du_r} = \frac{1}{2}C_d\rho_w b\sqrt{\frac{8}{\pi}}\sigma_{u_r}. \quad (5.13)$$

The linearization coefficient can be obtained iteratively through the following procedure. Starting from a static blade, an initial c is calculated from equation (5.13) with (5.11) by assuming $\gamma_s = 0$ and $\gamma_c = 0$. Once the blade displacement is obtained, c can be recalculated from (5.13) and (5.11) with (5.8) and (5.9). Using the new value of c, the blade displacement can be updated. The procedure is repeated until a convergent solution is achieved.

5.2.3.2. Buoy-on-rope model

The bull kelp (*Nereocystis luetkeana*) is used as an example to describe the buoy-on-rope model (Denny et al., 1997), which is also used for other species such as *Macrocystis pyrifera* (Utter and Denny, 1996). The pneumatocyst (the ball-shape "float" structure) of *Nereocystis luetkeana* is modeled as a buoy and the stipe is modeled as a rope (Figure 5.3). Therefore, the canopy component is modeled as a buoy attached to seabed by a thin, straight, non-buoyant rope. The inertia, drag and buoyancy act at the buoy center, $z_c = -d_1 - d_2/2$, where the canopy height d_2 is the diameter of the buoy. The horizontal displacement of the buoy and the fluid velocity at the buoy center is used to calculate the forces. The governing equation for buoy-on-rope model is given by

$$\rho_v V\ddot{\xi} + \frac{(\rho_w-\rho_v)Vg}{R}\xi = \rho_w V\,\dot{u}(z_c) + \frac{1}{2}C_d\rho_w A_p\left|u(z_c) - \dot{\xi}\right|\left[u(z_c) - \dot{\xi}\right] + C_m\rho_w V\left[\dot{u}(z_c) - \ddot{\xi}\right], \quad (5.14)$$

where R is the length of the tethered rope, V is the volume of the buoy with projected area of A_p. Similarly, the nonlinear drag force $1/2C_d\rho_w A_p\left|u(z_c) - \dot{\xi}\right|\left[u(z_c) - \dot{\xi}\right]$ is linearized as $C\left[u(z_c) - \dot{\xi}\right]$, where C is obtained using the Borgman (1967) method. Substituting (5.3) into (5.14) yields

$$M\,\ddot{\xi} + C\,\dot{\xi} + K\xi = \sum_\omega a\omega\Gamma(z_c)[C\cos(kx - \omega t + \psi) + \omega M_I\sin(kx - \omega t + \psi)], \quad (5.15)$$

where $M = (\rho_v + C_m\rho_w)V$, $K = (\rho_w - \rho_v)Vg/R$, and $M_I = (1 + C_m)\rho_w V$. The solution for (5.15) is

$$\xi = \sum_{\omega} a\Gamma[\gamma_s \sin(kx - \omega t + \psi) + \gamma_c \cos(kx - \omega t + \psi)], \tag{5.16}$$

where γ_s and γ_c are the transfer functions given by

$$\gamma_s = \frac{\Gamma(z_c)\omega}{\Gamma M} \frac{\omega M_I(\lambda^2 - \omega^2) - C(2\zeta\lambda\omega)}{(\lambda^2 - \omega^2)^2 + (2\zeta\lambda\omega)^2} \tag{5.17}$$

and

$$\gamma_c = \frac{\Gamma(z_c)\omega}{\Gamma M} \frac{C(\lambda^2 - \omega^2) + \omega M_I(2\zeta\lambda\omega)}{(\lambda^2 - \omega^2)^2 + (2\zeta\lambda\omega)^2}, \tag{5.18}$$

where $\lambda = \sqrt{K/M}$ and $2\zeta\lambda = C/M$. Similarly, the relative velocity $u_r = u - \dot{\xi}$ asymptotically approaches a normal distribution with zero mean and the variance $\sigma_{u_r}^2$ in a similar expression as (5.11) except for the transfer functions γ_s and γ_c, which are calculated using (5.17) and (5.18). Thus, the linearization coefficient (C) is given by

$$C = \frac{1}{2} C_d \rho_w A_p \sqrt{\frac{8}{\pi}} \sigma_{u_r}, \tag{5.19}$$

which is obtained iteratively using the same procedure for the cantilever-beam model.

5.2.4. Solutions for random wave attenuation

Following Dalrymple et al. (1984), Kobayashi et al. (1993), and Mendez and Losada (2004), the wave attenuation is assumed to come from the work of the canopy-induced drag force. The inertia force has a negligible contribution to wave attenuation since the mathematical expectation of the work due to the inertia force is zero because the relative acceleration and the relative velocity are out of phase in linear waves. The vertical frictional force is assumed negligible when compared with the horizontal drag force. The wave reflection from the canopy is also assumed negligible since the wave reflection has limited contributions to the wave attenuation for both submerged vegetation (Mendez and Losada, 2004) and suspended canopies (Seymour and Hanes, 1979). Some wave energy is converted into the kinematic and potential energy of the canopy at the beginning. However, once the canopy motion becomes steady, the energy needed to maintain the steady motion can be assumed negligible because the structural damping of the canopy components is negligible (Asano et al., 1992; Méndez et al., 1999). Lacking data, the velocity reduction in the canopy (Lowe, 2005), the sheltering effects (Raupach and Thom, 1981; Abdelrhman, 2007;

Etminan et al., 2019), and the porosity effects (Mei et al., 2011; Nepf, 2011; Liu et al., 2015; Arnaud et al., 2017; Suzuki et al., 2019) are not considered. Using the linearized drag force, the energy conservation equation can be written as

$$\frac{\partial}{\partial x}\int_0^\infty \rho_w g S_{\eta\eta}(\omega,x) c_g d\omega = -\int_{-d_1-d_2}^{-d_1} \langle N \frac{1}{2} C_d \rho_w b \sqrt{\frac{8}{\pi}} \sigma_{u_r} u_r^2 \rangle \, dz, \tag{5.20}$$

where $c_g = (\omega/k)(1 + 2kh/\sinh 2kh)/2$ is the group velocity and N is the number of canopy components per unit horizontal area (also referred to as the canopy density). Substituting (5.11) into (5.20) yields the transmitted wave spectrum at distance x in relation to the incident wave spectrum at $x = 0$,

$$S_{\eta\eta}(\omega,x) = S_{\eta\eta}(\omega,0) e^{-2\beta(\omega)x}, \tag{5.21}$$

where the frequency dependent decay coefficient (β) is given by

$$\beta(\omega) = \frac{2\sqrt{2}Nk^2 \sinh^2 kh}{\sqrt{\pi}\omega(2kh+\sinh 2kh)} \int_{-d_1-d_2}^{-d_1} C_d b \sigma_{u_r} \Gamma^2 [(1+\gamma_s)^2 + \gamma_c^2] dz. \tag{5.22}$$

The transfer functions γ_s and γ_c are selected based on the structural dynamics model used for the canopy motion. To evaluate the effect of the canopies on wave attenuation, the wave spectral dissipation ratio (SDR) and wave energy dissipation ratio (EDR) are used and defined as

$$SDR = 1 - \frac{S_{\eta\eta}(\omega,L_v)}{S_{\eta\eta}(\omega,0)} \tag{5.23}$$

and

$$EDR = 1 - \frac{\int_0^\infty S_{\eta\eta}(\omega,L_v) d\omega}{\int_0^\infty S_{\eta\eta}(\omega,0) d\omega}, \tag{5.24}$$

respectively.

5.3. Model-data comparison

5.3.1. Submerged canopy

The model results were first compared with the laboratory experiments by Jacobsen et al. (2019a) for a submerged canopy consisting of artificial vegetation. The wave conditions were based on a single peaked JONSWAP spectrum with a peak enhancement factor $\gamma = 3.3$ and peak wave period $T_p = 1.15$ s.

The incident significant wave height at the leading edge of the canopy was $H_{s0} = 3.7$ cm. The water depth was $h = 0.685$ m.

The artificial vegetation was made of 4 mm-wide polypropylene blades with $\rho_v \approx 920$ kg/m^3 and $E \approx 0.3$ GPa (Ghisalberti & Nepf, 2002). Four blades were taped to a 6 mm-diameter PVC dowel and 60 mm above the bed. The canopy was 7.5 m long with a density of 566 dowels/m^2 therefore 2264 blades/m^2. The blade length was 20, 40, and 60 cm such that $d_2/h = \{0.38, 0.67, 0.96\}$. The blade thickness was 0.12, 0.2, 0.5 and 1.0 mm for the 20 cm-long blade and 0.5 mm for the other blades. More details of the experiments can be found in Jacobsen et al. (2019a).

Based on the datasets for rigid flat plates in oscillatory flows (Keulegan and Carpenter, 1958; Sarpkaya and O'Keefe, 1996) with $1.7 \leq KC \leq 118.2$, Luhar and Nepf (2016) derived the drag coefficient and added mass coefficient,

$$C_d = \max\left(10KC^{-1/3}, 1.95\right) \tag{5.25}$$

and

$$C_m = \min(C_{m1}, C_{m2}), \tag{5.26}$$

respectively, where $C_{m1} = \begin{cases} 1 + 0.35KC^{2/3}, & KC < 20 \\ 1 + 0.15KC^{2/3}, & KC \geq 20 \end{cases}$ and $C_{m2} = 1 + (KC - 18)^2/49$ as described in Luhar (2012). Equations (5.25) amd (5.26) are robust in calculating the hydrodynamic forces acting on flexible blades in regular waves (Zhu et al., 2020). To apply (5.25) amd (5.26) to random waves, the KC number is calculated using the significant relative velocity ($2\sigma_{u_r}$) as $KC = 2\sigma_{u_r}T_p/b$.

The vegetation blade is modeled as a cantilever beam so that the wave attenuation model incorporating the cantilever beam model is used to calculate the wave decay coefficient, β. The model results using frequency dependent C_d and C_m in (5.25) amd (5.26) as well as constant $C_d = 1.95$ and $C_m = 1$ are compared with the datasets of Jacobsen et al. (2019a) on Figure 5.4. It is noted that $C_d = 1.95$ is the minimum drag coefficient for (5.25).

The model results are in a good agreement with the data with the root-mean-square-error (RMSE) of about 0.002 for the 20 cm-long blades ($l/h = 0.38$) with thickness $d \leq 0.5$ mm (Figure 5.4a-c). For the

thickest blades with $d = 1$ mm, the decay coefficient is slightly overestimated for the lower frequency wave components ($f < 0.8$ Hz) resulting in a larger RMSE of 0.0032 (Figure 5.4d). One possible reason is that the drag coefficient calculated using equation (5.25) might be overestimated for the thicker blades whose thickness-width ratio has reached 0.25 and much larger than the thickness-width ratio (< 0.1) of the experimental plates for the formula (5.25). The thicker blades are expected to have a smaller drag coefficient due to increased Reynolds number. Thus, the model results can be improved by using a smaller drag coefficient. For instance, the RMSE for the 1 mm-thick blades is reduced to 0.0016 by using $C_d = 1.95$ (Figure 5.4d).

For the longer blades that are nearly emergent ($l/h \geq 0.67$), the model results calculated with frequency dependent hydrodynamic coefficients underestimate the observation with RMSE=0.0046 and 0.0073 for $l = 40$ cm ($l/h = 0.67$) and 60 cm ($l/h = 0.96$), respectively, as shown on Figure 5.4(e and f) possibly due to the simplification of the cantilever beam model. Neglecting the large deflection-induced geometrical non-linearity, net buoyancy, and the net buoyancy-induced tension would underestimate the restoring capacity of the blades. Thus, the simplified model may overestimate the blade motion resulting in a smaller wave attenuation. This underestimation of wave attenuation is more obvious for longer blades because the effects of the large deflection-induced geometrical non-linearity, the net buoyancy and the net buoyancy-induced tension are more significant for longer blades. Compared to the shorter blade ($l = 20$ cm), the longer blade ($l \geq 40$ cm) is more flexible, therefore, the blade motion follows the flow more closely so that the relative velocity between the longer blade and flow is smaller, resulting in a larger C_d. Therefore, using a smaller $C_d = 1.95$ enhances the underestimation as indicated by RMSE=0.0055 and 0.0177 for the $l = 40$ cm ($l/h = 0.67$) and 60 cm ($l/h = 0.96$), respectively on Figure 5.4(e and f). A more precise formula for the hydrodynamic coefficients in random waves is desired for the nearly emergent canopies with $l/h \geq 0.67$. However, the hydrodynamic coefficients in (5.25) and (5.26) as well as the constant hydrodynamic coefficients work well for the submerged vegetation ($l/h \leq 0.38$) with a small RMSE of about 0.002.

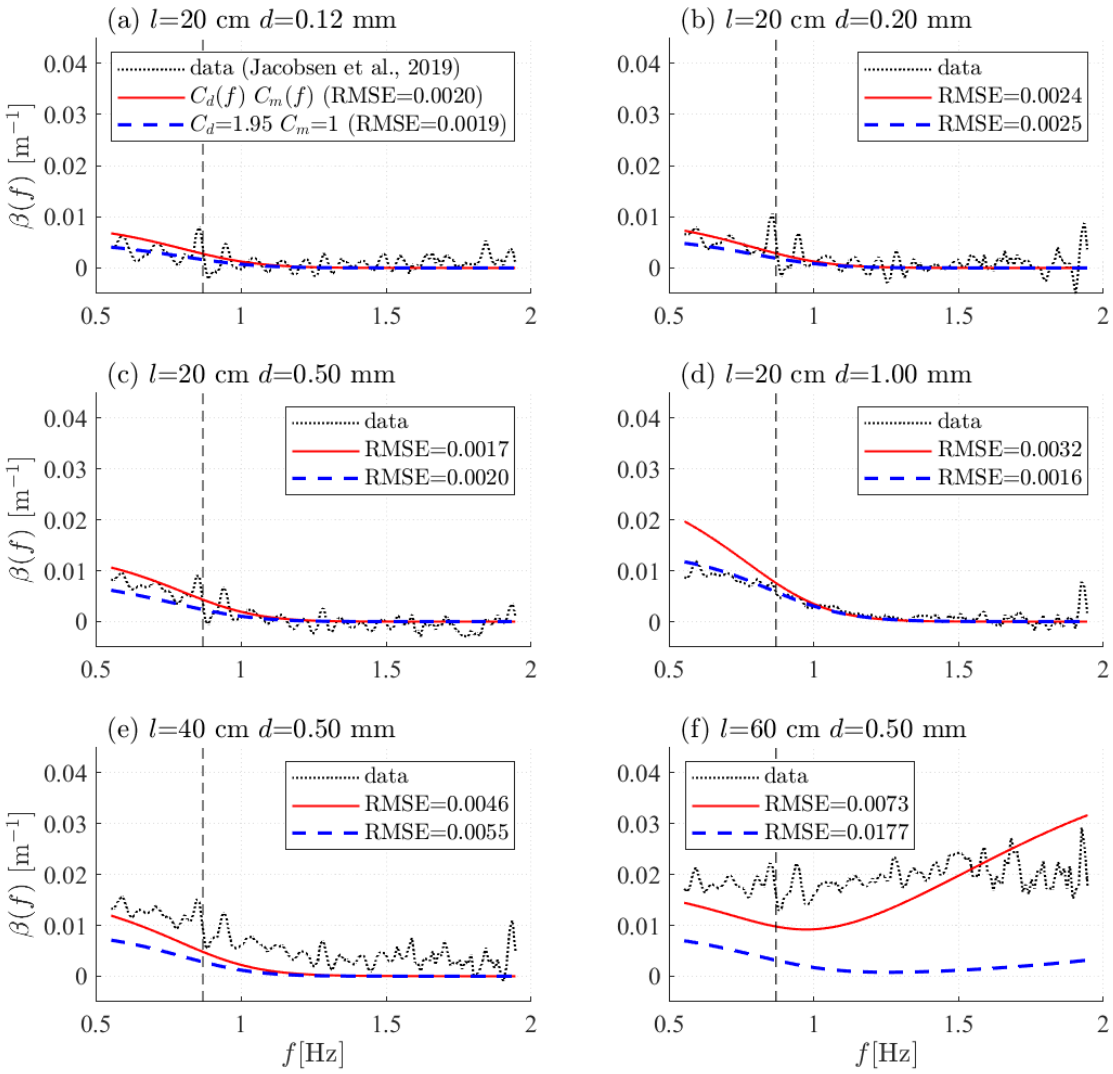

Figure 5.4. Comparisons of calculated frequency (f) dependent wave decay coefficient (β) by the present model and the data (black dotted lines) from Jacobsen et al. (2019a). The model results using frequency dependent and constant drag coefficient (C_d) and added mass coefficient (C_m) are denoted by red solid and blue dashed lines, respectively. The submerged canopies with blade lengths (l) of 20, 40 and 60 cm and thicknesses (d) of 0.12, 0.20, 0.5 and 1.0 mm are subjected to random waves of JONSWAP spectrum with peak enhancement factor $\gamma = 3.3$, peak wave period $T_p = 1.15$ s (vertical dashed black line) and incident significant wave height of 3.7 cm at a water depth $h = 0.685$ m with normalized blade length (l/h) of 0.38 (a-d), 0.67 (e) and 0.96 (f). The canopy density is 566 shoots/m^2 (2264 blades/m^2).

5.3.2. Suspended canopy

The model results were also compared with the laboratory and field experiments by Seymour and Hanes (1979) for a suspended canopy consisting of spherical buoys. The field experiments for a suspended canopy consisting of arrays of tethered sphere buoys (Figure 5.5) were conducted in San Diego Bay, California, USA. The half-scale model tests for the field experiments were conducted in the 40-m long Wind Wave Channel at the Hydraulics Laboratory of Scripps Institution of Oceanography (Seymour and Hanes, 1979). The properties of the canopies in the laboratory and field experiments are shown in Table 5.1.

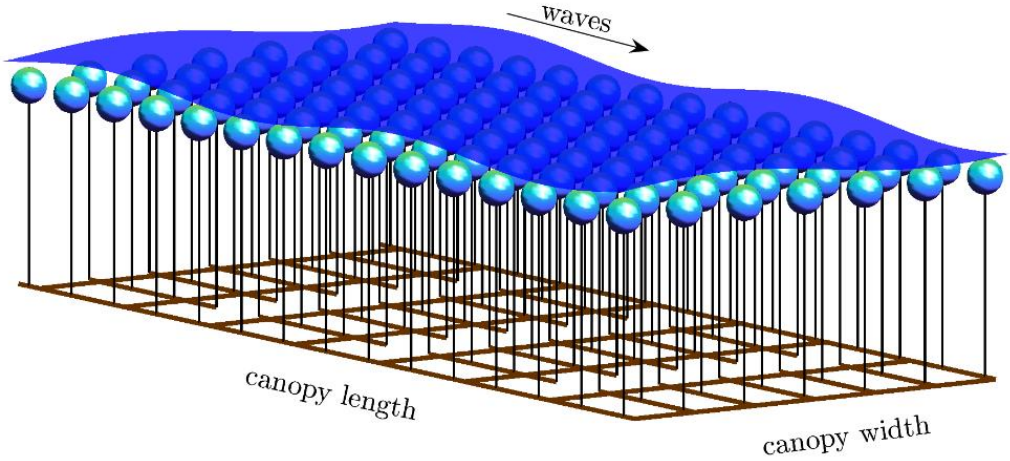

Figure 5.5. Sketch of the suspended canopy consisting of sphere components according to the description of Seymour and Hanes (1979).

For the laboratory experiments, the incident significant wave height was 0.069-0.176 m and the peak frequency was 0.19-0.883 Hz. For the field experiments, two storms were observed on Jan 22, 1976 and Feb 9, 1976. The measured significant wave height was 0.17 - 0.44 m. The drag coefficient and added mass coefficient for the tethered spheres are assumed as $C_d = 0.5$ and $C_m = 0.5$, respectively.

The calculated transmitted wave spectrum and spectral dissipation ratio (SDR) are shown on Figure 5.6. The calculated transmitted wave spectrum follows the shape of the incident wave spectrum. The SDR for the suspended canopy first increases and then decreases with increasing wave spectrum as expected.

Table 5.1. Properties for the suspended canopies consisting of sphere components in the laboratory and field experiments (Seymour and Hanes, 1979).

	In the lab (half scale)	In the field (full scale)
Sphere mass density [kg/m^3]	40	85
Sphere diameter [cm]	15.8	29.2
Depth of sphere center [cm]	7.36-15.24	21.9
Effective tether length [cm]	83.8	168.0
Sphere spacing (along canopy length) [cm]	31.6	58.41
Sphere spacing (along canopy width) [cm]	31.6	58.41
Canopy width (perpendicular to wave direction) [m]	2.39	46
Canopy length (along wave direction) [m]	23	6
Water depth [m]	1.78	8

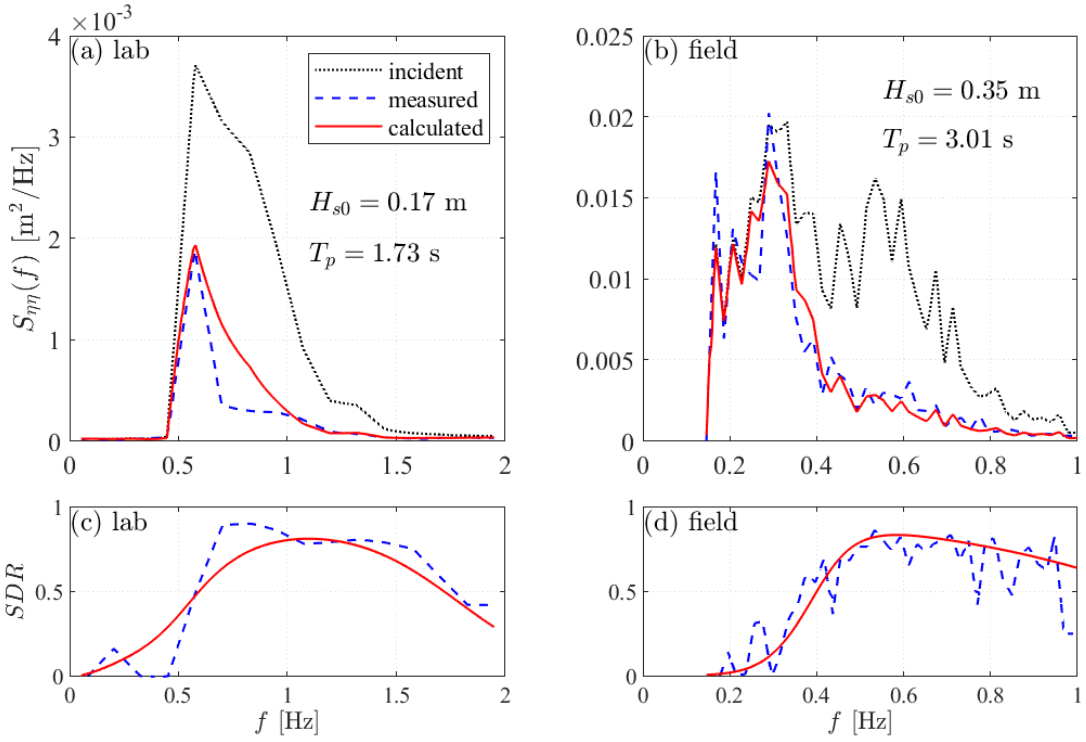

Figure 5.6. Comparisons between calculated and measured transmitted wave spectrum ($S_{\eta\eta}$) as well as spectral dissipation ratio (SDR) versus wave frequency (f) for suspended canopies with spheres in (a) laboratory and (b) field experiments by Seymour and Hanes (1979). The incident significant wave height is H_{s0} and the peak period is T_p.

The comparison between the calculated and measured energy dissipation ratio (EDR) is shown on Figure 5.7. Good agreement (RMSE=0.073) between model and data indicates that the present generalized analytical solutions are also applicable to suspended aquaculture farms with simple structures in other forms, such as cylinders, as long as the appropriate hydrodynamic coefficients are available.

5.4. Case study at the field site

The present frequency dependent theoretical model is now applied to analyze the wave attenuation capacity of suspended aquaculture farms at a field site and compared with that of submerged aquatic vegetation, as well as a combination of these two nature-based shore protection schemes.

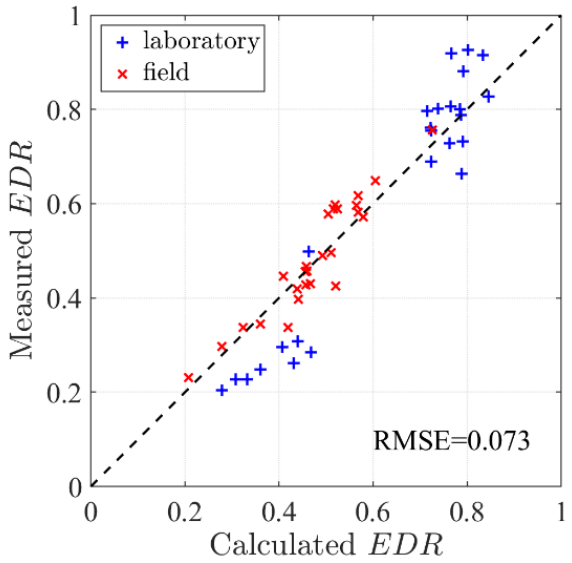

Figure 5.7. Comparisons between the calculated and measured wave energy dissipation ratio (EDR) for laboratory (blue +) and field experiments (red \times) by Seymour and Hanes (1979).

The study site ($42°28'2''$ N, $70°21'2''$ W) is located at Saco Bay, Maine, USA as shown on Figure 5.8 with a water depth of about 10.6 m. The January 2015 North American blizzard was a powerful and destructive extratropical storm that swept across the Saco Bay and along the coast of the Northeastern United States in January of 2015. To assess coastal flood risk and sea level rise effects during this storm event, Xie et al. (2019) constructed an integrated atmosphere-ocean-coast and overtopping-drainage modeling framework based on the coupled tide, surge and wave model, SWAN+ADCIRC. The wave

spectrum and water level conditions output from the SWAN+ADCIRC model (Xie et al., 2019) are used to drive the present theoretical model. The canopies are oriented to be parallel to the dominant wave direction so that the present 1-D solutions can be applied.

5.4.1. Properties for the mussel farm and submerged aquatic vegetation

The mussel farm is simplified as arrays of cylinders which represent the mussel droppers. The cylinders have similar mechanical and hydrodynamic performances to the actual droppers. In this study, the geometric and physical properties of the cylinders are based on the measurements of the live droppers at the University of New Hampshire nearshore multi-trophic aquaculture site in the Gulf of Maine, USA (Knysh et al., 2019). The measured dropper diameter was 0.13 m, mass per unit length was 7.53 kg/m, and flexural rigidity was 0.79 N/m^2 on July 3 (Knysh et al., 2019), which was about 160 days (years are not considered) after the January 2015 North American blizzard arrived at the study site. The geometrical properties of the droppers in January were estimated by assuming a growth rate of 7.5% per 40 days (Lauzon-Guay et al., 2006; Gagnon and Bergeron, 2017), which indicates that the diameter of the mussel dropper in January was about 75% of that in July. Therefore, the cylinder diameter was taken as $b = 0.10$ m, the mass per unit length was assumed as $\rho_v A_c = 4.46$ kg/m, and the flexural rigidity was assumed as $EI = 0.28$ N/m^2. The cylinders are assumed to be submerged half meter below the water surface so that $d_1 = 0.5$ m. The length of the mussel dropper is assumed as $l = 8$ m following Plew et al. (2005) and Stevens et al. (2007) for a similar water depth. A sparse configuration with 0.06 droppers/m^2 (Plew et al., 2005; Gagnon and Bergeron, 2017) and a dense configuration with 0.125 droppers/m^2 (e.g., mussel droppers are 0.5 m apart and the longline interval is about 16 m) are compared. Following Plew et al. (2009), Dewhurst (2016) and Knysh et al. (2020), the drag coefficient and added mass coefficient are assumed as $C_d = 1.3$ and $C_m = 1$, respectively, which are also comparable to the values in Raman-Nair and Colbourne (2003), Raman-Nair et al. (2008), Stevens et al. (2008), Plew et al. (2009), Gagnon and Bergeron (2017) and Landmann et al. (2019).

Figure 5.8. The study site at Saco Bay, Maine, USA (Sources: Esri, GEBCO, NOAA, National Geographic, DeLorme, HERE, Geonames.org, and other contributors).

The SAV is modeled as a rectangular plate based on the properties of Zostera marina, which is a common SAV in the Gulf of Maine, USA (Mattila et al., 1999; Gaeckle and Short, 2002; Beal et al., 2004; Neckles et al., 2005; Beem and Short, 2009; Newell et al., 2010). The length of Zostera marina ranges from 10 to 150 cm and the shoot density is about 50-1100 shoots/m^2 with 3-7 blades per shoot (Abdelrhman, 2007; Beem and Short, 2009; Boström and Bonsdorff, 1997; Gaeckle and Short, 2002; Mattila et al., 1999; Ondiviela et al., 2014). In January, however, the averaged blade length of Zostera marina is about 16 cm (Gaeckle and Short, 2002; Ondiviela et al., 2014). Thus, the SAV blade length is assumed as 16 cm. The corresponding blade width and thickness as well as the sheath length and width are estimated using the empirical formula provided by Abdelrhman (2007), which yields a blade width of 3.7 mm, blade thickness of 0.11 mm, sheath length of 8 cm and sheath width of 3.4 mm. Following Abdelrhman (2007), the mass density is assumed $\rho_v = 700$ kg/m^3. The Young's modulus is assumed $E = 0.26$ GPa for the blades based on the measurements by Fonseca et al. (2007). The sheath is considered rigid following Lei and Nepf (2019b). A sparse SAV meadow with 200 shoots/m^2 and a dense meadow with 400 shoots/m^2 are used in the study to investigate the variation of wave attenuation with vegetation density. The number of blades per shoot is assumed to be 5 so that there are 1000 blades/m^2 for the sparse configuration and 2000 blades/m^2 for the dense configuration. Due to small blade width and large significant wave height and peak period in

a storm event, the calculated KC number is greater than 135, yielding a constant drag coefficient of 1.95 based on equation (5.25) The data comparison in section 5.3.1 has shown that $C_d = 1.95$ and $C_m = 1$ work well for submerged vegetation with $l/h < 0.38$ (Figure 5.4). Therefore, the drag coefficient and added mass coefficient are assumed $C_d = 1.95$ and $C_m = 1$, respectively, for this case study. The properties of the mussel farm and SAV meadow are summarized in Table 5.2. In this study, both mussel droppers and SAV are modeled as cantilever beams.

5.4.2. Mussel farm and SAV at the same water depth

The time evolution of tide, storm tide, storm surge at the study site during the January 2015 North American blizzard is given by the SWAN+ADCIRC model (Xie et al., 2019) and shown on Figure 5.9(a). The tidal range is around 3.3 m and the largest storm surge is about 0.8 m at the study site. The incident significant wave height (H_{s0}) and corresponding peak wave period (T_p) for every 30 minutes are shown on Figure 5.9(b). At the study site during the storm, the significant wave height reached 3.6 m with peak wave periods ranging from 5.2 s to 13.5 s.

Table 5.2. Properties of the mussel farm and submerged aquatic vegetation (SAV) meadow.

	Mussel farm	SAV
Canopy component	Mussel dropper	*Zostera marina*
Component properties	Length: 8 m Diameter: 0.10 m Flexural rigidity: $EI = 0.28$ Nm^2 Mass per length: $\rho_v A_c$ =4.46 kg/m	Blade length: 0.16 m Blade width: 3.7 mm Blade thickness: 0.11 mm Young's modulus: 0.26 GPa Mass density: 700 kg/m^3 Sheath length: 8 cm Sheath width: 3.4 mm
Canopy density	Sparse: 0.060 droppers/m^2 Dense: 0.125 droppers/m^2	Sparse: 200 shoots/m^2 (1000 blades/m^2) Dense: 400 shoots/m^2 (2000 blades/m^2)
Drag coefficient (C_d)	1.3	1.95
Added mass coefficient (C_m)	1	1

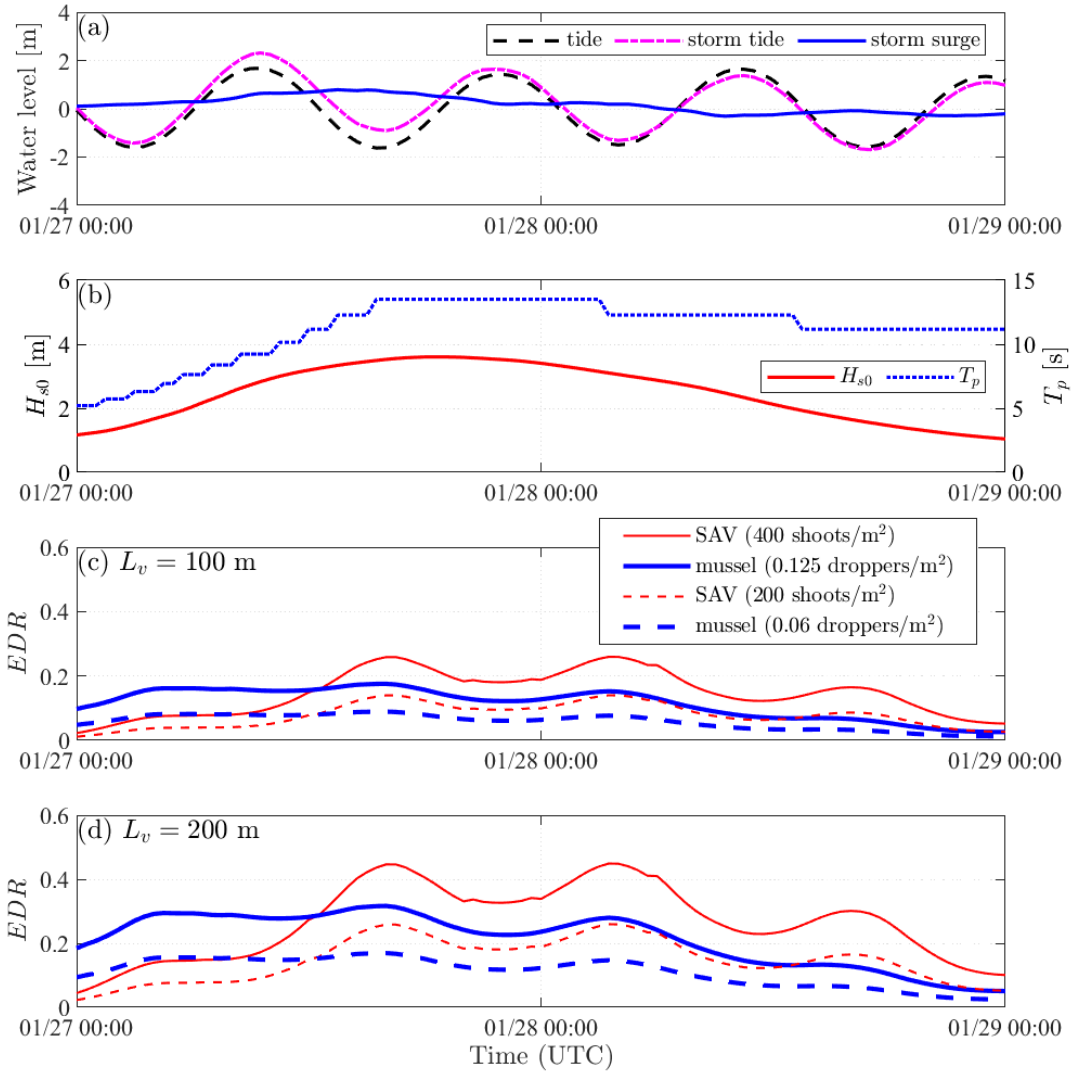

Figure 5.9. Time evolution of (a) tide, storm tide and storm surge during the January 2015 North American blizzard, (b) significant wave height H_{s0} and the corresponding peak wave period T_p, (c) and (d) calculated wave energy dissipation ratio (EDR) by the suspended mussel farm (blue lines) and submerged aquatic vegetation (SAV, red lines) using the wave spectrum data. The canopy lengths are $L_v = 100$ m in (c) and $L_v = 200$ m in (d). The canopy densities are shown in the legend.

The wave attenuation by the mussel farm and SAV at the same still water depth of 10.6 m during the storm is calculated with the wave spectral data from the SWAN+ADCIRC model. The calculated wave energy dissipation ratio (EDR) is shown on Figure 5.9 (c and d). The EDR of both SAV and mussels increases with incident significant wave height. However, the EDR decreases with water level resulting in an oscillating wave attenuation with the same period of the tidal cycle. This periodic behavior is more

obvious for SAV because the mussels are less influenced by the tidal change since the mussels can move up and down with the buoys. The largest wave attenuation value occurs at the highest wave height during low tide. The larger ($L_v = 200$ m) and denser (0.125 droppers/m^2) mussel farm provides a more pronounced wave attenuation with EDR up to 0.32 (Figure 5.9d), which is a bit more than that of the same size ($L_v = 200$ m) but sparse (200 shoots/m^2) SAV with EDR up to 0.26. However, for the denser (400 shoots/m^2) SAV with the same size ($L_v = 200$ m), the EDR can reach to 0.45. For the shorter period waves with $T_p < 9$ s as shown on Figure 5.9 (c and d), the mussel farm can damp more wave energy than the same size SAV since SAV at the ocean bottom has little effect on wave attenuation for short period waves whose energy is concentrated near the ocean surface.

The comparisons for the selected wave spectrum as well as the associated spectral dissipation ratio (SDR) at 10:00 UTC (high tide with $H_{s0} = 2.9$ m and $T_p = 9.2$ s), 16:00 UTC (low tide with $H_{s0} = 3.5$ m and $T_p = 13.5$ s), and 22:00 UTC (high tide with $H_{s0} = 3.5$ m and $T_p = 13.5$ s) on Jan 27 are shown on Figure 5.10. The SDR of the suspended mussel farm increases with wave frequency until reaching the maximum value, while the SDR of SAV decreases with wave frequency. As a result, the suspended mussel farm shows the advantage of reducing higher frequency (shorter period) wave components over SAV. For example on Figure 5.10 (a2) with smaller H_{s0} and T_p, the SDR of the dense suspended mussel farm (0.125 droppers/m^2) is larger than that of dense SAV (400 shoots/m^2) for $f > 0.12$ Hz (wave period $T < 8.3$ s) and sparse SAV (200 shoots/m^2) for wave frequency $f > 0.055$ Hz ($T < 18$ s). The SDR of the sparse suspended mussel farm (0.06 droppers/m^2) is larger than that of the dense SAV for wave frequency $f > 0.16$ Hz ($T < 6.25$ s) and sparse SAV for $f > 0.12$ Hz ($T < 8.3$ s). As H_{s0} and T_p, increases, the threshold value of the wave frequency where the SDR of suspended mussel farm is larger than that of SAV increases to $f > 0.167$ Hz ($T < 6$ s) for the dense mussel farm and the dense SAV, $f > 0.1$ Hz ($T < 10$ s) for the dense mussel farm and the sparse SAV, $f > 0.21$ Hz ($T < 4.8$ s) for the sparse mussel farm and the dense SAV, and $f > 0.17$ Hz ($T < 5.9$ s) for the sparse mussel farm and the sparse SAV as shown on Figure 5.10(b2). For the same H_{s0} and T_p at high tide, the SDR of both the mussel farm and SAV decreases due to

the increase of water level. The threshold value of the wave frequency where the SDR of suspended mussel farm is larger than that of SAV decreases to $f > 0.147$ Hz ($T < 6.8$ s) for the dense mussel farm and the dense SAV, $f > 0.095$ Hz ($T < 10.5$ s) for the dense mussel farm and the sparse SAV, $f > 0.18$ Hz ($T < 5.5$ s) for the sparse mussel farm and the dense SAV, and $f > 0.15$ Hz ($T < 6.7$ s) for the sparse mussel farm and the sparse SAV as shown on Figure 5.10 (c2).

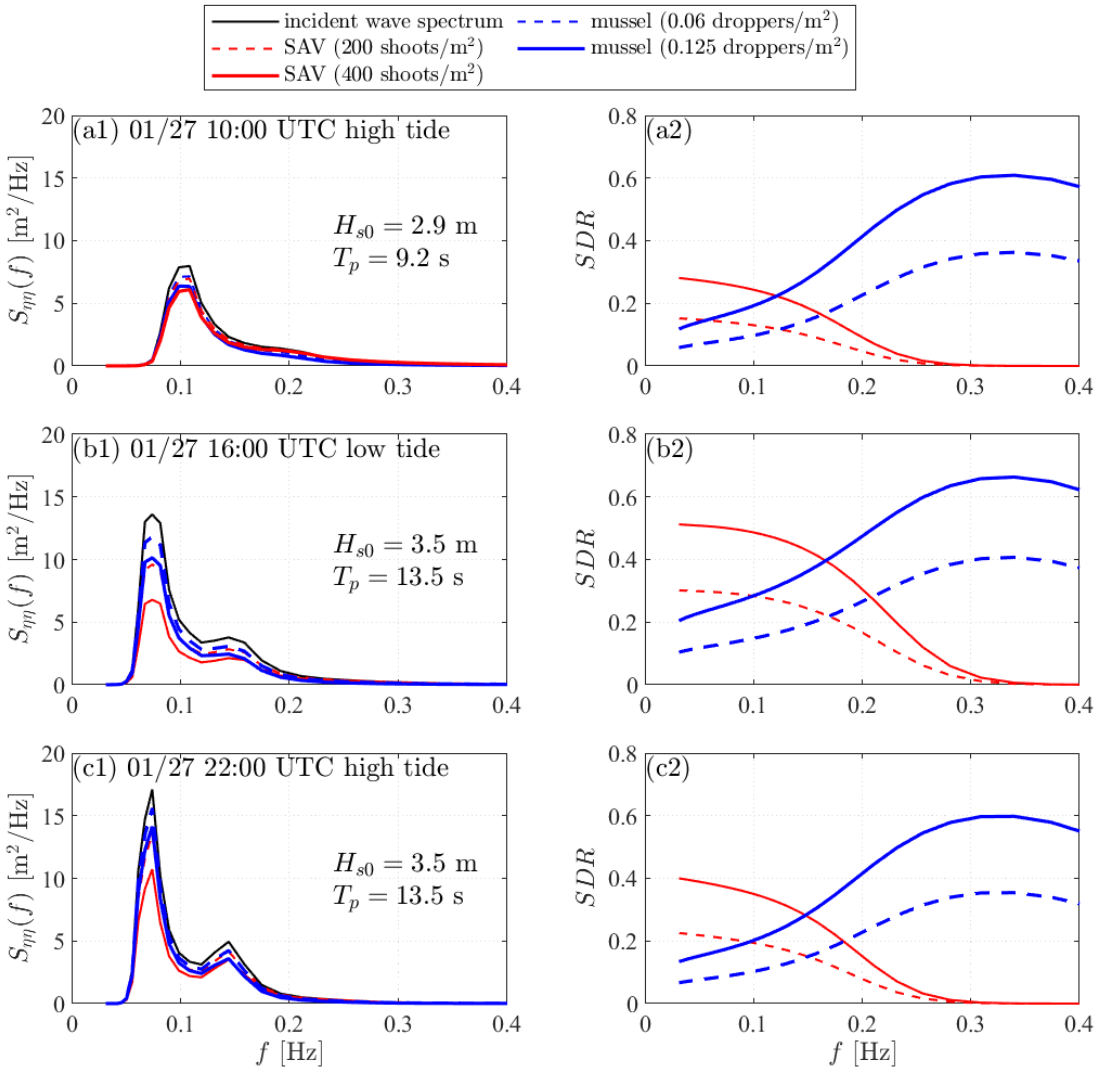

Figure 5.10. Comparisons of wave spectrum ($S_{\eta\eta}$) and wave spectral dissipation ratio (SDR) versus wave frequency (f) between the suspended mussel farm and submerged aquatic vegetation (SAV) with different canopy densities (shown in legend) at 10:00 UTC (a), 16:00 UTC (b), and 22:00 UTC (c) on Jan 27. The canopy length is 200 m for both canopies. The incident significant wave height and peak period are denoted by H_{s0}, and T_p, respectively.

5.4.3. Mussel farm and SAV at different water depths

The previous section shows the advantages of suspended mussel farms on damping high frequency wave energy over SAV at the same water depth. Usually, SAV colonizes in shallower water as shown on Figure 5.1. To compare the performances of the suspended mussel farm and the shallow water SAV meadow, the water depth for SAV is set at 6 m so that maximum $H_{s0}/h = 0.79$ to avoid wave breaking. The water depth for the suspended mussel farm keeps the same at 10.6 m. The wave shoaling is incorporated using shoaling coefficient $K_s(\omega) = \sqrt{c_{gd}(\omega)/c_{gs}(\omega)}$ (Dean and Dalrymple, 1991), where $c_{gd}(\omega)$ and $c_{gs}(\omega)$ are the wave group speed at deeper and shallower water depths, respectively. Correspondingly, EDR and SDR are calculated using the shoaled wave energy and wave spectrum. The canopy density is set as 200 shoots/m^2 (1000 blades/m^2) for SAV meadow and 0.125 droppers/m^2 for the mussel farm. The canopy length for SAV meadow is set as $L_v = 100$ m. For the mussel farm, two canopy lengths of 100 m and 200 m are designed for comparison.

The wave attenuations of SAV and mussel farms as well as their combinations are shown on Figure 5.11. The wave attenuation by SAV decreases dramatically with increasing water level while the suspended mussel farm is less affected by the water level change. For example (Figure 5.11a), the EDR of SAV decreases by 49% from 0.51 at low tide (Jan 27 16:00 UTC) to 0.26 at high tide (Jan 27 22:00 UTC) with water level increment of 2.5 m while the EDR of the suspended mussel farm decreases by 29%. The combination of the suspended mussel farm and SAV provides a larger wave attenuation, especially for smaller significant wave period and low tide (Figure 5.11a). For example at 10:00 UTC on Jan 27 with $T_p = 9.2$ s and $H_{s0} = 2.9$ m, the EDR of SAV and a large mussel farm ($L_v = 200$ m) is 0.37, which is 1.5 times of the $EDR = 0.15$ of SAV. Adding a small mussel farm ($L_v = 100$ m) to SAV can also favorably improve the EDR of SAV to 0.27 by 80%. As H_{s0} and T_p increases to $H_{s0} = 3.5$ m and $T_p = 13.5$ s, the improvements of the wave attenuation of SAV by adding mussel farms are reduced because the mussel farm is more effective for reducing shorter period waves. However, the improvements still can reach up to 31% by adding a small mussel farm and 54% by adding a large mussel farm. The improvements of

combined SAV and mussels hold for wave energy at all frequencies by taking the advantage of the canopy density of SAV and the vertical position of the suspended mussel as shown on Figure 5.11 (b2, c2 and d2).

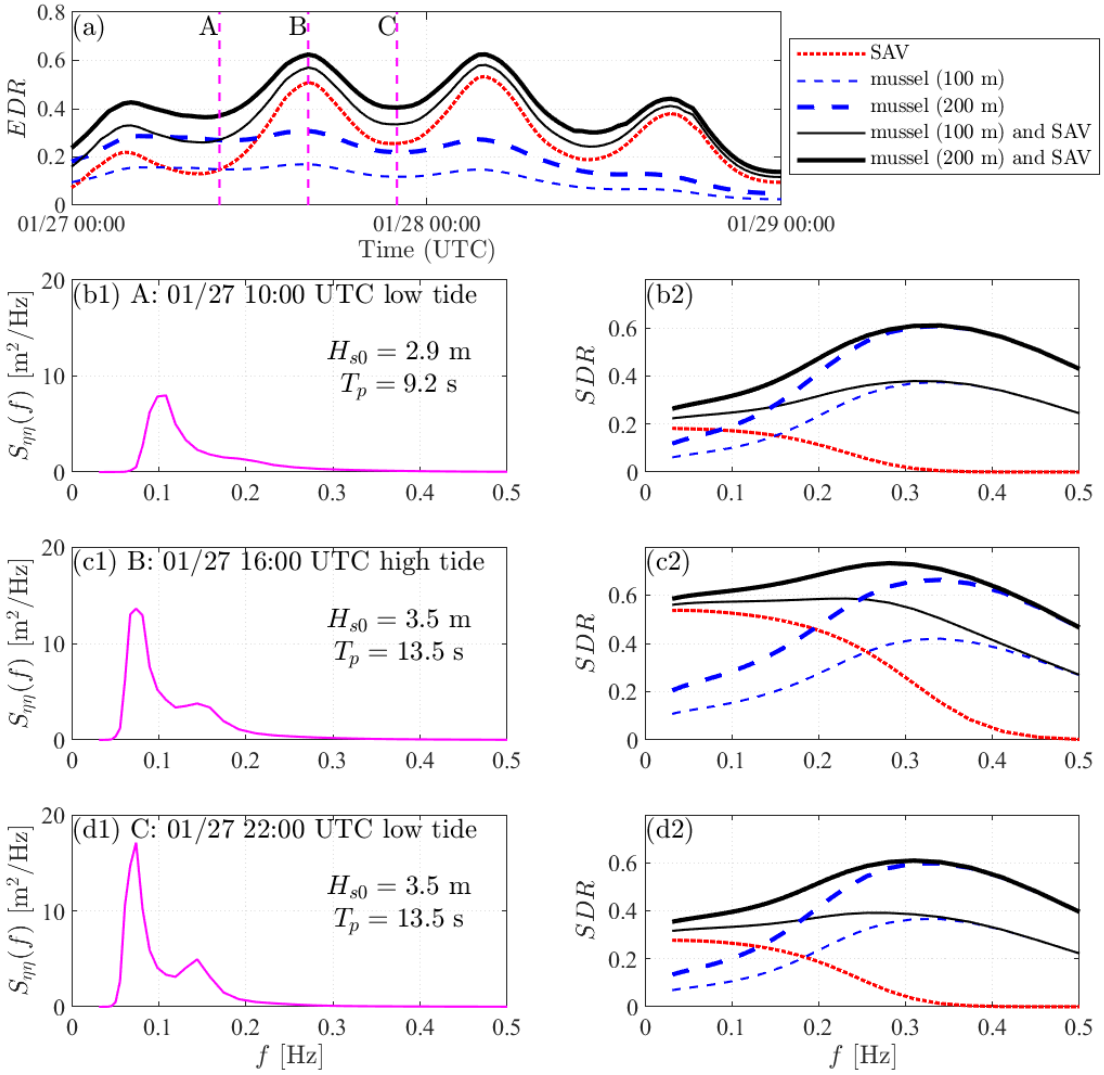

Figure 5.11. (a) Comparisons of wave energy dissipation ratio (EDR) between the suspended mussel farm and submerged aquatic vegetation (SAV). The canopy densities are 0.125 droppers/m^2 for the suspended mussel farm and 200 shoots/m^2 (1000 blades/m^2) for the SAV meadow, respectively. The canopy length is 100 m for the SAV meadow. The canopy length for the mussel farm is shown in the legend. (b1, c1, d1) The incident wave spectrum ($S_{\eta\eta}$) and (b2, c2, d2) Comparisons of wave spectral dissipation ratio (SDR) versus wave frequency (f) at 10:00 UTC (A), 16:00 UTC (B) and 22:00 UTC (C) on Jan 27. The incident significant wave height and peak wave period are denoted by H_{s0}, and T_p, respectively.

5.5. Discussion

5.5.1. Wave attenuation characteristics of suspended aquaculture farms and SAV

Wave attenuation occurs through the drag force which is determined by the horizontal wave orbital velocity. In shallow water waves, the amplitude of the horizontal wave orbital velocity is almost uniform with depth. Thus, the vertical position of the canopy has little effect on attenuating shallow water waves. Taking the advantages of canopy density, SAV can dissipate more wave energy than suspended mussel farms for long period waves. However, the wave attenuation of SAV is influenced by changes of water level. In shallow water, the wave attenuation of SAV decreases dramatically during high tide, storm surge, or storm tide (tide plus storm surge), which highlights the weakness of SAV in protecting coastlines during large storm tide conditions. This implies that severe erosion by storms may occur during high storm tide levels (in addition, higher waves may arrive at the shore without breaking during high tide). Therefore, living shorelines represented by SAV would be less effective during extreme events.

Suspended aquaculture farms can work as living breakwaters to protect the coast due to their capacity for wave attenuation. The wave attenuation capacity of suspended aquaculture farms is mainly dictated by the canopy density and the size (length) in the wave direction. Unlike SAV, which is limited by water depth due to light and nutrients, the vertical locations of suspended aquaculture farms can be adjusted to optimize their growth. Consequently, there is no depth restriction for suspended farms and they can be quite large, e.g., the suspended mussel aquaculture farm off Gouqi Island in East China Sea has an area of about 8 km^2 (Lin et al., 2016). In theory, the size of suspended aquaculture farms can be designed to achieve optimal wave attenuation. For example, for the incident significant wave height (H_{s0}) to be reduced to the transmitted significant wave height (H_{sT}) that will allow the living shorelines to thrive and mitigate coastal erosion, the size of the aquaculture farms can be designed as

$$L_v > \frac{1}{\beta(\omega_c)} \ln \frac{H_{s0}}{H_{sT}}, \tag{5.27}$$

where ω_c is the critical angular frequency such that $\int_0^\infty S_{\eta\eta}(\omega,0) e^{-2\beta(\omega)L_v} d\omega = e^{-2\beta(\omega_c)L_v} \int_0^\infty S_{\eta\eta}(\omega,0) d\omega$. The existence of ω_c is guaranteed according to the mean value theorem for

definite integrals. For narrow-banded waves, ω_c can be approximated using the peak wave angular frequency, $\omega_c \approx \omega_p = 2\pi/T_p$. The external factors such as the water depth and the vertical position of aquaculture farms should also be considered during the design. For places that are not suitable to establish living shorelines, such as low-nutrient seabeds, the suspended aquaculture farms offer a viable alternative to SAV for nature-based coastal defense.

This work has shown that suspended aquaculture farms can supplement SAV in wave attenuation. Suspended aquaculture farms attenuate shorter peak period waves and high frequency wave components more than SAV. Hence, adding suspended aquaculture farms to SAV-based living shorelines can compensate for the limitations of SAV for attenuating shorter period waves (such as boat wake) and enhance the wave attenuation capacity of SAV-based living shorelines for a wider range of wave frequency. The wave attenuation by SAV decreases during high tide or storm surge due to the increase in water level. The water level, however, has fewer influences on suspended aquaculture farms since they are located near the surface and move up and down with water level. Therefore, suspended aquaculture farms can enhance the wave attenuation capacity of SAV-based living shorelines during extreme events. The combination of suspended aquaculture farms and traditional living shorelines (such as SAV) is therefore a desirable nature-based coastal defense strategy.

5.5.2. Simplified analytical solutions

The generalized three-layer frequency dependent theoretical wave attenuation model developed in this paper is applicable to analyze the wave attenuation capacity of submerged, emerged, suspended, and floating canopies for random waves including narrow-banded and wide-banded wave conditions. The present analytical model provided a more precise consideration of the blade motion by incorporating the effects of inertia (neglected in Mullarney and Henderson, 2010; Henderson, 2019) and the mode shape (not considered in Asano et al., 1992; Méndez et al., 1999).

The present model can reduce to previous models for submerged rigid vegetation without motion by setting the transfer functions γ_s and γ_c as 0. Therefore, the decay coefficient β in (5.22) reduces to the solution for rigid blades and given by

$$\beta_R(\omega) = \frac{2\sqrt{2}Nk^2}{\sqrt{\pi}\omega(2kh+\sinh 2kh)} \int_{-d_1-d_2}^{-d_1} C_d b \sigma_u [\cosh k(h+z)]^2 dz, \tag{5.28}$$

where $\sigma_u^2 = \int_0^\infty [\omega \cosh k(h+z) / \sinh kh]^2 S_{\eta\eta}(\omega, 0) d\omega$. If $d_3 = 0$, the solution in (5.28) reduces to the solution by Jacobsen et al. (2019a) for submerged rigid vegetation. In this model, the nonlinear drag is linearized using the Borgman (1967) method such that $|u| \approx \sqrt{8/\pi}\sigma_u$. If using the root mean square velocity to linearize the drag force following Madsen et al. (1988) such that $|u| \approx \sqrt{2}\sigma_u$, the solution reduces to the Hasselmann and Collins (1968) based solution in Chen and Zhao (2012) for submerged rigid vegetation. For idealized narrow-banded waves such that $S_{\eta\eta} \approx 0$ when $\omega \neq \omega_p$, the damping coefficient in (5.28)

$$\beta_{RN} = \frac{1}{12\sqrt{\pi}} C_d b N k_p H_{rms0} \frac{9\sinh k_p(d_2+d_3) - 9\sinh k_p d_3 + \sinh 3k_p(d_2+d_3) - \sinh 3k_p d_3}{(\sinh 2k_p h + 2kh)\sinh k_p h}, \tag{5.29}$$

where $H_{rms0} = \sqrt{8\int_0^\infty S_{\eta\eta}(\omega, 0) d\omega}$ is the root mean square incident wave height and k_p is the peak wave number calculated by solving $\omega_p^2 = g k_p \tanh k_p h$. For bottom-rooted rigid vegetation such that $d_3 = 0$, β_{RN} in (5.29) reduces to the solution of Mendez and Losada (2004). The relationship between the present and previous models are shown on Figure 5.12.

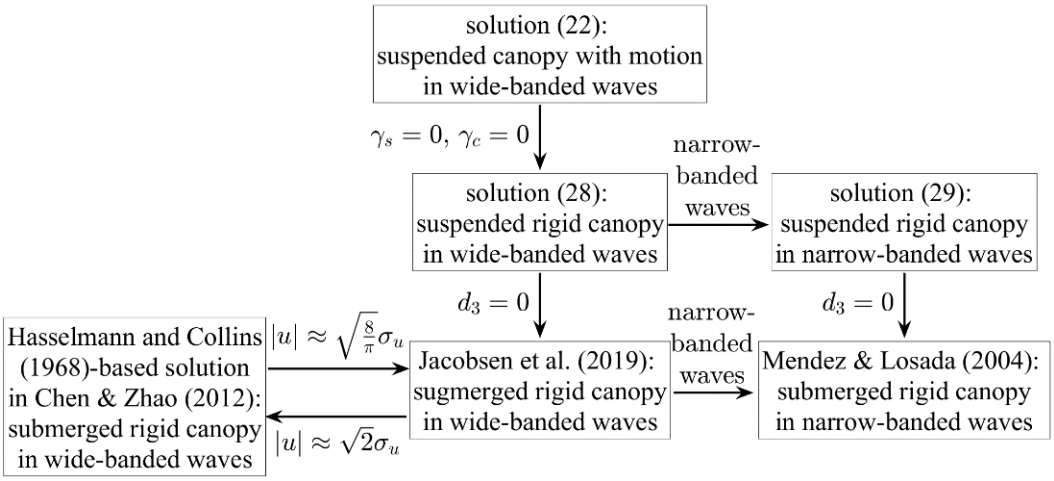

Figure 5.12. Relationship between the present solutions (5.22), (5.28), (5.29) and previous solutions by Chen and Zhao (2012), Jacobsen et al. (2019a), and Mendez and Losada (2004), where γ_s and γ_c are the transfer function for the motion of canopy component, d_3 is the thickness of the gap between the canopy and sea bed, u is the horizontal wave velocity and σ_u is the stand deviation of u.

5.6. Summary

A generalized three-layer frequency-dependent theoretical model for the wave attenuation by submerged and suspended canopies subjected to random waves was derived and validated with laboratory and field data. This model incorporates the motion of canopies using a cantilever-beam model for slender canopy components and a buoy-on-rope model for canopy components with concentrated mass and buoyancy. This frequency-dependent solution was used to demonstrate the shoreline protection capability of suspended mussel farms alone and in combination with submerged aquatic vegetation (SAV) to damp wave energy at a field site in Saco Bay, Maine, USA during a January 2015 Blizzard. The results showed that both suspended mussel farms and SAV have the potential to damp wave energy considerably during storm events. Suspended mussel farms are more effective at damping shorter waves and high frequency wave components of the wave spectrum while dense SAV colonized in shallower water have the advantages of damping longer waves and lower frequency wave components more effectively. However, the wave attenuation of SAV in shallow water decreases dramatically at the peak of storm tide due to increased water level, which decreases the wave motion reaching the ocean bottom. In contrast, suspended aquaculture farms can move up and down with water level change and are less affected by water level change. As a consequence, the combination of suspended aquaculture farms and traditional SAV-based living shorelines provide an optimized nature-based shore protection scheme that can damp more wave energy for a wider wave frequency and water level range.

The research of wave attenuation by suspended and floating canopies is still in its infancy. More laboratory and field experiments data for the hydrodynamic properties of suspended aquaculture farms (e.g., mussels and kelp) as well as wave attenuation are desirable. The present theoretical model assumed the blade motion as a linear vibration with small-amplitude. However, as long as the nonlinear effects of large-amplitude blade motion is negligible, the present theoretical model remains valid. In addition, the bottom friction, bedforms, bottom slope as well as wave-driven currents, wave and current conditions may also be significant for certain types of bottom rooted vegetation (e.g., Jensen et al., 1989; Myrhaug, 1995; Zou, 2004; Zou and Hay, 2003; Smyth and Hay, 2002; Maza et al., 2019; Abdolahpour et al., 2017; van Rooijen

et al., 2020). Therefore, it is worthwhile to investigate the nonlinear effects of large-amplitude blade motion on the wave damping capacity of suspended canopies as well as the effects of bottom properties and wave-current conditions in the future work.

5.7. Acknowledgments

This work was completed as part of the PhD research of Longhuan Zhu who is supported by National Science Foundation, USA award #IIA-1355457 to Maine EPSCoR at the University of Maine. The authors benefited from discussions with Zhilong Liu and Haifei Chen. The authors wish to thank Stephen Cousins and Shane Moeykens at the University of Maine Advanced Research Computing for the computa- tional support. The authors would like to thank Niels G. Jacobsen for sharing the data used on Figure 5.4. The authors would also like to thank the anonymous reviewers for constructive comments that helped to improve this manuscript greatly.

CHAPTER 6

CONCLUSIONS

6.1. Chapter summary

In this thesis, the wave attenuation capacity of suspended aquaculture structures were investigated using the comprehensive approaches described in each of the chapters. Firstly, the blade dynamics in waves was investigated using a cable model with focus on the asymmetric blade motion as described in Chapter 2. The cable model was then used to develop a scale frame for the physical model for *S. latissima* to consider dynamical similarity as described in Chapter 3. Chapter 3 also described the physical model experiments for wave attenuation by suspended kelp farms. To predict the wave attenuation by suspended canopy, an analytical wave attenuation model incorporating blade motion was developed as described in Chapter 4. Chapter 5 described the extension of the analytical wave attenuation model to random waves and the application of aquaculture structures as nature-based solutions with a case study.

6.2. Findings and academic contributions

6.2.1. Chapter 2: Asymmetric blade motion in waves

The mass-consistent cable model approach described in this chapter has improved the blade motion modeling, especially for "second-normal-mode-like" blade motion. The improvements were achieved by incorporating (i) the effects of the blade-motion-induced rotations of local Lagrangian coordinates along the blade on inertial force, (ii) the compatibility relations for geometrical continuity of the blade segments, and (iii) the spatial variation of wave orbital velocity encountered by the blade due to blade displacements. The accurate blade posture predictions are required to fully resolve the flow-vegetation interaction, wave-driven currents in a canopy, and the wave attenuation by canopies. This model can also be used to estimate the internal stress of the blade and the total force at the bottom of the blade in order to analyze the breakage and the sediment holding properties of the vegetation.

With this cable model, two major factors were found to influence asymmetric blade motion other than wave orbital motion asymmetry. These factors are (i) the spatial asymmetry of the encountered wave

orbital velocities induced by the blade displacements and (ii) the asymmetric action on the blade by the vertical wave orbital velocities. When near symmetric motion exists, conditions are (i) the blade length is much smaller than the wavelength, (ii) in shallow water waves or (iii) the blade length is much smaller than the water depth in finite-depth-water waves. Peak asymmetry occurs when the ratio of blade length to wavelength reaches the critical value. Peak asymmetry was found to increase with wave height and blade length but decrease with increasing blade flexural rigidity. The asymmetric blade motion can be utilized in coastal erosion control since the inclination of the blade provides 'shelter' that could inhibit sendiment suspension.

6.2.2. Chapter 3: Physical model experiments for wave attenuation by suspended kelp canopies

In this chapter, the morphological and mechanical properties of the cultivated *S. latissima* in Saco, Maine, USA were presented. Based this data, a set of 1:10 scale physical model experiments were conducted to investigate the wave attenuation by suspended kelp canopies. The results showed that the designed model kelp canopy can reduce up to 39% wave energy in the experiments. A numerical wave attenuation model based on the cable model described in Chapter 2 was developed and validated by the experiments. The numerical results indicated that 200 longlines of 1 m-long kelp blades with 400 plants/m could reduce 50% wave energy of 6.3 s waves in 4 m-deep water, indicating the potential of suspended kelp aquaculture farms on coastal wave attenuation. Wave attenuation increases with wave frequency, wave height, and the vertical positions and size of the aquaculture farms. Empirical formulas for the bulk drag coefficient and effective blade length of the suspended kelp canopy for wave attenuation were fitted with $R^2 = 0.80$ and $R^2 = 0.90$, respectively. The bulk drag coefficient and effective blade length methods with the fitted empirical formulas have improved the numerical results by 33% and 61%, respectively. The bulk drag coefficient and effective blade length formulas are convenient to implement in large-scale models.

6.2.3. Chapter 4: Analytical wave attenuation model for flexible canopies

To predict the wave attenuation by suspended flexible canopies, an analytical wave attenuation model that resolved blade motion was developed and validated with the experiments. With the analytical model, solutions for bulk drag coefficient and effective blade length were obtained. The solved bulk drag

coefficient and effective blade length by the analytical model has the same precision with the fitted formulas for wave attenuation. Therefore, this approach can be an alternative to obtaining these parameters with reduce physical experiments. The analytical solutions were also useful to analyze the mechanisms of blade motion on wave attenuation and guide the selection of parameters to fit bulk drag coefficient and effective blade length. Similar to bulk drag coefficient and effective blade length methods, the analytical wave attenuation model is convenient to implement in large-scale models.

6.2.4. Chapter 5: Random wave attenuation by flexible canopies

A generalized three-layer frequency-dependent theoretical model for the wave attenuation by submerged and suspended canopies subjected to random waves was derived and validated with laboratory and field data. This model incorporated the motion of canopies using a cantilever-beam model for slender canopy components and a buoy-on-rope model for canopy components with concentrated mass and buoyancy. This frequency-dependent solution was used to demonstrate the shoreline protection capability of suspended mussel farms alone and in combination with submerged aquatic vegetation (SAV) to damp wave energy at a field site in Saco Bay, Maine, USA during a January 2015 Blizzard. The results showed that both suspended mussel farms and SAV have the potential to damp wave energy considerably during storm events. Suspended mussel farms are more effective at damping shorter waves and high frequency wave components of the wave spectrum while dense SAV colonized in shallower water have the advantages of damping longer waves and lower frequency wave components more effectively. However, the wave attenuation of SAV in shallow water decreases dramatically at the peak of storm tide due to increased water level, which decreases the wave motion reaching the ocean bottom. In contrast, suspended aquaculture farms can move up and down with water level change and are less affected by water level change. As a consequence, the combination of suspended aquaculture farms and traditional SAV-based living shorelines provide an optimized nature-based shore protection scheme that can damp more wave energy for a wider wave frequency and water level range.

6.3. Engineering implications for nature-based solutions

The behavior of asymmetric blade motion can be used to guide planting strategies of submerged aquatic vegetation for sediment settlement. The asymmetric motion is expected to benefit sediment settlement because the "shelter" created by the blade inclination could hinder sediment suspension at the seabed. To take advantage of the peak asymmetry, it is recommended to choose the submerged aquatic vegetation species such that the ratio of the blade length and the dominant wavelength is close to the peak length ratio. Longer blades are preferred because they increase the peak asymmetry and provide a larger "shelter". In addition, the vegetation meadow with longer blades can reduce more wave energy resulting in a smaller flow velocity near the bed. The low flow environment benefits the sediment settlement.

Large suspended aquaculture farms can work as living breakwaters to protect the coast due to their capacity for wave attenuation. The wave attenuation capacity of suspended aquaculture farms is mainly dictated by the canopy density and the size (length) in the wave direction. Unlike SAV, which is limited by water depth due to light and nutrients, the vertical locations of suspended aquaculture farms can be adjusted to optimize their growth. Consequently, there is no depth restriction for suspended farms and they can be quite large, e.g., the suspended mussel aquaculture farm off Gouqi Island in East China Sea has an area of about 8 km^2 (Lin et al., 2016). The size of suspended aquaculture farms can be designed to achieve optimal wave attenuation. The external factors such as the water depth and the vertical position of aquaculture farms should also be considered during the design. For places that are not suitable to establish living shorelines, such as low-nutrient seabeds, the suspended aquaculture farms offer a viable alternative to SAV for nature-based coastal defense.

Combination of onshore and nearshore submerged aquatic vegetation and offshore suspended aquaculture farms can be a new option as nature-based solution for coastal protection. Offshore suspended aquaculture farms are found to enhance the wave attenuation capacity of SAV-based living shorelines for a wider range of wave frequency. The shelter provided by offshore aquaculture farms can also improve the survival rate and benefit growth of nearshore SAV. Besides wave dissipation and flow reduction, SAV can

stabilize the sediment by root hosting and blade sheltering. Taking the advantages of both aquaculture farms and SAV would be a desirable strategy for nature-based coastal protection.

The wave attenuation models developed in this study can be used to analyze the wave attenuation of nature-based infrastructures and design the nature-based infrastructures for expected wave attenuation. The models can also be used to calculate bulk drag coefficient and effective blade length of the nature-based infrastructures for wave attenuation. The analytical wave attenuation models are convenient to be implemented into large-scale models to analyze the influences of wave attenuation on coastal morphology, current circulation and material transport.

The analytical wave attenuation models developed in this study have some limitations when applied in practice due to some simplifications. The simplifications include the assumption of linear waves and linear blade motion, ignorance of the motion effects of the mooring systems of the aquaculture farms, simplification of the sheltering effects in a dense canopy, and without consideration of the back ground currents. The effects of the simplifications on wave attenuation are not fully understood and recommendations for future research is provided in the next section. In practice, some modification of the wave attenuation models should be made to consider the effects of these simplifications.

6.4. Suggestions for future research

Based on the limitations of this study, some suggestions are proposed for the future research as following.

1. The interaction between flow and flexible blades. While the approach in Chapter 2 described the wave-induced dynamics of flexible blades, the influence of the blade motion on the flow is needs to be investigated. The future work can incorporate the cable model into a computational fluid dynamics (CFD) model to study the two-way interaction between the flow and flexible blades. It can focus on the influence of the blade motion on the variance of the flow field such as the turbulence, wave attenuation and wave-driven currents in a canopy.
2. Sheltering effects among the blades in the canopy. As described in Chapter 3, the sheltering effects were simply considered using a sheltering factor defined as the averaged force ratio of

the sheltered blade and unsheltered blade. The effects of the canopy orientation, the number of blades, blades configuration, blade property and wave conditions on the sheltering factor need to be investigated. The future work can improve the sheltering factor as a function of these parameters based on numerous experiments or numerical simulations. Accurate consideration of sheltering effects can improve the prediction of the canopy drag as well as the wave attenuation.

3. Full-scale experiments and field measurements. The experiments described in Chapter 3 was downscaled without considering the effects of small features such as blade stipe, blade ruffles and other morphological variance of the blade. The future work can do full-scale experiments to investigate the effects of kelp stipe on wave attenuation. The field measurements are also desired.
4. Nonlinear effects of the large-amplitude blade motion. The analytical wave attenuation model described in Chapter 4 resolved the blade motion using linear beam theory and considered the geometrical nonlinearity using a fitted constant factor. The effects of blade deflection on the nonlinear effects need to be investigated. The future work can develop a more accurate factor as a function of blade properties and wave conditions to consider the nonlinear effects using experimental or numerical techniques.
5. Hydrodynamic coefficients for random waves. As described in Chapter 5, the hydrodynamic coefficients for random waves were modified from the empirical formulas for regular waves. The hydrodynamic coefficients for random waves are in need. The future work can focus on developing empirical formulas for the hydrodynamic coefficients for canopies in random waves. The hydrodynamic coefficients for random waves are better expressed as frequency dependent as the wave spectrum.
6. Current effects on wave attenuation. While this study focused on the wave attenuation by canopies in waves without currents, the effects of currents on wave attenuation needs to be investigated. The future work can investigate the current effects using experimental techniques.

Also the present wave attenuation models can be further improved by considering the current effects.

7. Dynamics of the aquaculture longline system. In this study, the kelp longline was fixed at both ends without motion. The effects of the motion of the longline system on wave attenuation need to be investigated. The future work can do laboratory or field experiments for a whole kelp longline system in waves and currents. In addition, modeling the dynamics of longline system as well as its impact on wave attenuation is also worthy research.
8. Orientation of aquaculture longlines. This study considered one orientation of the longline configuration. The influences of the orientations of aquaculture longlines on wave attenuation needs to be investigated. The future work can study the effects of canopy orientations on wave attenuations using experimental techniques. It can focuses on the effects of canopy orientation on the sheltering factor.

BIBLIOGRAPHY

Abdelrhman, M. (2007). Modeling coupling between eelgrass Zostera marina and water flow. *Marine Ecology Progress Series*, *338*, 81–96. https://doi.org/10.3354/meps338081

Abdolahpour, M., Ghisalberti, M., McMahon, K., & Lavery, P. S. (2018). The impact of flexibility on flow, turbulence, and vertical mixing in coastal canopies. *Limnology and Oceanography*, *63*(6), 2777–2792. https://doi.org/10.1002/lno.11008

Abdolahpour, M., Hambleton, M., & Ghisalberti, M. (2017). The wave-driven current in coastal canopies. *Journal of Geophysical Research: Oceans*, *122*(5), 3660–3674. https://doi.org/10.1002/2016JC012446

Anderson, D., Tannehill, J. C., & Pletcher, R. H. (2016). Computational Fluid Mechanics and Heat Transfer, Third Edition. In *Computational Fluid Mechanics and Heat Transfer, Third Edition*. CRC Press. https://doi.org/10.1201/b12884

Anderson, M. E., & Smith, J. M. (2014). Wave attenuation by flexible, idealized salt marsh vegetation. *Coastal Engineering*, *83*, 82–92. https://doi.org/10.1016/j.coastaleng.2013.10.004

Arkema, K. K., Verutes, G. M., Wood, S. A., Clarke-Samuels, C., Rosado, S., Canto, M., Rosenthal, A., Ruckelshaus, M., Guannel, G., Toft, J., Faries, J., Silver, J. M., Griffin, R., & Guerry, A. D. (2015). Embedding ecosystem services in coastal planning leads to better outcomes for people and nature. *Proceedings of the National Academy of Sciences*, *112*(24), 7390–7395. https://doi.org/10.1073/pnas.1406483112

Arnaud, G., Rey, V., Touboul, J., Sous, D., Molin, B., & Gouaud, F. (2017). Wave propagation through dense vertical cylinder arrays: Interference process and specific surface effects on damping. *Applied Ocean Research*, *65*, 229–237. https://doi.org/10.1016/j.apor.2017.04.011

Asano, T., Deguchi, H., & Kobayashi, N. (1992). INTERACTION BETWEEN WATER WAVES AND VEGETATION. *Coastal Engineering Proceedings*, *3*, 2710–2723. https://icce-ojs-tamu.tdl.org/icce/index.php/icce/article/view/4885

Augyte, S., Yarish, C., Redmond, S., & Kim, J. K. (2017). Cultivation of a morphologically distinct strain of the sugar kelp, Saccharina latissima forma angustissima, from coastal Maine, USA, with implications for ecosystem services. *Journal of Applied Phycology*, *29*(4), 1967–1976. https://doi.org/10.1007/s10811-017-1102-x

Beal, B. F., Vadas Sr., R. L., Wright, W. A., & Nickl, S. (2004). Annual Aboveground Biomass and Productivity Estimates for Intertidal Eelgrass (Zostera marina L.) in Cobscook Bay, Maine. *Northeastern Naturalist*, *11*, 197–224. https://doi.org/10.1656/1092-6194(2004)11[197:AABAPE]2.0.CO;2

Beem, N. T., & Short, F. T. (2009). Subtidal Eelgrass Declines in the Great Bay Estuary, New Hampshire and Maine, USA. *Estuaries and Coasts*, *32*(1), 202–205. https://doi.org/10.1007/s12237-008-9110-3

Bilkovic, D. M., Mitchell, M., Mason, P., & Duhring, K. (2016). The Role of Living Shorelines as Estuarine Habitat Conservation Strategies. *Coastal Management*, *44*(3), 161–174. https://doi.org/10.1080/08920753.2016.1160201

Borgman, L. E. (1967). Random Hydrodynamic Forces on Objects. *The Annals of Mathematical Statistics*, *38*(1), 37–51. https://doi.org/10.1214/aoms/1177699057

Borsje, B. W., van Wesenbeeck, B. K., Dekker, F., Paalvast, P., Bouma, T. J., van Katwijk, M. M., & de Vries, M. B. (2011). How ecological engineering can serve in coastal protection. *Ecological Engineering*, *37*(2), 113–122. https://doi.org/10.1016/j.ecoleng.2010.11.027

Boström, C., & Bonsdorff, E. (1997). Community structure and spatial variation of benthic invertebrates associated with Zostera marina (L.) beds in the northern Baltic Sea. *Journal of Sea Research*, *37*(1–2), 153–166. https://doi.org/10.1016/S1385-1101(96)00007-X

Bouma, T. J., De Vries, M. B., Low, E., Peralta, G., Tánczos, I. C., Van De Koppel, J., & Herman, P. M. J. (2005). Trade-offs related to ecosystem engineering: A case study on stiffness of emerging macrophytes. *Ecology*, *86*(8), 2187–2199. https://doi.org/10.1890/04-1588

Bouma, T. J., van Belzen, J., Balke, T., Zhu, Z., Airoldi, L., Blight, A. J., Davies, A. J., Galvan, C., Hawkins, S. J., Hoggart, S. P. G., Lara, J. L., Losada, I. J., Maza, M., Ondiviela, B., Skov, M. W., Strain, E. M., Thompson, R. C., Yang, S., Zanuttigh, B., … Herman, P. M. J. (2014). Identifying knowledge gaps hampering application of intertidal habitats in coastal protection: Opportunities & steps to take. *Coastal Engineering*, *87*, 147–157. https://doi.org/10.1016/j.coastaleng.2013.11.014

Bradley, K., & Houser, C. (2009). Relative velocity of seagrass blades: Implications for wave attenuation in low-energy environments. *Journal of Geophysical Research*, *114*(F1), F01004. https://doi.org/10.1029/2007JF000951

Buck, B. H., & Buchholz, C. M. (2005). Response of offshore cultivated Laminaria saccharina to hydrodynamic forcing in the North Sea. *Aquaculture*, *250*(3–4), 674–691. https://doi.org/10.1016/j.aquaculture.2005.04.062

Campbell, I., Macleod, A., Sahlmann, C., Neves, L., Funderud, J., Øverland, M., Hughes, A. D., & Stanley, M. (2019). The Environmental Risks Associated With the Development of Seaweed Farming in Europe - Prioritizing Key Knowledge Gaps. *Frontiers in Marine Science*, *6*(MAR), 107. https://doi.org/10.3389/fmars.2019.00107

Chatjigeorgiou, I. K. (2008). A finite differences formulation for the linear and nonlinear dynamics of 2D catenary risers. *Ocean Engineering*, *35*(7), 616–636. https://doi.org/10.1016/j.oceaneng.2008.01.006

Chen, H., Liu, X., & Zou, Q. (2019). Wave-driven flow induced by suspended and submerged canopies. *Advances in Water Resources*, *123*, 160–172. https://doi.org/10.1016/j.advwatres.2018.11.009

Chen, H., & Zou, Q.-P. (2019). Eulerian–Lagrangian flow-vegetation interaction model using immersed boundary method and OpenFOAM. *Advances in Water Resources*, *126*, 176–192. https://doi.org/10.1016/j.advwatres.2019.02.006

Chen, H., Ni, Y., Li, Y., Liu, F., Ou, S., Su, M., Peng, Y., Hu, Z., Uijttewaal, W., & Suzuki, T. (2018). Deriving vegetation drag coefficients in combined wave-current flows by calibration and direct measurement methods. *Advances in Water Resources*, *122*, 217–227. https://doi.org/10.1016/j.advwatres.2018.10.008

Chen, Q., & Zhao, H. (2012). Theoretical Models for Wave Energy Dissipation Caused by Vegetation. *Journal of Engineering Mechanics*, *138*(2), 221–229. https://doi.org/10.1061/(ASCE)EM.1943-7889.0000318

Chen, S.-N., Sanford, L. P., Koch, E. W., Shi, F., & North, E. W. (2007). A nearshore model to investigate the effects of seagrass bed geometry on wave attenuation and suspended sediment transport. *Estuaries and Coasts*, *30*(2), 296–310. https://doi.org/10.1007/BF02700172

Chen, X., Chen, Q., Zhan, J., & Liu, D. (2016). Numerical simulations of wave propagation over a vegetated platform. *Coastal Engineering*, *110*, 64–75. https://doi.org/10.1016/j.coastaleng.2016.01.003

Currin, C. A., Chappell, W. S., & Deaton, A. (2010). Developing Alternative Shoreline Armoring Strategies : The Living Shoreline Approach in North Carolina. In H. Shipman, M. N. Dethier, G. Gelfenbaum, K. L. Fresh, & R. S. Dinicola (Eds.), *Shipman, Hugh and Dethier, Megan N. and Gelfenbaum, Guy and Fresh, Kurt L. and Dinicola, Richard S. (eds.) Puget Sound shorelines and the impacts of armoring—proceedings of a state of the science workshop* (pp. 91–102). US Geological Survey. http://aquaticcommons.org/14844/

Dalrymple, R. A., Kirby, J. T., & Hwang, P. A. (1984). Wave Diffraction Due to Areas of Energy Dissipation. *Journal of Waterway, Port, Coastal, and Ocean Engineering*, *110*(1), 67–79. https://doi.org/10.1061/(ASCE)0733-950X(1984)110:1(67)

Davis, J. L., Currin, C. A., O'Brien, C., Raffenburg, C., & Davis, A. (2015). Living Shorelines: Coastal Resilience with a Blue Carbon Benefit. *PLOS ONE*, *10*(11), e0142595. https://doi.org/10.1371/journal.pone.0142595

Dean, R. G., & Dalrymple, R. A. (1991). Water Wave Mechanics for Engineers and Scientists. In Intergovernmental Panel on Climate Change (Ed.), *Journal of Physics A: Mathematical and Theoretical* (Vol. 2, Issue 8). WORLD SCIENTIFIC. https://doi.org/10.1142/1232

Denny, M. W., Gaylord, B. P., & Cowen, E. A. (1997). Flow and flexibility II. The roles of size and shape in determining wave forces on the bull kelp Nereocystis luetkeana. *Journal of Experimental Biology*, *200*(24), 3165–3183. https://jeb.biologists.org/content/200/24/3165

Dewhurst, T. (2016). Dynamics of a Submersible Mussel Raft. *Thesis*. https://scholars.unh.edu/dissertation/1380/

Döbken, J. W. D. (2015). Modeling the interaction of wave hydrodynamics with flexible aquatic vegetation. *M.Sc. Thesis, Delft University of Technology*. http://citeseerx.ist.psu.edu/viewdoc/download?doi=10.1.1.970.1539&rep=rep1&type=pdf

Duarte, C. M., Wu, J., Xiao, X., Bruhn, A., & Krause-Jensen, D. (2017). Can Seaweed Farming Play a Role in Climate Change Mitigation and Adaptation? *Frontiers in Marine Science*, *4*(APR), 100. https://doi.org/10.3389/fmars.2017.00100

Dubi, A., & Tørum, A. (1995). Wave Damping by Kelp Vegetation. *Coastal Engineering 1994*, 142–156. https://doi.org/10.1061/9780784400890.012

Elgar, S., Freilich, M. H., & Guza, R. T. (1990). Model-data comparisons of moments of nonbreaking shoaling surface gravity waves. *Journal of Geophysical Research*, *95*(C9), 16055. https://doi.org/10.1029/JC095iC09p16055

Elwany, M. H. S., O'Reilly, W. C., Guza, R. T., & Flick, R. E. (1995). Effects of Southern California Kelp Beds on Waves. *Journal of Waterway, Port, Coastal, and Ocean Engineering*, *121*(2), 143–150. https://doi.org/10.1061/(ASCE)0733-950X(1995)121:2(143)

Etminan, V., Lowe, R. J., & Ghisalberti, M. (2019). Canopy resistance on oscillatory flows. *Coastal Engineering*, *152*, 103502. https://doi.org/10.1016/j.coastaleng.2019.04.014

Ferrario, F., Beck, M. W., Storlazzi, C. D., Micheli, F., Shepard, C. C., & Airoldi, L. (2014). The effectiveness of coral reefs for coastal hazard risk reduction and adaptation. *Nature Communications*, *5*(1), 3794. https://doi.org/10.1038/ncomms4794

Folkard, A. M. (2005). Hydrodynamics of model Posidonia oceanica patches in shallow water. *Limnology and Oceanography*, *50*(5), 1592–1600. https://doi.org/10.4319/lo.2005.50.5.1592

Fonseca, M. S., Koehl, M. A. R., & Kopp, B. S. (2007). Biomechanical factors contributing to self-organization in seagrass landscapes. *Journal of Experimental Marine Biology and Ecology*, *340*(2), 227–246. https://doi.org/10.1016/j.jembe.2006.09.015

Foster-Martinez, M. R., Lacy, J. R., Ferner, M. C., & Variano, E. A. (2018). Wave attenuation across a tidal marsh in San Francisco Bay. *Coastal Engineering*, *136*, 26–40. https://doi.org/10.1016/j.coastaleng.2018.02.001

Fredriksson, D. W., Dewhurst, T., Drach, A., Beaver, W., St. Gelais, A. T., Johndrow, K., & Costa-Pierce, B. A. (2020). Hydrodynamic characteristics of a full-scale kelp model for aquaculture applications. *Aquacultural Engineering*, *90*, 102086. https://doi.org/10.1016/j.aquaeng.2020.102086

Fringer, O. B., Dawson, C. N., He, R., Ralston, D. K., & Zhang, Y. J. (2019). The future of coastal and estuarine modeling: Findings from a workshop. *Ocean Modelling*, *143*, 101458. https://doi.org/10.1016/j.ocemod.2019.101458

Gaeckle, J. L., & Short, F. T. (2002). A plastochrone method for measuring leaf growth in eelgrass, Zostera marina L. *Bulletin of Marine Science*, *71*(3), 1237–1246. https://www.ingentaconnect.com/content/umrsmas/bullmar/2002/00000071/00000003/art00010

Gagnon, M., & Bergeron, P. (2017). Observations of the loading and motion of a submerged mussel longline at an open ocean site. *Aquacultural Engineering*, *78*, 114–129. https://doi.org/10.1016/j.aquaeng.2017.05.004

Garzon, J. L., Maza, M., Ferreira, C. M., Lara, J. L., & Losada, I. J. (2019). Wave Attenuation by Spartina Saltmarshes in the Chesapeake Bay Under Storm Surge Conditions. *Journal of Geophysical Research: Oceans*, *124*(7), 5220–5243. https://doi.org/10.1029/2018JC014865

Gaylord, B. P., Denny, M. W., & Koehl, M. A. R. (2003). Modulation of wave forces on kelp canopies by alongshore currents. *Limnology and Oceanography*, *48*(2), 860–871. https://doi.org/10.4319/lo.2003.48.2.0860

Gaylord, B., Rosman, J. H., Reed, D. C., Koseff, J. R., Fram, J., Macintyre, S., Arkema, K. K., Mcdonald, C., Brzezinski, M. A., Largier, J. L., Monismith, S. G., Raimondi, P. T., & Mardian, B. (2007). Spatial patterns of flow and their modification within and around a giant kelp forest. *Limnol. Oceanogr*, *52*(5), 1838–1852. https://aslopubs.onlinelibrary.wiley.com/doi/pdf/10.4319/lo.2007.52.5.1838

Gedan, K. B., Kirwan, M. L., Wolanski, E., Barbier, E. B., & Silliman, B. R. (2011). The present and future role of coastal wetland vegetation in protecting shorelines: answering recent challenges to the paradigm. *Climatic Change*, *106*(1), 7–29. https://doi.org/10.1007/s10584-010-0003-7

Gerard, V. A. (1987). Hydrodynamic streamlining of Laminaria saccharina Lamour. in response to mechanical stress. *Journal of Experimental Marine Biology and Ecology*, *107*(3), 237–244. https://doi.org/10.1016/0022-0981(87)90040-2

Ghisalberti, M., & Nepf, H. M. (2002). Mixing layers and coherent structures in vegetated aquatic flows. *Journal of Geophysical Research*, *107*(C2), 3011. https://doi.org/10.1029/2001JC000871

Gijón Mancheño, A. (2016). Interaction between wave hydrodynamics and flexible vegetation. *M.Sc. Thesis, Delft University of Technology*. http://resolver.tudelft.nl/uuid:bbaaf195-27e2-46ec-969c-603d6dd8f8c0

Gittman, R. K., Peterson, C. H., Currin, C. A., Joel Fodrie, F., Piehler, M. F., & Bruno, J. F. (2016). Living shorelines can enhance the nursery role of threatened estuarine habitats. *Ecological Applications*, *26*(1), 249–263. https://doi.org/10.1890/14-0716

Grebe, G. S., Byron, C. J., Gelais, A. S., Kotowicz, D. M., & Olson, T. K. (2019). An ecosystem approach to kelp aquaculture in the Americas and Europe. *Aquaculture Reports*, *15*, 100215. https://doi.org/10.1016/j.aqrep.2019.100215

Guannel, G., Ruggiero, P., Faries, J., Arkema, K. K., Pinsky, M., Gelfenbaum, G., Guerry, A. D., & Kim, C. K. (2015). Integrated modeling framework to quantify the coastal protection services supplied by vegetation. *Journal of Geophysical Research: Oceans*, *120*(1), 324–345. https://doi.org/10.1002/2014JC009821

Hansen, J. C. R., & Reidenbach, M. A. (2013). Seasonal Growth and Senescence of a Zostera marina Seagrass Meadow Alters Wave-Dominated Flow and Sediment Suspension Within a Coastal Bay. *Estuaries and Coasts*, *36*(6), 1099–1114. https://doi.org/10.1007/s12237-013-9620-5

Hasselmann, K., & Collins, J. I. (1968). Spectral dissipation of finite-depth gravity waves due to turbulent bottom friction. *Journal of Marine Research*, *26*(1), 1–12. http://www.journalofmarineresearch.org/

Henderson, S. M. (2019). Motion of buoyant, flexible aquatic vegetation under waves: Simple theoretical models and parameterization of wave dissipation. *Coastal Engineering*, *152*, 103497. https://doi.org/10.1016/j.coastaleng.2019.04.009

Henderson, S. M., Norris, B. K., Mullarney, J. C., & Bryan, K. R. (2017). Wave-frequency flows within a near-bed vegetation canopy. *Continental Shelf Research*, *147*, 91–101. https://doi.org/10.1016/j.csr.2017.06.003

Higuera, P., Lara, J. L., & Losada, I. J. (2013). Realistic wave generation and active wave absorption for Navier–Stokes models. *Coastal Engineering*, *71*, 102–118. https://doi.org/10.1016/j.coastaleng.2012.07.002

Houser, C., Trimble, S., & Morales, B. (2015). Influence of Blade Flexibility on the Drag Coefficient of Aquatic Vegetation. *Estuaries and Coasts*, *38*(2), 569–577. https://doi.org/10.1007/s12237-014-9840-3

Howell, C. T. (1992). *Investigation of the Dynamics of Low-Tension Cables* [Massachusetts Institute of Technology]. http://www.dtic.mil/docs/citations/ADA268458

Hsieh, S.-R., Shaw, S. W., & Pierre, C. (1994). Normal modes for large amplitude vibration of a cantilever beam. *International Journal of Solids and Structures*, *31*(14), 1981–2014. https://doi.org/10.1016/0020-7683(94)90203-8

Hu, J., Hu, Z., & Liu, P. L.-F. (2019). Surface water waves propagating over a submerged forest. *Coastal Engineering*, *152*, 103510. https://doi.org/10.1016/j.coastaleng.2019.103510

Hu, K., Chen, Q., Wang, H., Hartig, E. K., & Orton, P. M. (2018). Numerical modeling of salt marsh morphological change induced by Hurricane Sandy. *Coastal Engineering*, *132*, 63–81. https://doi.org/10.1016/j.coastaleng.2017.11.001

Hu, Z., Suzuki, T., Zitman, T., Uittewaal, W., & Stive, M. (2014). Laboratory study on wave dissipation by vegetation in combined current–wave flow. *Coastal Engineering*, *88*, 131–142. https://doi.org/10.1016/j.coastaleng.2014.02.009

Huai, W., Hu, Y., Zeng, Y., & Han, J. (2012). Velocity distribution for open channel flows with suspended vegetation. *Advances in Water Resources*, *49*, 56–61. https://doi.org/10.1016/j.advwatres.2012.07.001

Huang, I., Rominger, J., & Nepf, H. (2011). The motion of kelp blades and the surface renewal model. *Limnology and Oceanography*, *56*(4), 1453–1462. https://doi.org/10.4319/lo.2011.56.4.1453

Ikeda, S., Yamada, T., & Toda, Y. (2001). Numerical study on turbulent flow and honami in and above flexible plant canopy. *International Journal of Heat and Fluid Flow*, *22*(3), 252–258. https://doi.org/10.1016/S0142-727X(01)00087-X

Infantes, E., Orfila, A., Simarro, G., Terrados, J., Luhar, M., & Nepf, H. M. (2012). Effect of a seagrass (Posidonia oceanica) meadow on wave propagation. *Marine Ecology Progress Series*, *456*, 63–72. https://doi.org/10.3354/meps09754

Izaguirre, C., Méndez, F. J., Menéndez, M., & Losada, I. J. (2011). Global extreme wave height variability based on satellite data. *Geophysical Research Letters*, *38*(10), n/a-n/a. https://doi.org/10.1029/2011GL047302

Jackson, G. A. (1997). Currents in the high drag environment of a coastal kelp stand off California. *Continental Shelf Research*, *17*(15), 1913–1928. https://doi.org/10.1016/S0278-4343(97)00054-X

Jackson, G. A. (1984). Internal Wave Attenuation by Coastal Kelp Stands. *Journal of Physical Oceanography*, *14*(8), 1300–1306. https://doi.org/10.1175/1520-0485(1984)014<1300:IWABCK>2.0.CO;2

Jacobsen, N. G., McFall, B. C., & van der A, D. A. (2019). A frequency distributed dissipation model for canopies. *Coastal Engineering*, *150*, 135–146. https://doi.org/10.1016/j.coastaleng.2019.04.007

Jacobsen, N. G., Bakker, W., Uijttewaal, W. S. J., & Uittenbogaard, R. (2019). Experimental investigation of the wave-induced motion of and force distribution along a flexible stem. *Journal of Fluid Mechanics*, *880*, 1036–1069. https://doi.org/10.1017/jfm.2019.739

Jadhav, R. S., Chen, Q., & Smith, J. M. (2013). Spectral distribution of wave energy dissipation by salt marsh vegetation. *Coastal Engineering*, *77*, 99–107. https://doi.org/10.1016/j.coastaleng.2013.02.013

Jensen, B. L., Sumer, B. M., & Fredsøe, J. (1989). Turbulent oscillatory boundary layers at high Reynolds numbers. *Journal of Fluid Mechanics*, *206*, 265–297. https://doi.org/10.1017/S0022112089002302

Keller, H. B. (1971). A new difference scheme for parabolic problems. In *Numerical Solution of Partial Differential Equations--II* (pp. 327–350). Elsevier. https://doi.org/10.1016/B978-0-12-358502-8.50014-1

Keulegan, G. H., & Carpenter, L. H. (1958). Forces on Cylinders and Plates in an Oscillating Fluid. *Journal of Research of the National Bureau of Standards*, *60*(5), 423–440. https://nvlpubs.nist.gov/nistpubs/jres/60/jresv60n5p423_A1b.pdf

Knysh, A., Tsukrov, I., Chambers, M., Swift, M. R., Sullivan, C., & Drach, A. (2020). Numerical modeling of submerged mussel longlines with protective sleeves. *Aquacultural Engineering*, *88*, 102027. https://doi.org/10.1016/j.aquaeng.2019.102027

Kobayashi, N., Raichle, A. W., & Asano, T. (1993). Wave Attenuation by Vegetation. *Journal of Waterway, Port, Coastal, and Ocean Engineering*, *119*(1), 30–48. https://doi.org/10.1061/(ASCE)0733-950X(1993)119:1(30)

Koch, E. W., Barbier, E. B., Silliman, B. R., Reed, D. J., Perillo, G. M. M. E., Hacker, S. D., Granek, E. F., Primavera, J. H., Muthiga, N., Polasky, S., Halpern, B. S., Kennedy, C. J., Kappel, C. V., & Wolanski, E. (2009). Non-linearity in ecosystem services: Temporal and spatial variability in coastal protection. In *Frontiers in Ecology and the Environment* (Vol. 7, Issue 1, pp. 29–37). Ecological Society of America. https://doi.org/10.1890/080126

Koehl, M. A. R., Silk, W. K., Liang, H., & Mahadevan, L. (2008). How kelp produce blade shapes suited to different flow regimes: A new wrinkle. *Integrative and Comparative Biology*, *48*(6), 834–851. https://doi.org/10.1093/icb/icn069

Landmann, J., Ongsiek, T., Goseberg, N., Heasman, K., Buck, B., Paffenholz, J.-A., & Hildebrandt, A. (2019). Physical Modelling of Blue Mussel Dropper Lines for the Development of Surrogates and Hydrodynamic Coefficients. *Journal of Marine Science and Engineering*, *7*(3), 65. https://doi.org/10.3390/jmse7030065

Lauzon-Guay, J. S., Barbeau, M. A., Watmough, J., & Hamilton, D. J. (2006). Model for growth and survival of mussels Mytilus edulis reared in Prince Edward Island, Canada. *Marine Ecology Progress Series*, *323*, 171–183. https://doi.org/10.3354/meps323171

Leclercq, T., & de Langre, E. (2018). Reconfiguration of elastic blades in oscillatory flow. *Journal of Fluid Mechanics*, *838*, 606–630. https://doi.org/10.1017/jfm.2017.910

Lei, J., & Nepf, H. (2019a). Blade dynamics in combined waves and current. *Journal of Fluids and Structures*, *87*, 137–149. https://doi.org/10.1016/j.jfluidstructs.2019.03.020

Lei, J., & Nepf, H. (2019b). Wave damping by flexible vegetation: Connecting individual blade dynamics to the meadow scale. *Coastal Engineering*, *147*, 138–148. https://doi.org/10.1016/j.coastaleng.2019.01.008

Lei, J., & Nepf, H. M. (2016). Impact of current speed on mass flux to a model flexible seagrass blade. *Journal of Geophysical Research: Oceans*, *121*(7), 4763–4776. https://doi.org/10.1002/2016JC011826

Leonardi, N., Carnacina, I., Donatelli, C., Ganju, N. K., Plater, A. J., Schuerch, M., & Temmerman, S. (2018). Dynamic interactions between coastal storms and salt marshes: A review. *Geomorphology*, *301*, 92–107. https://doi.org/10.1016/j.geomorph.2017.11.001

Li, Y., Zhu, Q., Liu, L., & Tang, Y. (2018). Transient response of a SPAR-type floating offshore wind turbine with fractured mooring lines. *Renewable Energy*, *122*, 576–588. https://doi.org/10.1016/j.renene.2018.01.067

Lin, J., Li, C., & Zhang, S. (2016). Hydrodynamic effect of a large offshore mussel suspended aquaculture farm. *Aquaculture*, *451*, 147–155. https://doi.org/10.1016/j.aquaculture.2015.08.039

Liu, P. L. F., Chang, C.-W. W., Mei, C. C., Lomonaco, P., Martin, F. L., & Maza, M. (2015). Periodic water waves through an aquatic forest. *Coastal Engineering*, *96*, 100–117. https://doi.org/10.1016/j.coastaleng.2014.11.002

Longuet-Higgins, M. S. (1983). On the joint distribution of wave periods and amplitudes in a random wave field. *Proceedings of the Royal Society of London. A. Mathematical and Physical Sciences*, *389*(1797), 241–258. https://doi.org/10.1098/rspa.1983.0107

Losada, I. J., Maza, M., & Lara, J. L. (2016). A new formulation for vegetation-induced damping under combined waves and currents. *Coastal Engineering*, *107*, 1–13. https://doi.org/10.1016/j.coastaleng.2015.09.011

Lowe, R. J. (2005). Oscillatory flow through submerged canopies: 1. Velocity structure. *Journal of Geophysical Research*, *110*(C10), C10016. https://doi.org/10.1029/2004JC002788

Lowe, R. J., Falter, J. L., Koseff, J. R., Monismith, S. G., & Atkinson, M. J. (2007). Spectral wave flow attenuation within submerged canopies: Implications for wave energy dissipation. *Journal of Geophysical Research: Oceans*, *112*(5), C05018. https://doi.org/10.1029/2006JC003605

Luhar, M. (2012). Analytical and Experimental Studies of Plant-Flow Interaction at Multiple Scales [Massachusetts Institute of Technology]. In *Thesis*. http://dspace.mit.edu/handle/1721.1/78142

Luhar, M., Coutu, S., Infantes, E., Fox, S., & Nepf, H. M. (2010). Wave-induced velocities inside a model seagrass bed. *Journal of Geophysical Research: Oceans*, *115*(12), C12005. https://doi.org/10.1029/2010JC006345

Luhar, M., Infantes, E., & Nepf, H. (2017). Seagrass blade motion under waves and its impact on wave decay. *Journal of Geophysical Research: Oceans*, *122*(5), 3736–3752. https://doi.org/10.1002/2017JC012731

Luhar, M., Infantes, E., Orfila, A., Terrados, J., & Nepf, H. M. (2013). Field observations of wave-induced streaming through a submerged seagrass (Posidonia oceanica) meadow. *Journal of Geophysical Research: Oceans*, *118*(4), 1955–1968. https://doi.org/10.1002/jgrc.20162

Luhar, M., & Nepf, H. M. (2016). Wave-induced dynamics of flexible blades. *Journal of Fluids and Structures*, *61*, 20–41. https://doi.org/10.1016/j.jfluidstructs.2015.11.007

Luhar, M., & Nepf, H. M. (2011). Flow-induced reconfiguration of buoyant and flexible aquatic vegetation. *Limnology and Oceanography*, *56*(6), 2003–2017. https://doi.org/10.4319/lo.2011.56.6.2003

Madsen, O. S., Poon, Y.-K., & Graber, H. C. (1988). SPECTRAL WAVE ATTENUATION BY BOTTOM FRICTION: THEORY. *Coastal Engineering Proceedings*, *1*(21), 492–504. https://doi.org/10.1061/9780872626874.035

Marsooli, R., Orton, P. M., & Mellor, G. (2017). Modeling wave attenuation by salt marshes in Jamaica Bay, New York, using a new rapid wave model. *Journal of Geophysical Research: Oceans*, *122*(7), 5689–5707. https://doi.org/10.1002/2016JC012546

Mattila, J., Chaplin, G., Eilers, M. R., Heck, K. L., O'Neal, J. P., & Valentine, J. F. (1999). Spatial and diurnal distribution of invertebrate and fish fauna of a Zostera marina bed and nearby unvegetated sediments in Damariscotta River, Maine (USA). *Journal of Sea Research*, *41*(4), 321–332. https://doi.org/10.1016/S1385-1101(99)00006-4

Maza, M., Lara, J. L. L., Losada, I. J., Ondiviela, B., Trinogga, J., & Bouma, T. J. (2015). Large-scale 3-D experiments of wave and current interaction with real vegetation. Part 2: Experimental analysis. *Coastal Engineering*, *106*, 73–86. https://doi.org/10.1016/j.coastaleng.2015.09.010

Maza, M., Lara, J. L., & Losada, I. J. (2019). Experimental analysis of wave attenuation and drag forces in a realistic fringe Rhizophora mangrove forest. *Advances in Water Resources*, *131*, 103376. https://doi.org/10.1016/j.advwatres.2019.07.006

McGehee, D. D. (2016). Design and Monitoring of a Small Living Shoreline Scaled for Private Properties on Exposed, Rapidly-Eroding Coasts. *B. Crookston & B. Tullis (Eds.), Hydraulic Structures and Water System Management. 6th IAHR International Symposium on Hydraulic Structures, Portland, OR, 27-30 June*, 488–497. https://doi.org/10.15142/T3530628160853

McKone, K. L. (2009). Light available to the seagrass zostera marina when exposed to currents and waves. *M.Sc. Thesis, University of Maryland, College Park*. https://drum.lib.umd.edu/bitstream/handle/1903/9352/McKone_umd_0117N_10401.pdf?sequence=1

MEA. (2005). Ecosystems and human well-being: current state and trends. *Millennium Ecosystem Assessment, Global Assessment Reports*, *1*. https://www.millenniumassessment.org/documents/document.766.aspx.pdf

Mei, C. C., Chan, I.-C., Liu, P. L.-F., Huang, Z., & Zhang, W. (2011). Long waves through emergent coastal vegetation. *Journal of Fluid Mechanics*, *687*, 461–491. https://doi.org/10.1017/jfm.2011.373

Mendez, F. J., & Losada, I. J. (2004). An empirical model to estimate the propagation of random breaking and nonbreaking waves over vegetation fields. *Coastal Engineering*, *51*(2), 103–118. https://doi.org/10.1016/j.coastaleng.2003.11.003

Méndez, F. J., Losada, I. J., & Losada, M. A. (1999). Hydrodynamics induced by wind waves in a vegetation field. *Journal of Geophysical Research*, *104*(C8), 18383–18396. https://doi.org/10.1029/1999JC900119

Möller, I. (2006). Quantifying saltmarsh vegetation and its effect on wave height dissipation: Results from a UK East coast saltmarsh. *Estuarine, Coastal and Shelf Science*, *69*(3–4), 337–351. https://doi.org/10.1016/j.ecss.2006.05.003

Möller, I. (2019). Applying Uncertain Science to Nature-Based Coastal Protection: Lessons From Shallow Wetland-Dominated Shores. *Frontiers in Environmental Science*, *7*. https://doi.org/10.3389/fenvs.2019.00049

Möller, I., Kudella, M., Rupprecht, F., Spencer, T., Paul, M., van Wesenbeeck, B. K., Wolters, G., Jensen, K., Bouma, T. J., Miranda-Lange, M., & Schimmels, S. (2014). Wave attenuation over coastal salt marshes under storm surge conditions. *Nature Geoscience*, *7*(10), 727–731. https://doi.org/10.1038/ngeo2251

Möller, I., & Spencer, T. (2002). Wave dissipation over macro-tidal saltmarshes: Effects of marsh edge typology and vegetation change. *Journal of Coastal Research*, *36*(36), 506–521. https://doi.org/ISSN:0749-0208

Moore, K. A. (2004). Influence of Seagrasses on Water Quality in Shallow Regions of the Lower Chesapeake Bay. *Journal of Coastal Research*, *10045*(45), 162–178. https://doi.org/10.2112/SI45-162.1

Moosavi, S. (2017). Ecological Coastal Protection: Pathways to Living Shorelines. *Procedia Engineering*, *196*(2017), 930–938. https://doi.org/10.1016/j.proeng.2017.08.027

Morison, J. R., Johnson, J. W., & Schaaf, S. A. (1950). The Force Exerted by Surface Waves on Piles. *Journal of Petroleum Technology*, *2*(05), 149–154. https://doi.org/10.2118/950149-G

Mork, M. (1996). The effect of kelp in wave damping. *Sarsia*, *80*(4), 323–327. https://doi.org/10.1080/00364827.1996.10413607

Morris, R. L., Graham, T. D. J., Kelvin, J., Ghisalberti, M., & Swearer, S. E. (2019). Kelp beds as coastal protection: wave attenuation of Ecklonia radiata in a shallow coastal bay. *Annals of Botany*, *125*, 235–246. https://doi.org/10.1093/aob/mcz127

Mullarney, J. C., & Henderson, S. M. (2010). Wave-forced motion of submerged single-stem vegetation. *Journal of Geophysical Research*, *115*(C12), C12061. https://doi.org/10.1029/2010JC006448

Myrhaug, D. (1995). Bottom friction beneath random waves. *Coastal Engineering*, *24*(3–4), 259–273. https://doi.org/10.1016/0378-3839(94)00023-Q

Neckles, H. H. A., Short, F. T. F., Barker, S., & Kopp, B. S. B. (2005). Disturbance of eelgrass Zostera marina by commercial mussel Mytilus edulis harvesting in Maine: dragging impacts and habitat recovery. *Marine Ecology Progress Series*, *285*, 57–73. https://doi.org/10.3354/meps285057

Nepf, H. M. (2011). Flow Over and Through Biota. In *Treatise on Estuarine and Coastal Science* (Vol. 2, pp. 267–288). Elsevier. https://doi.org/10.1016/B978-0-12-374711-2.00213-8

Nepf, H. M. (2012). Flow and Transport in Regions with Aquatic Vegetation. *Annual Review of Fluid Mechanics*, *44*(1), 123–142. https://doi.org/10.1146/annurev-fluid-120710-101048

Newell, C. R., Short, F., Hoven, H., Healey, L., Panchang, V., & Cheng, G. (2010). The dispersal dynamics of juvenile plantigrade mussels (Mytilus edulis L.) from eelgrass (Zostera marina) meadows in Maine, U.S.A. *Journal of Experimental Marine Biology and Ecology*, *394*(1–2), 45–52. https://doi.org/10.1016/j.jembe.2010.06.025

Nowacki, D. J., Beudin, A., & Ganju, N. K. (2017). Spectral wave dissipation by submerged aquatic vegetation in a back-barrier estuary. *Limnology and Oceanography*, *62*(2), 736–753. https://doi.org/10.1002/lno.10456

Ondiviela, B., Losada, I. J., Lara, J. L., Maza, M., Galván, C., Bouma, T. J., & van Belzen, J. (2014). The role of seagrasses in coastal protection in a changing climate. *Coastal Engineering*, *87*, 158–168. https://doi.org/10.1016/j.coastaleng.2013.11.005

Ozeren, Y., Wren, D. G., & Wu, W. (2014). Experimental Investigation of Wave Attenuation through Model and Live Vegetation. *Journal of Waterway, Port, Coastal, and Ocean Engineering*, *140*(5), 04014019. https://doi.org/10.1061/(ASCE)WW.1943-5460.0000251

Pace, N. L. (2011). Wetlands or Seawalls? Adapting Shoreline Regulation to Address Sea Level Rise and Wetland Preservation in the Gulf of Mexico. *Journal of Land Use & Environmental Law*, *26*(2), 327–363. https://www.jstor.org/stable/42842968

Paul, M., & Amos, C. L. (2011). Spatial and seasonal variation in wave attenuation over Zostera noltii. *Journal of Geophysical Research*, *116*(C8), C08019. https://doi.org/10.1029/2010JC006797

Paul, M., Bouma, T. J., & Amos, C. L. (2012). Wave attenuation by submerged vegetation: combining the effect of organism traits and tidal current. *Marine Ecology Progress Series*, *444*, 31–41. https://doi.org/10.3354/meps09489

Paul, M. (2018). The protection of sandy shores – Can we afford to ignore the contribution of seagrass? *Marine Pollution Bulletin*, *134*, 152–159. https://doi.org/10.1016/j.marpolbul.2017.08.012

Peirce, F. T. (1930). 26—THE "HANDLE" OF CLOTH AS A MEASURABLE QUANTITY. *Journal of the Textile Institute Transactions*, *21*(9), T377–T416. https://doi.org/10.1080/19447023008661529

Peng, Z., Zou, Q., Reeve, D., & Wang, B. (2009). Parameterisation and transformation of wave asymmetries over a low-crested breakwater. *Coastal Engineering*, *56*(11–12), 1123–1132. https://doi.org/10.1016/j.coastaleng.2009.08.005

Peteiro, C., & Freire, Ó. (2013). Biomass yield and morphological features of the seaweed Saccharina latissima cultivated at two different sites in a coastal bay in the Atlantic coast of Spain. *Journal of Applied Phycology*, *25*(1), 205–213. https://doi.org/10.1007/s10811-012-9854-9

Peteiro, C., Sánchez, N., & Martínez, B. (2016). Mariculture of the Asian kelp Undaria pinnatifida and the native kelp Saccharina latissima along the Atlantic coast of Southern Europe: An overview. *Algal Research*, *15*, 9–23. https://doi.org/10.1016/j.algal.2016.01.012

Pinsky, M. L., Guannel, G., & Arkema, K. K. (2013). Quantifying wave attenuation to inform coastal habitat conservation. *Ecosphere*, *4*(8), art95. https://doi.org/10.1890/ES13-00080.1

Plew, D. R. (2011). Depth-Averaged Drag Coefficient for Modeling Flow through Suspended Canopies. *Journal of Hydraulic Engineering*, *137*(2), 234–247. https://doi.org/10.1061/(ASCE)HY.1943-7900.0000300

Plew, D. R., Enright, M. P., Nokes, R. I., & Dumas, J. K. (2009). Effect of mussel bio-pumping on the drag on and flow around a mussel crop rope. *Aquacultural Engineering*, *40*(2), 55–61. https://doi.org/10.1016/j.aquaeng.2008.12.003

Plew, D. R., Stevens, C. L., Spigel, R. H., & Hartstein, N. D. (2005). Hydrodynamic Implications of Large Offshore Mussel Farms. *IEEE Journal of Oceanic Engineering*, *30*(1), 95–108. https://doi.org/10.1109/JOE.2004.841387

Raman-Nair, W., & Colbourne, B. (2003). Dynamics of a mussel longline system. *Aquacultural Engineering*, *27*(3), 191–212. https://doi.org/10.1016/S0144-8609(02)00083-3

Raman-Nair, W., Colbourne, B., Gagnon, M., & Bergeron, P. (2008). Numerical model of a mussel longline system: Coupled dynamics. *Ocean Engineering*, *35*(13), 1372–1380. https://doi.org/10.1016/j.oceaneng.2008.05.008

Rao, S. S. (2007). *Vibration of Continuous Systems*. John Wiley & Sons, Inc. https://wp.kntu.ac.ir/hrahmanei/Adv-Vibrations-Books/Continuous-Vibrations-Rao.pdf

Rao, S. S. (2010). Mechanical Vibrations Fifth Edition. In *English*.

Raupach, M. R., & Thom, A. S. (1981). Turbulence in and above Plant Canopies. *Annual Review of Fluid Mechanics*, *13*(1), 97–129. https://doi.org/10.1146/annurev.fl.13.010181.000525

Riffe, K. C., Henderson, S. M., & Mullarney, J. C. (2011). Wave dissipation by flexible vegetation. *Geophysical Research Letters*, *38*(18), n/a-n/a. https://doi.org/10.1029/2011GL048773

Rosman, J. H., Denny, M. W., Zeller, R. B., Monismith, S. G., & Koseff, J. R. (2013). Interaction of waves and currents with kelp forests (Macrocystis pyrifera): Insights from a dynamically scaled laboratory model. *Limnology and Oceanography*, *58*(3), 790–802. https://doi.org/10.4319/lo.2013.58.3.0790

Rosman, J. H., Koseff, J. R., Monismith, S. G., & Grover, J. (2007). A field investigation into the effects of a kelp forest (Macrocystis pyrifera) on coastal hydrodynamics and transport. *Journal of Geophysical Research: Oceans*, *112*(2), 1–16. https://doi.org/10.1029/2005JC003430

Rupprecht, F., Möller, I., Paul, M., Kudella, M., Spencer, T., van Wesenbeeck, B. K., Wolters, G., Jensen, K., Bouma, T. J., Miranda-Lange, M., & Schimmels, S. (2017). Vegetation-wave interactions in salt marshes under storm surge conditions. *Ecological Engineering*, *100*, 301–315. https://doi.org/10.1016/j.ecoleng.2016.12.030

Saleh, F., & Weinstein, M. P. (2016). The role of nature-based infrastructure (NBI) in coastal resiliency planning: A literature review. *Journal of Environmental Management*, *183*, 1088–1098. https://doi.org/10.1016/j.jenvman.2016.09.077

Sánchez-González, J. F., Sánchez-Rojas, V., & Memos, C. D. (2011). Wave attenuation due to Posidonia oceanica meadows. *Journal of Hydraulic Research*, *49*(4), 503–514. https://doi.org/10.1080/00221686.2011.552464

Sarpkaya, T., & O'Keefe, J. L. (1996). Oscillating Flow About Two and Three-Dimensional Bilge Keels. *Journal of Offshore Mechanics and Arctic Engineering*, *118*(1), 1–6. https://doi.org/10.1115/1.2828796

Schneider, C. A., Rasband, W. S., & Eliceiri, K. W. (2012). NIH Image to ImageJ: 25 years of image analysis. *Nature Methods*, *9*(7), 671–675. https://doi.org/10.1038/nmeth.2089

Schulze, D., Rupprecht, F., Nolte, S., & Jensen, K. (2019). Seasonal and spatial within-marsh differences of biophysical plant properties: implications for wave attenuation capacity of salt marshes. *Aquatic Sciences*, *81*, 65. https://doi.org/10.1007/s00027-019-0660-1

Scyphers, S. B., Powers, S. P., Heck, K. L., & Byron, D. (2011). Oyster Reefs as Natural Breakwaters Mitigate Shoreline Loss and Facilitate Fisheries. *PLoS ONE*, *6*(8), e22396. https://doi.org/10.1371/journal.pone.0022396

Seymour, R. J., & Hanes, D. (1979). Performance analysis of tethered float breakwater. *Journal of the Waterway, Port, Coastal and Ocean Division*, *105*(3), 265–280. https://cedb.asce.org/CEDBsearch/record.jsp?dockey=0008922

Smyth, C., & Hay, A. E. (2002). Wave Friction Factors in Nearshore Sands. *Journal of Physical Oceanography*, *32*(12), 3490–3498. https://doi.org/10.1175/1520-0485(2002)032<3490:WFFINS>2.0.CO;2

Sollitt, C. K., & Cross, R. H. (1972). WAVE TRANSMISSION THROUGH PERMEABLE BREAKWATERS. *Coastal Engineering Proceedings*, *1*(13), 99. https://doi.org/10.9753/icce.v13.99

Sparks, C. P. (2009). The Influence of Tension, Pressure and Weight on Pipe and Riser Deformations and Stresses. *Journal of Energy Resources Technology*, *106*(1), 46. https://doi.org/10.1115/1.3231023

Stévant, P., Rebours, C., & Chapman, A. (2017). Seaweed aquaculture in Norway: recent industrial developments and future perspectives. *Aquaculture International*, *25*(4), 1373–1390. https://doi.org/10.1007/s10499-017-0120-7

Stevens, C. L., Plew, D. R., Smith, M. J., & Fredriksson, D. W. (2007). Hydrodynamic Forcing of Long-Line Mussel Farms: Observations. *Journal of Waterway, Port, Coastal, and Ocean Engineering*, *133*(3), 192–199. https://doi.org/10.1061/(ASCE)0733-950X(2007)133:3(192)

Stevens, C., Plew, D., Hartstein, N., & Fredriksson, D. (2008). The physics of open-water shellfish aquaculture. *Aquacultural Engineering*, *38*(3), 145–160. https://doi.org/10.1016/j.aquaeng.2008.01.006

Sutton-Grier, A. E., Wowk, K., & Bamford, H. (2015). Future of our coasts: The potential for natural and hybrid infrastructure to enhance the resilience of our coastal communities, economies and ecosystems. *Environmental Science & Policy*, *51*, 137–148. https://doi.org/10.1016/j.envsci.2015.04.006

Suzuki, T., Hu, Z., Kumada, K., Phan, L. K., & Zijlema, M. (2019). Non-hydrostatic modeling of drag, inertia and porous effects in wave propagation over dense vegetation fields. *Coastal Engineering*, *149*, 49–64. https://doi.org/10.1016/j.coastaleng.2019.03.011

Suzuki, T., Zijlema, M., Burger, B., Meijer, M. C., & Narayan, S. (2012). Wave dissipation by vegetation with layer schematization in SWAN. *Coastal Engineering*, *59*(1), 64–71. https://doi.org/10.1016/j.coastaleng.2011.07.006

Syvitski, J. P. M., Kettner, A. J., Overeem, I., Hutton, E. W. H., Hannon, M. T., Brakenridge, G. R., Day, J., Vörösmarty, C., Saito, Y., Giosan, L., & Nicholls, R. J. (2009). Sinking deltas due to human activities. *Nature Geoscience*, *2*(10), 681–686. https://doi.org/10.1038/ngeo629

Tan, C., Huang, B., Liu, D., Qiu, J., Chen, H., Li, Y., & Hu, Z. (2019). Effect of Mimic Vegetation with Different Stiffness on Regular Wave Propagation and Turbulence. *Water*, *11*(1), 109. https://doi.org/10.3390/w11010109

Tang, C., Lei, J., & Nepf, H. M. (2019). Impact of Vegetation-Generated Turbulence on the Critical, Near-Bed, Wave-Velocity for Sediment Resuspension. *Water Resources Research*, *55*(7), 5904–5917. https://doi.org/10.1029/2018WR024335

Tebaldi, C., Strauss, B. H., & Zervas, C. E. (2012). Modelling sea level rise impacts on storm surges along US coasts. *Environmental Research Letters*, *7*(1), 014032. https://doi.org/10.1088/1748-9326/7/1/014032

Temmerman, S., Meire, P., Bouma, T. J., Herman, P. M. J., Ysebaert, T., & De Vriend, H. J. (2013). Ecosystem-based coastal defence in the face of global change. In *Nature* (Vol. 504, Issue 7478, pp. 79–83). Nature Publishing Group. https://doi.org/10.1038/nature12859

Tjavaras, A. A., Zhu, Q., Liu, Y., Triantafyllou, M. S., & Yue, D. K. P. (1998). THE MECHANICS OF HIGHLY-EXTENSIBLE CABLES. *Journal of Sound and Vibration*, *213*(4), 709–737. https://doi.org/10.1006/jsvi.1998.1526

Triantafyllou, M. S., & Howell, C. T. (1994). Dynamic Response of Cables Under Negative Tension: an Ill-Posed Problem. *Journal of Sound and Vibration*, *173*(4), 433–447. https://doi.org/10.1006/jsvi.1994.1239

UNEP. (2006). Marine and coastal ecosystems and human well-being: A synthesis report based on the findings of the Millennium Ecosystem Assessment. *UNEP*, 76. https://www.millenniumassessment.org/documents/Document.799.aspx.pdf

Utter, & Denny. (1996). Wave-induced forces on the giant kelp Macrocystis pyrifera (Agardh): field test of a computational model. *The Journal of Experimental Biology*, *199*, 2645–2654. https://jeb.biologists.org/content/199/12/2645.short

van Rooijen, A., Lowe, R., Rijnsdorp, D., Ghisalberti, M., Jacobsen, N. G., & McCall, R. (2020). Wave-driven mean flow dynamics in submerged canopies. *Journal of Geophysical Research: Oceans*, 0–3. https://doi.org/10.1029/2019JC015935

Van Veelen, T. J., Fairchild, T. P., Reeve, D. E., Karunarathna, H., Van Veelen, T. J., Fairchild, T. P., & Karunarathna, D. E. (2020). Experimental study on vegetation flexibility as control parameter for wave damping and velocity structure. *Coastal Engineering*, *157*, 103648. https://doi.org/10.1016/j.coastaleng.2020.103648

Vettori, D., & Nikora, V. (2019). Flow-seaweed interactions of Saccharina latissima at a blade scale: turbulence, drag force, and blade dynamics. *Aquatic Sciences*, *81*(4), 61. https://doi.org/10.1007/s00027-019-0656-x

Vettori, D., & Nikora, V. (2018). Flow–seaweed interactions: a laboratory study using blade models. *Environmental Fluid Mechanics*, *18*(3), 611–636. https://doi.org/10.1007/s10652-017-9556-6

Vettori, D., & Nikora, V. (2020). Hydrodynamic performance of vegetation surrogates in hydraulic studies: a comparative analysis of seaweed blades and their physical models. *Journal of Hydraulic Research*, *58*(2), 248–261. https://doi.org/10.1080/00221686.2018.1562999

Vettori, D., & Nikora, V. (2017). Morphological and mechanical properties of blades of Saccharina latissima. *Estuarine, Coastal and Shelf Science*, *196*, 1–9. https://doi.org/10.1016/j.ecss.2017.06.033

Vuik, V., Jonkman, S. N., Borsje, B. W., & Suzuki, T. (2016). Nature-based flood protection: The efficiency of vegetated foreshores for reducing wave loads on coastal dikes. *Coastal Engineering*, *116*, 42–56. https://doi.org/10.1016/j.coastaleng.2016.06.001

Vuik, V., Suh Heo, H. Y., Zhu, Z., Borsje, B. W., & Jonkman, S. N. (2018). Stem breakage of salt marsh vegetation under wave forcing: A field and model study. *Estuarine, Coastal and Shelf Science*, *200*, 41–58. https://doi.org/10.1016/j.ecss.2017.09.028

Walls, A. M., Kennedy, R., Edwards, M. D., & Johnson, M. P. (2017). Impact of kelp cultivation on the Ecological Status of benthic habitats and Zostera marina seagrass biomass. *Marine Pollution Bulletin*, *123*(1–2), 19–27. https://doi.org/10.1016/j.marpolbul.2017.07.048

Weinkle, J., Landsea, C., Collins, D., Musulin, R., Crompton, R. P., Klotzbach, P. J., & Pielke, R. (2018). Normalized hurricane damage in the continental United States 1900–2017. *Nature Sustainability*, *1*(12), 808–813. https://doi.org/10.1038/s41893-018-0165-2

Weitzman, J. S., Aveni-Deforge, K., Koseff, J. R., & Thomas, F. (2013). Uptake of dissolved inorganic nitrogen by shallow seagrass communities exposed to wave-driven unsteady flow. *Marine Ecology Progress Series*, *475*, 65–83. https://doi.org/10.3354/meps09965

Weitzman, J. S., Zeller, R. B., Thomas, F. I. M., & Koseff, J. R. (2015). The attenuation of current- and wave-driven flow within submerged multispecific vegetative canopies. *Limnology and Oceanography*, *60*(6), 1855–1874. https://doi.org/10.1002/lno.10121

Wu, W.-C., Ma, G., & Cox, D. T. (2016). Modeling wave attenuation induced by the vertical density variations of vegetation. *Coastal Engineering*, *112*, 17–27. https://doi.org/10.1016/j.coastaleng.2016.02.004

Xiao, X., Agusti, S., Lin, F., Li, K., Pan, Y., Yu, Y., Zheng, Y., Wu, J., & Duarte, C. M. (2017). Nutrient removal from Chinese coastal waters by large-scale seaweed aquaculture. *Scientific Reports*, *7*(1), 46613. https://doi.org/10.1038/srep46613

Xie, D., Zou, Q.-P., Mignone, A., & MacRae, J. D. (2019). Coastal flooding from wave overtopping and sea level rise adaptation in the northeastern USA. *Coastal Engineering*, *150*, 39–58. https://doi.org/10.1016/j.coastaleng.2019.02.001

Yang, Y., Chai, Z., Wang, Q., Chen, W., He, Z., & Jiang, S. (2015). Cultivation of seaweed Gracilaria in Chinese coastal waters and its contribution to environmental improvements. *Algal Research*, *9*, 236–244. https://doi.org/10.1016/j.algal.2015.03.017

Zeller, R. B., Weitzman, J. S., Abbett, M. E., Zarama, F. J., Fringer, O. B., & Koseff, J. R. (2014). Improved parameterization of seagrass blade dynamics and wave attenuation based on numerical and laboratory experiments. *Limnology and Oceanography*, *59*(1), 251–266. https://doi.org/10.4319/lo.2014.59.1.0251

Zeller, R. B., Zarama, F. J., Weitzman, J. S., & Koseff, J. R. (2015). A simple and practical model for combined wave–current canopy flows. *Journal of Fluid Mechanics*, *767*, 842–880. https://doi.org/10.1017/jfm.2015.59

Zhang, Y., Tang, C., & Nepf, H. M. (2018). Turbulent Kinetic Energy in Submerged Model Canopies Under Oscillatory Flow. *Water Resources Research*, *54*(3), 1734–1750. https://doi.org/10.1002/2017WR021732

Zhu, L., & Chen, Q. (2015). Numerical Modeling of Surface Waves over Submerged Flexible Vegetation. *Journal of Engineering Mechanics*, *141*(8), A4015001. https://doi.org/10.1061/(ASCE)EM.1943-7889.0000913

Zhu, L., Huguenard, K., & Fredriksson, D. (2018). INTERACTION BETWEEN WAVES AND HANGING HIGHLY FLEXIBLE KELP BLADES. *Coastal Engineering Proceedings*, *1*(36), 31. https://doi.org/10.9753/icce.v36.papers.31

Zhu, L., Huguenard, K., & Fredriksson, D. W. (2019). Dynamic Analysis of Longline Aquaculture Systems with a Coupled 3D Numerical Model. *The Twenty-Ninth (2019) International Ocean and Polar Engineering Conference*, 1305–1310. https://onepetro.org/conference-paper/ISOPE-I-19-235

Zhu, L., Huguenard, K., Zou, Q., Fredriksson, D. W., & Xie, D. (2020a). Aquaculture farms as nature-based coastal protection: Random wave attenuation by suspended and submerged canopies. *Coastal Engineering*, *160*, 103737. https://doi.org/10.1016/j.coastaleng.2020.103737

Zhu, L., & Zou, Q. (2017). THREE-LAYER ANALYTICAL SOLUTION FOR WAVE ATTENUATION BY SUSPENDED AND NONSUSPENDED VEGETATION CANOPY. *Coastal Engineering Proceedings*, *1*(35), 27. https://doi.org/10.9753/icce.v35.waves.27

Zhu, L., Zou, Q., Huguenard, K., & Fredriksson, D. W. (2020b). Mechanisms for the Asymmetric Motion of Submerged Aquatic Vegetation in Waves: A Consistent-Mass Cable Model. *Journal of Geophysical Research: Oceans*, *125*(2), 1–31. https://doi.org/10.1029/2019JC015517

Zijlema, M., Stelling, G., & Smit, P. (2011). SWASH: An operational public domain code for simulating wave fields and rapidly varied flows in coastal waters. *Coastal Engineering*, *58*(10), 992–1012. https://doi.org/10.1016/j.coastaleng.2011.05.015

Zou, Q. (2004). NOTES AND CORRESPONDENCE A Simple Model for Random Wave Bottom Friction and Dissipation. *Journal of Physical Oceanography*, *34*(6), 1459–1467. https://doi.org/10.1175/1520-0485(2004)034<1459:ASMFRW>2.0.CO;2

Zou, Q., & Hay, A. E. (2003). The Vertical Structure of the Wave Bottom Boundary Layer over a Sloping Bed: Theory and Field Measurements. *Journal of Physical Oceanography*, *33*(7), 1380–1400. https://doi.org/10.1175/1520-0485(2003)033<1380:TVSOTW>2.0.CO;2

Zou, Q., Hay, A. E., & Bowen, A. J. (2003). Vertical structure of surface gravity waves propagating over a sloping seabed: Theory and field measurements. *Journal of Geophysical Research: Oceans*, *108*(8), 3265. https://doi.org/10.1029/2002JC001432

Zou, Q., & Peng, Z. (2011). Evolution of wave shape over a low-crested structure. *Coastal Engineering*, *58*(6), 478–488. https://doi.org/10.1016/j.coastaleng.2011.01.001

APPENDIX A: CONDITIONS FOR SYMMETRIC BLADE MOTION IN SYMMETRIC WAVES

The absolute symmetric motion does not exist due to the phase differences Ψ_t and Ψ_n. However, when Ψ_t and Ψ_n are close to 0, equations (2.28) and (2.29) hold such that $\{T(s,t), u(s,t), -w(s,t), -\phi(s,t)\}$ is also a solution to the governing equations (2.18) and (2.19), resulting in a relatively symmetric motion. Therefore, the conditions for relatively symmetric motion are obtained, i.e., $|\Psi_t| \ll 1$ in (2.36) and $|\Psi_n| \ll 1$ in (2.37).

According to equations (2.24) to (2.25) and (2.30) to (2.31), the wave orbital velocities at time t and $t + T_w/2$ have the same amplitude. Therefore, the hydrodynamic coefficients C_d, C_f, and C_m are the same at both positions, indicating that the hydrodynamic coefficients do not contribute to the generation of asymmetric motion. Generally, the driving forces in the normal direction dominate so that the contributions of Ψ_n to asymmetric motion is expected to be more significant and the tangential phase difference Ψ_t can be neglected due to the negligible forces in the tangential direction. Thus, the blade motion is symmetric when only equation (2.37) is satisfied.

For bottom-rooted blade configuration such that $|x| \le l$ and $|z| \le l$, it is evident that $kx + \arctan(\tan\phi \tanh kz) < kl + |\tan\phi \tanh kz| < (1 + |\tan\phi|)\, kl = 2\pi(1 + |\tan\phi|)l/L$. Since the blade cannot be fully horizontal, thus, $|\tan\phi|$ is finited. Therefore, one condition for $|\Psi_n| \ll 1$ in (2.37) can be obtained,

$$l/L \ll 1. \tag{A.1}$$

In fact, if $l/L \ll 1$, $\tanh kz \approx 0$ so that $|\Psi_t| \approx 2kx < 4\pi l/L \ll 1$ such that equation (2.36) is also satisfied. Therefore, equation (A.1) is one condition for symmetric blade motion. For completely submerged blades such that $l \le h$, then $l/L \le h/L$ so that the following condition for equation (A.1) can be obtained,

$$h/L \ll 1, \tag{A.2}$$

which is also a condition for symmetric blade motion. One example of blade symmetric motion in shallow water waves is shown on Figure A.1. In finite-water-depth waves with $h/L \sim O(1)$, $l/L = (h/L) \cdot (l/h) \sim O(l/h)$ so that the following condition for equation (A.1) can be obtained,

$$l/h \ll 1, \tag{A.3}$$

which is also a condition for symmetric blade motion.

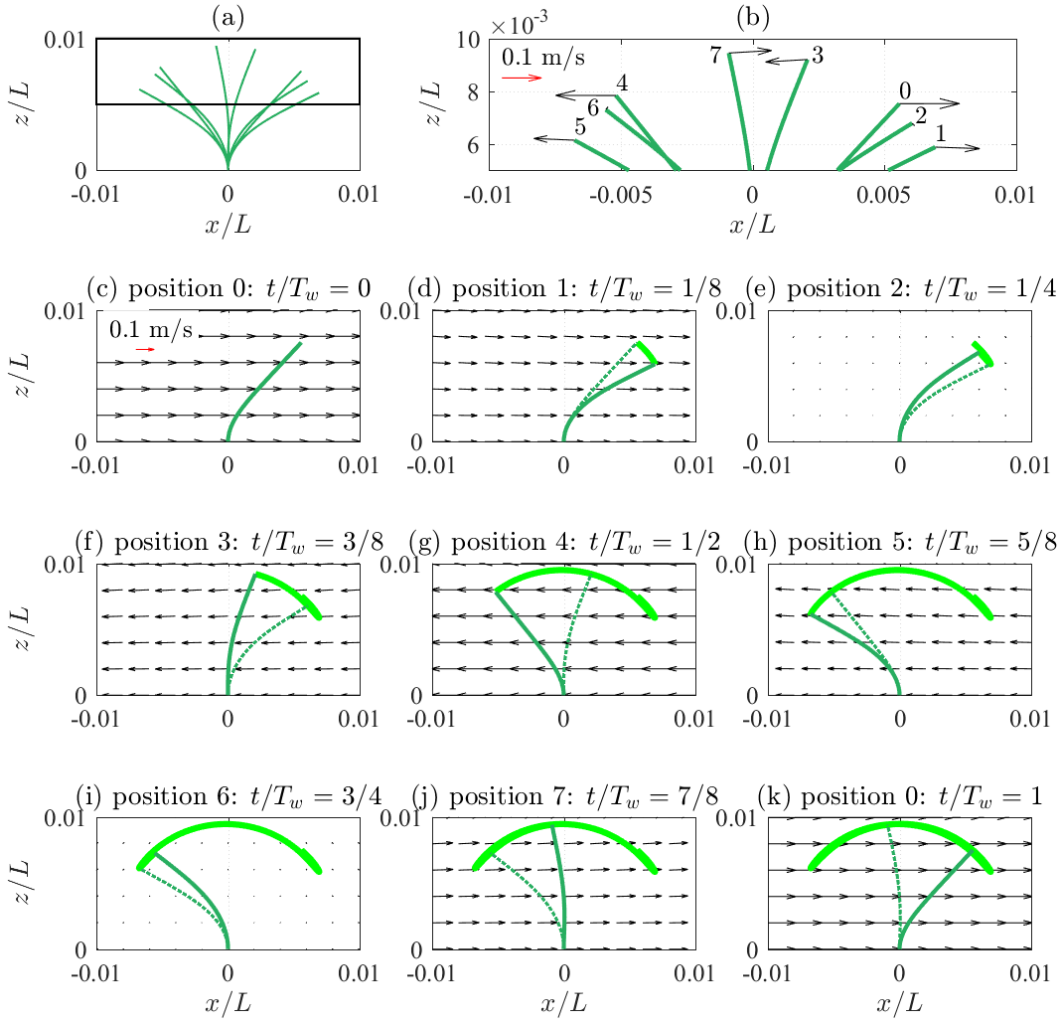

Figure A.1. The postures of a 20 cm-long blade (in green) in the wave flow field with wave period $T_w =$ 6.8 s and amplitude $a_w = 5$ cm in 1 m-deep water (shallow water waves). The blade posture asymmetry is $\beta_{xT} = 0.04$. The waves propagate from left to right. The dark thin green lines indicate the blade postures. The blade displacements (x, z) are normalized by wavelength (L). (a) The blade postures from positions 0 to 7. (b) The upper parts (zoom in) of the blade postures labeled number 0 to 7, which indicate the blade positions at 8 wave phases with $t/T_w = 0$, 1/8, 1/4, 3/8, 1/2, 5/8, 3/4, 7/8, and 1. The black arrows indicate wave orbital velocity at the blade tip. (c) to (k) show the blade postures and wave flow field. The green solid line indicates the current blade posture and the dashed green lines indicate the blade posture at previous one position. The light thick green line indicates the trajectory of the blade tip. The black arrows indicate the wave flow field.

APPENDIX B: WAVE HEIGHT FITTING ALONG A CANOPY WITH REFLECTIVE WAVES

Assuming the incident wave height (H_{I0}) and reflective wave height (H_{RL_v}) decay at the same decay coefficient k_D following (3.12), the incident water elevation (η_I) and reflective water elevation (η_R) can be expressed as

$$\eta_I = \frac{H_{I0}}{2}\frac{1}{1+k_D H_{I0} x}\cos(kx - \omega t + \epsilon_I) \tag{B.1}$$

and

$$\eta_R = \frac{H_{Rl}}{2}\frac{1}{1+k_D H_{RL_v}(L_v - x)}\cos(kx + \omega t + \epsilon_R), \tag{B.2}$$

respectively, where ϵ_I and ϵ_R are the incident wave phase and reflective wave phase, respectively. Therefore, the combined water elevation,

$$\eta = \eta_I + \eta_R = \frac{1}{2}\left[\frac{H_{I0}}{1+k_D H_{I0} x}\cos(kx + \epsilon_I) + \frac{H_{RL_v}}{1+k_D H_{RL_v}(L_v - x)}\cos(kx + \epsilon_R)\right]\cos(\omega t) +$$

$$\frac{1}{2}\left[\frac{H_{I0}}{1+k_D H_{I0} x}\sin(kx + \epsilon_I) - \frac{H_{RL_v}}{1+k_D H_{RL_v}(L_v - x)}\sin(kx + \epsilon_R)\right]\sin(\omega t) =$$

$$\frac{1}{2}\sqrt{\left(\frac{H_{I0}}{1+k_D H_{I0} x}\right)^2 + \left(\frac{H_{RL_v}}{1+k_D H_{Rl}(L_v - x)}\right)^2 + 2\frac{H_{I0}}{1+k_D H_{I0} x}\frac{H_{RL_v}}{1+k_D H_{Rl}(L_v - x)}\cos(2kx + \epsilon)}\cos(\omega t + \psi), \tag{B.3}$$

where $\epsilon = \epsilon_I + \epsilon_R$, and $\psi = -\frac{H_{I0}(1+k_D H_{RL_v}(L_v - x))\sin(kx+\epsilon_I) - H_{RL_v}(1+k_D H_{I0} x)\sin(kx+\epsilon_R)}{H_{I0}(1+k_D H_{RL_v}(L_v - x))\cos(kx+\epsilon_I) + H_{RL_v}(1+k_D H_{I0} x)\cos(kx+\epsilon_R)}$. Thus, the wave height along the canopy can be obtained,

$$H(x) = \sqrt{\left(\frac{H_{I0}}{1+k_D H_{I0} x}\right)^2 + \left(\frac{H_{RL_v}}{1+k_D H_{Rl}(L_v - x)}\right)^2 + 2\frac{H_{I0}}{1+k_D H_{I0} x}\frac{H_{RL_v}}{1+k_D H_{Rl}(L_v - x)}\cos(2kx + \epsilon)}. \tag{B.4}$$

As the exponential decay form $\frac{H}{H_0} = e^{-k_D H_0 x}$ is also often used, the fitting formula for the wave height decay can also be obtained using a similar method, yielding

$$H(x) = \sqrt{H_{I0}^2 e^{-2k_D H_{I0} x} + H_{RL_v}^2 e^{-2k_D H_{RL_v}(L_v - x)} + 2H_{I0}H_{RL_v}e^{-k_D H_{I0} x - k_D H_{RL_v}(L_v - x)}\cos(2kx + \epsilon)}. \tag{B.5}$$

APPENDIX C: PIECEWISE FUNCTION METHDOD REALTING KOBAYASHI AND DALRYMPLE WAVE ATTENUATION MODELS

Appendix C.1. Extension of the solution by Kobayashi et al. (1993) to suspended canopy

In this derivation, the blade motion is not resolved but considered using bulk drag coefficient. The drag force of the canopy per unit water column (F_x) can be quantified using Morison equation (Morison et al., 1950) so that

$$F_x = \frac{1}{2}\rho C_D b N|u|u, \qquad -d_1 - d_2 \le z \le -d_1 \tag{C.1}$$

where ρ is water density, C_D is the bulk drag coefficient, b is blade width, N is the number of blades per unit horizontal area (also referred to as the canopy density), u is the wave orbital velocity, d_1 is the distance above the canopy to the still water level (SWL), d_2 is the length of the blade, z. Is vertical coordinate and positive upward with $z = 0$ at SWL.

By solving the linearized momentum equations, Kobayashi et al. (1993) derived the first-order approximated analytical solution for wave height decay with linearized drag for submerged canopy. To extend the solution to suspended canopy, the quadratic drag expressed in equation (C.1) is linearized as

$$F_x = \rho D u, \qquad -d_1 - d_2 \le z \le -d_1 \tag{C.2}$$

where D is the constant damping coefficient and obtained from the Lorentz's condition of equivalent work (Sollitt & Cross, 1972). This requires that the linear and quadratic drag from equations (C.2) and (C.1), respectively, accounts for the same amount of energy dissipation averaged over one wave period such that $\int_{-d_1-d_2}^{-d_1} \overline{\rho D u^2} dz = \int_{-d_1-d_2}^{-d_1} \overline{\frac{1}{2}\rho C_D b N|u|u^2} dz$ which can be rewritten as

$$D = \frac{\int_{-d_1-d_2}^{-d_1} \overline{\frac{1}{2}\rho C_D b N|u|u^2} dz}{\int_{-d_1-d_2}^{-d_1} \overline{\rho u^2} dz} \tag{C.3}$$

where the overbar indicates time average over one wave period. To formulate the analytical solution for wave height decay by weak damping ($D/2\omega \ll 1$, $\omega = 2\pi/T$ is the wave angular frequency), the local wave height (H) is assumed to decay exponentially as a function of horizontal distance (x) through the

canopy. Solving the linearized momentum equations and continuity equation (in Appendix D) yields the local wave height, $H(x)$, and given by

$$\frac{H(x)}{H_0} = e^{-k_D H x}, \tag{C.4}$$

where H_0 is the incident wave height such that $H(0) = H_0$, and k_D is the decay coefficient ([m^{-2}]) given by

$$k_D = \frac{C_D b N k}{9\pi} \frac{9\sinh k(d_2+d_3) - 9\sinh k d_3 + \sinh 3k(d_2+d_3) - \sinh 3k d_3}{\sinh kh(2kh+\sinh 2kh)}, \tag{C.5}$$

where k is the wave number defined by the dispersion relation, $\omega^2 = gk\tanh kh$, and g is the gravitational acceleration. The step by step procedure to derive equation (C.5) is provided in Appendix D. In Appendix D, the variation of wave orbital velocities through the canopy due to damping by vegetation is also presented, which can be used with Morison equations (Morison et al., 1950) to calculate the instantaneous wave load on the canopy. It should be noted that H on the right-hand side of equation (C.4) is the local wave height, which is an unknown. To obtain the explicit analytical solution, H on the righthand side of equation (C.4) is approximated by H_0 such that

$$\frac{H(x)}{H_0} = e^{-k_D H_0 x}, \tag{C.6}$$

However, approximating H with H_0 overestimates wave attenuation since $H \leq H_0$. To address this issue, a piecewise function method will be introduced in Appendix C.3. If $d_3 = 0$, equation (C.5) reduces to the solution by Kobayashi et al. (1993) for bottom-rooted submerged and emergent canopies.

Appendix C.2. Extension of the solution by Dalrymple et al. (1984) to suspended canopy

Assuming linear wave theory within a submerged canopy, Dalrymple et al. (1984) derived the solution for wave height decay through submerged vegetation by solving the energy conservation equation. For suspended canopy, the energy conservation equation becomes

$$\frac{\partial E c_g}{\partial x} = -\int_{-d_1-d_2}^{-d_1} \overline{F_x u}\, dz, \tag{C.7}$$

where $E = \rho g H^2/8$ is the local wave energy per unit horizontal area, $c_g = cn$ is the wave group velocity with $c = \omega/k$ being the wave celerity and $n = (1 + 2kh/\sinh 2kh)/2$. Substitution of the linearized

drag expressed in equation (C.2) into equation (C.7) yields the Kobayashi-based solution expressed in equation (C.6). Substituting the quadratic drag (C.1) into equation (C.7) yields the Dalrymple-based solution,

$$\frac{H(x)}{H_0} = \frac{1}{1+k_D H_0 x}, \tag{C.8}$$

where k_D has the same expression of equation (C.5). For bottom-rooted submerged canopy with $d_3 = 0$, equation (C.5) reduces to the solution by Dalrymple et al. (1984).

Appendix C.3. Piecewise function method linking Kobayashi- and Dalrymple-based techniques

To investigate the relationship between Kobayashi- and Dalrymple-based techniques, the piecewise function method is introduced as shown on Figure C.1. The canopy is divided into m equal segments in the wave direction such that the *j*th segment ranged between $x_{j-1} \le x \le x_j$ $(j = 1,2,\cdots,m)$ with $x_0 = 0$. Assuming equation (C.4) is applicable to the *j*th segment with the local incident wave height $H(x_{j-1})$, the local wave height can be obtained,

$$H(x) = H(x_{j-1}) e^{-k_D H(x_{j-1})(x-x_{j-1})}. \tag{C.9}$$

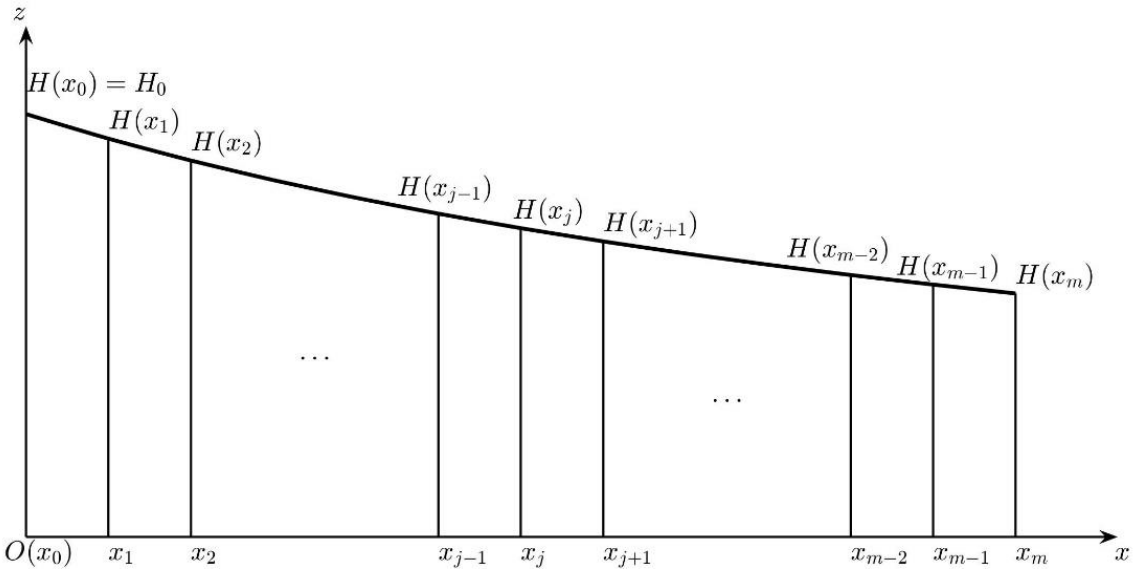

Figure C.1. A schematic illustration showing the piecewise function method. The waves propagate from left to right with incident wave height of H_0. The canopy is divided into m equal segments. For segment $j(j = 1,2,\cdots,m)$ with $x_{j-1} \le x \le x_j$, the local wave height is $H(x)$. At the leading edge of the canopy, $x_0 = 0$ and $H(x_0) = H_0$.

Reversing equation (C.9) and expanding the result into a series yields

$$\frac{1}{H(x)} = \frac{1}{H(x_{j-1})} + k_D(x - x_{j-1}) + 0\left[(x - x_{j-1})^2\right]. \quad \text{(C.10)}$$

Noting that

$$\frac{1}{H(x_{j-1})} = \frac{1}{H(x_{j-2})} + k_D(x_j - x_{j-2}) + 0\left[(x_{j-1} - x_{j-2})^2\right] \quad (j = 2,3,4,\dots). \quad \text{(C.11)}$$

adding equations (C.10) and (C.11) and taking the limit of the result as m approaches to infinity yields

$$\frac{1}{H(x)} = \frac{1}{H(x_0)} + k_D(x - x_{j-1} + x_j - x_{j-2} + \cdots + x_1 - x_0) = \frac{1}{H_0} + k_D x, \quad \text{(C.12)}$$

which can be rewritten as $H(x)/H_0 = 1/(1 + k_D H_0 x)$ in the form of Dalrymplebased solution in equation (C.8). The piecewise function method links the Kobayashi- and Dalrymple-based solutions, where the Kobayashi-based solution (C.6) is the approximation with one segment while the Dalrymple-based solution (C.8) is the approximation with infinite segments as shown on Figure C.2 given by $k_D H_0 L_v = 1$. Therefore, the Kobayashi-based solution provides a larger wave decay than Dalrymple-based solution.

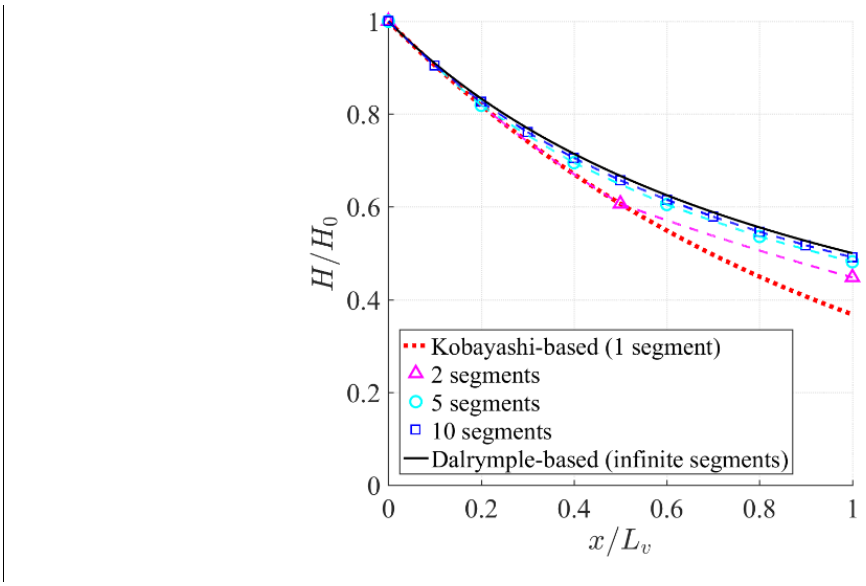

Figure C.2. Relations between the wave height decay solutions by Kobayashi- and Dalrymplebased techniques from the perspective of the piecewise function method, where $k_D H_0 L_v = 1$. larger wave decay than Dalrymple-based solution.

To find a suitable theoretical solution for the wave attenuation by canopies, the existing representative analytical models, i.e., Dalrymple- and Kobayashibased techniques, were analyzed. Based on energy conservation equations, the Dalrymple-based technique is able to consider a quadratic drag force formulation but cannot be used to determine the evolution (such as phase change) of wave orbital velocity in the canopy. To derive the explicit expressions of wave orbital velocity in the canopy, the Kobayashi-based technique solves the continuity and momentum equations by assuming an exponential wave decay and linearizing the drag force. However, the linearization of the drag force provides an overestimation in the wave attenuation. To address this issue, the piecewise function method was developed to link these two techniques and clarify their relationships. From the aspects of the piecewise function method, the Kobayashi-based technique overestimates the wave attenuation. However, the overestimation is less than 10% when $k_D H_0 L_v \leq 0.5$. Therefore these two techniques perform similar for the canopy having small size or/and small damping such that $k_D H_0 L_v \leq 0.5$. Otherwise, the Dalrymple-based technique is recommended.

As a first step to analyze the wave attenuation by suspended aquaculture farms, the models only considered the wave energy loss caused by the work performed by the drag force. Other wave energy loss sources such as wave reflection and the work by the frictional force from the canopy are neglected. In addition, the assumptions made during the derivation also could produce difference. For example, the drag coefficient should increase along the canopy length since the wave orbital velocity decreases due to wave decay. Therefore, the assumption of constant drag coefficient along the canopy length would underestimate the wave attenuation. Other assumptions, such as neglecting the advection terms, viscous stresses, interactions between wave components and the sheltering effects from neighbor blades could also introduce difference. Thus, in some cases, the Kobayashi-based solutions with slight overestimation may work better than Dalrymple-based solutions due to the uncertainty, which remains to be fully understood.

APPENDIX D: THE THREE-LAYER THEORETICAL SOLUTION FOR SUSPENDED AND SUBMERGED CANOPY BASED ON MOMENTUM AND CONTINUITY EQUATIONS

Appendix D.1. Governing equations

For the three-layer model shown on Figure 4.1, the free surface elevation above the still water level (SWL) is denoted by η_1, the vertical displacement of the interface between Layer 1 and 2 above $z = -d_1$ is denoted by η_2, and the vertical displacement of the interface between Layer 2 and 3 above $z = -d_1 - d_2$ is denoted by η_3, where d_1, d_2 and d_3 are the thicknesses for three layers. Thus, the water depth is $h = d_1 + d_2 + d_3$. In Layer $j(j = 1,2,3)$, the horizontal fluid velocity is denoted by u_j, the vertical fluid velocity is w_j, and the dynamics pressure is p_j. The total pressure is defined as $p_j - \rho g z$, where ρ is constant water mass density and g is gravitational acceleration.

Fluid motion is governed by the Navier-Stokes equations, taken as secondorder, nonlinear partial differential equations. To obtain the analytical solution at the first order, the second-order nonlinear advection terms as well as the viscous stresses are assumed to be negligible following Kobayashi et al. (1993).

In Layer 1, where $\eta_2 - d_1 < z < \eta_1$, continuity with linearized horizontal and vertical momentum are expressed as

$$\frac{\partial u_1}{\partial x} + \frac{\partial w_1}{\partial z} = 0, \tag{D.1}$$

$$\frac{\partial u_1}{\partial t} = -\frac{1}{\rho}\frac{\partial p_1}{\partial x}, \tag{D.2}$$

and

$$\frac{\partial w_1}{\partial t} = -\frac{1}{\rho}\frac{\partial p_1}{\partial z}, \tag{D.3}$$

with t as time. The linearized kinematic and dynamic boundary conditions at the free surface are given by

$$w_1 = \frac{\partial \eta_1}{\partial t} \quad \text{at} \quad z = 0 \tag{D.4}$$

and

$$p_1 = \rho g \eta_1 \quad \text{at} \quad z = 0. \tag{D.5}$$

In Layer 2, where $\eta_3 - d_1 - d_2 < z < \eta_2 - d_1$, continuity with linearized momentum are expressed as

$$\frac{\partial u_2}{\partial x} + \frac{\partial w_2}{\partial z} = 0, \tag{D.6}$$

$$\frac{\partial u_2}{\partial t} = -\frac{1}{\rho}\frac{\partial p_2}{\partial x} - \frac{F_x}{\rho}, \tag{D.7}$$

and

$$\frac{\partial w_2}{\partial t} = -\frac{1}{\rho}\frac{\partial p_2}{\partial z}, \tag{D.8}$$

where F_x is the horizontal force per unit volume acting on the canopy and expressed as

$$F_x = \frac{1}{2}\rho C_D b N |u_2| u_2, \tag{D.9}$$

where b is the averaged diameter or width of the canopy canopy component, N is the number of the canopy components per unit horizontal area, i.e., canopy density, C_D is the bulk drag coefficient. The linearized kinematic boundary condition at the interface between the Layer 1 and 2 is given by

$$w_2 = \frac{\partial \eta_2}{\partial t} \quad \text{at} \quad z = -d_1 \tag{D.10}$$

In addition, the linearized boundary conditions are also matched at the interface such that

$$p_2 = p_1 \quad \text{at} \quad z = -d_1 \tag{D.11}$$

and

$$w_2 = w_1 \quad \text{at} \quad z = -d_1. \tag{D.12}$$

In Layer 3, where $-h < z < \eta_3 - d_1 - d_2$, continuity and linearized momentum are expressed as

$$\frac{\partial u_3}{\partial x} + \frac{\partial w_3}{\partial z} = 0, \tag{D.13}$$

$$\frac{\partial u_3}{\partial t} = -\frac{1}{\rho}\frac{\partial p_3}{\partial x}, \tag{D.14}$$

and

$$\frac{\partial w_3}{\partial t} = -\frac{1}{\rho}\frac{\partial p_3}{\partial z}, \tag{D.15}$$

without consideration of the bottom friction. The linearized kinematic boundary conditions at the interface between Layer 2 and 3 and at the horizontal, impermeable bottom are given by

$$w_3 = \frac{\partial \eta_3}{\partial t} \quad \text{at} \quad z = -d_1 - d_2 \tag{D.16}$$

and

$$w_3 = 0 \quad \text{at} \quad z = -h. \tag{D.17}$$

Similarly, the linearized boundary conditions are continuity equations at the interface of Layers 2 and 3 at the interface such that

$$p_3 = p_2 \quad \text{at} \quad z = -d_1 - d_2 \tag{D.18}$$

and

$$w_3 = w_2 \quad \text{at} \quad z = -d_1 - d_2. \tag{D.19}$$

Appendix D.2. Linear solution

To derive the analytical solution for the above governing equations, the local wave height (H) is assumed to decay exponentially as a function of horizontal distance (x) through the canopy following Kobayashi et al. (1993) and is expressed as

$$H(x) = H_0 e^{-k_v x}, \tag{D.20}$$

where H_0 is the incident wave height, $H_0 = H(0)$, and k_v represents the rate of the exponentially decay. The corresponding free surface elevation is then expressed as

$$\eta_1 = \frac{H_0}{2} e^{-k_v x} \cos(kx - \omega t), \tag{D.21}$$

where k is the wave number and ω is the angular frequency. In this context, it is convenient to introduce a complex wave number ($\mathbf{k}$) defined as

$$\mathbf{k} = k + ik_v, \tag{D.22}$$

where $i = \sqrt{-1}$. Therefore, equation (D.21) can be rewritten as

$$\eta_1 = R\left\{\frac{H_0}{2} \exp[i(\mathbf{k}x - \omega t)]\right\}, \tag{D.23}$$

where $R\{\quad\}$ denotes the real part of the complex function in equation (D.23) and will be omitted hereafter. Therefore, the surface and interface elevations, velocities and pressures associated with equations (D.1)-(D.19) are also proportional to the exponential term in equation (D.23).

For Layer 1, u_1 and w_1 can be expressed in terms of p_1 according to equations (D.2) and (D.3),

$$u_1 = \frac{\mathbf{k}}{\rho\omega} p_1 \tag{D.24}$$

and

$$w_1 = \frac{1}{i\rho\omega}\frac{\partial p_1}{\partial z}. \tag{D.25}$$

Substituting equations (D.24) and (D.25) into equation (D.1) and solving with boundary conditions equations (D.4) and (D.5) yields the expression of p_1,

$$p_1 = \rho g \frac{H_0}{2}(\cosh \mathbf{k}z + \frac{\omega^2}{\mathbf{k}g}\sinh \mathbf{k}z)\exp[i(\mathbf{k}x - \omega t)]. \tag{D.26}$$

Substitution of equation (D.26) into equations (D.24) and (D.25) yields the expressions of u_1 and w_1,

$$u_1 = \frac{\mathbf{k}g}{\omega}\frac{H_0}{2}(\cosh \mathbf{k}z + \frac{\omega^2}{\mathbf{k}g}\sinh \mathbf{k}z)\exp[i(\mathbf{k}x - \omega t)] \tag{D.27}$$

and

$$w_1 = \frac{\mathbf{k}g}{i\omega}\frac{H_0}{2}(\sinh \mathbf{k}z + \frac{\omega^2}{\mathbf{k}g}\cosh \mathbf{k}z)\exp[i(\mathbf{k}x - \omega t)]. \tag{D.28}$$

For Layer 2, the nonlinear drag force is linearized following Kobayashi et al. (1993) to derive an analytical solution. The linearized drag force is

$$F_x = \rho D u_2, \tag{D.29}$$

where D is a constant damping coefficient in (C.3) and also shown here

$$D = \frac{\int_{-d_1-d_2}^{-d_1} \overline{\frac{1}{2}\rho C_D b N |u_2| u_2^2} dz}{\int_{-d_1-d_2}^{-d_1} \overline{\rho u_2^2} dz}. \tag{D.30}$$

Hence, u_2 and w_2 can be expressed in terms of p_2 according to equations (D.7), (D.8), and (D.29), with

$$u_2 = \frac{\mathbf{k}}{\rho(\omega + iD)} p_2 \tag{D.31}$$

and

$$w_2 = \frac{1}{i\rho\omega}\frac{\partial p_2}{\partial z}. \tag{D.32}$$

Substituting equations (D.31) and (D.32) into (D.6) and solving with boundary conditions defined by equations (D.11) and (D.12), the expression for p_2 can be obtained as

$$p_2 = \rho g \frac{H_0}{2}\left[\left(\cosh \mathbf{k}d_1 - \frac{\omega^2}{\mathbf{k}g}\sinh \mathbf{k}d_1\right)\cosh \gamma(d_1 + z) + \frac{\mathbf{k}}{\gamma}\left(-\sinh \mathbf{k}d_1 + \frac{\omega^2}{\mathbf{k}g}\cosh \mathbf{k}d_1\right)\sinh \gamma(d_1 + z)\right]\exp[i(\mathbf{k}x - \omega t)]. \tag{D.33}$$

where

$$\gamma^2 = \frac{\omega}{\omega + iD}\mathbf{k}^2. \tag{D.34}$$

Substituting equation (D.33) into (D.31) and (D.32) yields the explicit expressions of u_2 and w_2,

$$u_2 = \frac{\mathbf{k}g}{\omega + iD}\frac{H_0}{2}\left[\left(\cosh \mathbf{k}d_1 - \frac{\omega^2}{\mathbf{k}g}\sinh \mathbf{k}d_1\right)\cosh \gamma(d_1 + z) + \frac{\mathbf{k}}{\gamma}\left(-\sinh \mathbf{k}d_1 + \frac{\omega^2}{\mathbf{k}g}\cosh \mathbf{k}d_1\right)\sinh \gamma(d_1 + z)\right]\exp[i(\mathbf{k}x - \omega t)]. \tag{D.35}$$

and

$$w_2 = \frac{\gamma g}{i\omega}\frac{H_0}{2}\left[\left(\cosh \mathbf{k}d_1 - \frac{\omega^2}{\mathbf{k}g}\sinh \mathbf{k}d_1\right)\sinh \gamma(d_1 + z) + \frac{\mathbf{k}}{\gamma}\left(-\sinh \mathbf{k}d_1 + \frac{\omega^2}{\mathbf{k}g}\cosh \mathbf{k}d_1\right)\cosh \gamma(d_1 + z)\right]\exp[i(\mathbf{k}x - \omega t)]. \tag{D.36}$$

For Layer 3, u_3 and w_3 are expressed in the same manner as u_1 and w_1, i.e., both in terms of p_3 according to equation (D.14) and (D.15),

$$u_3 = \frac{\mathbf{k}}{\rho\omega}p_3 \tag{D.37}$$

and

$$w_3 = \frac{1}{i\rho\omega}\frac{\partial p_3}{\partial z}. \tag{D.38}$$

Substituting equation (D.37) and (D.38) into (D.13) and solving with boundary conditions as defined in equations (D.17) and (D.18), p_3 can be obtained as

$$p_3 = \rho g \frac{H_0}{2}\frac{\cosh \mathbf{k}(h+z)}{\cosh \mathbf{k}d_3}\left[\left(\cosh \mathbf{k}d_1 - \frac{\omega^2}{\mathbf{k}g}\sinh \mathbf{k}d_1\right)\cosh \gamma d_2 + \frac{\mathbf{k}}{\gamma}\left(\sinh \mathbf{k}d_1 - \frac{\omega^2}{\mathbf{k}g}\cosh \mathbf{k}d_1\right)\sinh \gamma d_2\right]\exp[i(\mathbf{k}x - \omega t)]. \tag{D.39}$$

Substitution of equation (D.39) into (D.37) and (D.38) yields the explicit expressions of u_3 and w_3,

$$u_3 = \frac{\mathbf{k}g}{\omega}\frac{H_0}{2}\frac{\cosh \mathbf{k}(h+z)}{\cosh \mathbf{k}d_3}\left[\left(\cosh \mathbf{k}d_1 - \frac{\omega^2}{\mathbf{k}g}\sinh \mathbf{k}d_1\right)\cosh \gamma d_2 + \frac{\mathbf{k}}{\gamma}\left(\sinh \mathbf{k}d_1 - \frac{\omega^2}{\mathbf{k}g}\cosh \mathbf{k}d_1\right)\sinh \gamma d_2\right]\exp[i(\mathbf{k}x - \omega t)]. \quad \text{(D.40)}$$

and

$$w_3 = \frac{\mathbf{k}g}{i\omega}\frac{H_0}{2}\frac{\sinh \mathbf{k}(h+z)}{\cosh \mathbf{k}d_3}\left[\left(\cosh \mathbf{k}d_1 - \frac{\omega^2}{\mathbf{k}g}\sinh \mathbf{k}d_1\right)\cosh \gamma d_2 + \frac{\mathbf{k}}{\gamma}\left(\sinh \mathbf{k}d_1 - \frac{\omega^2}{\mathbf{k}g}\cosh \mathbf{k}d_1\right)\sinh \gamma d_2\right]\exp[i(\mathbf{k}x - \omega t)]. \quad \text{(D.41)}$$

In the final step, the substitution of equations (D.36) and (D.41) into the boundary condition described by equation (D.19) yields the equation for the unknown complex wave number

$$\omega^2 = g\mathbf{k}\frac{\tanh \mathbf{k}d_1 + \frac{\gamma}{\mathbf{k}}\tanh \gamma d_2 + \tanh \mathbf{k}d_3 + \frac{\mathbf{k}}{\gamma}\tanh \mathbf{k}d_1 \tanh \gamma d_2 \tanh \mathbf{k}d_3}{1 + \frac{\gamma}{\mathbf{k}}\tanh \mathbf{k}d_1 \tanh \gamma d_2 + \tanh \mathbf{k}d_1 \tanh \mathbf{k}d_3 + \frac{\mathbf{k}}{\gamma}\tanh \gamma d_2 \tanh \mathbf{k}d_3}. \quad \text{(D.42)}$$

Substitution of equations (D.36) and (D.41) into the boundary conditions (D.10) and (D.16), respectively, can yield the expressions of η_2 and η_3.

Appendix D.3. First-order approximation for the linear solution

To simplify equation (D.42), a dimensionless damping coefficient ϵ is introduced as

$$\epsilon = \frac{D}{2\omega}. \quad \text{(D.43)}$$

For the case of weak damping such that $\epsilon \ll 1$, substituting equation (D.43) into (D.34) and neglecting the higher order terms $O(\epsilon^2)$ yields the first-order approximation of γ,

$$\gamma \approx \mathbf{k}(1 - i\epsilon). \quad \text{(D.44)}$$

Substituting equation (D.44) and (D.22) into (D.42) yields the first order approximation for the wave number (k),

$$\omega^2 \approx gk\tanh kh, \quad \text{(D.45)}$$

and the decay rate,

$$k_v \approx k\epsilon c_\epsilon, \quad \text{(D.46)}$$

where

$$c_\epsilon = \frac{2kd_2+\sinh 2k(d_2+d_3)-\sinh 2kd_3}{2kh+\sinh 2kh}. \tag{D.47}$$

The dispersion relationship described in equation (D.45) is identical to the form derived for linear waves without canopies. Therefore, the wave number (k) and the wave phase velocity are not affected by weak damping ($\epsilon \ll 1$).

In a similar manner, the first-order approximation for the dynamic pressure, horizontal and vertical velocity in each layer can also be obtained and given by

$$p_1 = \rho g \frac{H(x)}{2} \frac{\cosh k(h+z)}{\cosh kh} \cos(kx - \omega t + \epsilon c_{p_1}), \tag{D.48}$$

$$u_1 = \frac{gk}{\omega} \frac{H(x)}{2} \frac{\cosh k(h+z)}{\cosh kh} \cos(kx - \omega t + \epsilon c_{u_1}), \tag{D.49}$$

$$w_1 = \frac{gk}{\omega} \frac{H(x)}{2} \frac{\sinh k(h+z)}{\cosh kh} \cos(kx - \omega t + \epsilon c_{w_1}), \tag{D.50}$$

$$p_2 = \rho g \frac{H(x)}{2} \frac{\cosh k(h+z)}{\cosh kh} \cos(kx - \omega t + \epsilon c_{p_2}), \tag{D.51}$$

$$u_2 = \frac{gk}{\omega} \frac{H(x)}{2} \frac{\cosh k(h+z)}{\cosh kh} \cos(kx - \omega t + \epsilon c_{u_2}), \tag{D.52}$$

$$w_2 = \frac{gk}{\omega} \frac{H(x)}{2} \frac{\sinh k(h+z)}{\cosh kh} \cos(kx - \omega t + \epsilon c_{w_2}), \tag{D.53}$$

$$p_3 = \rho g \frac{H(x)}{2} \frac{\cosh k(h+z)}{\cosh kh} \cos(kx - \omega t + \epsilon c_{p_3}), \tag{D.54}$$

$$u_3 = \frac{gk}{\omega} \frac{H(x)}{2} \frac{\cosh k(h+z)}{\cosh kh} \cos(kx - \omega t + \epsilon c_{u_3}), \tag{D.55}$$

and

$$w_3 = \frac{gk}{\omega} \frac{H(x)}{2} \frac{\sinh k(h+z)}{\cosh kh} \cos(kx - \omega t + \epsilon c_{w_3}), \tag{D.56}$$

where

$$c_{p_1} = c_\epsilon[-\sinh kh \sinh kz \operatorname{sech} k(h+z) + kz \tanh k(h+z)], \tag{D.57}$$

$$c_{u_1} = c_\epsilon[\cosh kh \cosh kz \operatorname{sech} k(h+z) + kz \tanh k(h+z)], \tag{D.58}$$

$$c_{w_1} = c_\epsilon[\cosh kh \sinh kz \operatorname{csch} k(h+z) + kz \coth k(h+z)], \tag{D.59}$$

$$c_{p_2} = c_{p_1} - \sinh k(d_1-h) \sinh k(d_1+z) \operatorname{sech} k(h+z) - k(d_1+z) \tanh k(h+z), \tag{D.60}$$

$$c_{u_2} = c_{u_1} - \frac{1}{2}[3 + \cosh 2k(d_1 - h) + \sinh 2k(d_1 - h)\tanh k(h + z) + 2k(d_1 + z)\tanh k(h + z)],$$

(D.61)

$$c_{w_2} = c_{w_1} - \frac{1}{2}[1 + \cosh 2k(d_1 - h) + \sinh 2k(d_1 - h)\coth k(h + z) + 2k(d_1 + z)\coth k(h + z)],$$

(D.62)

$$c_{p_3} = c_\epsilon[-\sinh kh \sinh k(d_3 - h)\operatorname{sech} kd_3 - kh\tanh kd_3 + k(h + z)\tanh k(h + z)] + \sinh kd_2 \sinh k(d_1 - h)\operatorname{sech} kd_3 + kd_2\tanh kd_3, \quad \text{(D.63)}$$

$$c_{u_3} = c_\epsilon[\cosh kh \cosh k(d_3 - h)\operatorname{sech} kd_3 - kh\tanh kd_3 + k(h + z)\tanh k(h + z)] + \sinh kd_2 \sinh k(d_1 - h)\operatorname{sech} kd_3 + kd_2\tanh kd_3, \quad \text{(D.64)}$$

and

$$c_{u_3} = c_\epsilon[\cosh kh \cosh k(d_3 - h)\operatorname{sech} kd_3 - kh\tanh kd_3 + k(h + z)\coth k(h + z)] + \sinh kd_2 \sinh k(d_1 - h)\operatorname{sech} kd_3 + kd_2\tanh kd_3. \quad \text{(D.65)}$$

Compared with the linear wave theory without a canopy, the influence of the canopy on the dynamic pressure and the velocity described in equations (D.48)-(D.56) is represented as the wave height reduction and a phase lag.

Substituting equation (D.52) into (D.30), integrating and neglecting the higher order terms) yields the first order approximation of the damping coefficient,

$$D \approx H(x)\frac{2\omega C_D bN}{9\pi}\frac{9\sinh k(d_2+d_3) - 9\sinh kd_3 + \sinh 3k(d_2+d_3) - \sinh 3kd_3}{\sinh kh[2kd_2 + \sinh 2k(d_2+d_3) - \sinh 2kd_3]}, \quad \text{(D.66)}$$

where $H(x)$ is the local wave height considering decay. Substituting equation (D.66) into (D.43) yields the approximate expression of the dimensionless damping coefficient,

$$\epsilon \approx H(x)\frac{C_D bN}{9\pi}\frac{9\sinh k(d_2+d_3) - 9\sinh kd_3 + \sinh 3k(d_2+d_3) - \sinh 3kd_3}{\sinh kh[2kd_2 + \sinh 2k(d_2+d_3) - \sinh 2kd_3]}, \quad \text{(D.67)}$$

Substituting equation (D.67) into (D.46) yields the approximate expression of the decay rate,

$$k_v = k_D H(x), \quad \text{(D.68)}$$

where the decay coefficient

$$k_D = \frac{C_D bNk}{9\pi}\frac{9\sinh k(d_2+d_3) - 9\sinh kd_3 + \sinh 3k(d_2+d_3) - \sinh 3kd_3}{\sinh kh(2kh + \sinh 2kh)}. \quad \text{(D.69)}$$

To achieve constant values of D, ϵ, and k_v, the local wave heights in equations (D.66) to (D.68) are approximated using the incident wave height H_0 following Kobayashi et al. (1993).

APPENDIX E: NORMAL MODE SOLUTIONS FOR BLADE DISPLACEMENTS IN RANDOM WAVES

The governing equation (5.6) for the blade displacement in random waves is given by

$$m\ddot{\xi} + c\dot{\xi} + EI\xi'''' = \sum_{\omega} a\omega\Gamma[c\cos(kx - \omega t + \psi) + \omega m_I \sin(kx - \omega t + \psi)] \tag{E.1}$$

with the boundary conditions $\xi(0,t) = 0$, $\xi'(0,t) = 0$, $\xi''(l,t) = 0$, and $\xi'''(l,t) = 0$ for a cantilever beam. The solution of (E.1) can be written as the linear superposition of components of different frequencies

$$\xi = \Sigma_{\omega}\xi_{\omega}, \tag{E.2}$$

where ξ_{ω} is the solution of

$$m\ddot{\xi}_{\omega} + c\dot{\xi}_{\omega} + EI\xi_{\omega}'''' = a\omega\Gamma[c\cos(kx - \omega t + \psi) + \omega m_I \sin(kx - \omega t + \psi)]. \tag{E.3}$$

According to normal mode approach (Rao, 2007), the solution of (E.3) can be assumed as a linear superposition of the normal modes of the cantilever beam as

$$\xi_{\omega} = \sum_n \phi_n(s)\, q_n(t)\,, \tag{E.4}$$

where $\phi_n(s)$ is the nth normal mode and $q_n(t)$ is the nth generalized coordinate or modal participation coefficient. The normal modes for a cantilever beam are found from the equation

$$\phi'''' - \mu^4\phi = 0 \tag{E.5}$$

with boundary conditions $\phi(0) = 0$, $\phi'(0) = 0$, $\phi''(l) = 0$, and $\phi'''(l) = 0$. Solving (E.5) yields the nth normal mode,

$$\phi_n = (\cos\mu_n l + \cosh\mu_n l)(\sin\mu_n s - \sinh\mu_n s) + (\sin\mu_n l + \sinh\mu_n l)(\cosh\mu_n s - \cos\mu_n s), \tag{E.6}$$

where μ_n is the nth solution of

$$1 + \cos\mu l \cosh\mu l = 0. \tag{E.7}$$

Using (E.5) associated with the boundary conditions, the normal modes are proved to satisfy the orthogonality conditions,

$$\int_0^l G(s)\phi_n\phi_m ds = \begin{cases} \int_0^l G(s)\phi_n^2 ds\,, & n = m, \\ 0, & n \neq m. \end{cases} \tag{E.8}$$

where $G(s)$ is an arbitrary function. Substituting (E.4) into (E.3) yields

$$m\sum_n \phi_n \ddot{q}_n + c\sum_n \phi_n \dot{q}_n + EI\sum_n \phi_n'''' q_n = a\omega\Gamma[c\cos(kx-\omega t+\psi) + \omega m_I \sin(kx-\omega t+\psi)]. \tag{E.9}$$

Multiplying (E.9) by ϕ_m and integrating from 0 to l result in

$$\sum_n \left(\int_0^l m\phi_n\phi_m ds\, \ddot{q}_n + \int_0^l c\,\phi_n\phi_m ds\, \dot{q}_n + \int_0^l EI\phi_n''''\phi_m ds\, q_n\right) = a\omega\left[\int_0^l c\,\Gamma\phi_m ds\cos(kx-\omega t+\psi) + \omega\int_0^l m_I\Gamma\phi_m ds\sin(kx-\omega t+\psi)\right]. \tag{E.10}$$

Substituting (E.5) into (E.10) and using the orthogonality conditions (E.8) yield

$$\ddot{q}_n + 2\zeta_n\lambda_n\dot{q}_n + \lambda_n^2 q_n = a\omega[D_n\cos(kx-\omega t+\psi) + \omega I_n\sin(kx-\omega t+\psi)], \tag{E.11}$$

where $2\,\zeta_n\lambda_n = \int_0^l c\phi_n^2 ds \,/\, \int_0^l m\phi_n^2 ds$, $\lambda_n^2 = \mu_n^4 \int_0^l EI\phi_n^2 ds \,/\, \int_0^l m\phi_n^2 ds$, $D_n = \int_0^l c\Gamma\phi_n ds \,/\, \int_0^l m\phi_n^2 ds$, and $I_n = \int_0^l m_I\Gamma\phi_n ds \,/\, \int_0^l m\phi_n^2 ds$. The steady state solution for (E.11) is

$$q_n = a\omega Q_s\sin(kx-\omega t+\psi) + a\omega Q_c\cos(kx-\omega t+\psi), \tag{E.12}$$

where

$$Q_s = \frac{\omega I_n(\lambda_n^2-\omega^2) - D_n 2\zeta_n\lambda_n\omega}{(\lambda_n^2-\omega^2)^2 + (2\zeta_n\lambda_n\omega)^2} \tag{E.13}$$

and

$$Q_c = \frac{D_n(\lambda_n^2-\omega^2) + \omega I_n 2\zeta_n\lambda_n\omega}{(\lambda_n^2-\omega^2)^2 + (2\zeta_n\lambda_n\omega)^2} \tag{E.14}$$

Substituting (E.6) and (E.12) into (E.4) and the result into (E.2) yields the blade displacement,

$$\xi = \sum_\omega a\Gamma[\gamma_s\sin(kx-\omega t+\psi) + \gamma_c\cos(kx-\omega t+\psi)], \tag{E.15}$$

where the transfer functions γ_s and γ_c are given by

$$\gamma_s = \frac{\omega}{\Gamma}\sum_{n=1}^{\infty}\phi_n\frac{\omega I_n(\lambda_n^2-\omega^2) - D_n 2\zeta_n\lambda_n\omega}{(\lambda_n^2-\omega^2)^2 + (2\zeta_n\lambda_n\omega)^2} \tag{E.16}$$

and

$$\gamma_c = \frac{\omega}{\Gamma}\sum_{n=1}^{\infty}\phi_n\frac{D_n(\lambda_n^2-\omega^2) + \omega I_n 2\zeta_n\lambda_n\omega}{(\lambda_n^2-\omega^2)^2 + (2\zeta_n\lambda_n\omega)^2}. \tag{E.17}$$

BIOGRAPHY OF THE AUTHOR

Longhuan Zhu was born in Chongqing, China on November 17, 1989. He was raised in Chongqing and graduated from Chongqing Nankai Secondary School in 2008. Longhuan attended Tianjin University in China and obtained his Bachelor's degree and Master's degree in Naval Architecture and Ocean Engineering in 2012 and 2015, respectively. He started his PhD study at the University of Maine in 2015. During his PhD study, he has the following peer-reviewed journal articles and conference proceedings published:

[6] Bricknell, I.R., Birkel, S.D., Brawley, S.H., Van Kirk, T., Hamlin, H., Capistrant-Fossa, K., Huguenard, K., Van Walsum, G., Liu, Z.L., **Zhu, L.H.**, Grebe, G., Taccardi, E., Miller, M., Preziosi, B.M., Duffy, K., Byron, C.J., Quigley, C.T.C., Bowden T.J., Brady, D., Beal, B.F., Sappati, P.K., Johnson, T.R., Moeykens, S. (2020). Resilience of cold water aquaculture: A review of likely scenarios as climate changes in the Gulf of Maine. Reviews in Aquaculture. https://doi.org/10.1111/raq.12483

[5] **Zhu, L.**, Huguenard, K., Zou, Q., Fredriksson, D. W., & Xie, D. (2020). Aquaculture farms as nature-based coastal protection: Random wave attenuation by suspended and submerged canopies. *Coastal Engineering*. https://doi.org/10.1016/j.coastaleng.2020.103737

[4] **Zhu, L.**, Zou, Q., Huguenard, K., & Fredriksson, D. W. (2020). Mechanisms for the Asymmetric Motion of Submerged Aquatic Vegetation in Waves: A Consistent-Mass Cable Model. *Journal of Geophysical Research: Oceans*, 125(2). https://doi.org/10.1029/2019jc015517

[3] **Zhu, L.**, Huguenard, K., & Fredriksson, D. W. (2019). Dynamic Analysis of Longline Aquaculture Systems with a Coupled 3D Numerical Model. *Proceedings of the Twenty-Ninth (2019) International Ocean and Polar Engineering Conference*, 1305–1310. https://onepetro.org/conference-paper/ISOPE-I-19-235

[2] **Zhu, L.**, Huguenard, K., & Fredriksson, D. (2018). INTERACTION BETWEEN WAVES AND HANGING HIGHLY FLEXIBLE KELP BLADES. *Coastal Engineering Proceedings*, 1(36), 31. https://doi.org/10.9753/icce.v36.papers.31

[1] **Zhu, L.**, & Zou, Q. (2017). THREE-LAYER ANALYTICAL SOLUTION FOR WAVE ATTENUATION BY SUSPENDED AND NONSUSPENDED VEGETATION CANOPY. *Coastal Engineering Proceedings*, 1(35), 27. https://doi.org/10.9753/icce.v35.waves.27

Longhuan is a candidate for the Doctor of Philosophy degree in Civil and Environmental Engineering from the University of Maine in August 2020.